



UNIVERSITAT POLITÈCNICA DE CATALUNYA  
BARCELONATECH

---

Escola Tècnica Superior d'Enginyeria  
de Camins, Canals i Ports de Barcelona



---

Industrial doctoral programme in Civil and Geoenvironmental Engineering

# **GRANULAR FLOW CHARACTERISATION TOWARDS AN ENHANCED BULK FEEDER SELECTION**

by

Joel Torres Serra

Advisors:

Antonio Rodríguez Ferran    Enrique Romero Morales

---

Department of Civil and Environmental Engineering

Barcelona, 14 January 2021



## Abstract

In the packaging industry, a wide range of powders and bulk solids are handled in bagging equipment using different bulk feeding techniques. Quality of the packaging is critically affected by feeder performance, which is conditioned by the flowability of granular materials. Therefore, selecting the adequate feeder for every application is still a challenging industrial issue, commonly approached using a combination of conventional material tests and engineering know-how. The main goal of this thesis is to develop a testing protocol suited to better assess the flowability of industrial granular materials and to inform a methodology to objectify the decision-making process of feeder selection. The new TMI granular flow tester (GFT) is presented, consisting of a quasi-two-dimensional granular column collapse set-up, which is fully-instrumented to observe granular flow phenomena. The GFT covers the aeration and deaeration of the granular columns by packing state pre-conditioning, surface morphology of the initial granular columns and the final deposit configurations at run-out, basal load profiles of material deposition for the flow stages after collapse, and the flow front propagation and near-wall kinematics by particle image velocimetry analysis. This protocol is used to define new relevant flow parameters for industrial granular materials with sizes typically ranging from the order of  $\mu\text{m}$  to a few mm. A data analysis methodology is proposed to verify the feeder-type classification of granular materials in industrial practice by cluster analysis on data sets of material properties describing their flowability. Using conventional properties, granular materials are clustered into as many groups as main bulk feeder classes but a significant mismatch is noted, attributed to common industrial practice and incomplete flow characterisation. For this reason, the relevant flow parameters are included in an extended property data set, notably improving detection of similarly flowing materials. Furthermore, granular flow problems are modelled by the discrete element method to include the effects of material properties at the particle level (grain shape and size, segregation, and hygroscopicity issues) in the flow behaviour observed at the bulk level. Simulation results for the GFT set-up and an industrial case study of hopper filling are incorporated into this thesis.

*Keywords:* flowability, granular column collapse, particle image velocimetry, bulk feeding, classification, cluster analysis, discrete element method



## Acknowledgements

I am grateful to the following people for their help and support throughout this work:

The tandem formed by my thesis advisors, Antonio Rodríguez and Enriqué Romero, for their guidance, patience, and continued encouragement.

All members of the TMI team, including: my supervisor at TMI, Joan Caba, for his commitment to the project and proactive leadership; Xavier Arderiu, for his innovative contributions to the conception of the TMI granular flow tester (GFT); Manel Padullés, for fruitful discussions; Josep Manel Padullés, for creating the data acquisition platform for the GFT; David Padullés, for his concern for the IP protection of the GFT; Juanjo González, for his responsiveness and perseverance; the people at the Technical Department, for taking me in, especially Oriol Liarte and Alex Arbiol, for their help with the GFT design; Jordi Llovera and the people at the Workshop, for their continuous assistance; Ricard Benajas, for his dedication to the automation of the GFT; Pau Gairí, for his help with sensor communications; and Helena Bordes, for her help with funding applications and tracking.

Oscar Álvarez at DIBTEC 3D, for his help with the GFT design; Rodrigo Gómez, for his help during my two stays at the Geotechnical Laboratory of the UPC; Ferran Parera, for his generosity in allowing me to run preliminary tests with his sand slope box; Ignasi Mallafre, for his support in accessing the LaCàN computer cluster from outside the UPC; Deepak R. Tunuguntla, Irana F.C. Denissen, and the people at the MESA+ Institute (University of Twente), for their cooperation and for the invitation to visit them; the Industrial Doctorates Plan of the Government of Catalonia (2014 DI 075) and the Centre for the Development of Industrial Technology of the Government of Spain (IDI-20160298), for their financial support.

Last but not least, my family, my mother Núria, my brother August, and Louis, for standing by me through my *foggy* adventure.



# CONTENTS

<b>1</b>	<b>Introduction</b>	<b>1</b>
1.1	Background and motivation . . . . .	1
1.2	Aims and objectives . . . . .	2
1.3	Thesis layout . . . . .	3
1.4	Publications related to this thesis . . . . .	3
1.4.1	Journal papers . . . . .	4
1.4.2	Conference papers . . . . .	4
1.4.3	Patents . . . . .	5
1.4.4	Research data . . . . .	5
1.4.5	Technical magazine articles . . . . .	5
1.5	References . . . . .	5
<b>2</b>	<b>A new column collapse apparatus for the characterisation of the flowability of granular materials</b>	<b>7</b>
2.1	Introduction . . . . .	9
2.2	Experimental set-up . . . . .	10
2.3	Materials and testing protocols . . . . .	12
2.4	Results and discussion . . . . .	13
2.4.1	Initial packing state pre-conditioning . . . . .	14
2.4.2	Free surface morphology and angle of repose . . . . .	15
2.4.3	Basal load profiles and equilibrium flow heights . . . . .	16
2.4.4	Frontal flow visualisations and transient flow heights . . . . .	18
2.4.5	PIV-based near-wall kinematics and energy balance . . . . .	19
2.5	Summary and conclusions . . . . .	22
2.5.1	Column collapse apparatus . . . . .	23
2.5.2	Flow characterisation . . . . .	23
2.5.3	Outlook . . . . .	24
2.6	List of symbols . . . . .	24
2.6.1	Latin symbols . . . . .	24
2.6.2	Greek symbols . . . . .	24
2.7	Acknowledgements . . . . .	24
2.8	Appendix A. Energy balance by DEM simulations . . . . .	24
2.9	References . . . . .	25

<b>3</b>	<b>Classification of granular materials via flowability-based clustering with application to bulk feeding</b>	<b>29</b>
3.1	Introduction . . . . .	31
3.2	Data analysis methodology . . . . .	33
3.2.1	Observation selection . . . . .	33
3.2.2	Variable reduction . . . . .	34
3.2.3	Cluster analysis . . . . .	34
3.3	Analysis of an extended property data set . . . . .	35
3.4	Conclusions . . . . .	39
3.5	Declaration of Competing Interest . . . . .	39
3.6	Acknowledgements . . . . .	39
3.7	Appendix A. Cluster analysis validation . . . . .	40
3.8	Appendix B. Granular PIV approach . . . . .	41
3.9	Appendix C. Interpretation of PCA in high dimensions . . . . .	42
3.10	References . . . . .	44
<b>4</b>	<b>Study of grain-scale effects in bulk handling using discrete element simulations</b>	<b>47</b>
4.1	Introduction . . . . .	49
4.1.1	Particle size . . . . .	50
4.1.2	Particle shape . . . . .	50
4.1.3	Particle hygroscopicity . . . . .	50
4.1.4	Motivation . . . . .	50
4.2	DEM contact model . . . . .	50
4.3	Results and discussion . . . . .	51
4.3.1	Problem set-up . . . . .	51
4.3.2	Particle size dispersity . . . . .	51
4.3.2.1	Height profiles . . . . .	52
4.3.2.2	Micro-macro mapping . . . . .	52
4.3.3	Particle shape non-sphericity . . . . .	53
4.3.3.1	Granular column porosity . . . . .	53
4.3.3.2	Particle orientation . . . . .	53
4.3.3.3	Height profiles . . . . .	54
4.3.3.4	Energy balance . . . . .	55
4.3.4	Particle hygroscopicity . . . . .	55
4.3.4.1	Height profiles . . . . .	55
4.3.4.2	Energy balance . . . . .	56
4.3.5	Particle size segregation . . . . .	57
4.3.5.1	Zero alternative . . . . .	57
4.3.5.2	Analysis of alternatives . . . . .	57
4.4	Concluding remarks . . . . .	59
4.5	List of symbols . . . . .	63
4.5.1	Latin symbols . . . . .	63
4.5.2	Greek symbols . . . . .	63
4.6	Declaration of Competing Interest . . . . .	63



4.7	Acknowledgements . . . . .	63
4.8	References . . . . .	63
<b>5</b>	<b>Conclusions</b>	<b>65</b>
5.1	Contributions . . . . .	65
5.2	Outlook . . . . .	67
5.3	References . . . . .	68
<b>A</b>	<b>Spanish Patent ES2695451B2: <i>Dispositivo para ensayo de colapso de una columna de material pulverulento o granular</i></b>	<b>69</b>
A.1	Bibliographic data . . . . .	71
A.2	Description . . . . .	72
A.3	Claims . . . . .	82
A.4	Drawings . . . . .	84
<b>B</b>	<b>Image analysis manual: PIV Analysis of SuperSlow Motion videos</b>	<b>89</b>
B.1	Pre-process . . . . .	89
B.2	Post-process . . . . .	92
B.3	MATLAB scripts . . . . .	94
B.4	ImageJ scripts . . . . .	103
B.5	References . . . . .	104



## 1.1 Background and motivation

Técnicas Mecánicas Ilerdenses, S.L. (TMI) is a company founded in the year 2000 and based in Lleida (Spain), dedicated to the design, manufacture, and supply of bulk handling equipment for bagging, palletising, and stretch wrapping of powders and bulk solids [1]. A wide range of granular materials produced by different industrial sectors (Figure 1.1) are processed in bagging lines using different material conveying techniques for the operation of bulk feeding [2], as illustrated in Figure 1.2. Performance of the feeder systems critically affects the quality of the packaging, and thus the selection of the adequate feeder for every application is of major interest [3]. Bulk feeder performance is conditioned by the flow behaviour or flowability of the granular materials [4], which is often estimated in everyday industrial practice from a combination of qualitative testing and the engineering know-how of the decision maker. Therefore, there is still a need for finding new testing protocols to quantify flowability and help to develop objective strategies for proper equipment selection.

Various approaches have been proposed to assess flowability from experiments based on the effect that material properties have on the observed behaviour for different flow regimes [5]. At the particle level, mainly

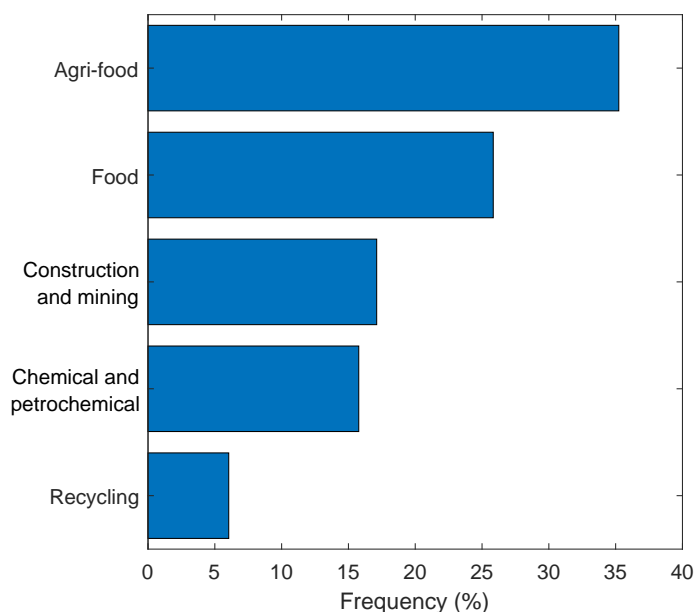


**Figure 1.1** TMI projects grouped by industrial sectors of the end user. Data provided by TMI from 298 projects executed in the period from 2001 to 2018.

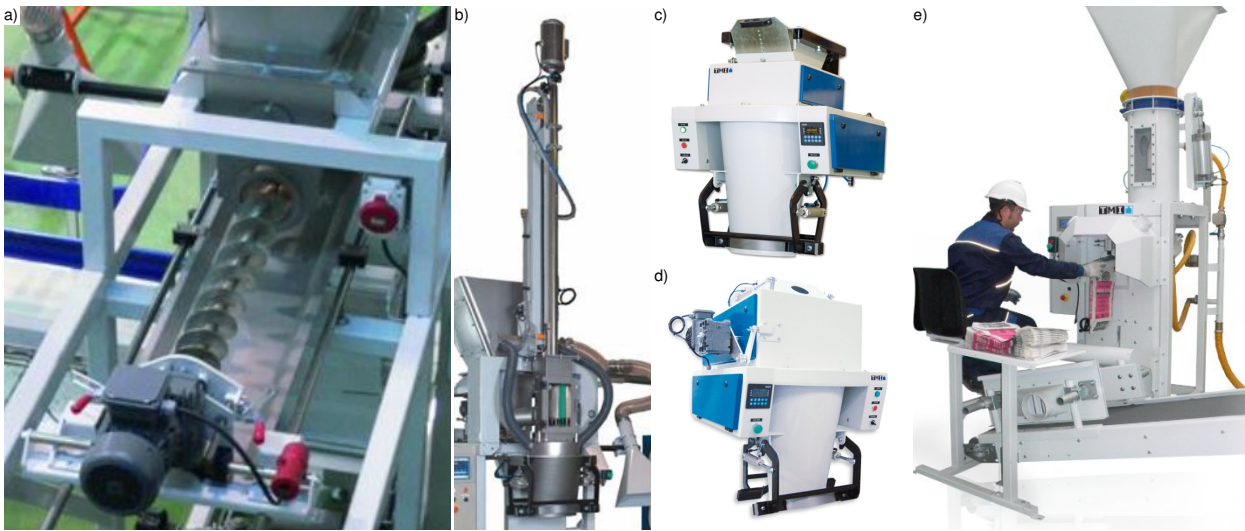


**Figure 1.2** Views of main bulk feeding systems: a) detachable screw feeder; b) vacuum nozzle shaft for screw feeding with deaeration; gravity (c) and belt (d) feeder systems coupled to the bag filling spout and clamp; e) operation of a semi-automatic bagging machine with fluidisation chamber feeding system. Reproduced with permission from TMI.

the particle size [6], shape [7], and density [8] have been studied. At the bulk level, small-scale laboratory tests have been used to measure flow properties at the quasi-static [9], dense [10], and dilute [11] flow regimes. Full-scale pilot plant testing can also be used to reproduce specific processing conditions. Alternatively, intermediate-scale tests such as the granular column collapse experiment [12, 13] provide a simple set-up to investigate complex granular flows [14], thus opening the door to the analysis and modelling for the wide range of materials, with particle sizes from the order of  $\mu\text{m}$  to a few mm.

From the numerical point of view, many continuum and discrete approaches to granular flow simulations have been studied [15]. The Discrete Element Method (DEM) [16] allows controlling the particle parameters involved in granular flows at the bulk level [17]. For this reason, the DEM is increasingly used to better understand and reproduce flows of complex particle systems for industrial applications [18].

## 1.2 Aims and objectives

In response to the industrial needs, the primary aim of this thesis is to develop an ad hoc experimental characterisation protocol for measuring the flowability of powders and bulk solids, which is used to propose a methodology for selecting the adequate feeding techniques. The following specific research objectives stem from the general purpose of this work:

1. Designing, manufacturing, testing, and calibrating an experimental granular column collapse apparatus suited to flow characterisation of industrial granular materials.
2. Finding relevant flow parameters from measurements obtained with the newly developed testing protocol.
3. Defining a material classification methodology to assist in the decision-making process of bulk feeder selection based on the relevant flow parameters and other fundamental material properties from standard tests.
4. Modelling the effect of material properties at the particle level to gain insight into intermediate and full-scale problem set-ups by DEM simulations.

### 1.3 Thesis layout

The body of this industrial doctoral thesis is divided into three chapters:

**Chapter 2** presents a new fully-instrumented granular column collapse apparatus, hereafter the TMI granular flow tester (GFT), and the experimental methodology to characterise flowability from observations, namely the fluidisation and deaeration of the granular columns by a reversible pneumatic circuit; the free surface morphology of the samples at rest by a 3D laser line profile sensor; the basal load distribution during flow propagation by a set of load cells; and the frontal flow kinematics and energy balance by particle image velocimetry (PIV) analysis of high-speed video recordings. The study of three representative granular materials illustrates the capabilities of the GFT showing that it is an effective tool to measure distinctive traits of granular flow. This chapter is a published journal paper (Torres-Serra *et al.*, 2020) reproduced here in its final version. *Objectives addressed:* 1 and 2.

**Chapter 3** proposes a methodology based on cluster analysis of data sets including quantitative flow descriptors. A first data set of 174 powders and grains characterised by six conventional material properties is used to identify the sources of uncertainty in feeder-type classification, including incomplete characterisation by standard flow descriptors. Accordingly, the analysis is refined on a second data set of 11 representative materials, fully-characterised by eight conventional properties and 118 new variables from measurements of 20 specialised properties obtained with the GFT. The findings confirm that the detection of similarly flowing granular materials is significantly improved by considering their full characterisation. This chapter is a published journal paper (Torres-Serra *et al.*, 2021a) reproduced here in its final version. *Objectives addressed:* 2 and 3.

**Chapter 4** examines by DEM simulations the effects of particle size dispersity, shape, and hygroscopicity, for the GFT set-up, and particle size segregation during filling of a material reception hopper. For the granular column collapse set-up, identical and narrow disperse particle size distributions are compared, and coarse-graining of the discrete results into continuum fields is introduced; systems of spheroidal particles ranging from spheres to prolate spheroids are modelled to evaluate changes in the average porosity and particle orientation with increasing non-sphericity; and a liquid bridge model is explored to reproduce capillary forces for liquid contents within the pendular regime. Next, the industrial case study is simulated using quasi-bidisperse mixtures of spheres to analyse three different design alternatives for the observed segregation mechanisms. This chapter is a published journal paper (Torres-Serra *et al.*, 2021b) reproduced here in its final version. *Objectives addressed:* 4.

Each chapter presents a self-contained structure, with introductory sections providing research background and reviewing the state of the art of the fields covered, and with closing sections detailing the main concluding remarks and the outlook for future research. With this in mind, a concluding overview of the contributions and outlook of this thesis is given in [Chapter 5](#).

The GFT invention has been granted a Spanish Patent (Técnicas Mecánicas Ilerdenses, S.L., 2019), which is included in [Appendix A](#). In addition, a manual with accompanying scripts describing image analysis pre- and post-processing for PIV analysis of high-speed video recordings can be found in [Appendix B](#).

### 1.4 Publications related to this thesis

The following is a list of all the publications produced in the course of this research.

### 1.4.1 Journal papers

J. Torres-Serra, E. Romero, and A. Rodríguez-Ferran, A new column collapse apparatus for the characterisation of the flowability of granular materials, *Powder Technology*, vol. 362, pp. 559–577, 2020. DOI: [10.1016/j.powtec.2019.11.080](https://doi.org/10.1016/j.powtec.2019.11.080).

J. Torres-Serra, A. Rodríguez-Ferran, and E. Romero, Classification of granular materials via flowability-based clustering with application to bulk feeding, *Powder Technology*, vol. 378, pp. 288–302, 2021a. DOI: [10.1016/j.powtec.2020.09.022](https://doi.org/10.1016/j.powtec.2020.09.022).

J. Torres-Serra, A. Rodríguez-Ferran, and E. Romero, Study of grain-scale effects in bulk handling using discrete element simulations, *Powder Technology*, vol. 382, pp. 284–299, 2021b. DOI: [10.1016/j.powtec.2020.12.029](https://doi.org/10.1016/j.powtec.2020.12.029).

### 1.4.2 Conference papers

J. Torres-Serra, E. Romero, A. Rodríguez-Ferran, J. Caba, X. Arderiu, J.-M. Padullés, and J. González, Flowability of granular materials with industrial applications - An experimental approach, in *8th International Conference on Micromechanics of Granular Media, Powders and Grains 2017*, (Montpellier, France, 3-7 July 2017), F. Radjai, S. Nezamabadi, S. Luding, and J. Y. Delenne, Eds., *EPJ Web of Conferences*, vol. 140, 2017, p. 03 068. DOI: [10.1051/epjconf/201714003068](https://doi.org/10.1051/epjconf/201714003068).

J. Torres-Serra, D. R. Tunuguntla, I. F. C. Denissen, A. Rodríguez-Ferran, and E. Romero, Discrete element modelling of granular column collapse tests with industrial applications, in *5th International Conference on Particle-Based Methods - Fundamentals and Applications, PARTICLES 2017*, (Hannover, Germany, 26-28 September 2017), P. Wriggers, M. Bischoff, E. Oñate, D. R. J. Owen, and T. Zohdi, Eds., International Centre for Numerical Methods in Engineering (CIMNE), 2017, pp. 530–538. [Online]. Available: <http://hdl.handle.net/2117/115116>.

J. Torres-Serra, E. Romero, and A. Rodríguez-Ferran, A New Granular Column Collapse Device to Characterise Flowability of Bulk Materials, in *18th International Conference on Experimental Mechanics, ICEM 2018*, (Brussels, Belgium, 1–5 July 2018), D. Van Hemelrijck, D. Aggelis, N. De Belie, F. Delaunois, T. Geernaerts, P. Guillaume, A. M. Habraken, P. Hendrick, E. Reynders, A. Simar, and S. Vanlanduit, Eds., *Proceedings*, vol. 2, no. 8, 2018, p. 488. DOI: [10.3390/ICEM18-05389](https://doi.org/10.3390/ICEM18-05389).

J. Torres-Serra, E. Romero, and A. Rodríguez-Ferran, Hygroscopicity issues in powder and grain technology, in *7th International Conference on Unsaturated Soils, UNSAT 2018*, (Hong Kong, China, 3-5 August 2018), C. W. W. Ng, A. K. Leung, A. C. F. Chiu, and C. Zhou, Eds., Hong Kong University of Science and Technology, 2018, pp. 805–810. [Online]. Available: <http://hdl.handle.net/2117/129402>.

J. Torres-Serra, J. Caba, A. Rodríguez-Ferran, and E. Romero, Classifying granular materials for feeding performance using experimental and numerical techniques, in *9th International Conference on Conveying and Handling of Particulate Solids, CHoPS 2018*, (London, United Kingdom, 10-14 September 2018), Wolfson Centre for Bulk Solids Handling Technology, 2018. [Online]. Available: <http://hdl.handle.net/2117/129673>.

### 1.4.3 Patents

Técnicas Mecánicas Ilerdenses, S.L., *Dispositivo para ensayo de colapso de una columna de material pulverulento o granular*, inventors: J. Torres Serra, X. Arderiu Cabau, J.M. Padullés Ribalta, J. Caba Muntada, J.J. González Toledano, E.E. Romero Morales, A. Rodríguez Ferran, Spanish Patent ES2695451B2, 2019. [Online]. Available: <https://patentscope.wipo.int/search/en/detail.jsf?docId=ES235596513>.

### 1.4.4 Research data

J. Torres-Serra, *Data for: Classification of granular materials via flowability-based clustering with application to bulk feeding*, version V1, Mendeley Data, 2020. [Dataset]. DOI: [10.17632/sxg3hg3txw.1](https://doi.org/10.17632/sxg3hg3txw.1).

### 1.4.5 Technical magazine articles

J. Torres Serra, Caracterización de sólidos para su manejo en maquinaria de ensacado, *Industria Química*, no. 32, pp. 66–69, Feb. 2016, ISSN: 2340-2113. [Online]. Available: <https://www.industriaquimica.es/articulos/20160316/caracterizacion-solidos-manejo-maquinaria-ensacado>.

## 1.5 References

- [1] Técnicas Mecánicas Ilerdenses, S.L. (2021). Líneas completas de ensacado, paletizado y enfardado - TMI, [Online]. Available: <https://www.tmipal.com/>.
- [2] A. W. Roberts, Bulk Solids Handling. An Historical Overview and Current Developments, *Bulk Solids Handling*, vol. 26, no. 6, pp. 392–414, 416–419, 2006, ISSN: 0173-9980.
- [3] J. W. Carson, “Hopper/Bin Design,” in *Bulk Solids Handling: Equipment Selection and Operation*, D. McGlinchey, Ed. Blackwell Publishing, Ltd, 2008, pp. 68–98. DOI: [10.1002/9781444305449.ch2](https://doi.org/10.1002/9781444305449.ch2).
- [4] J. A. H. de Jong, A. C. Hoffmann, and H. J. Finkers, Properly determine powder flowability to maximize plant output, *Chemical Engineering Progress*, vol. 95, no. 4, pp. 25–34, 1999, ISSN: 0360-7275.
- [5] H. M. Jaeger, S. R. Nagel, and R. P. Behringer, Granular solids, liquids, and gases, *Reviews of Modern Physics*, vol. 68, pp. 1259–1273, 4 1996. DOI: [10.1103/RevModPhys.68.1259](https://doi.org/10.1103/RevModPhys.68.1259).
- [6] F. Boschini, V. Delaval, K. Traina, N. Vandewalle, and G. Lumay, Linking flowability and granulometry of lactose powders, *International Journal of Pharmaceutics*, vol. 494, no. 1, pp. 312–320, 2015. DOI: [10.1016/j.ijpharm.2015.08.030](https://doi.org/10.1016/j.ijpharm.2015.08.030).
- [7] T. Börzsönyi and R. Stannarius, Granular materials composed of shape-anisotropic grains, *Soft Matter*, vol. 9, pp. 7401–7418, 31 2013. DOI: [10.1039/C3SM50298H](https://doi.org/10.1039/C3SM50298H).
- [8] A. Santomaso, P. Lazzaro, and P. Canu, Powder flowability and density ratios: The impact of granules packing, *Chemical Engineering Science*, vol. 58, no. 13, pp. 2857–2874, 2003. DOI: [https://doi.org/10.1016/S0009-2509\(03\)00137-4](https://doi.org/10.1016/S0009-2509(03)00137-4).
- [9] J. Schwedes, Review on testers for measuring flow properties of bulk solids, *Granular Matter*, vol. 5, no. 1, pp. 1–43, 2003. DOI: [10.1007/s10035-002-0124-4](https://doi.org/10.1007/s10035-002-0124-4).
- [10] R. Freeman, Measuring the flow properties of consolidated, conditioned and aerated powders — A comparative study using a powder rheometer and a rotational shear cell, *Powder Technology*, vol. 174, no. 1, pp. 25–33, 2007. DOI: [10.1016/j.powtec.2006.10.016](https://doi.org/10.1016/j.powtec.2006.10.016).

- [11] J. M. Valverde and A. Castellanos, Types of gas fluidization of cohesive granular materials, *Physical Review E*, vol. 75, p. 031 306, 3 2007. DOI: [10.1103/PhysRevE.75.031306](https://doi.org/10.1103/PhysRevE.75.031306).
- [12] G. Lube, H. E. Huppert, R. S. J. Sparks, and M. A. Hallworth, Axisymmetric collapses of granular columns, *Journal of Fluid Mechanics*, vol. 508, pp. 175–199, 2004. DOI: [10.1017/S0022112004009036](https://doi.org/10.1017/S0022112004009036).
- [13] E. Lajeunesse, A. Mangeney-Castelnau, and J. P. Vilotte, Spreading of a granular mass on a horizontal plane, *Physics of Fluids*, vol. 16, no. 7, pp. 2371–2381, 2004. DOI: [10.1063/1.1736611](https://doi.org/10.1063/1.1736611).
- [14] M. Cabrera and N. Estrada, Granular column collapse: Analysis of grain-size effects, *Physical Review E*, vol. 99, p. 012 905, 1 2019. DOI: [10.1103/PhysRevE.99.012905](https://doi.org/10.1103/PhysRevE.99.012905).
- [15] F. Radjai, J.-N. Roux, and A. Daouadji, Modeling Granular Materials: Century-Long Research across Scales, *Journal of Engineering Mechanics*, vol. 143, no. 4, p. 04 017 002, 2017. DOI: [10.1061/\(ASCE\)EM.1943-7889.0001196](https://doi.org/10.1061/(ASCE)EM.1943-7889.0001196).
- [16] P. A. Cundall and O. D. L. Strack, A discrete numerical model for granular assemblies, *Géotechnique*, vol. 29, no. 1, pp. 47–65, 1979. DOI: [10.1680/geot.1979.29.1.47](https://doi.org/10.1680/geot.1979.29.1.47).
- [17] C. J. Coetzee, Calibration of the discrete element method and the effect of particle shape, *Powder Technology*, vol. 297, pp. 50–70, 2016. DOI: [10.1016/j.powtec.2016.04.003](https://doi.org/10.1016/j.powtec.2016.04.003).
- [18] M. Marigo and E. H. Stitt, Discrete Element Method (DEM) for Industrial Applications: Comments on Calibration and Validation for the Modelling of Cylindrical Pellets, *KONA Powder and Particle Journal*, vol. 32, pp. 236–252, 2015. DOI: [10.14356/kona.2015016](https://doi.org/10.14356/kona.2015016).

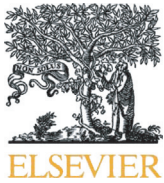


# **A NEW COLUMN COLLAPSE APPARATUS FOR THE CHARACTERISATION OF THE FLOWABILITY OF GRANULAR MATERIALS**

---

Reproduced from: J. Torres-Serra, E. Romero, and A. Rodríguez-Ferran, A new column collapse apparatus for the characterisation of the flowability of granular materials, *Powder Technology*, vol. 362, pp. 559–577, 2020. DOI: [10.1016/j.powtec.2019.11.080](https://doi.org/10.1016/j.powtec.2019.11.080)





Contents lists available at ScienceDirect

## Powder Technology

journal homepage: [www.elsevier.com/locate/powtec](http://www.elsevier.com/locate/powtec)

## A new column collapse apparatus for the characterisation of the flowability of granular materials

J. Torres-Serra<sup>a,b,\*</sup>, E. Romero<sup>b</sup>, A. Rodríguez-Ferran<sup>b</sup>

<sup>a</sup> *Técnicas Mecánicas Ilerdenses, S.L., Polígono industrial Camí dels Frares, c. Alcarràs, parc. 66, 25190 Lleida, Spain*

<sup>b</sup> *Department of Civil and Environmental Engineering, Universitat Politècnica de Catalunya, Campus Nord, c. Jordi Girona, 1-3, 08034 Barcelona, Spain*

### ARTICLE INFO

#### Article history:

Received 10 April 2019

Received in revised form 10 October 2019

Accepted 22 November 2019

Available online 23 November 2019

#### Keywords:

Granular column collapse

Run-out

Flow height

Particle image velocimetry

Flowability

### ABSTRACT

The packaging industry is lacking a standard methodology to characterise the granular flow of a wide range of powders and grains in actual handling conditions. We present a new fully-instrumented granular column collapse apparatus for the experimental investigation of granular flow phenomena, by a quasi-two-dimensional set-up with novel features including: a lifting gate activated by a parallelogram mechanism for material release; a reversible pneumatic circuit to impose fluidised and vacuum conditions to the initial granular column; a set of load cells to monitor the basal load distribution during flow propagation; a 3D laser line profile sensor to scan the free surface morphology of the samples at rest; and a high-speed video recording set to capture near-wall flow visualisations and relevant kinematic measures by particle image velocimetry. The selected results on dry flows of oat flakes, copper sulphate fertiliser, and talc powder samples show their distinctive flow dynamics, indicating the good flowability of fertiliser compared to the poor flowability of talc. This research has implications for the selection and design of bulk solids handling equipment, and the calibration and validation of mechanical and numerical models.

© 2019 Elsevier B.V. All rights reserved.

### 1. Introduction

A wide range of powders and grains are handled in the packaging industry using bulk solids handling equipment, among which bag filling systems are of our interest. The performance of bagging machinery and the packaging quality rely on the first unit operation of dosing of the granular materials [1]. Dosing is carried out by gain-in-weight batching systems, consisting of a volumetric feeder that regulates the flow of bulk solids out of a supply hopper and into a weighing hopper [2]. Based on the applied material conveying techniques, a variety of feeder types exist [3]: free discharge by gravity feeders and rotary valves; positive displacement by belt, screw, and vibratory tray feeders; and pneumatic transport by fluidisation chambers. The operating efficiency of the feeders is critically affected by the flowability of the granular materials [4]. Nevertheless, it is still a common practice in the industry to base the feeder selection and design strategies solely on a qualitative assessment of flowability, the unreliability of which entails financial and environmental costs throughout the life cycle of the

equipment. Therefore, the lack of a standard protocol for characterising granular flow phenomena remains a challenging issue in practical handling [5]. This motivates the development of experimental methodologies that can be equally applied to the diversity of powders and grains on the market. Then, robust classification strategies can be designed, relying on redundant material databases of the extracted parameters, combined with the engineering know-how and the mechanical behaviour modelling from experimental observations.

Flowability of granular materials involves complex mechanical behaviour issues, such as particle size segregation, affecting the homogeneity of free-flowing material batches [6], and jamming processes [7], which lead to the formation of stable arch and rathole structures [8,9]. The constitutive behaviour of bulk solids is otherwise affected by environmental conditions such as the ambient temperature and the relative humidity, the latter affecting the amount of stored water in hygroscopic materials [10]. In turn, the exposure to environmental conditions alters flowability by controlling slip-stick and caking processes [11,12]. The effect on flowability of the material properties of powders and grains produced by the food and agri-food, construction and mining, chemical and pharmaceutical, and recycling industries [13–17] has been studied using techniques at different scales. At the microscopic or grain scale, most work has focused on the investigation of the particle size, shape, and density; whereas at the macroscopic or bulk scale, attention has been paid to robust physical measurements including the compressibility, defined in terms of uniaxial compression stress, and shear testing in

\* Corresponding author at: Department of Civil and Environmental Engineering, Universitat Politècnica de Catalunya, Campus Nord, c. Jordi Girona, 1-3, 08034 Barcelona, Spain.

E-mail addresses: [joel.torres@upc.edu](mailto:joel.torres@upc.edu) (J. Torres-Serra), [enrique.romero-morales@upc.edu](mailto:enrique.romero-morales@upc.edu) (E. Romero), [antonio.rodriiguez-ferran@upc.edu](mailto:antonio.rodriiguez-ferran@upc.edu) (A. Rodríguez-Ferran).

the quasi-static regime [18]. Moreover, flowability for specific applications—for instance additive manufacturing or die filling—has been researched respectively by avalanching and indentation [19,20]. Other methodologies exist that provide conventional parameters, albeit with indirect physical interpretations, such as the discharge rates, compressibility in terms of tapping densities, or the angle of repose [21,22].

Over the last two decades, granular column collapse experiments have received rising attention, aiming at understanding natural and industrial granular flows [23]. Fig. 1 shows the experimental set-up consisting of a reservoir in which the granular column is prepared and pre-conditioned. The reservoir wall is instantaneously removed, allowing the granular material to flow over the base, driven by gravity, until the final deposit configuration is attained at rest.

We distinguish different types of granular column collapse experimental set-ups by their main features, as found in the literature:

- The geometry of the initial column has been considered to be either quasi-two-dimensional [24–30], assuming plane strain conditions inside a rectangular channel, or axi-symmetrical [23,24,28,31–35], which does not allow inspecting the internal structure of the mobilised mass during flow propagation. So-called semiaxisymmetric geometries have been explored to circumvent such drawbacks with consistent results compared to cylindrical set-ups [25]. For a quasi-two-dimensional set-up, we define the initial column aspect ratio as  $a = h_0/l_0$ , with  $h_0$  the average initial granular column height after pre-conditioning, and  $l_0$  the reservoir base length, see Fig. 1. The explored values of a range typically between around 0.5 [24,25,30] and 10 [29,30].
- In the case of quasi-two-dimensional set-ups, the procedure for material release generally consists in the instantaneous removal of a vertically lifted gate, ensuring that the time to completely separate the gate from the granular material is shorter than the elapsed time for the onset of flow [31]. Alternatively, some authors have resorted to swinging gates [26,27,36].
- The basal surface geometry and properties have been investigated. Beyond the usual horizontal surface configuration, the special case of a rotating horizontal table has been analysed in [33]. A smooth basal surface has been adopted in most cases, whereas experiences with rough surfaces—e.g. covered with sandpaper of a roughness of the same order as the tested granular material—have shown little effect on the results [23]. Furthermore, flows down rough inclined surfaces have been studied primarily in the field of earth sciences [37,38] to understand phenomena such as landslides or debris flows. Other works have presented results from inclined plane observations with rough [39] and smooth [40,41] basal surfaces. The maximum reported inclinations with respect to the horizontal range from 15 to 35°. Erodeable beds, formed by layers of variable thickness of a granular material, have also shown negligible difference in the flow behaviour and

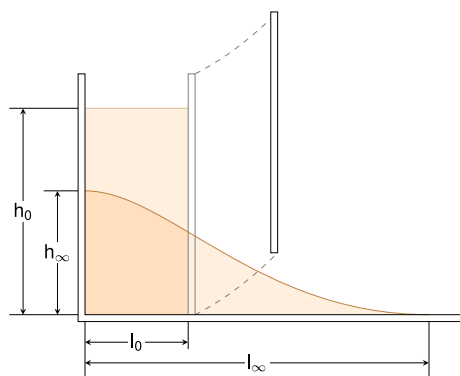


Fig. 1. Schematic of a quasi-two-dimensional granular column collapse experimental set-up, showing the initial granular column ( $h_0, l_0$ ) and final deposit ( $h_\infty, l_\infty$ ) configurations. (Adapted from [55]).

deposit morphology on horizontal set-ups [31], whereas the flow dynamics and run-out have been confirmed to be controlled by erosion in the case of inclined channels or steps, as reviewed in [42].

- The interstitial fluid surrounding the granular material, either gas or liquid, has been also taken into account. Dry granular flows have been mostly researched, without control of the packing state of the material. Air fluidisation of granular columns both previous to and during flow has been reported in [43,44]. The inclusion of a liquid phase, in the form of capillary water in the pendular state, has been examined in [45–47]. Finally, fully saturated granular samples, immersed in distilled water or in various mixtures of water with soluble agents, have been tested in [48–50]. The pore fluid pressures at the basal surface have been controlled in the cases of air fluidisation and fully immersed set-ups [43,48].

We have developed a new fully-instrumented granular column collapse apparatus [51,52] that provides for a direct observation of granular flow regimes generated in actual handling conditions [53], and suitable for a wide range of powders and grains with particle sizes from the scale of  $\mu\text{m}$  to mm. The apparatus allows us to characterise the effect of their varying physical and mechanical properties at the grain and bulk scales on their flowability. Few researchers have addressed the question of the granular column collapse of fine-grained cohesive powders—for instance gypsum plaster [30]—and have largely focused on studying free-flowing non-cohesive coarser materials such as monodisperse spherical glass beads or quartz sand. We have equipped our experimental apparatus with complementary measurement techniques to visualise granular flow by looking at: the fluidisation and deaeration of the granular columns, the basal load distribution after collapse, the near-wall kinematics during flow propagation, and the free surface morphology of the final deposits. With the instrumentation redundancy, we seek to circumvent the eventual operational issues, as well as the problems associated with the material properties, such as the particle colour and granular texture affecting the feasibility of the image analysis of the flows.

This paper is organised as follows. First, we describe our experimental apparatus and the integrated instrumentation in Section 2. Next, we present three representative granular materials, and we detail our testing protocol in Section 3. We illustrate the capabilities of the apparatus by following the testing protocol to analyse the chosen materials. We show and discuss a selection of the obtained results in Section 4. Last, we summarise the highlights of our work and draw our conclusions in the final Section 5.

## 2. Experimental set-up

Fig. 2 shows views of our new fully-instrumented granular column collapse apparatus, consisting of a horizontal rectangular channel (1) of width 160 mm and length 2150 mm, which comprises a smooth anodised aluminium plate at the base, and vertical glass walls of height varying between 350 mm to 150 mm for ease of operation. The prismatic configuration permits the thorough visualisation and instrumentation of the set-up, by exploiting the quasi-two-dimensional nature of the generated granular flows. This in turn facilitates the interpretation and modelling of the experimental results.

An automated lifting gate (2) is closed at a distance  $l_0 = 150$  mm, forming a prismatic reservoir (3)  $150 \times 150 \times 350$  mm<sup>3</sup> where the granular material column is prepared. The lightweight gate consists of a carbon fibre reinforced polymer sheet, held by a 3D-printed polymeric frame, and reinforced with an aluminium sheet. The gate opening is controlled by a parallelogram mechanism (9) automated by pneumatic cylinders, providing a uniformly accelerated circular motion of the gate, as illustrated in Fig. 3. A constant angular acceleration of  $8 \text{ rad s}^{-2}$  is achieved at an adjusted operating gauge pressure of the cylinders of 0.4 MPa, attaining a speed of  $0.4\text{--}0.5 \text{ m s}^{-1}$  after 0.1 s starting from repose. Our design addresses the main limitations of commonly used gate

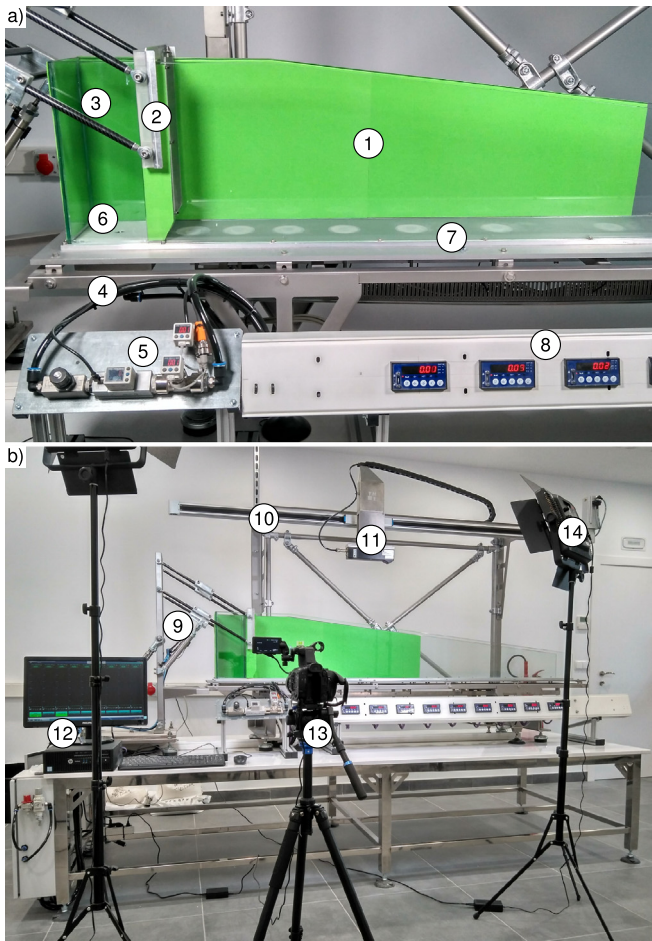


**Fig. 2.** New fully-instrumented apparatus with numbered parts. a) Close-up view of the channel: 1. horizontal channel ( $160 \times 2150 \text{ mm}^2$ ); 2. automated lifting gate; 3. reservoir ( $150 \times 150 \times 350 \text{ mm}^3$ ); 4. air chamber; 5. air flow control panel; 6. permeable plate; 7. membranes and beam load cells; 8. signal filtering and transmission panel. b) General view of the experimental set-up: 9. automated parallelogram mechanism of the lifting gate; 10. linear guide held by a detachable structure; 11. 3D laser line profile sensor; 12. PC for data acquisition and control; 13. high-speed video camera on tripod; 14. LED illumination.

systems. First, the gate is instantaneously removed horizontally from its closed position, thus reducing the shear stresses on the granular column in contact with the gate during fast vertical lifting. Second, the parallelogram mechanism also reduces drag forces on the granular column caused by swinging gates in the direction of flow, to which materials with low particle density are more susceptible, while operating at a comparable velocity to the reported value of  $0.4 \text{ m s}^{-1}$  [36].

The initially poured random packing state of the granular column in the reservoir can be pre-conditioned either to a fluidised state of the material, obtained by injecting a positive air flow into the sample, or to a deaerated state of the material, generated under negative pressure conditions with the reversible pneumatic circuit depicted in Fig. 4. This circuit allows us to reproduce actual conditions in bulk solids handling operations: aeration in fluidisation chambers for bag filling [54], and deaeration to densify granular masses and prepare the package to be closed. A source of dried compressed air is connected through a solenoid valve to an air chamber (4) attached to the reservoir base. To create vacuum conditions inside the reservoir, the compressed air is redirected by the solenoid valve to a vacuum ejector to reverse the air flow out of the air chamber. A control panel (5) is installed between the solenoid valve and the air chamber, where the air flow is regulated and measured using a flowmeter (SMC Corporation of America, US) with a measuring

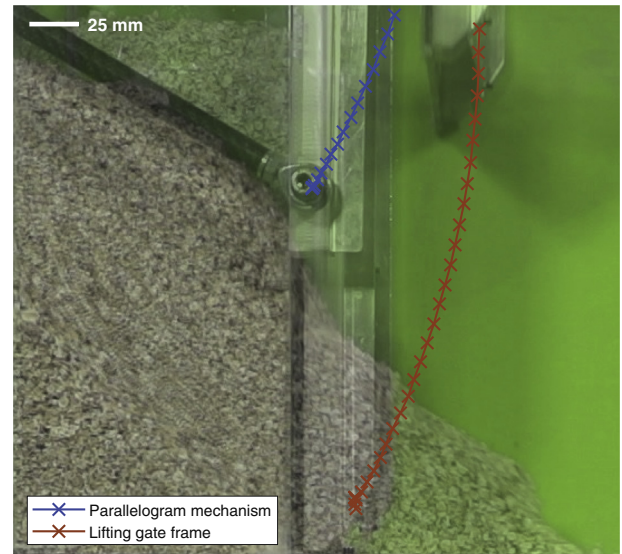


**Fig. 3.** Pathlines of two points on the lifting gate along the opening.

range of  $3 \times 10^{-4}$  to  $3 \times 10^{-2} \text{ m}^3 \text{ s}^{-1}$  and an accuracy of  $\pm 0.05 \%$  FS. Two pressure transducers (SMC Corporation of America, US), with a measuring range of  $\pm 100 \text{ kPa}$  and an accuracy of  $\pm 0.05 \%$  FS, are also used to assess the air pressure inside the pneumatic circuit and, foremost, at the reservoir base, where a permeable polyester needle-punched felt plate (6) is placed to prevent the escape of fine particles.

Once the sample is prepared within the reservoir and its packing state pre-conditioned, the onset of flow is triggered by opening the gate synchronised in turn with a set of nine logarithmically-spaced beam load cells (UTILCELL, Spain) distributed along the channel base (7). The sensors are ordered by measuring range from 300 to 30 mN with an accuracy of  $\pm 0.02 \%$  FS, since the flow dynamics produce higher basal loading at channel locations closer to the reservoir. Embedded in the centre line of the channel base width are nine moulded silicone membranes, see Fig. 5a, that transmit the loads acting on the channel surface to the respective force transducers fixed to the channel

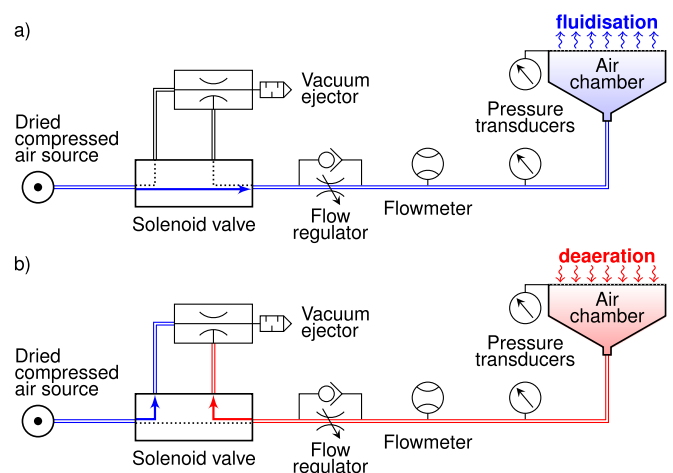


**Fig. 4.** Air flow diagram of the reversible pneumatic circuit with two operating modes: a) fluidisation; b) deaeration. The blue colour indicates positive air pressure and flow sense from the air source to the air chamber. The red colour indicates negative air pressure and flow sense from the air chamber to the vacuum ejector.

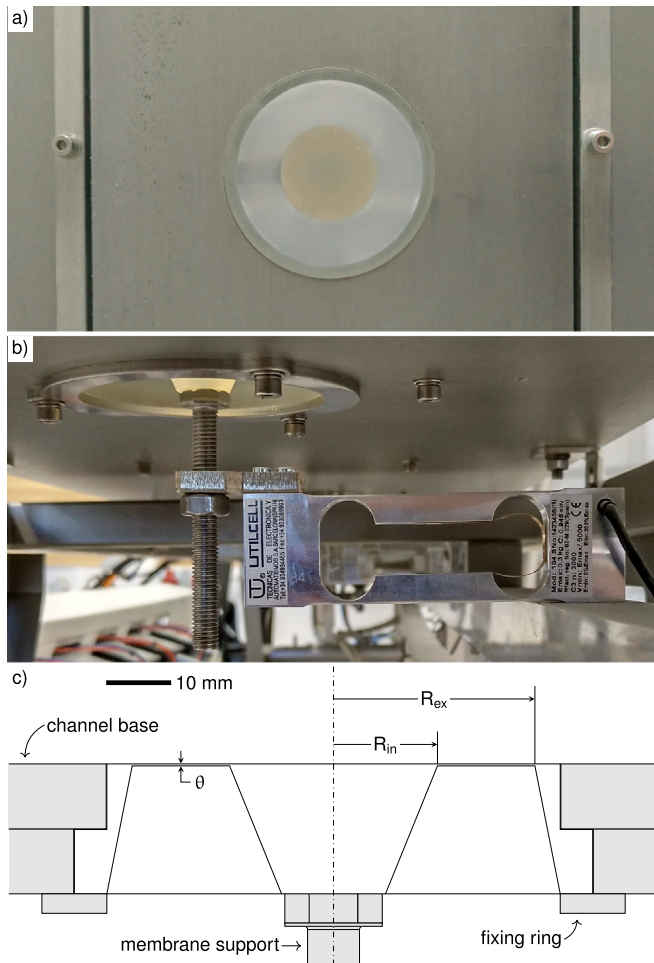


**Fig. 5.** Silicone membrane and load cell mounting: a) top view of the membrane embedded in the channel base; b) side view of the beam load cell arrangement with membrane support; c) diagram of the membrane design with internal radius  $R_{in} = 16$  mm and external radius  $R_{ex} = 31$  mm.

structure, as shown in Fig. 5b. The membrane design is detailed in Fig. 5c, consisting of a circular sheet of thickness  $\theta = 0.3$  mm, which deforms elastically under the action of the granular material deposited on it; a central block transmits the reaction force to the load cell on which it is supported. The load cells monitor flow propagation and load distribution of the granular material along the channel surface, through a set of high-speed transmitters (UTILCELL, Spain) installed on a signal filtering and transmission panel (8).

Aligned with the channel, a detachable structure holds a linear guide (10) covering the whole channel length with an effective stroke of 2200 mm, and encasing a toothed belt with positioning control by a stepper motor with a repetition accuracy of  $\pm 0.01$  % FS. Coupled to the slide (11) of the linear guide is a 3D laser line profile sensor (LMI Technologies Inc., Canada) positioned as depicted in Fig. 6. The profile sensor provides measurements of the top free surface morphology of the granular material at rest: first, of the granular column in the reservoir before testing; and second, of the final deposit along the channel after the flow stops. The analysis of the run-out is required to verify the quasi-two-dimensional hypothesis on the mechanical behaviour of the bulk material in the prismatic channel, as well as to observe shape parameters of the deposit such as the angle of repose [28,55]. We consider the reference frame shown in Fig. 6, with the origin in the midpoint of the inner bottom left edge of the reservoir. Therefore, the spatial resolution of the profile sensor lies between 19–60  $\mu\text{m}$ , with a range of 400 mm in the z-axis direction, and a field of view between

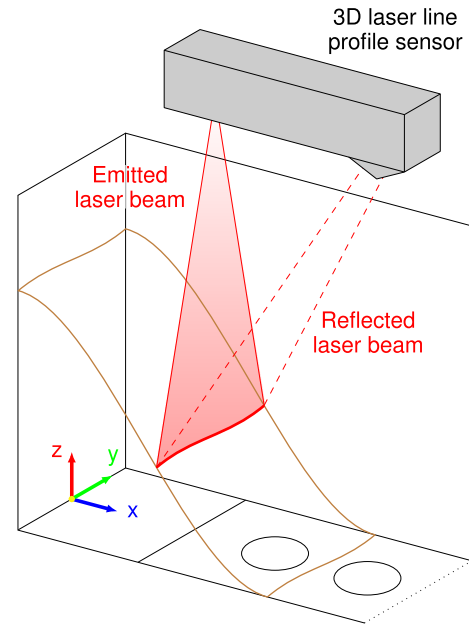


**Fig. 6.** Schematic view of the profile sensor positioning with respect to the frame of reference fixed on the channel base.

158 to 365 mm in the y-axis direction. We use a desktop computer (12) for data acquisition and control by a custom interface of the linear guide, as well as the automated lifting gate, the reversible pneumatic circuit, and the signal filtering and transmission panel. The Gocator Web Interface by LMI Technologies is used to configure and control the profile sensor.

Near-wall flow visualisations through the glass walls of the channel are obtained using a high-speed video camera (SONY Corporation, Japan) at a frame rate of 200 fps and with a pixel resolution of  $1920 \times 1080$  px<sup>2</sup>. The digital imaging set includes a tripod (13) to ensure both the stability of the camera and the repeatability of the measurements, as well as two LED light panels (14) providing continuous lighting of the channel recordings. Kinematic fields are extracted from image analysis by (PIV) [56], a widespread technique for the study of steady-state flows down inclines in both dry [36,57,58] and saturated [59,60] conditions. PIV analysis has been further incorporated to granular column collapse experiments [24,25,29,39,61] and similar set-ups [62]. We use the open-source software PIVlab [63], which implements a cross-correlation algorithm performing iterative deformation and refinement of all interrogation areas in each frame pair being processed. Several approaches exist for image pre-processing to define object boundaries, as briefly reviewed in [64]. Automatic image masking for background exclusion is required to delimit the region of interest, i.e. the flowing granular material; we ensure a uniform background by the chroma key in Fig. 2. Other moving objects in view throughout the recording, such as the lifting gate frame, are masked out by adapting the pattern matching scheme in the PIV to the object detection of reference images containing distinctive features. Granular materials able to produce particle texture above the pixel scale are properly tracked, whereas mixing the material with marker particles at low mass fraction may be required in the case of materials with insufficient inherent texture or with finer monochrome particles [52].

### 3. Materials and testing protocols

We have chosen three materials representative of common industrial practice to illustrate the capabilities of our experimental apparatus, namely: oat flakes, copper sulphate fertiliser, and talc powder. Table 1 shows material properties of the selected materials.

**Table 1**  
Material properties of tested oat flakes, copper sulphate fertiliser, and talc powder samples.

Material	Bulk density ( $\text{kg m}^{-3}$ )		Vacuum $\rho_{\text{vac}}$	Vibrated $\rho_{\text{vib}}$	Friction coefficient $\mu_s$ (-)	Particle size (mm)			Circularity coefficient $C_c$ (-)	Gravimetric water content $w$ (%)
	Poured $\rho_p$	Aerated $\rho_{\text{aer}}$				$d_{10}$	$d_{50}$	$d_{90}$		
Oats	447	444	470	464	0.53 – 0.62	1.45	2.66	3.94	0.63	12
Fertiliser	1136	1131	1142	1230	0.08 – 0.15	0.105	0.185	0.353	0.76	1.2
Talc	455	427	530	466	0.4 – 0.8	0.034	0.056	0.092	0.35	0.4

We report poured bulk density  $\rho_p$  values corresponding to samples gently funnelled into the reservoir. The funnel is gradually lifted during filling to maintain a maximum distance of 150 mm between the release point and the surface of the accumulated material. The free surface of the resulting granular columns is manually levelled with a spatula, without exerting downward compaction of the poured samples. From the values of  $\rho_p$ , the aerated  $\rho_{\text{aer}}$  and vacuum  $\rho_{\text{vac}}$  densities are measured by the volume change of the granular columns subject to air flows ranging between  $\pm 2.5 \times 10^{-3} \text{ m}^3 \text{ s}^{-1}$ . The vibrated density  $\rho_{\text{vib}}$  is obtained by gently pouring granular material samples into a measuring cylinder, to which a vibration is applied (of frequency 50 Hz, maximum amplitude 0.3 mm, and peak acceleration  $40 \text{ m s}^{-2}$ ) until volume change ceases. Additionally, we present values of the friction coefficient  $\mu_s$  for the oats from published results in a review of properties of seeds and grains in [65]; values for fertiliser are estimated from measurements on copper oxide films exposed to air tested at short reaction times after their formation in [66]; and values for dry talc samples are also taken from experiments with slip distances of the order  $10^{-2}$  to 1 m [67], at the same scale of our run-out observations. Furthermore, we extract the particle sizes of these powders and bulk solids from the sieve analyses presented in Fig. 7. Of the three materials, the oat flakes show the coarsest particle sizes up to 5 mm. All the samples lie below the threshold value of 5 % of the channel width, thereby confirming their testing suitability [18].

Complementary material properties include: the circularity coefficient  $C_c$  describing the particle shape by image analysis, as the ratio of the projected particle area to that of a circle with the same perimeter [68]; and the gravimetric water content  $w$  by oven-drying at  $110^\circ \text{C}$  of samples at an ambient relative humidity of 54 % and a room temperature of  $20^\circ \text{C}$ . In our view, the procedure to measure  $w$  overestimates

the amount of absorbed moisture on the oat flakes, by partially removing the adsorbed water in the organic constituents of the grains. Considering the conventional storage conditions of the three materials, we assume that our results illustrate the experimental investigation of dry granular flow.

We establish a testing protocol, valid for any granular material, to exploit all the redundant measurement systems incorporated to our column collapse apparatus, comprising the following steps:

- Step 1. The lifting gate is closed and the sample is prepared by following the methodology described above to form a granular column of density  $\rho_p$  at an initial column aspect ratio  $a \leq 2$ .
- Step 2. The initial packing state is either as-prepared or pre-conditioned using one of the two operating modes of the reversible pneumatic circuit.
- Step 3. Pre-conditioning is stopped and the profile sensor is used to scan the initial free surface of the granular column.
- Step 4. The high-speed video camera is manually triggered to capture the whole experiment during the camera recording time of 9 s at 200 fps. At the post-processing stage, we determine the start of our experiment when the difference of two consecutive frames first exceeds a threshold value. In the presented results, we have set threshold values at 1.2 to 2.0 % of the peak frame difference throughout the videos, depending on the camera adjustments and the evolution of the experiment.
- Step 5. Immediately after the high-speed video camera starts recording, a signal is sent that triggers both the lifting gate opening, and thus the onset of flow, as well as the data acquisition from the load cells, until the final deposit is formed. In the presented results, we represent the load profiles to start at the time instants obtained by the procedure described in step 4. We delimit reaction times ranging from 134 to 247 ms that account for the lapse between the opening signal transmission and the activation of the pneumatic cylinders controlling the motion of the lifting gate.
- Step 6. Once the flow stops, the lifting gate is completely detached from the channel to allow inspecting the final deposit, and the profile sensor is used again to measure the surface of the final deposit along the channel.

#### 4. Results and discussion

In this section, we present selected results on three representative granular materials to display the main features of our experimental apparatus. We explore the pre-conditioning state of the granular columns by fluidisation and deaeration before collapse in Section 4.1. We use the profile sensor to analyse the free surface morphology of the samples at rest, before and after collapse, to find out the run-out lengths and the slopes of the final deposits in Section 4.2. The data gathered by the load cells enables us to study the load distribution at the channel base during flow propagation in Section 4.3. We also define the equilibrium flow heights as the relationship between the transmitted forces to the load cells and the height map measured by the profile sensor. In Section 4.4, we investigate the flow dynamics captured in the high-

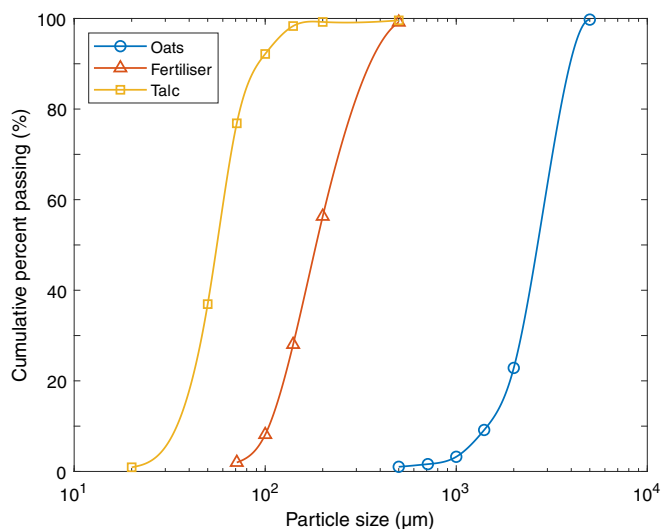


**Fig. 7.** Particle size distribution curves of tested oat flakes, copper sulphate fertiliser, and talc powder samples.

speed video recordings of the evolution of the near-wall height profiles, the flow front location, and the transient flow heights monitored jointly with the load cells. We deepen our analysis of flow kinematics in the last Section 4.5, by examining the PIV visualisations of the incremental displacement, velocity, and shear strain rate fields. This information allows determining the energy balance of the granular systems during the experiments.

Notice that, throughout this section, we nondimensionalise several physical quantities—including length, time, force, and energy—whenever we need to compare the findings from different tests. The versatility of our column collapse apparatus offers multiple combinations of testing steps, granular materials, and pre-conditioning of the samples, which have been considered for a thorough characterisation of flowability. Thereby, for the sake of clarity, we conveniently employ different characteristic quantities of interest in each nondimensional representation of our results.

#### 4.1. Initial packing state pre-conditioning

Two different granular packing states result from initially poured samples at the random packing state. On the one hand, air fluidisation generates loose packing of the granular material. For fine-grained materials, an expansion behaviour is observed at air velocities above the minimum fluidisation value, which also involves gas channelling [69]. The initial column height without pre-conditioning  $h_p = 128$  mm of a talc sample is shown in Fig. 8a. Air fluidisation provides an increase of the height with respect to  $h_p$  by 5.22%, see Fig. 8b, resulting in the average initial column height after pre-conditioning  $h_0 = 135$  mm. We observe the formation of preferential air flow paths, dominantly along the vertical direction, i.e. orthogonal to the minor principal stress direction. We also note the migration of fine particles at higher air velocities. On the other hand, deaeration produces dense packing of the granular material. The effect on the packing state is again greater for fine powders, which become densified under negative pressures preventing the formation of flow paths. However, as the column shrinks, some cracks open at the

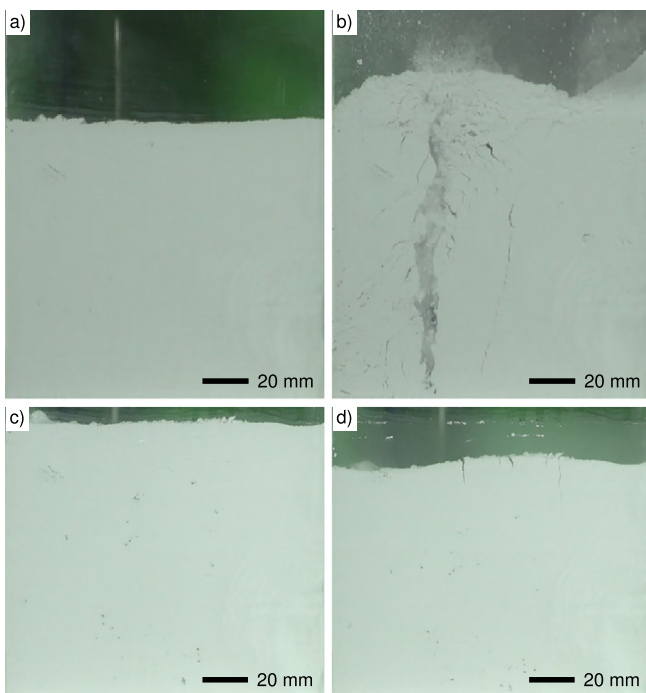


Fig. 8. Packing states of talc powder: a) initial random packing before fluidisation; b) fluidisation; c) initial random packing before deaeration; d) deaeration.

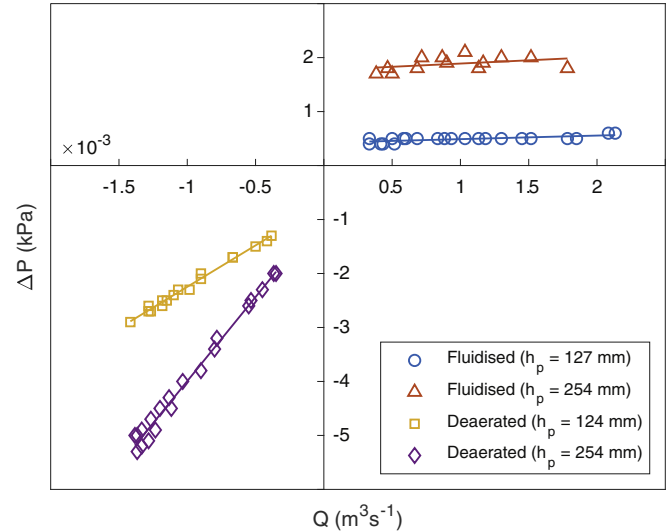


Fig. 9. Air pressure drop across fertiliser granular columns  $\Delta P$  versus imposed air flow  $Q$ .

free surface of the sample. The average column height at the deaerated packing state  $h_0 = 109$  mm is observed in Fig. 8d to be 15.1% shorter than the initially randomly packed granular column of height  $h_p = 129$  mm shown in Fig. 8c.

The air pressure drop across granular columns  $\Delta P$  of fertiliser samples, as a function of the applied air flow  $Q$ , is depicted in Fig. 9. We observe that, as expected during fluidisation [70], the measured air pressures remain almost stable with the increase of air flow. The air pressure drop values are below the vertical stress at the reservoir base stress  $\sigma_z$ , due to self-weight of the poured column at random packing state

$$\sigma_z = \rho_p g h_p \quad (1)$$

where  $g$  is the gravity acceleration. Vertical stresses range from 1.41 to 2.82 kPa for columns of initial heights  $h_p$  between 124 and 254 mm. Samples with larger initial column height correspond to higher air pressure drops, since air pressure accumulates towards balancing the body force. In the case of deaeration, the absence of air flow paths explains the faster and more homogeneous distribution of the vacuum at lower negative air pressure values. At the same imposed air flow, larger negative air pressure drops are observed for columns with higher  $h_p$ .

We use the data in Fig. 9 to derive the intrinsic air permeability  $K$  of the fertiliser sample from the generalised Darcy's law

$$\frac{Q}{A} = -\frac{K}{\mu_{\text{air}}} \left( \frac{\Delta P}{H} - \rho_{\text{air}} g \right) \quad (2)$$

where  $A$  is the cross-sectional area of the reservoir, and  $H$  is the estimated average height, between  $h_p$  and  $h_0$ .  $H$  is identified as the elevation head of the granular column, subject to a vertical air flux for the successive stationary stages of pre-conditioning, in terms of the air pressure and flow conditions. The air dynamic viscosity and the air density, respectively  $\mu_{\text{air}} = 1.82 \times 10^{-5} \text{ kg m}^{-1} \text{ s}^{-1}$  and  $\rho_{\text{air}} = 1.20 \text{ kg m}^{-3}$ , are measured at 20 °C and 101 kPa. With maximum and minimum values as error bars, Fig. 10 shows the variation of  $K$  as a function of porosity

$$\varepsilon = 1 - \frac{m}{\rho_s A H} \quad (3)$$

where  $m$  is the sample mass, and  $\rho_s = 2.3 \text{ kg m}^{-3}$  is the density of the fertiliser particles, resulting in an explored range of porosities from 0.49



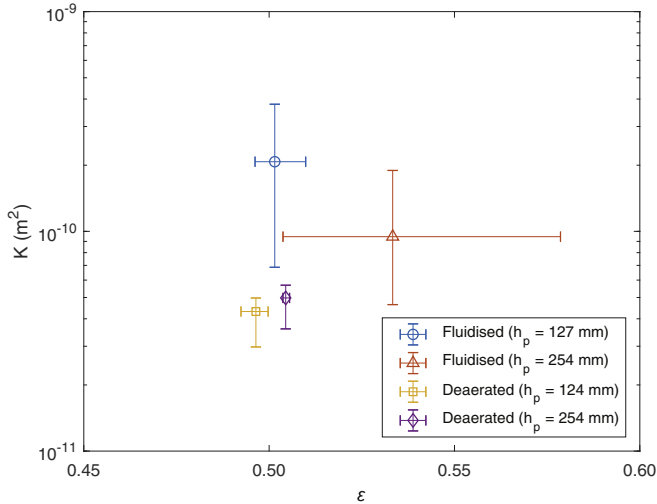


Fig. 10. Intrinsic air permeability  $K$  versus average porosity  $\varepsilon$  of the fertiliser samples.

to 0.58. The air permeability of the fluidised states shows a large dispersion around the mean value  $K = 1.5 \times 10^{-10} \text{ m}^2$ , which is related to large pore distribution changes caused by the gas channelling and particle size segregation phenomena that take place for air flow values above the minimum fluidisation. On deaeration, the air permeability is around  $K = 4.6 \times 10^{-11} \text{ m}^2$ , roughly an order of magnitude smaller with respect to the fluidised samples, which we attribute to a reduction in the number of accessible pores in the densified granular columns.

#### 4.2. Free surface morphology and angle of repose

Before the onset of flow, the initial free surface of the granular columns is scanned using the 3D laser line profile sensor. We use the generated height maps of points  $\mathbf{x} = (x, y, z)$  to assess the average volume change of the samples corresponding to their packing state. Fig. 11 shows the nondimensional height variation of the free surface  $-\Delta z/h_p$  (compressive deformation is considered positive) of talc samples at the three packing states. Comparing the density measurements in Table 1, the compression response depends on the testing procedure and the material properties. Similar values of  $\rho_{vac}$  and  $\rho_{vib}$  are observed for the coarse oats samples. Fine-grained powders show larger compressions: fertiliser arranges into more compact packing states using vibration, with an average density increase by 8% with respect to  $\rho_p$ ; whereas deaeration provides the closest particle packing observed in the case of talc, see the average compression by 15% in Fig. 11c.

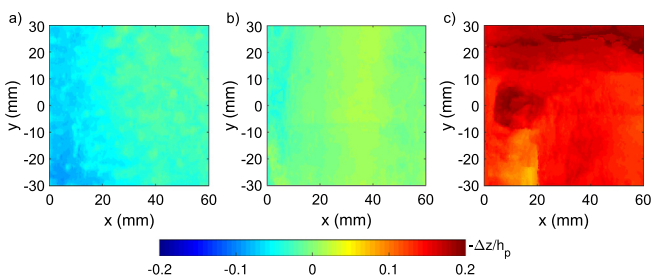


Fig. 11. Top views of the nondimensional height variation of the free surface  $-\Delta z/h_p$  of talc sample columns at different configurations: a) fluidised packing state ( $h_p = 128 \text{ mm}$ ,  $h_0 = 135 \text{ mm}$ ); b) random packing state ( $h_p = h_0 = 127 \text{ mm}$ ); c) deaerated packing state ( $h_p = 129 \text{ mm}$ ,  $h_0 = 109 \text{ mm}$ ).

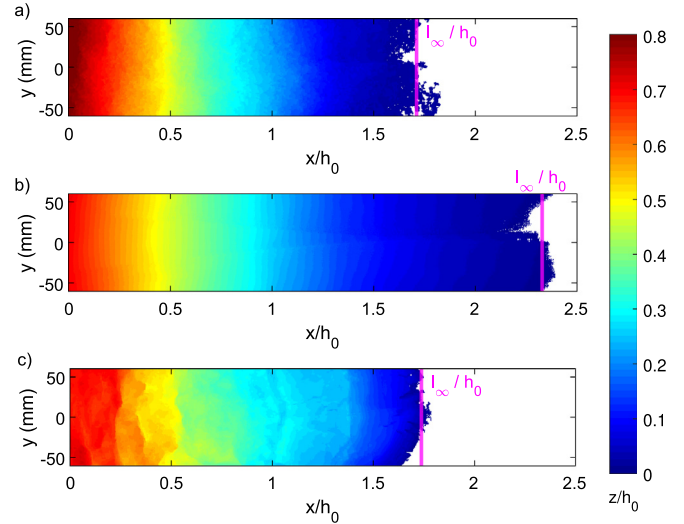
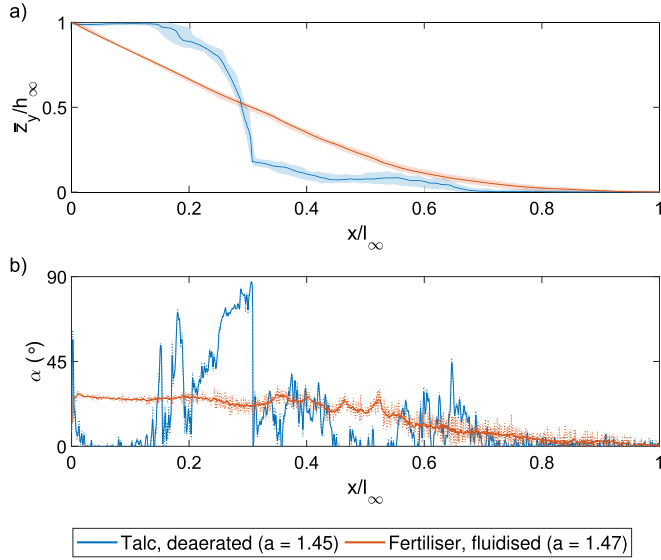


Fig. 12. Top views of the nondimensional free surface  $z/h_0$  and runout lengths  $l_\infty/h_0$  of three final deposits of tested samples without pre-conditioning: a) oats ( $h_0 = 282 \text{ mm}$ ); b) fertiliser ( $h_0 = 253 \text{ mm}$ ); c) talc ( $h_0 = 243 \text{ mm}$ ).

Regarding the effect of fluidisation, the fine-graded talc powder shows the largest average density reduction of the three materials, see the average expansion around 5% in Fig. 11a. The aerated density  $\rho_{aer}$  of the other two coarser granular materials is reduced by  $<1$ . As expected [69], smaller expansion in comparison with the talc is observed for the oats considering its larger particle size (despite the similar  $\rho_p$ ), as well as for the fertiliser given its higher particle density.

At the end of our experiment, we measure again the free surface of the final deposits, as shown in Fig. 12. We take the initial volume of the granular columns into consideration by nondimensionalising the height and run-out length with respect to the initial column height after pre-conditioning  $h_0$ . This allows us to compare the observations of the different materials, based on their material properties. We observe that the maximum heights of the final deposits  $h_\infty$  (Fig. 1) are  $h_\infty/h_0 = 0.8$ ,  $0.7$  and  $0.7$  respectively for oats, fertiliser and talc samples. This indicates the complete collapse of the granular columns of initial column aspect ratio  $a > 1$ . However, this behaviour is not always observed, especially in the case of samples with lower values of  $a$  or that are pre-conditioned to a denser packing state, for which large fractions of the sample mass remain static during flow. Throughout the channel width, we observe on the one hand a lower variation of the height map in the case of fertiliser, see Fig. 12b, a non-cohesive material with small particle sizes relative to the dimensions of our experimental apparatus. On the other hand, the free surface of the final deposit is more unevenly distributed along the  $y$ -axis for the cohesive talc powder and the oats, a material with coarser and more irregularly-shaped particles. We define the run-out length  $l_\infty$  (Fig. 1) as the average spreading of the tested samples. To this end, we use the average height profile of the final deposit in the  $y$ -axis direction  $\bar{z}_y(x)$ , taking into account the irregular distribution of the free surface along the channel width. We represent  $l_\infty$  by vertical stripes located at the largest  $x$ -coordinate with  $\bar{z}_y$  above the vertical resolution of the sensor. Consequently, we identify fertiliser as the material with larger spreading  $l_\infty/h_0 = 2.3$  compared to the oats and talc samples, which show similar locations of the deposited flow front at  $l_\infty/h_0 = 1.7$ .

In Fig. 13a we compare  $\bar{z}_y$  of an initially deaerated talc sample with a fluidised fertiliser sample. The height profile data is nondimensionalised in the  $x$ -axis and  $z$ -axis directions by the respective maximum values  $l_\infty$  and  $h_\infty$ , to compare the height variation along the same unitary run-out. The gate opening generates a reduction of horizontal stresses in the



**Fig. 13.** Front views of two final deposit configurations of talc and fertiliser samples: a) nondimensional average height profile  $\bar{z}_y/h_\infty$  along the nondimensional run-out length  $x/l_\infty$  with shaded ranges of minimum to maximum  $z(x)$ ; b) angle  $\alpha$  along  $x/l_\infty$ .

granular material that causes collapse of the fluidised fertiliser sample. The deaerated talc column is nevertheless sustained by cohesion, where we observe the formation of a vertical cut at the final deposit configuration.

The angle of repose is a commonly used parameter in industrial practice [71], which we can recover from the slope of our final deposit measurements

$$\alpha(x) = \tan^{-1}\left(-\frac{d\bar{z}_y}{dx}\right) \quad (4)$$

as shown in Fig. 13b, where the moving mean of slope is represented using an averaging length  $20 d_{50}$  along the final deposit. The physical relevance of the angle of repose can be discussed by comparison with the friction coefficient  $\mu_s$ , which governs the shearing mechanics of dry non-cohesive granular materials [53]. The flow of fertiliser develops an angle of the final deposit below  $28^\circ$  at the head and central parts of the deposit, gradually decreasing towards the run-out length to lower slope values within the range of  $\mu_s$ , see Table 1. However,  $\alpha$  of the deaerated talc sample shows peak angle values reaching  $87^\circ$  around the vertical cut, and large  $\alpha$  variations along the deposit length, which are not contained within the range of expected  $\mu_s$ . These observations indicate that generally the angle also incorporates masks other physically relevant phenomena, including cohesion, besides the friction coefficient.

#### 4.3. Basal load profiles and equilibrium flow heights

We investigate the granular flow propagation from the load distribution on the channel base in time for the different samples represented in Fig. 15. We define the nondimensional load  $\lambda(x_k, t)$  by the ratio of the force  $f(t)$  measured by each transducer at the  $x$ -axis location  $x_k$ ,  $k = \{1, \dots, 9\}$ , to the weight force of the initial column  $mg$ ,

$$\lambda(x_k, t) = \frac{f(x_k, t)}{mg} \quad (5)$$

Moreover, we define the nondimensional time  $\tau = t/t_c$ , where  $t_c = \sqrt{h_0/g}$  is the characteristic time elapsed by a particle in free fall from

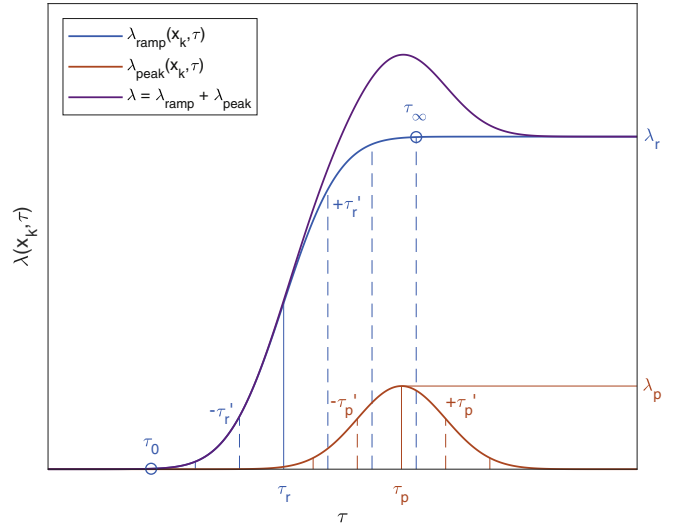


**Fig. 14.** Graph of the exponential model showing the combination of the two Gaussian functions  $\lambda_{\text{ramp}}$  and  $\lambda_{\text{peak}}$ , respectively controlled by the model parameters  $\lambda_r$ ,  $\tau_r$ ,  $\tau_r'$  and  $\lambda_p$ ,  $\tau_p$ ,  $\tau_p'$ .

an initial height  $h_0$ . Then, the experimental measurements obtained from the load cells  $(\tau, \lambda)$  are fitted at each point  $x_k$  by a nonlinear least squares criterion to the exponential model

$$\lambda(x_k, \tau) = \lambda_{\text{ramp}}(x_k, \tau) + \lambda_{\text{peak}}(x_k, \tau) \quad (6)$$

combining two Gaussian functions to explain the evolution of the basal loads in time, see Fig. 14. On the one hand, the first summand in Eq. (6)

$$\lambda_{\text{ramp}}(x_k, \tau) = \frac{\lambda_r}{2} \left[ 1 + \operatorname{erf}\left(\frac{\tau - \tau_r}{\tau_r' \sqrt{2}}\right) \right] \quad (7)$$

describes a load deposition ramp from the initial  $\lambda = 0$  to  $\lambda = \lambda_r$  at equilibrium, with three model parameters to be fitted: the basal load at equilibrium  $\lambda_r(x_k)$ , the central ramp time  $\tau_r(x_k)$ , and the ramp shape parameter  $\tau_r'(x_k)$ . We use the load deposition ramp model parameters  $\tau_r$  and  $\tau_r'$  to estimate the times at which the ramp starts  $\tau_0$  and ends  $\tau_\infty$  by

$$\tau_0 = \tau_r - 3\tau_r' \quad \tau_\infty = \tau_r + 3\tau_r' \quad (8)$$

as shown in Fig. 14. On the other hand, we observe an overshoot effect mainly for  $a > 1$  and sensed by the first force transducer,  $\lambda_p(x_1)$ . Only in these cases we consider the second summand in Eq. (6)

$$\lambda_{\text{peak}}(x_k, \tau) = \lambda_p \exp\left[-\frac{1}{2} \left(\frac{\tau - \tau_p}{\tau_p'}\right)^2\right] \quad (9)$$

accounting for the occurrence of load peaks with three model parameters: the basal load peak  $\lambda_p(x_k)$ , the central peak time  $\tau_p(x_k)$ , and the peak shape parameter  $\tau_p'(x_k)$ . We have confirmed that the load peaks are negligible otherwise, since small values  $|\lambda_p| < 10^{-4}$  are obtained in the fitting, and the physical interpretation of both  $\tau_p$  and  $\tau_p'$  is lost.

Fig. 15 depicts the results of two representative trials of each experiment, and the average value of the fitted model parameters is detailed in Table 2. After the onset of flow at  $\tau = 0$ , the flow front propagates along the channel, reaching the first membrane at times  $\tau_0(x_1)$  depending on the initial column aspect ratio: for  $a < 1$ , fertiliser is the fastest advancing material and talc is notably delayed with respect to the other materials; for  $a > 1$ , times  $\tau_0(x_1)$  are reduced in average. Once the flow

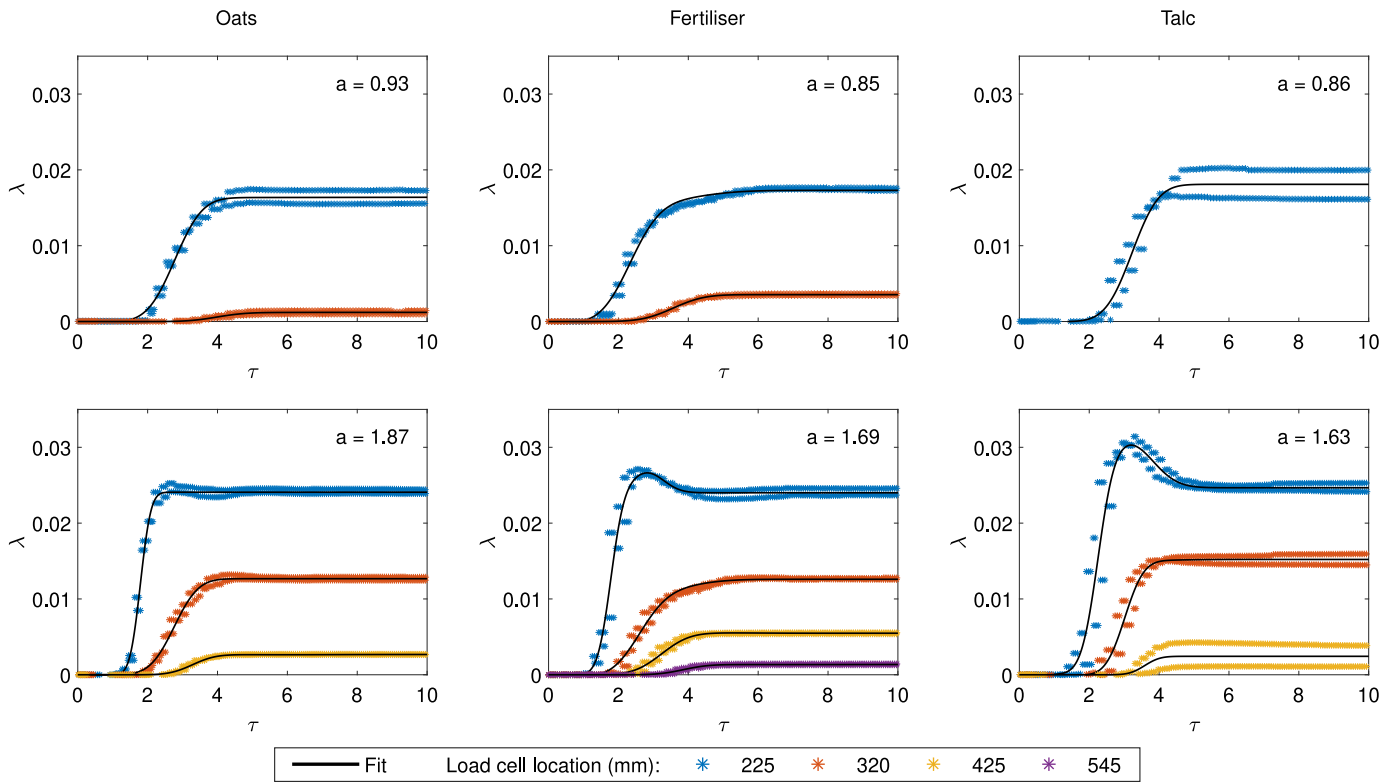
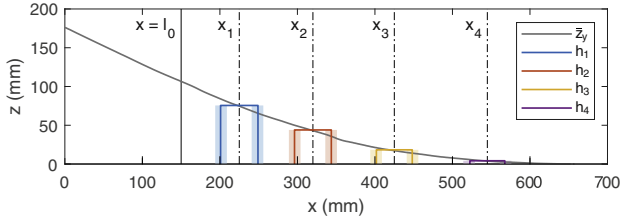


Fig. 15. Basal load profiles at the load cell locations  $x_1, \dots, x_4$ : nondimensional transmitted load  $\lambda$  against nondimensional time  $\tau$  for oats (left), fertiliser (centre) and talc (right) samples tested at the random packing state with varying values of  $a$ .

Table 2

Nondimensional Gaussian model parameters fitted to average results at the load cell locations  $x_1, \dots, x_4$ , of oats, fertiliser and talc samples of initial column aspect ratios  $a$ , tested at the random packing state.

Materials	$a$		Load cell location (mm)			
			$x_1 = 225$	$x_2 = 320$	$x_3 = 425$	$x_4 = 545$
Oats	0.93	$\lambda_r$	0.016	0.001		
		$\tau_r$	2.78	3.97		
		$\tau_r'$	0.68	0.64		
	1.87	$\lambda_r$	0.024	0.013	0.003	
		$\tau_r$	1.79	2.76	3.29	
		$\tau_r'$	0.24	0.54	0.52	
Fertiliser	0.85	$\lambda_r$	0.017	0.004		
		$\tau_r$	2.31	3.57		
		$\tau_r'$	0.69	0.70		
		$\lambda_p$	-0.001	-		
		$\tau_p$	2.99	-		
		$\tau_p'$	1.24	-		
	1.69	$\lambda_r$	0.024	0.013	0.005	0.001
		$\tau_r$	1.77	2.55	3.24	3.86
		$\tau_r'$	0.29	0.65	0.63	0.56
	$\lambda_p$	0.003	-0.001	-	-	
	$\tau_p$	2.82	2.99	-	-	
	$\tau_p'$	0.48	1.06	-	-	
Talc	0.86	$\lambda_r$	0.018			
		$\tau_r$	3.22			
		$\tau_r'$	0.60			
	1.63	$\lambda_r$	0.025	0.015	0.002	
		$\tau_r$	2.23	3.01	3.59	
		$\tau_r'$	0.36	0.43	0.34	
	$\lambda_p$	0.006	-	-	-	
	$\tau_p$	3.14	-	-	-	
	$\tau_p'$	0.69	-	-	-	



**Fig. 16.** Front view of the average height profile of the final deposit  $\bar{z}_y$  and the flow heights  $h_1, \dots, h_4$  of an initially deaerated fertiliser sample ( $a = 1.69$ ), where  $\bar{z}_k$  are plotted as coloured lines spanning  $R_k$  around the load cell locations  $x_k$  and enclosed by shaded bars marking the range between the membrane radii  $R_{in}$  and  $R_{ex}$ .

front advance is first detected at  $\tau_0$ , a depositional process develops at each load cell location on the channel base. During this process, loads increase monotonically at deposition rates up to around  $\lambda_r/\tau_r'\sqrt{2\pi}$  at  $\tau = \tau_r$ , until the final deposit at rest is formed after  $\tau_\infty$  and loads stabilise around  $\lambda_r$ . For  $a < 1$ , maximum deposition rates between 0.010–0.012 are observed, whereas the maximum rates rise to values between 0.032–0.040 as the initial column aspect ratio increases to  $a > 1$ , showing similar values independently of the material. We notice comparable load profiles registered at the consecutive membrane positions, although with lower deposition rates at the successive  $x_k$ . The overshoot effect before load stabilisation is observed clearly for the fertiliser and talc samples, respectively showing load increments  $\lambda_p(x_1)/\lambda_r(x_1)$  of 11 % and 23 % at peak times  $\tau_p(x_1)$  around the estimated  $\tau_\infty(x_1)$ . Close values of the peak shape parameter  $\tau_p'(x_1)$  are found for both materials. Small negative load peaks are also captured by the model, which describe a smooth deceleration of the depositional process towards the equilibrium load  $\lambda_r$  albeit with a negligible effect on the basal load propagation trends. We interpret the load peaks to be caused by an initial flow stage of vertical collapse [24,25], which generates the downward acceleration of the mobilised mass. This results in impulses exerted on the channel base at positions closer to the reservoir, that are in turn quickly dissipated as the motion becomes governed by the horizontal inertia of the propagating flow. Comparing the performance of the different materials, we observe that the talc powder at  $a > 1$  shows the largest  $\lambda_p(x_1)$ , due to its abrupt vertical collapse, which also produces a steeper deposition rate on the second membrane. Talc shows the highest deviation in the attained values of  $\lambda_r(x_k)$ , denoting an irregular distribution of flow front along the channel width, especially at the run-out configuration.

We identify a relationship between the basal load distribution registered at run-out and the free surface of the final deposit configuration. At equilibrium, the flow height  $h_k$  at the  $k$ -th membrane location is

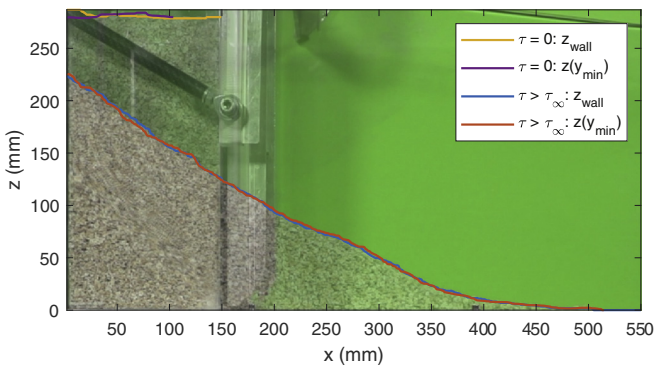


**Fig. 17.** Front views at the initial ( $\tau = 0$ ) and final ( $\tau > \tau_\infty$ ) configurations of the near-wall height profiles of an oats sample tested without pre-conditioning,  $z_{wall}$  and  $z(y_{min})$ , respectively obtained from high-speed camera and profile sensor measurements.

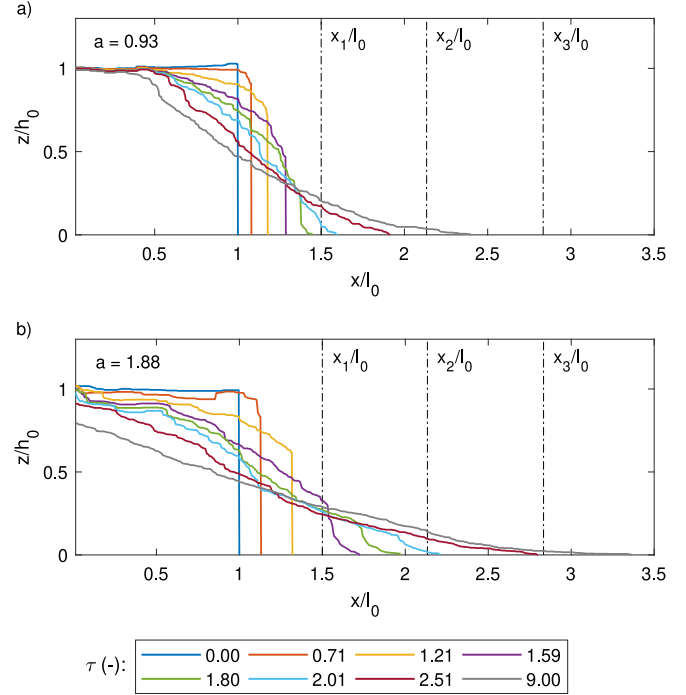


**Fig. 18.** Evolution in the nondimensional time  $\tau$  of the nondimensional height profiles  $z_{wal}/h_0$  of two oats samples tested at the random packing state with different values of  $a$ .

determined by the balance of forces between the load detected by the respective load cell  $f(x_k)$  and the self-weight of an a priori unknown tributary volume of granular mass accumulated over the membrane. We assume a tributary volume consisting of a vertical cylinder of unknown radius  $R_k$ , expectedly between the minimum and maximum membrane radii  $R_{in}$  and  $R_{ex}$ , with a flat face on the channel base and the top face described by the free surface of the final deposit with average height  $\bar{z}_k$ . At the final static state, we take the flow height to be equal to the average height of the tributary volume,  $h_k(\tau > \tau_\infty) = \bar{z}_k$ , resulting in the balance of forces

$$f(x_k) - \rho g \pi R_k^2 h_k = 0 \quad (10)$$

where  $\rho$  is the time-dependent bulk density, evaluated by the volume change of the sample with respect to the initial granular column. We observe an overall increase of the bulk density of the final deposit by 1.9 % with respect to the initial  $\rho_{vac}$  of the material. The results depicted in Fig. 16 show  $R_k$  to lie around the midpoint between the membrane radii, with the calculated values ranging from 22.5 to 24.1 mm. The observations systematically confirm the assumption on the tributary volumes for the calculation of the flow heights. Therefore, the measurements of the silicone membrane and load cell mountings can be verified at the final static state by means of the profile sensor system, thus benefiting from the instrumentation redundancy of our experimental apparatus.

#### 4.4. Frontal flow visualisations and transient flow heights

We study the frontal flow propagation along the rectangular channel to obtain a direct description of the granular motion close to the vertical glass wall from the high-speed video camera recordings. For all the tested samples, we accept the plane strain hypothesis on the granular flows, i.e. their quasi-two-dimensionality, despite the uneven distribution of the free surface in the  $y$ -axis direction discussed in Section 4.2.

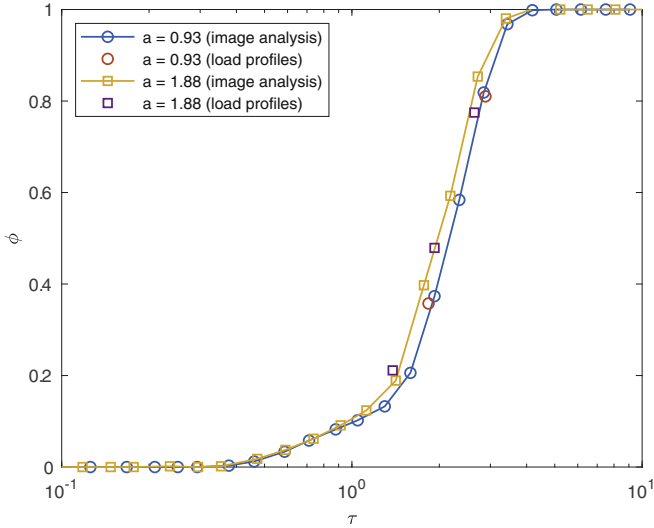


**Fig. 19.** Normalised flow front location  $\phi$  in the nondimensional time  $\tau$  of two oats samples of varying initial column aspect ratio  $a$ , tested at the random packing state.

We interpret the near-wall results accordingly as representative of the overall behaviour within the channel.

To quantify the image analyses, first we perform the scaling of the video frames recorded by the high-speed camera. We use the calibrated profile sensor measurements of the initial granular column and the corresponding final deposit configuration. In Fig. 17, we establish a pixel scale of  $0.58 \text{ px mm}^{-1}$  by matching the near-wall height profile of the granular pile  $z_{\text{wall}}$  to the free surface at the frontmost  $y$ -coordinate,  $z(y_{\text{min}})$ .

In Fig. 18, we represent the evolution of  $z_{\text{wall}}$  at the same instants in time  $\tau$ —nondimensional with respect to the characteristic time  $t_c$  of free fall from height  $h_0$ —during the flow of two oats samples of initial column aspect ratios  $a = 0.93$  and  $1.87$ , tested at the random packing state. We use the characteristic lengths  $l_0$  and  $h_0$  for the nondimensional representation of the height profile data in the  $x$ -axis and  $z$ -axis directions, respectively. This allows tracking the changes in the surface morphology starting from similar reference unitary regions. We distinguish three different stages of flow during propagation, starting immediately after collapse. In the first stage, the granular column deforms by maintaining a step-shaped free surface that advances in the  $x$ -axis direction. For  $a < 1$ , we observe the free surface converging gradually towards a wedge-shaped surface for a time interval from  $\tau = 0$  to over  $\tau = 1.59$ , see Fig. 18a. This initial stage of flow develops more rapidly for  $a > 1$ , completing before  $\tau = 1.59$ . Next, we detect a second stage of steady propagation of the flow front, which advances rapidly in regions closer to the channel base, until approximately  $\tau = 2.51$  in all cases. The height profile gradually develops into a wedge in the case of  $a < 1$ , while the initial step-shaped configuration is preserved for  $a > 1$  until around  $\tau = 2.01$ , as shown in Fig. 18b. Finally, in a third flow stage, the advance of the flow front stops at the run-out lengths  $l_{\infty}/l_0 = 2.40$  and  $3.37$  for  $a = 0.93$  and  $1.87$ , respectively. In the final deposit configuration, we observe for  $a < 1$  that the granular material is only partially mobilised to an extent of approximately half the reservoir length, whereas for  $a > 1$  the complete collapse of the initial column takes place.

Fig. 19 shows the location in time  $\tau$  of the flow front  $\phi$  of the tests depicted in Fig. 18, normalised by

$$\phi(\tau) = \frac{x(\tau) - l_0}{l_{\infty} - l_0} \quad (11)$$

to track the mobility reach of the flow front, evolving between the initial reservoir length  $l_0$  and the final run-out length  $l_{\infty}$ . The image analysis results are contrasted with the basal load profile measurements, showing

good agreement between the flow front trajectory and the load profile times  $\tau_0(x_k)$ —at which the  $k$ -th load cell locations are reached. The propagation of the flow front shows similar trends for the two oats samples at two different initial column aspect ratios. We observe an initial phase of slow propagation from  $\tau = 0.4$  to  $1.5$ , reaching  $\phi = 0.2$  in average, which corresponds to the first flow stage. Subsequently, we notice a phase of rapid propagation during the second flow stage, until the run-out length is reached at  $\tau = 4.2$ .

Moreover, we use the basal load profiles as an estimate of the flow heights  $h_k$  during the dynamic propagation of the granular material along the channel. In Fig. 20, we compare  $h_k$  of the same deaerated fertiliser sample in Fig. 16 to the near-wall height profiles  $z_{\text{wall}}$ . At time  $\tau = 2.30$ , we compute the flow heights  $h_k(\tau)$  by the balance of forces in Eq. (10), assigning to the tributary radii  $R_k$  the values calculated at the final static state of the sample, and using the instantaneous bulk density  $\rho(\tau)$ . An overall negligible decrease of the density by  $0.6 \%$  is observed with respect to the initial  $\rho_{\text{vac}}$ . We observe that the transient flow heights  $h_k$  do not correspond with the average profile heights  $\bar{z}_k$ . On the one hand, at the head of the wedge-shaped flow front, we find  $h_1 > \bar{z}_1$  by  $29 \%$ , which we correlate with the peaks observed in the basal load profiles, see Fig. 15, caused by the downward vertical acceleration of the mobilised mass due to the collapse of samples with  $a > 1$ . On the other hand, we notice at the consecutive load cell locations that  $h_2 < \bar{z}_2$  and  $h_3 < \bar{z}_3$ , respectively by  $34$  and  $84 \%$ . At the toe of the flow front, we observe that the propagation is dominated by the horizontal inertia of the flow, and hence the reason for the reduced flow heights.

#### 4.5. PIV-based near-wall kinematics and energy balance

We perform PIV analyses on the high-speed video recordings of the near-wall flow propagation of the granular materials. The outcome of the post-process is the description of the incremental displacement field  $\Delta \mathbf{u} = (\Delta u_x, \Delta u_z)$  between all pairs of consecutive video frames (recorded at  $200 \text{ fps}$ , i.e. with fixed time steps  $\Delta t = 0.005 \text{ s}$ ), from which we derive the average velocity field in the elapsed time between frame pairs by  $\mathbf{v} = \Delta \mathbf{u} / \Delta t = (v_x, v_z)$ . In Fig. 21, we observe the near-wall kinematics of the flow of an oats sample of initial column aspect ratio  $a = 1.88$  by representing the velocity modulus

$$|\mathbf{v}| = \sqrt{v_x^2 + v_z^2} \quad (12)$$

which shows the behaviour of mass mobilisation, alongside the absolute value of the incremental shear strain rate

$$|\dot{\gamma}| = \left| \frac{\partial v_z}{\partial x} + \frac{\partial v_x}{\partial z} \right| \quad (13)$$

indicating the regions of localisation of the rate of change of the shear strains, at three representative time instants  $\tau$  during flow. At

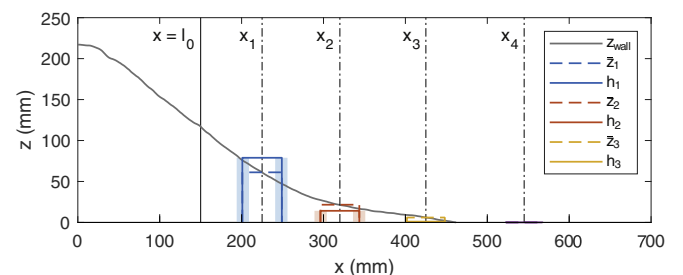


**Fig. 20.** Front view of the near-wall height profile  $z_{\text{wall}}$  and the flow heights  $h_1, \dots, h_3$  at the recording time  $\tau = 2.30$  of the initially deaerated fertiliser sample ( $a = 1.69$ ) depicted in Fig. 16. The average profile height  $\bar{z}_k$  around the load cell locations  $x_k$  is represented by dashed lines spanning  $R_k$ .

$\tau = 1.16$ , we observe the displacement of an upper sliding block with respect to the static mass fraction at the bottom of the collapsing column, as shown in Fig. 21a. During the first flow stage of deformation of the granular column due to collapse, the motion of the vertical flow front is dominated by large downward velocities showing peak values close to the free surface. The larger shear strain rates concentrate at the toe of the sliding block, as can be seen in Fig. 21b, where we detect a localised shear band spreading over to the top free surface of the granular column. We notice two peaks of the velocity modulus at  $\tau = 1.90$ , during the second flow stage of rapid propagation of the wedge-shaped flow front depicted in Fig. 21c: one at the head of the wedge, where the downward velocities generate the avalanching of the granular material that is mobilised towards the toe; and the other peak located at the toe of the wedge with increasing horizontal velocities. The direction of the velocity field towards the toe of the wedge is gradually aligned with the horizontal surface of the channel base. Simultaneously, the shear strain rates represented in Fig. 21d develop closer to the free surface

in comparison with observations at  $\tau = 1.16$ . We notice large shear strain rates around the upper avalanching front and also at the lower part of the flow front. In Fig. 21e and f, the third flow stage of deceleration of the flow is illustrated at  $\tau = 2.93$ . The mass mobilisation slows down, as showed by the reduced values of the average velocity modulus and the incremental shear strain rate distributed close to the free surface.

Fig. 22 shows the evolution in time  $\tau$  of the maximum near-wall horizontal  $v_x^{\max}$  and vertical  $v_z^{\max}$  (with downward velocities positive for ease of representation) components of the velocity field during flow propagation of two oats samples alongside two fertiliser samples of varying initial column aspect ratios  $a < 1$  and  $a > 1$ . All the samples are tested at random packing state. We observe an initially rapid increase of both maximum velocities during the first flow stage in the case of oats, followed by a deceleration of both maximum components. For the fertiliser,  $v_x^{\max}$  continues to rise though slightly delayed with respect to  $v_z^{\max}$ . Both maximum components reach their peak values during the

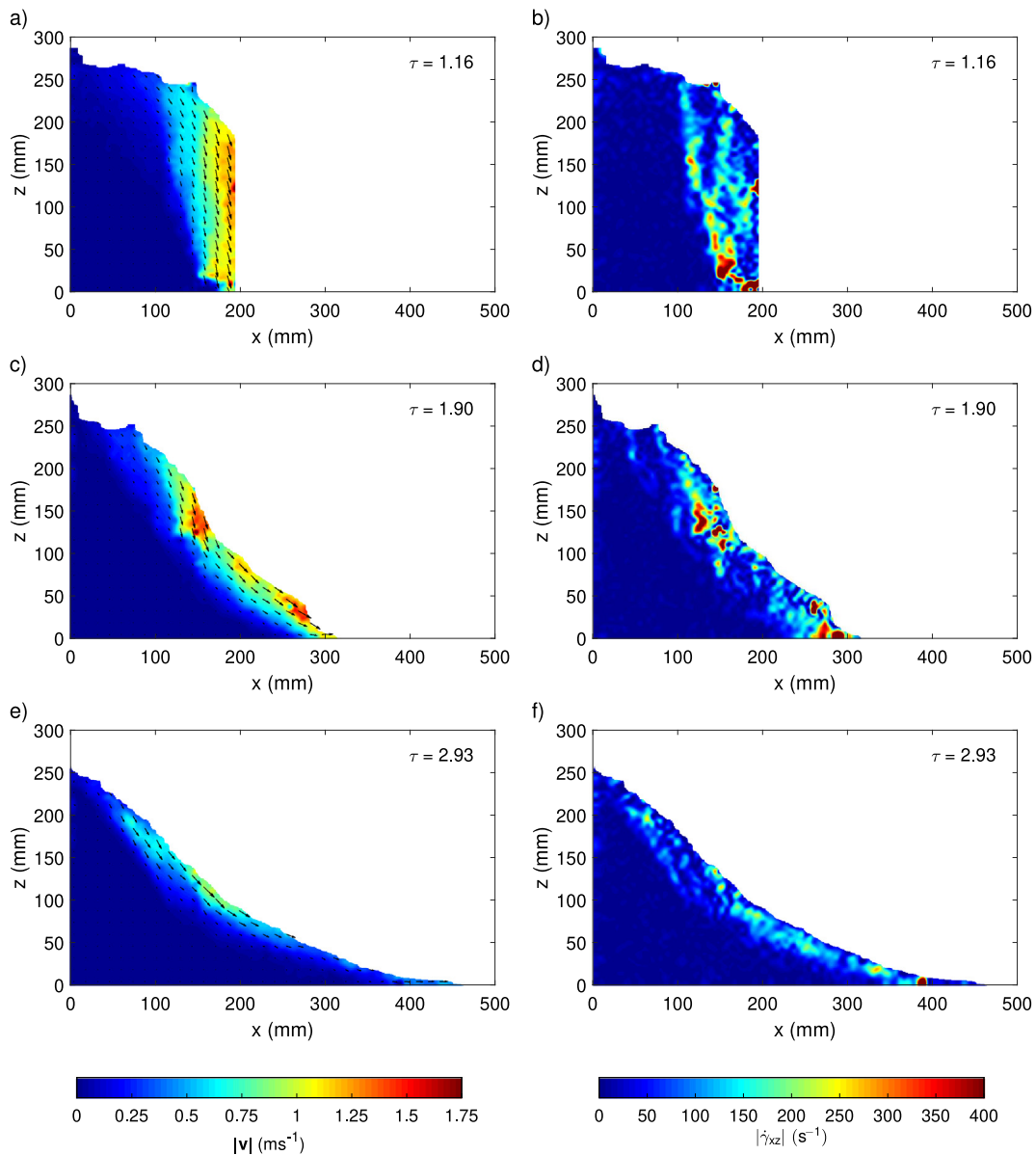


**Fig. 21.** Average velocity modulus (left) and absolute value of the incremental shear strain rate (right) fields at three different nondimensional time  $\tau$  instants during the flow propagation of an oats sample ( $a = 1.88$ ) tested at the random packing state. For reasons of readability, the colour scales are saturated below the peak velocity  $1.90 \text{ ms}^{-1}$  and shear strain rate  $925 \text{ s}^{-1}$  at  $\tau = 1.90$ .

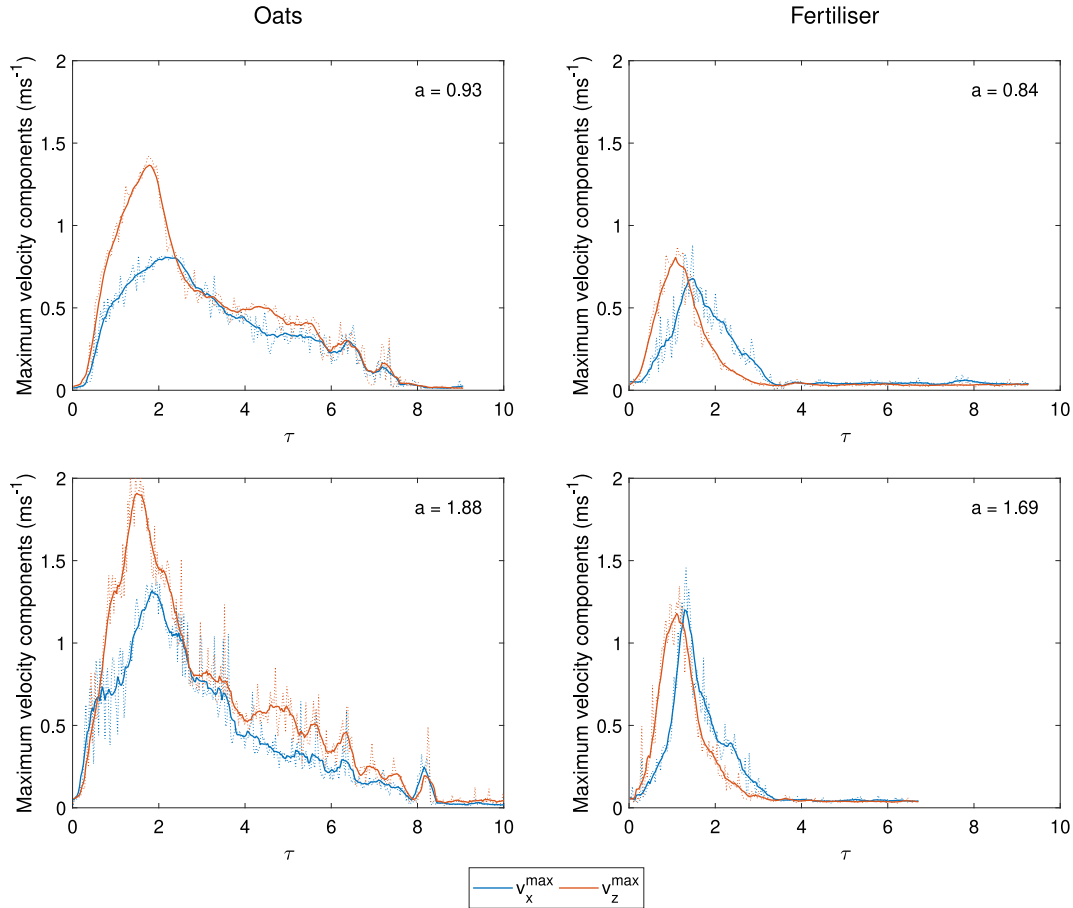


**Fig. 22.** Maximum near-wall horizontal  $v_x^{\max}$  and vertical  $v_z^{\max}$  components of velocity against the nondimensional time  $\tau$  for oats (left) and fertiliser (right) samples tested at the random packing state with varying values of  $a$ .

second flow stage, first  $v_z^{\max}$  at a time  $\tau < 2$ , followed by  $v_x^{\max}$ . We observe larger maximum vertical velocity peaks of the oats with respect to the fertiliser by 63 % and 50 %, respectively for  $a < 1$  and  $a > 1$ . For the oats, the peak values of  $v_x^{\max}$  are 42 % and 32 % lower than the peak values of  $v_z^{\max}$ , respectively for  $a < 1$  and  $a > 1$ , whereas similar peak values of both velocity components are obtained in the case of fertiliser. Afterwards, both velocity components decrease gradually during the last flow stage, until the final static state is reached by the oats sample. Velocities halt to a complete stop at  $\tau < 4$  for the fertiliser. In addition, we notice a greater dispersion of both velocity components in the oats samples throughout the flow. We explain this effect by a dominant avalanching mechanism in the flow, due to particle interlocking caused by the irregular shape of oat flakes. In contrast, the finer-grained fertiliser samples show a smoother evolution of the maximum velocity components. Our observations are in line with the schematic division of the flow dynamics originally proposed in [24,25], as regards the description of the first two stages of flow. Although two flow stages are sufficient for the description of the flow dynamics of non-cohesive granular materials, such as fertiliser, we require adding a final third stage in the case of oats to describe the flow from when the run-out length is reached, by the end of the second flow stage, until the mass mobilisation ceases.

We analyse the granular flow behaviour from the point of view of the energy balance [72]

$$E_{\text{tot}} = E_{\text{pot}} + E_{\text{kin}} + U \quad (14)$$

where  $E_{\text{tot}}$  is the total energy of the granular system, which is conserved,  $E_{\text{pot}} = mgz_{\text{CM}}$  is the gravitational potential energy, where  $z_{\text{CM}}$  is the height of the centroid of the granular system,  $E_{\text{kin}} = E_{\text{kin}}^{\text{trans}} + E_{\text{kin}}^{\text{rot}}$  is the kinetic energy, described by the mean square of the velocity fields resulting from the PIV analysis [62], and  $U$  is the internal energy of the granular system, which accounts for the energy dissipated during flow. We compute  $E_{\text{kin}}$  by the addition of the translational  $E_{\text{kin}}^{\text{trans}} = m\bar{v}^2/2$  and rotational  $E_{\text{kin}}^{\text{rot}} = \bar{\omega}^2/2$  contributions, where  $I \approx md_{50}^2/10$  is the moment of inertia of the granular system, approximated by the sum of the moments of inertia of all the particles assumed spherical, and  $\omega = (\partial v_z/\partial x, \partial v_x/\partial z)$  is the average angular velocity field in each time step. We use the near-wall height profile  $z_{\text{wall}}$ , and the average velocity fields  $\mathbf{v}$  and  $\omega$ , respectively to calculate the instantaneous  $E_{\text{pot}}$ , and  $E_{\text{kin}}$ . We normalise the energy components with respect to  $E_{\text{tot}}$ , allowing the response of the different materials to be compared. All energy components are redistributed in time  $\tau$ , as shown in Fig. 23 for two oats and two fertiliser samples, both with initial column aspect ratios  $a < 1$  and  $a > 1$ , and tested at the random packing state. In all cases, we observe that  $E_{\text{tot}} = E_{\text{pot}}$  at  $\tau = 0$ , which is gradually transformed into the variations of  $E_{\text{kin}}$  and  $U$  during flow of the granular material. We find a final decrease of  $E_{\text{pot}}$  with respect to the initial values by 28 and 34 % for  $a < 1$ , and by 47 and 55 % for  $a > 1$ . The fertiliser samples show the larger reductions of the potential energy, which we explain by the greater spreading of the mobilised mass along the channel.

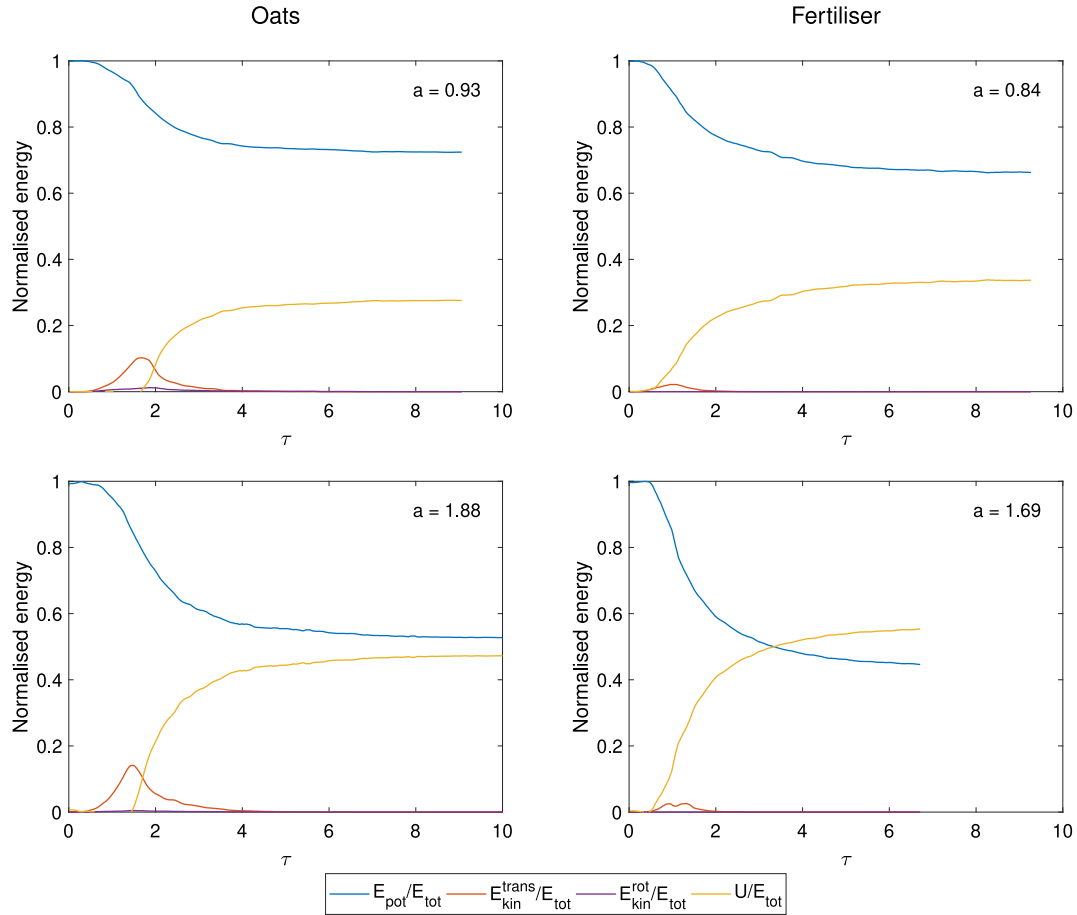


**Fig. 23.** Energy balance of the normalised potential  $E_{\text{pot}}$ , kinetic  $E_{\text{kin}}^{\text{trans}}$  and  $E_{\text{kin}}^{\text{rot}}$ , and internal  $U$  energies with respect to the total energy  $E_{\text{pot}}$ , during flow of oats (left) and fertiliser (right) samples tested at the random packing state with varying values of  $a$ .

Regarding  $E_{\text{kin}}$ , we notice that its variation is controlled by  $E_{\text{kin}}^{\text{trans}}$ , whereas we find the contribution of  $E_{\text{kin}}^{\text{rot}}$  to kinetic energy to be negligible in the case of fertiliser, with peak values between 0.2 and 0.5 % of the peak  $E_{\text{kin}}^{\text{trans}}$ . However, the peak  $E_{\text{kin}}^{\text{rot}}$  values attain 4 and 13 % of the peak  $E_{\text{kin}}^{\text{trans}}$  for the oats samples, as expected for a granular material whose mass mobilisation is dominated by avalanching mechanisms, see Fig. 21. We notice a peak of  $E_{\text{kin}}^{\text{trans}}$  at  $\tau < 2$ , which we relate to the evolution of the instantaneous maximum velocity components shown in Fig. 22, reaching 11 and 14 % of the respective  $E_{\text{tot}}$  for the oats, and 2.6 and 3.0 % in the case of fertiliser, larger for  $a < 1$  in both cases. Finally, in all cases, the increase of internal energy  $U$  at the final static state is equal to the reduction of  $E_{\text{pot}}$ . According to [62], the continuous decay of  $E_{\text{pot}}$  and the peak trend of  $E_{\text{kin}}^{\text{trans}}$  suggest that the initial collapse (first flow stage) is dominated by gravity whereas flow propagation (second and third flow stages) is governed by dissipation processes. Consistently, we attribute the increase of  $U$  mainly to irreversible particle interactions, including plastic normal collisions and the work of tangential forces and torques [73]. As a result, the larger energy dissipation takes place for the fertiliser samples, which show greater mass mobilisation for all values of

the initial column aspect ratio. Furthermore, our experimental evaluation of the model of energy balance in Eq. (14) is validated by our observations in Appendix A, based on the numerical simulation results presented in [74].

## 5. Summary and conclusions

We have presented our new fully-instrumented granular column collapse apparatus responding to the need for an experimental methodology to characterise granular flow of a wide range of powders and grains. Our experimental set-up and the approach followed to interpret the results can be used as a reference framework to inform decision-making strategies for the adequate selection of bulk solids handling equipment, based on a quantitative evaluation of flowability of granular materials. Moreover, our experimental set-up can be further useful for granular flow modelling, with implications for the calibration of numerical model parameters, and the validation of the effect of the material properties and environmental conditions on flowability.



### 5.1. Column collapse apparatus

We have equipped our quasi-two-dimensional channel set-up with novel features and a diversity of redundant measuring techniques, which provide considerable insight into the flowability of powders and grains:

- A new lifting gate design, automated by a parallelogram mechanism that reduces the fast shearing and dragging effects on the samples during gate opening induced by existing vertical and swinging gates.
- A reversible pneumatic circuit with air flow and pressure control to study fluidisation and deaeration effects on the material in granular column collapse set-ups. The air flow range of the circuit allows pre-conditioning the random packing state of the initial granular columns poured into the reservoir, reproducing actual handling conditions.
- An original system with silicone membranes and beam load cells to monitor the basal load distribution during flow at discrete positions along the channel surface. We adapt the weighing technology, employed for dosing in bag filling systems, to the analysis of flow propagation and deposition processes.
- A 3D line profile sensor controlled by a linear guide to scan the free surface morphology of the initial granular column and final deposit configurations of the tested samples. Laser scanning has been used previously on granular column collapse set-ups [34], and overcomes the measuring accuracy of other techniques, such as vernier scales with sliding laser pointers used in [23,28].
- A high-speed video recording set, including a camera and LED lighting, to visualise the near-wall dynamics, as well as to extract kinematic measures and energy balances during the flow by PIV analysis of the video recordings. The use of PIV analysis has mainly been limited to characterising the flow velocities on granular column collapse set-ups [24,25]. Few examples of the experimental evaluation of physical quantities derived from PIV analyses have been reported, though using different set-ups [58], or to validate numerical simulations [61].

### 5.2. Flow characterisation

We have demonstrated the capabilities of the apparatus with selected results from our granular flow tests with oat flakes, copper sulphate fertiliser, and talc powder samples, the highlights of which we summarise as follows:

- Fine-graded materials (fertiliser, talc) are pre-conditioned more effectively by our reversible pneumatic circuit. However, in the explored range of imposed air flow, neither full bed fluidisation nor significant vacuum compaction is attained for coarser materials (oats). In fluidisation conditions, the air pressure drop  $\Delta P$  of powders reaches stabilisation due to the formation of preferential air flow paths, also influencing the variability of the intrinsic permeability  $K$  of the material, whereas we observe a linear decrease of negative  $\Delta P$  with the imposed vacuum, along with a reduction of  $K$ .
- We assume the plane strain hypothesis on the flow dynamics from the profile sensor measurements. The final deposits of fertiliser show a smooth slope and a larger run-out length  $l_\infty$  with respect to the oats and talc samples. The talc flow presents the most uneven distribution of the mobilised mass—due to its cohesive nature—and shows a no-flow scenario when subjected to pre-conditioning by deaeration. We question the use of the angle  $\alpha$  as a suitable flow descriptor for cohesive powders.

- We detect the basal load profiles with the set of load cells, which we fit to an exponential model describing a load deposition ramp  $\lambda_{\text{ramp}}$  between times  $\tau_0$  and  $\tau_\infty$ , and up to the equilibrium load  $\lambda_r$  at the final static state. For fertiliser and talc columns with initial column aspect ratio  $a > 1$ , we observe the formation of a load peak  $\lambda_{\text{peak}}$ , which we attribute to the initial downward acceleration of the mobilised mass after collapse.
- We determine the flow heights  $h_k$  from the basal load distribution in time. We contrast the flow heights with the profile sensor measurements of the free surface of the final deposit over the load cell locations  $\bar{z}_k$  at equilibrium, and the transient near-wall height profiles  $z_{\text{wall}}$  obtained by image analysis of the video recordings. The flowing fertiliser shows  $h_k > \bar{z}_k$  at the cell locations closer to the head of the wedge-shaped flow front, coinciding with the development of  $\lambda_{\text{peak}}$ . We also find  $h_k > \bar{z}_k$  at the load cell locations closer to the toe of the flow front, which we relate to its rapid propagation being dominated by the horizontal inertia of the spreading mass.
- We carry out PIV analyses of the video recordings to obtain the evolving near-wall kinematic fields (displacements, velocities, shear strain rates). We complement our visualisations with morphological data, comprising  $z_{\text{wall}}$  and the flow front trajectory  $\phi$ . We use all this information to differentiate three stages describing the flow dynamics, for all values of  $a$ :
  - an initial flow stage dominated by the vertical component of velocity  $v_z$ , in which an upper sliding block is moving with respect to the material at rest at the bottom of the column, and thus explaining the mechanism leading to the registered  $\lambda_p$  in the basal load profiles;
  - a second flow stage of rapid propagation of  $\phi$ —described by the horizontal component of velocity  $v_x$  at the toe of the wedge-shape flow front, and by  $v_z$  at the head—which stops abruptly at length  $l_\infty$ ;
  - and a third and final flow stage of deceleration of the mass mobilisation, where both  $v_x$  and  $v_z$  are gradually reduced until the static final state is reached, which we clearly observe in the case of oats unlike for fertiliser.
- The energy balance of the granular system during flow propagation is controlled mainly by the redistribution of the potential energy  $E_{\text{pot}}$  and the translational component of the kinetic energy  $E_{\text{kin}}^{\text{trans}}$ , both of which we estimate from the image analysis of the frontal flow visualisations. We approximate the magnitude of the rotational component of the kinetic energy  $E_{\text{kin}}^{\text{rot}}$ , showing its little impact on the flow dynamics of the tested oats samples, and being almost negligible in the case of fertiliser. We attribute the increase in the internal energy  $U$  to the dissipation generated by the interparticle contacts governing the mass mobilisation, this effect being more dominant for flows of fertiliser than in the case of oats. We validate the energy balance by DEM simulations.

In conclusion, we notice the good flowability of the copper sulphate fertiliser in that it is an easily aeratable material with a large mobility reach, as can be seen by the long run-out length and basal load distribution, exhibiting a flow propagation mechanism governed by frictional sliding in two stages of flow. The oat flakes show moderate flowability, having low sensitivity to both fluidisation and deaeration, and a flow dynamics controlled by avalanching related to particle interlocking that results into larger velocity peaks but an overall reduced mass mobilisation. We observe a poor flowability of the cohesive talc powder, which shows an uneven distribution of the deposited material in the static final state and a flow dynamics with short run-out lengths.

## 5.3. Outlook

We are currently investigating a methodology to predict the most suitable feeder type for the dosing of any given granular material by its classification into flowability clusters [75], defined by cluster analysis of a database of powders and grains. Conventional laboratory results, as well as the results from our experimental apparatus, provide us with key information to address this cluster analysis correctly. Therefore, the efficiency of the bulk dosing operations can be improved, yielding environmental and economic benefits for the packaging industry.

Future work will continue to explore the effect of particle shape non-sphericity using superquadrics [76], and the use of micro-macro transition methods [77] to calibrate and validate our DEM simulations against the experimental flow kinematics results from the PIV analyses.

## List of symbols

## Latin symbols

$A$	Cross-sectional area of the granular column ( $\text{m}^2$ )
$a$	Initial column aspect ratio (—)
$C_c$	Circularity coefficient (—)
$d$	Particle size by sieving, percent mass fraction passing in subscript (mm)
$E_{\text{kin}}$	Kinetic energy of the granular system (J)
$E_{\text{kin}}^{\text{rot}}$	Rotational kinetic energy of the granular system (J)
$E_{\text{kin}}^{\text{trans}}$	Translational kinetic energy of the granular system (J)
$E_{\text{pot}}$	Potential energy of the granular system (J)
$E_{\text{tot}}$	Total energy of the granular system (J)
$f$	Force transmitted to the load cells (mN)
$g$	Acceleration of gravity ( $\text{ms}^{-2}$ )
$H$	Average height of the granular column during pre-conditioning (mm)
$h_{\infty}$	Maximum height of the final deposit (mm)
$h_0$	Initial height of the granular column after pre-conditioning, if any (mm)
$h_k$	Flow height at the $k$ -th membrane location (mm)
$h_p$	Initial height of the granular column at the random packing state (mm)
$I$	Moment of inertia of the granular system ( $\text{kg m}^2$ )
$K$	Intrinsic air permeability ( $\text{m}^2$ )
$l_{\infty}$	Run-out length of the final deposit (mm)
$l_0$	Reservoir length (mm)
$m$	Sample mass (kg)
$Q$	Air flow ( $\text{m}^3 \text{s}^{-1}$ )
$R_{\text{ex}}$	External radius of the membranes (mm)
$R_{\text{in}}$	Internal radius of the membranes (mm)
$R_k$	Radius of the cylindrical tributary volume of granular mass over the $k$ -th membrane (mm)
$t$	Time (s)
$t_c$	Characteristic time (s)
$U$	Internal energy of the granular system (J)
$\mathbf{v}$	Average velocity field ( $\text{m s}^{-1}$ )
$w$	Gravimetric water content (%)
$x_k$	Location of the load cells on the $x$ -axis, $k = \{1, \dots, 9\}$ (mm)
$y_{\text{min}}$	Frontmost $y$ -coordinate of the channel width (mm)
$z_{\text{CM}}$	Height of the centre of mass of the granular system (m)
$\bar{z}_k$	Average height of the free surface of the final deposit over the $k$ -th membrane location (mm)
$z_{\text{wall}}$	Near-wall height profile of the granular pile (mm)
$\bar{z}_y$	Average height profile of the final deposit in the $y$ -axis direction (mm)

## Greek symbols

$\alpha$	Angle of the final deposit ( $^{\circ}$ )
$\dot{\gamma}_{xz}$	Incremental shear strain rate ( $\text{s}^{-1}$ )
$\Delta P$	Air pressure drop across the granular column (kPa)
$\Delta t$	Fixed time step between consecutive video frames (s)
$\Delta \mathbf{u}$	Incremental displacement field between consecutive video frames (m)
$\Delta z$	Height variation of the free surface of the granular column after preconditioning (m)
$\varepsilon$	Average porosity (—)
$\theta$	Membrane thickness (mm)
$\lambda$	Nondimensional transmitted load (—)
$\lambda_p$	Nondimensional peak load of the basal load profile peak model (—)
$\lambda_{\text{peak}}$	Nondimensional basal load profile peak model (—)
$\lambda_r$	Nondimensional equilibrium load of the basal load profile ramp model (—)
$\lambda_{\text{ramp}}$	Nondimensional basal load profile ramp model (—)
$\mu_{\text{air}}$	Air dynamic viscosity ( $\text{kg m}^{-1} \text{s}^{-1}$ )
$\mu_s$	Sliding friction coefficient (—)
$\rho$	Time-dependent bulk density during flow propagation ( $\text{kg m}^{-3}$ )
$\rho_{\text{aer}}$	Bulk density after aeration pre-conditioning ( $\text{kg m}^{-3}$ )
$\rho_{\text{air}}$	Air density ( $\text{kg m}^{-3}$ )
$\rho_p$	Bulk density at the random packing state ( $\text{kg m}^{-3}$ )
$\rho_s$	Particle density ( $\text{kg m}^{-1} \text{s}^{-1}$ )
$\rho_{\text{vac}}$	Bulk density after vacuum pre-conditioning ( $\text{kg m}^{-3}$ )
$\rho_{\text{vib}}$	Bulk density after sample vibration ( $\text{kg m}^{-3}$ )
$\sigma_z$	Vertical stress at the base of the poured granular column (kPa)
$\tau$	Nondimensional time (—)
$\tau_{\infty}$	Nondimensional ramp ending time of the basal load profile model (—)
$\tau_0$	Nondimensional ramp starting time of the basal load profile model (—)
$\tau_p$	Nondimensional central time of the basal load profile peak model (—)
$\tau_p'$	Shape coefficient of the basal load profile peak model (—)
$\tau_r$	Nondimensional central time of the basal load profile ramp model (—)
$\tau_r'$	Shape coefficient of the basal load profile ramp model (—)
$\phi$	Normalised flow front location (—)
$\omega$	Average angular velocity field ( $\text{ms}^{-1}$ )

## Acknowledgements

This work was supported by the Industrial Doctorates Plan of the Government of Catalonia [Project 2014 DI 075: Optimization of dosing systems for bulk solids using experimental and numerical techniques]. The authors would like to thank Joan Caba, Xavier Arderiu, Josep-Manel Padullés, and Juanjo González at TMI for their valuable contribution to the design and start-up of our experimental apparatus. The first author would like to acknowledge the support received by the Geotechnical Laboratory at the UPC in the early stages of this research.

## Appendix A. Energy balance by DEM simulations

We validate the energy balance in Eq. (14) with numerical simulations to support our experimental findings. The simulation of granular column collapse tests by the discrete element method (DEM) gives us a direct insight into bulk scale flowability issues by involving the grain

scale properties as model parameters, for instance the particle size polydispersity [78]. We present new results from our investigations in [74] on the effect of hygroscopicity on the mass mobilisation of granular columns using the open-source software MercuryDPM [79]. We implement a linear spring-dashpot particle contact model coupled with a capillary model, assuming the liquid to be distributed onto adsorbed films and capillary bridges between the particles. The published results indicate that liquid contents in the pendular regime lead to the formation of particle aggregates or caking, and thus a decrease in flowability of the granular materials. Therefore, we compare the energy balance of two particle systems of identical mono-disperse spheres with initial column aspect ratios  $a > 2$ , but with differing flowability caused by the different liquid contents  $w = 0.0\%$  and  $7.5\%$  of the dry and wet granular flows, respectively, as shown in Fig. A.1. The decay of  $E_{\text{pot}}$  is attained around  $t = 0.85$  s after collapse in both cases, reaching final energy decreases of 64 % and 47 % with respect to the initial values. The large mass mobilisation of the dry particle system explains the greater  $E_{\text{pot}}$  reduction, as observed in the fertiliser results. The variation of  $E_{\text{kin}}$  is governed by the  $E_{\text{kin}}^{\text{trans}}$  component—with peak values of 13 % and 5 % of the  $E_{\text{tot}}$ , respectively for the dry and wet set-ups—whereas the contribution of  $E_{\text{kin}}^{\text{rot}}$  is not relevant to the energy balance, consistently with numerical results on non-cohesive granular flows in [80]. However, we notice dissimilarities between the  $E_{\text{kin}}^{\text{trans}}$  trends of the numerical results compared to the experimental results in terms of their flowability: larger peak  $E_{\text{kin}}^{\text{trans}}$  values are found for the oats samples experimentally but for the dry set-up numerically, which shows a more free-flowing behaviour as observed for the fertiliser. This is probably due to different particle shapes of the studied materials, especially that of the oat flakes, which enhances the avalanching behaviour that entails large peak velocities during flow propagation. Overall, the evolution of the energy components in the simulations appears to be analogous to the experimental results for  $a > 1$  in Fig. 23 thereby validating the energy balance. Moreover, the agreement between the analyses of the simulation results and the near-wall visualisations also supports the plane strain hypothesis on the flow dynamics.

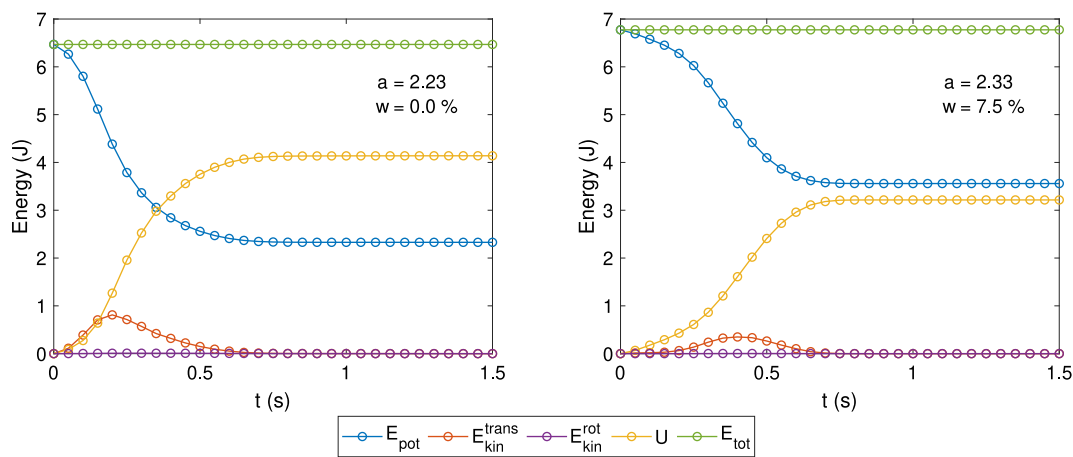


Fig. A.1. Energy balance of dry (left) and wet (right) granular column collapse set-ups used in the DEM simulations.

## References

- [1] W.E. Engisch, F.J. Muzzio, Method for characterization of loss-in-weight feeder equipment, *Powder Technol.* 228 (2012) 395–403, <https://doi.org/10.1016/j.powtec.2012.05.058>.
- [2] C. Fahlenbock, Gain-in-weight batching: choosing system components for maximum accuracy, *Powder Bulk Eng.* 17 (9) (2003) 25–32.
- [3] D. McGlinchey (Ed.), *Bulk Solids Handling: Equipment Selection and Operation*, Wiley-Blackwell, 2008.
- [4] M. Leturia, M. Benali, S. Lagarde, I. Ronga, K. Saleh, Characterization of flow properties of cohesive powders: a comparative study of traditional and new testing methods, *Powder Technol.* 253 (2014) 406–423, <https://doi.org/10.1016/j.powtec.2013.11.045>.
- [5] M. Krantz, H. Zhang, J. Zhu, Characterization of powder flow: static and dynamic testing, *Powder Technol.* 194 (3) (2009) 239–245, <https://doi.org/10.1016/j.powtec.2009.05.001>.
- [6] J.M.N.T. Gray, P. Gajjar, P. Kokelaar, Particle-size segregation in dense granular avalanches, *C. R. Phys.* 16 (1) (2015) 73–85, <https://doi.org/10.1016/j.crh.2015.01.004>.
- [7] M.E. Cates, J.P. Wittmer, J.-P. Bouchaud, P. Claudin, Jamming, force chains, and fragile matter, *Phys. Rev. Lett.* 81 (1998) 1841–1844, <https://doi.org/10.1103/PhysRevLett.81.1841>.
- [8] A.J. Matchett, The shape of the cohesive arch in hoppers and silos – some theoretical considerations, *Powder Technol.* 171 (3) (2007), 133145, <https://doi.org/10.1016/j.powtec.2006.10.010>.
- [9] K. Johanson, Rathole stability analysis for aerated powder materials, *Powder Technol.* 141 (1) (2004) 161–170, <https://doi.org/10.1016/j.powtec.2004.02.004>.
- [10] E. Juarez-Enriquez, G.I. Olivas, P.B. Zamudio-Flores, E. Ortega-Rivas, S. Perez-Vega, D.R. Sepulveda, Effect of water content on the flowability of hygroscopic powders, *J. Food Eng.* 205 (2017) 12–17, <https://doi.org/10.1016/j.jfoodeng.2017.02.024>.
- [11] O. Pozo, B. Soulestin, N. Olivi-Tran, Stick slip motion in grain grain friction in a humid atmosphere, *Multidiscip. Model. Mater. Struct.* 4 (4) (2008) 393–405, <https://doi.org/10.1163/157361108785963037>.
- [12] M. Hartmann, S. Palzer, Caking of amorphous powders – material aspects, modelling and applications, *Powder Technol.* 206 (1) (2011) 112–121, <https://doi.org/10.1016/j.powtec.2010.04.014>.
- [13] J.J. Fitzpatrick, M. Hodnett, M. Twomey, P.S.M. Cerqueira, J. O’Flynn, Y.H. Roos, Glass transition and the flowability and caking of powders containing amorphous lactose, *Powder Technol.* 178 (2) (2007) 119–128, <https://doi.org/10.1016/j.powtec.2007.04.017>.
- [14] V. Ganesan, K.A. Rosentrater, K. Muthukumarappan, Flowability and handling characteristics of bulk solids and powders - a review with implications for DDGS, *Biosyst. Eng.* 101 (4) (2008) 425–435, <https://doi.org/10.1016/j.biosystemseng.2008.09.008>.
- [15] J.L. Amorós, G. Mallol, C. Feliu, M.J. Orts, Study of the rheological behaviour of monomodal quartz particle beds under stress. A model for the shear yield functions of powders, *Chem. Eng. Sci.* 66 (18) (2011) 4070–4077, <https://doi.org/10.1016/j.ces.2011.05.034>.
- [16] V. Garg, S.S. Mallick, P. Garcia-Trinanés, R.J. Berry, An investigation into the flowability of fine powders used in pharmaceutical industries, *Powder Technol.* 336 (2018) 375–382, <https://doi.org/10.1016/j.powtec.2018.06.014>.
- [17] M.R. Wu, D.L. Schott, G. Lodewijks, Physical properties of solid biomass, *Biomass Bioenergy* 35 (5) (2011) 2093–2105, <https://doi.org/10.1016/j.biombioe.2011.02.020>.
- [18] J. Schwedes, Review on testers for measuring flow properties of bulk solids, *Granul. Matter* 5 (1) (2003) 1–43, <https://doi.org/10.1007/s10035-002-0124-4>.
- [19] A.B. Spierings, M. Voegtlin, T. Bauer, K. Wegener, Powder flowability characterisation methodology for powder-bed-based metal additive manufacturing, *Prog. Addit. Manuf.* 1 (1) (2016) 9–20, <https://doi.org/10.1007/s40964-015-0001-4>.

- [20] U. Zafar, C. Hare, A. Hassanpour, M. Ghadiri, Ball indentation on powder beds for assessing powder flowability: analysis of operation window, *Powder Technol.* 310 (2017) 300–306, <https://doi.org/10.1016/j.powtec.2017.01.047>.
- [21] R. Baserinia, I.C. Sinka, Mass flow rate of fine and cohesive powders under differential air pressure, *Powder Technol.* 334 (2018) 173–182, <https://doi.org/10.1016/j.powtec.2018.04.041>.
- [22] G. Lumay, F. Boschini, K. Traina, S. Bontempi, J.-C. Remy, R. Cloots, N. Vandewalle, Measuring the flowing properties of powders and grains, *Powder Technol.* 224 (2012) 19–27, <https://doi.org/10.1016/j.powtec.2012.02.015>.
- [23] G. Lube, H.E. Huppert, R.S.J. Sparks, M.A. Hallworth, Axisymmetric collapses of granular columns, *J. Fluid Mech.* 508 (2004) 175–199, <https://doi.org/10.1017/S0022112004009036>.
- [24] G. Lube, H.E. Huppert, R.S.J. Sparks, A. Freundt, Collapses of twodimensional granular columns, *Phys. Rev. E* 72 (4) (2005), 041301, <https://doi.org/10.1103/PhysRevE.72.041301>.
- [25] E. Lajeunesse, J.B. Monnier, G.M. Homsy, Granular slumping on a horizontal surface, *Phys. Fluids* 17 (10) (2005), 103302, <https://doi.org/10.1063/1.2087687>.
- [26] N.J. Balmforth, R.R. Kerswell, Granular collapse in two dimensions, *J. Fluid Mech.* 538 (2005) 399–428, <https://doi.org/10.1017/S0022112005005537>.
- [27] S. Siavoshi, A. Kudrolli, Failure of a granular step, *Phys. Rev. E* 71 (2005), 051302, <https://doi.org/10.1103/PhysRevE.71.051302>.
- [28] E.L. Thompson, H.E. Huppert, Granular column collapses: further experimental results, *J. Fluid Mech.* 575 (2007) 177–186, <https://doi.org/10.1017/S0022112006004563>.
- [29] G. Lube, H.E. Huppert, R.S.J. Sparks, A. Freundt, Static and flowing regions in granular collapses down channels, *Phys. Fluids* 19 (4) (2007), 043301, <https://doi.org/10.1063/1.2712431>.
- [30] C. Meriaux, T. Triantafillou, Scaling the final deposits of dry cohesive granular columns after collapse and quasi-static fall, *Phys. Fluids* 20 (3) (2008), 033301, <https://doi.org/10.1063/1.2870148>.
- [31] E. Lajeunesse, A. Mangeney-Castelnau, J.P. Vilotte, Spreading of a granular mass on a horizontal plane, *Phys. Fluids* 16 (7) (2004) 2371–2381, <https://doi.org/10.1063/1.1736611>.
- [32] M. Trepanier, S.V. Franklin, Column collapse of granular rods, *Phys. Rev. E* 82 (2010), 011308, <https://doi.org/10.1103/PhysRevE.82.011308>.
- [33] J.M. Warnett, P. Denissenko, P.J. Thomas, M.A. Williams, Collapse of a granular column under rotation, *Powder Technol.* 262 (2014) 249–256, <https://doi.org/10.1016/j.powtec.2014.04.030>.
- [34] J.M. Warnett, P. Denissenko, P.J. Thomas, E. Kiraci, M.A. Williams, Scalings of axisymmetric granular column collapse, *Granul. Matter* 16 (1) (2014) 115–124, <https://doi.org/10.1007/s10035-013-0469-x>.
- [35] Z. Lai, L.E. Vallejo, W. Zhou, G. Ma, J.M. Espitia, B. Caicedo, X. Chang, Collapse of granular columns with fractal particle size distribution: implications for understanding the role of small particles in granular flows, *Geophys. Res. Lett.* 44 (24) (2017) 12181–12189, <https://doi.org/10.1002/2017GL075689>.
- [36] S.K. Bryant, W.A. Take, E.T. Bowman, Observations of grain-scale interactions and simulation of dry granular flows in a large-scale flume, *Can. Geotech. J.* 52 (5) (2015) 638–655, <https://doi.org/10.1139/cgj-2013-0425>.
- [37] A. Mangeney, O. Roche, O. Hung, N. Mangold, G. Faccanoni, A. Lucas, Erosion and mobility in granular collapse over sloping beds, *J. Geophys. Res. Earth Surf.* 115 (2010), F03040, <https://doi.org/10.1029/2009JF001462>.
- [38] M. Farin, A. Mangeney, O. Roche, Fundamental changes of granular flow dynamics, deposition, and erosion processes at high slope angles: insights from laboratory experiments, *J. Geophys. Res. Earth Surf.* 119 (3) (2014) 504–532, <https://doi.org/10.1002/2013JF002750>.
- [39] G. Lube, H.E. Huppert, R.S.J. Sparks, A. Freundt, Granular column collapses down rough, inclined channels, *J. Fluid Mech.* 675 (2011) 347–368, <https://doi.org/10.1017/jfm.2011.21>.
- [40] A.J. Hogg, Two-dimensional granular slumps down slopes, *Phys. Fluids* 19 (9) (2007), 093301, <https://doi.org/10.1063/1.2762254>.
- [41] F. Maeno, A.J. Hogg, R.S.J. Sparks, G.P. Matson, Unconfined slumping of a granular mass on a slope, *Phys. Fluids* 25 (2) (2013), 023302, <https://doi.org/10.1063/1.4792707>.
- [42] G.B. Crosta, S. Imposimato, D. Roddeman, Granular flows on erodible and non erodible inclines, *Granul. Matter* 17 (5) (2015) 667–685, <https://doi.org/10.1007/s10035-015-0587-8>.
- [43] O. Roche, S. Montserrat, Y. Niño, A. Tamburrino, Pore fluid pressure and internal kinematics of gravitational laboratory air-particle flows: insights into the emplacement dynamics of pyroclastic flows, *J. Geophys. Res. Solid Earth* 115 (2010), B09206, <https://doi.org/10.1029/2009JB007133>.
- [44] O. Roche, M. Attali, A. Mangeney, A. Lucas, On the run-out distance of geophysical gravitational flows: insight from fluidized granular collapse experiments, *Earth Planet. Sci. Lett.* 311 (3) (2011) 375–385, <https://doi.org/10.1016/j.epsl.2011.09.023>.
- [45] R. Artoni, A.C. Santomaso, F. Gabrieli, D. Tono, S. Cola, Collapse of quasi-two-dimensional wet granular columns, *Phys. Rev. E* 87 (3) (2013), 032205, <https://doi.org/10.1103/PhysRevE.87.032205>.
- [46] F. Gabrieli, R. Artoni, A. Santomaso, S. Cola, Discrete particle simulations and experiments on the collapse of wet granular columns, *Phys. Fluids* 25 (10) (2013), 103303, <https://doi.org/10.1063/1.4826622>.
- [47] A.C. Santomaso, S. Volpato, F. Gabrieli, Collapse and runoff of granular columns in pendular state, *Phys. Fluids* 30 (6) (2018), 063301, <https://doi.org/10.1063/1.5030779>.
- [48] L. Rondon, O. Pouliquen, P. Aussillous, Granular collapse in a fluid: role of the initial volume fraction, *Phys. Fluids* 23 (7) (2011), 073301, <https://doi.org/10.1063/1.3594200>.
- [49] A. Bougouin, L. Lacaze, Granular collapse in a fluid: different flow regimes for an initially dense-packing, *Phys. Rev. Fluids* 3 (2018), 064305, <https://doi.org/10.1103/PhysRevFluids.3.064305>.
- [50] C.-H. Lee, Z. Huang, M.-L. Yu, Collapse of submerged granular columns in loose packing: experiment and two-phase flow simulation, *Phys. Fluids* 30 (12) (2018), 123307, <https://doi.org/10.1063/1.5050994>.
- [51] J. Torres-Serra, E. Romero, A. Rodríguez-Ferran, J. Caba, X. Arderiu, J.-M. Padullés, J. González, Flowability of granular materials with industrial applications - an experimental approach, *EPJ Web Conf.* 140 (2017), 03068, <https://doi.org/10.1051/epjconf/201714003068>.
- [52] J. Torres-Serra, E. Romero, A. Rodríguez-Ferran, A new granular column collapse device to characterise flowability of bulk materials, *Proceedings* 2 (8) (2018) 488, <https://doi.org/10.3390/ICEM18-05389>.
- [53] Y. Forterre, O. Pouliquen, Flows of dense granular media, *Annu. Rev. Fluid Mech.* 40 (1) (2008) 1–24, <https://doi.org/10.1146/annurev.fluid.40.111406.102142>.
- [54] R.T. Schneider, Pneumatics and vacuum perform in packaging equipment, *Hydraul. Pneum.* 50 (9) (1997) 45–46.
- [55] K.A. Holsapple, Modeling granular material flows: the angle of repose, fluidization and the cliff collapse problem, *Planet. Space Sci.* 82–83 (2013) 11–26, <https://doi.org/10.1016/j.pss.2013.03.001>.
- [56] D. Golliu, W. Brevis, E.T. Bowman, P. Shepley, Performance of PIV and PTV for granular flow measurements, *Granul. Matter* 19 (3) (2017), 42, <https://doi.org/10.1007/s10035-017-0730-9>.
- [57] A.J. Holyoake, J.N. McElwaine, High-speed granular chute flows, *J. Fluid Mech.* 710 (2012) 35–71, <https://doi.org/10.1017/jfm.2012.331>.
- [58] L. Sarno, A. Carravetta, Y.-C. Tai, R. Martino, M. Papa, C.-Y. Kuo, Measuring the velocity fields of granular flows - employment of a multi-pass two-dimensional particle image velocimetry (2D-PIV) approach, *Adv. Powder Technol.* 29 (12) (2018) 3107–3123, <https://doi.org/10.1016/j.apt.2018.08.014>.
- [59] B. Turnbull, E.T. Bowman, J.N. McElwaine, Debris flows: experiments and modelling, *C. R. Phys.* 16 (1) (2015) 86–96, <https://doi.org/10.1016/j.crhy.2014.11.006>.
- [60] N. Sanvitale, E.T. Bowman, Visualization of dominant stress-transfer mechanisms in experimental debris flows of different particle-size distribution, *Can. Geotech. J.* 54 (2) (2017) 258–269, <https://doi.org/10.1139/cgj-2015-0532>.
- [61] T. Xu, Y.-C. Jin, Y.-C. Tai, C.-H. Lu, Simulation of velocity and shear stress distributions in granular column collapses by a mesh-free method, *J. Non-Newtonian Fluid Mech.* 247 (2017) 146–164, <https://doi.org/10.1016/j.jnnfm.2017.07.003>.
- [62] S.J. de Vet, B. Yohannes, K.M. Hill, J.R. de Bruyn, Collapse of a rectangular well in a quasi-two-dimensional granular bed, *Phys. Rev. E* 82 (2010), 041304, <https://doi.org/10.1103/PhysRevE.82.041304>.
- [63] W. Thielicke, E.J. Stamhuis, PIVlab - towards user-friendly, affordable and accurate digital particle image velocimetry in MATLAB, *J. Open Res. Softw.* 2 (1) (2014) e30, <https://doi.org/10.5334/jors.bl>.
- [64] A. Masullo, R. Theunissen, Automated mask generation for PIV image analysis based on pixel intensity statistics, *Exp. Fluids* 58 (6) (2017), 70, <https://doi.org/10.1007/s00348-017-2357-3>.
- [65] J.M. Boac, M.E. Casada, R.G. Maghirang, J.P. Harner III, Material and interaction properties of selected grains and oilseeds for Modeling discrete particles, *Trans. ASABE* 53 (4) (2010) 1201–1216, <https://doi.org/10.13031/2013.32577>.
- [66] T. Oishi, M. Goto, A. Kasahara, M. Tosa, Low frictional copper oxide film prepared with sodium hydroxide solution, *Surf. Interface Anal.* 36 (8) (2004) 1259–1261, <https://doi.org/10.1002/sia.1889>.
- [67] X. Chen, A.S. Elwood Madden, Z. Reches, The frictional strength of talc gouge in high-velocity shear experiments, *J. Geophys. Res. Solid Earth* 122 (5) (2017) 3661–3676, <https://doi.org/10.1002/2016JB013676>.
- [68] S.J. Blott, K. Pye, Particle shape: a review and new methods of characterization and classification, *Sedimentology* 55 (1) (2008) 31–63, <https://doi.org/10.1111/j.1365-3091.2007.00892.xc>.
- [69] T.H. Druitt, G. Avar, G. Bruni, P. Lettieri, F. Maez, Gas retention in fine-grained pyroclastic flow materials at high temperatures, *Bull. Volcanol.* 69 (8) (2007) 881–901, <https://doi.org/10.1007/s00445-007-0116-7>.
- [70] J.R. van Ommen, J.M. Valverde, R. Pfeffer, Fluidization of nanopowders: a review, *J. Nanopart. Res.* 14 (3) (2012), 737, <https://doi.org/10.1007/s11051-012-0737-4>.
- [71] D. Geldart, E.C. Abdullah, A. Hassanpour, L.C. Nwoke, I. Wouters, Characterization of powder flowability using measurement of angle of repose, *China Particul.* 4 (3) (2006) 104–107, [https://doi.org/10.1016/S1672-2515\(07\)60247-4](https://doi.org/10.1016/S1672-2515(07)60247-4).
- [72] E.J. Fern, K. Soga, The role of constitutive models in MPM simulations of granular column collapses, *Acta Geotech.* 11 (3) (2016) 659–678, <https://doi.org/10.1007/s11440-016-0436-x>.
- [73] Y. Guo, J.S. Curtis, Discrete element method simulations for complex granular flows, *Annu. Rev. Fluid Mech.* 47 (1) (2015) 21–46, <https://doi.org/10.1146/annurev-fluid-1010814-014644>.
- [74] J. Torres-Serra, E. Romero, A. Rodríguez-Ferran, Hygroscopicity issues in powder and grain technology, in: C.W.W. Ng, A.K. Leung, A.C.F. Chiu, C. Zhou (Eds.), 7th International Conference on Unsaturated Soils, UNSAT 2018, Hong Kong University of Science and Technology 2018, pp. 805–810.
- [75] J. Torres-Serra, J. Caba, A. Rodríguez-Ferran, E. Romero, Classifying granular materials for feeding performance using experimental and numerical techniques, 9th International Conference on Conveying and Handling of Particulate Solids, 2018, CHoPS, 2018.
- [76] A. Podlozhnyuk, S. Pirker, C. Kloss, Efficient implementation of superquadr particles in discrete element method within an open-source framework, *Comput. Part. Mech.* 4 (1) (2017) 101–118, <https://doi.org/10.1007/s40571-016-0131-6>.
- [77] D.R. Tunuguntla, A.R. Thornton, T. Weinhart, From discrete elements to continuum fields: extension to bidisperse systems, *Comput. Part. Mech.* 3 (3) (2016) 349–365, <https://doi.org/10.1007/s40571-015-0087-y>.

- [78] J. Torres-Serra, D.R. Tunuguntla, I.F.C. Denissen, A. Rodríguez-Ferran, E. Romero, Discrete element modelling of granular column collapse tests with industrial applications, in: P. Wriggers, M. Bischoff, E. Oñate, D. Owen, T. Zohdi (Eds.), 5th International Conference on Particle-Based Methods - Fundamentals and Applications, PARTICLES 2017, International Center for Numerical Methods in Engineering 2017, pp. 530–538.
- [79] T. Weinhart, D.R. Tunuguntla, M.P.v.S. Lantman, I.F. Denissen, C.R. Windows-Yule, H. Polman, J.M. Tsang, B. Jin, L. Orefice, K. van der Vaart, S. Roy, H. Shi, A. Pagano, W. den Breeijen, B.J. Scheper, A. Jarray, S. Luding, A.R. Thornton, MercuryDPM: fast, flexible particle simulations in complex geometries part II: applications, in: P. Wriggers, M. Bischoff, E. Oñate, D. Owen, T. Zohdi (Eds.), 5th International Conference on Particle-Based Methods - Fundamentals and Applications, PARTICLES 2017, International Center for Numerical Methods in Engineering 2017, pp. 123–134.
- [80] S. Utili, T. Zhao, G.T. Housby, 3D DEM investigation of granular column collapse: evaluation of debris motion and its destructive power, *Eng. Geol.* 186 (2015) 3–16, <https://doi.org/10.1016/j.enggeo.2014.08.018>.



# CLASSIFICATION OF GRANULAR MATERIALS VIA FLOWABILITY-BASED CLUSTERING WITH APPLICATION TO BULK FEEDING

---

Reproduced from: J. Torres-Serra, A. Rodríguez-Ferran, and E. Romero, Classification of granular materials via flowability-based clustering with application to bulk feeding, *Powder Technology*, vol. 378, pp. 288–302, 2021. DOI: [10.1016/j.powtec.2020.09.022](https://doi.org/10.1016/j.powtec.2020.09.022)

Research data associated to this article is available online at: J. Torres-Serra, *Data for: Classification of granular materials via flowability-based clustering with application to bulk feeding*, version V1, Mendeley Data, 2020. [Dataset]. DOI: [10.17632/sxg3hg3txw.1](https://doi.org/10.17632/sxg3hg3txw.1)

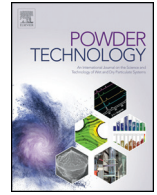






Contents lists available at ScienceDirect

## Powder Technology

journal homepage: [www.elsevier.com/locate/powtec](http://www.elsevier.com/locate/powtec)

# Classification of granular materials via flowability-based clustering with application to bulk feeding

J. Torres-Serra<sup>a,b,\*</sup>, A. Rodríguez-Ferran<sup>b</sup>, E. Romero<sup>b</sup>

<sup>a</sup> *Técnicas Mecánicas Ilerdenses, S.L., Polígono industrial Camí dels Frares, c. Alcarràs, parc. 66, 25190 Lleida, Spain*

<sup>b</sup> *Department of Civil and Environmental Engineering, Universitat Politècnica de Catalunya, Campus Nord, c. Jordi Girona, 1-3, 08034 Barcelona, Spain*

## ARTICLE INFO

## Article history:

Received 29 January 2020

Received in revised form 31 August 2020

Accepted 14 September 2020

Available online 17 September 2020

## Keywords:

Classification

Cluster analysis

Flowability

Bulk feeding

Granular column collapse

## ABSTRACT

Feeder selection impacts the performance of bagging machinery throughout its life cycle, and yet it is usually based on qualitative assessments of flowability. We propose a data analysis methodology aimed at verifying the feeder-type classification of powders and grains by cluster analysis on their material properties. Results for a first data set of conventional properties show the granular materials clustered into as many groups as main bulk feeding systems. Mismatch between feeder classes and flowability-based clusters is explained by common industrial practice and incomplete material characterisation. For this reason, we introduce a set of specialised properties measured with the granular flow tester we have recently developed. Results for principal component analysis on a second extended property data set show that similarly flowing granular materials are better detected considering the specialised properties. This research contributes to objectify the decision-making process of bulk feeder selection from the quantitative description of granular flow.

© 2020 Elsevier B.V. All rights reserved.

## 1. Introduction

Selecting the most suitable bulk feeding technique for dosing powders and grains is still a current design issue in the packaging industry. Reliability of the dosing operation is crucial for bagging line manufacturers such as Técnicas Mecánicas Ilerdenses, S.L. (TMI) [1]. Bag-filling machines incorporate various volumetric feeders that transport material batches in gain-in-weight systems [2] downstream towards the filling station. A wide range of granular materials are typically packaged in 5 kg to 50 kg bags and at competitive production rates of the order of  $10^2 \text{ kg h}^{-1}$  to  $10^4 \text{ kg h}^{-1}$ . Therefore, the chosen feeding system has a direct influence on the finished package quality as well as the overall performance of a bagging line. In industrial practice, the anticipation of the handling performance and the particle size distribution of any given material, together with the engineering know-how of the designer, constitute the empirical basis for selecting one of the feeder types in Fig. 1:

- Fluidisation chamber (F) feeders are used for valve bag filling [3] by pneumatic transport of the batches with a pressure vessel.
- Gravity (G) feeders allow free discharge of the granular materials from the supply hopper.

- Screw (S) feeders convey granular materials by positive displacement with one or more augers. Many applications require coupling with vacuum nozzles for deaeration (SD) of the already filled open-mouth bags [3] to densify the granular mass and prepare the package to be closed.
- Belt (T) feeders perform material conveying by positive displacement along a belt.

Fig. 2 shows typical ranges of the median particle size of the powders and bulk solids handled by the main feeding techniques, obtained from available data on the granular materials used in this study. Generally, F-type feeders are used for handling fine-grained materials, as well as S- and SD-fed systems are designed to handle fine-grained, cohesive materials. Moreover, G-type feeders are employed with free-flowing, coarse-grained materials, and T-fed systems are selected for coarse-grained materials including materials prone to jamming or with irregular particle shapes. Other feeding systems are less frequently adopted, including: vibratory tray (V) feeders for positive displacement of fragile, coarse-grained materials; rotary valve (R) feeders for free discharge free-flowing, fine-grained materials; and combined feeding systems, such as GV- and GS-type feeders, especially adapted to handling broad product families. Nevertheless, such a hands-on approach to the feeder selection process is potentially leading the decision maker to ill-informed choices, overly relying on a subjective appreciation of flowability, which is commonly estimated with qualitative *quick tests* [4].

\* Corresponding author at: Department of Civil and Environmental Engineering, Universitat Politècnica de Catalunya, Campus Nord, c. Jordi Girona, 1-3, 08034 Barcelona, Spain.

E-mail addresses: [joel.torres@upc.edu](mailto:joel.torres@upc.edu) (J. Torres-Serra), [antonio.rodriguez-ferran@upc.edu](mailto:antonio.rodriguez-ferran@upc.edu) (A. Rodríguez-Ferran), [enrique.romero-morales@upc.edu](mailto:enrique.romero-morales@upc.edu) (E. Romero).

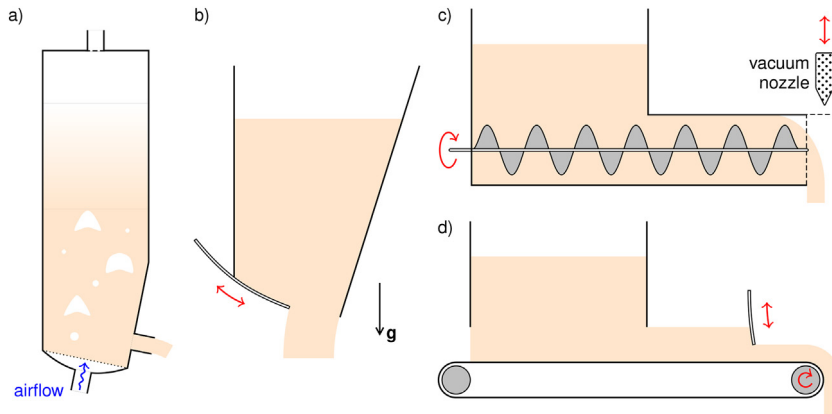


Fig. 1. Schematics of the main bulk feeding techniques: a) F-type feeder with lower inlet for air fluidisation; b) G-type feeder with adjustable gate opening; c) S-type feeder with variable screw rotation, and vacuum nozzle for bag deaeration in SD-fed systems; d) T-type feeder with adjustable belt speed and gate opening.

Traditionally, a number of experimental methods using small-scale laboratory tests have been proposed to quantitatively estimate granular flow, including:

- Jenike's flow function, expressing a relationship between yield loci, i.e. between the consolidation stress  $\sigma_1$  and the unconfined yield strength  $\sigma_c$ , usually measured by means of translational and ring shear testers [5]. Flowability according to Jenike is defined by constant values of the ratio  $ff_c = \sigma_1/\sigma_c$ , with five flowability levels from not flowing ( $ff_c < 1$ ) to free-flowing ( $ff_c > 10$ ).
- Carr's flowability index, defined as a weighed sum of parameters: two measures of the angle of repose, namely the angles of repose and of spatula; compressibility derived from the aerated and packed bulk densities; and the cohesion and uniformity coefficients obtained by sieving analysis [6]. The resulting point score ranks flowability into seven levels from very, very poor to excellent on a 0–100 scale.
- Geldart's powder classification diagram, described from observation of gas-fluidised beds, considering their mean particle size and particle-fluid density difference for classification [7]. Four fluidisation groups of powders—namely Geldart A (aeratable), B (bubbling), C (cohesive), and D (dense) powders—are identified by their behaviour at the minimum fluidisation and bubbling states.

- More recently, Freeman's flow energies, obtained by dynamic testing of powder samples with a powder rheometer [8]. Flow energy is determined by the resistance to blade rotation coupled with axial motion during powder displacement. Various flowability parameters are defined, such as the basic flowability energy and the specific energy, serving to distinguish powders with similar properties.

These methods offer a fundamental characterisation of powder flow, yet with limited feasibility for coarser granular materials at the standardised lower scales [9]. Alternatively, full-scale pilot plant testing can gauge flow behaviour in actual conditions, although at high costs that make it impractical for routine use [10]. Consequently, we designed, manufactured, and tested an intermediate scale apparatus to describe flow in a granular column collapse set-up [11], which we refer to as the TMI granular flow tester (GFT). This newly patented technology [12] is easily operated and applies to powders and bulk solids in the range of particle sizes from  $\mu\text{m}$  to mm.

Fig. 3 illustrates the wide range of granular materials studied in this paper. We observe the variability in two representative material properties: at the particle level, the median particle size in the range of  $3.5 \times 10^1 \mu\text{m}$  to  $1.8 \times 10^4 \mu\text{m}$ , and at the bulk level, the loose bulk density with values between  $5.5 \times 10^1 \text{kg m}^{-3}$  and  $1.7 \times 10^3 \text{kg m}^{-3}$ . Comparing

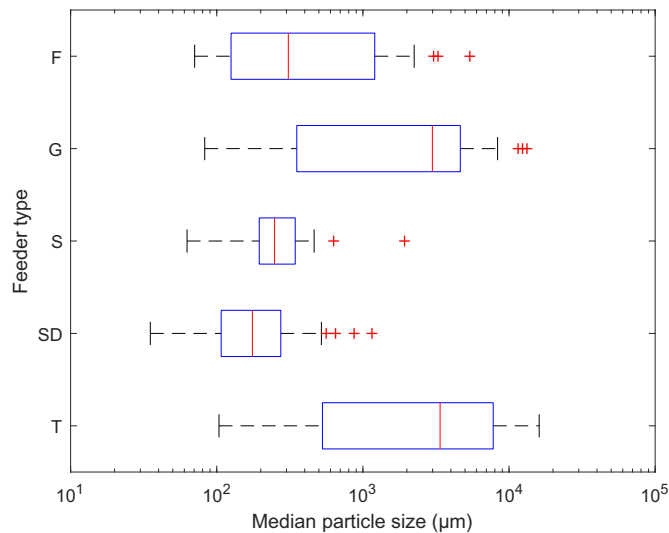


Fig. 2. Box plot of the median particle size of the granular materials studied, grouped by feeder types selected from industrial know-how.

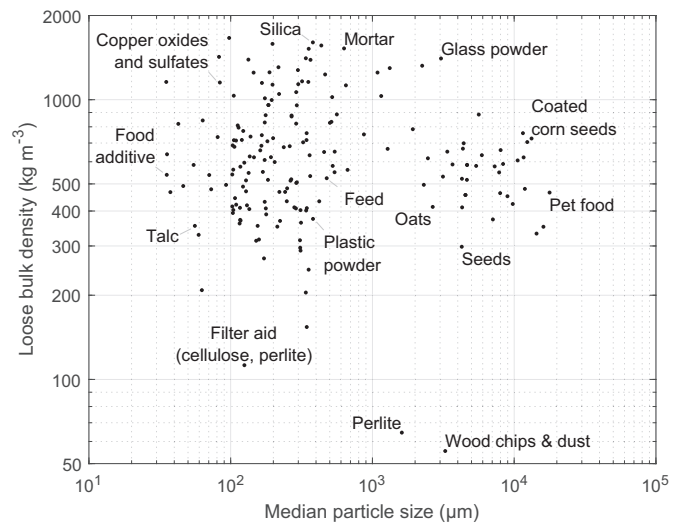


Fig. 3. Range of granular materials studied.

these two properties alone, the granular materials are not distinctively grouped by expected handling performance, and the description of their complex mechanical behaviour is incomplete. The aim of this study is to examine a systematic classification tool to organise the variability in properties describing the flowability of granular materials for practical application in industry.

In recent years, there has been a growing interest in exploiting multivariate analysis methods to predict flow behaviour from experimental measurements [13]. The particle size and shape of pharmaceutical powders have been used to estimate quasi-static flow descriptors, by partial least-squares [14], and using multiple linear regression of relevant parameters selected by principal component analysis (PCA) [15]. Another PCA model has been applied to observe the clustering tendencies and establish the dominant parameters in a pharmaceutical powder database [16]. Moreover, these statistical tools have been used to predict screw feeder performance at powder feeding rates between  $0.1 \text{ kg h}^{-1}$  and  $99.6 \text{ kg h}^{-1}$  [17–22]. Particularly, PCA has been reported to enhance the visualisation of pharmaceutical powder clusters with similar flowability [21].

Section 2 presents a data analysis methodology to evaluate the implemented bulk feeding techniques by cluster analysis and to help select the best suited feeder. The flowability of an extensive data set of powders and grains, produced in diverse industrial sectors, is described considering a few conventional material properties. Statistical pre-treatment of the data is based on outlier detection and variable reduction by PCA. In Section 3, we aim at improving the feeder selection associated with the flowability-based clustering. To this end, we complement the material characterisation using specialised material properties measured with the GFT, and discuss their contribution to a thorough description of flowability.

## 2. Data analysis methodology

We gather experimental results by conventional testing of an initial raw data set of 174 granular materials stored in the first data set (DS1) in [23]. We henceforth refer to the rows of DS1 as observations, i.e. the set of information from every granular material, and to the columns of DS1 as variables, containing the different material properties. Table 1 summarises the six available material properties. We denote by  $\rho_{\text{vib}}$  the bulk density after sample vibration, serving as tapped density in the calculation of the Hausner ratio. We carry out a data treatment scheme for all the granular materials in DS1 to verify their feeder-type classification from industrial know-how against the flowability based clustering from our analysis of the flow descriptors. For any new material, the workflow consists in updating the following scheme in three main steps, and checking the actually applied technical solution for the closest neighbours. First, we search the raw data set to discard outlying observations. Secondly, we obtain a reduced set of variables via PCA, which explain granular flow in a space of lower dimension. Thirdly, we apply cluster analysis to the low-dimensional space of variables to visualise the clustering tendency in the data. Fig. 4 depicts the data treatment before cluster analysis. We illustrate our methodology using three reference materials, namely

**Table 1**  
Conventional material properties in DS1.

Variable type	Symbol	Description	Protocols
State	$\rho_b$	Loose bulk density ( $\text{Mgm}^{-3}$ )	ASTM D7481 [50]
Mechanical	$HR$	Hausner ratio ( $\rho_b/\rho_{\text{vib}}$ )	ASTM D4253 [51], USP (1174) [52]
	$\theta$	Angle of repose ( $^\circ$ )	Hollow cylinder method [53]
Geometrical (size & shape)	$d_{50}$	Median particle size ( $\mu\text{m}$ )	ASTM C136 [54], ISO 3310-1 [55]
	$C_u$	Uniformity coefficient ( $d_{60}/d_{10}$ )	ISO 9276-6 [56]
	$C_c$	Circularity coefficient (–)	ISO 9276-6 [56]

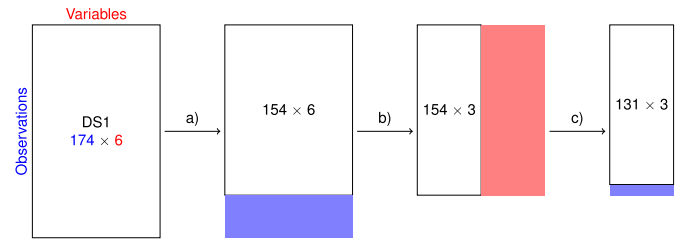


**Fig. 4.** Data set preparation for cluster analysis, detailed for DS1: a) removal of outlying observations; b) dimensionality reduction via PCA; c) removal of undefined and underpopulated class members.

O1, O2, and O3, tested as part of the same project for packaging of feed additive powders and bulk solids, which correspond respectively to observations 164, 165, and 166 in DS1.

### 2.1. Observation selection

Variables showing large dispersion are more likely to include outliers: measurements much smaller or larger than the quantities of interest, which make effectively differentiating between similar observations difficult. We apply a generalised expectation-maximisation algorithm [24] to Gaussian mixture models of the data to find distinct subpopulations in the variables and detect outlying observations. Fig. 5 shows the 174 values of the uniformity coefficient  $140 C_u$ , ranging between 1.0 and 7.8, with  $C_u = 3.1, 3.3,$  and  $3.9$  respectively for the reference observations O1, O2, and O3. Applying a three-component mixture model to the  $C_u$  data, we note that the values farther from the reference observations are comprised by ‘Subpopulation 3’, which we remove from further analysis. Analogously, we discard all observations with median particle sizes  $d_{50} > 8.1 \times 10^3 \mu\text{m}$ , given that the values of interest are between  $d_{50} = 1.9 \times 10^2 \mu\text{m}$  and  $1.9 \times 10^3 \mu\text{m}$ . We find outliers within the geometrical variables describing the particle size distribution of the samples: outlying observations in  $d_{50}$  include coarse-grained materials such as cereal seeds and flakes, hot melt adhesive pearls, and pet food pellets;  $C_u$  outliers correspond to well graded mortars, and mixed granular materials forming feed and food additives or chemical compounds. The remaining variables do not present significant outlier subpopulations and so, in total, we keep 154 observations.

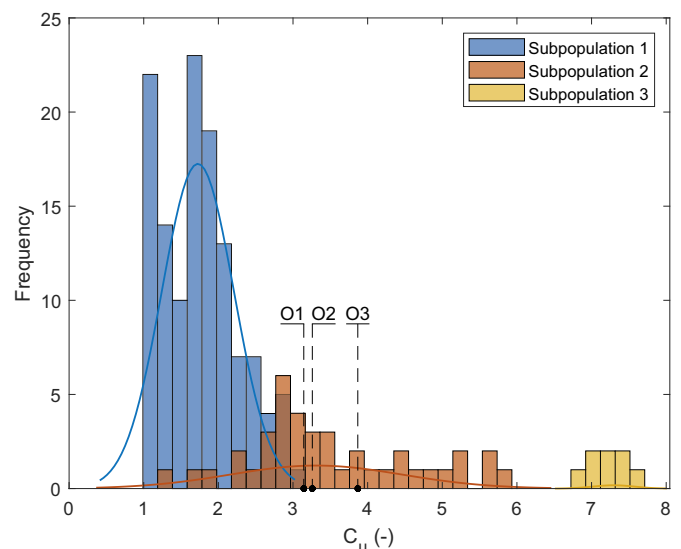


**Fig. 5.** Detected subpopulations in the  $C_u$  data in DS1.

## 2.2. Variable reduction

To compare the material property values in different scales, we first centre and normalise the original variables. Then, we perform principal component analysis [25] on the standardised variables, to project them into the orthogonal directions carrying the most relevant information from the variables. The projected principal components (PC) explain data variability in such a way that the  $n$ th PC explains more data variability from the original data set than the  $(n + 1)$ th PC. We need the first five principal components to capture more than 90% of the information in the six original variables, as shown by the cumulative explained variance plot in Fig. 6. For data visualisation purposes, we use the reduced set consisting of the first three projected variables, capturing over 75% of the information in DS1. Fig. 7 shows the coefficients of the principal components, also known as PC loadings: the point areas are proportional to the relative weights of the variables, whereas the contrasting point colours represent the sign patterns of the correlation between variables. The meanings of positive or negative correlation associated with the two colours are interchangeable, since the sign of any given PC is arbitrary [25]. We discuss the data trends in the elements, or PC scores, of the first three principal components, which describe flowability in terms of the conventional material properties:

**PC1** Identifies a positive correlation between the mechanical variables,  $HR$  and  $\theta$ , for observations with inversely proportional values of  $\rho_b$ ,  $d_{50}$ , and  $C_c$ . Among the analysed materials, fine-grained materials with irregular particle shape show lower bulk density, related to higher compressibility, and steeper angle of repose values. Observation 148 shows the minimum PC1 score for a filter aid material, mixing cellulose and perlite powders. Conversely, as in the case of observation O3, lower  $HR$  and  $\theta$  values are shown by denser packings of coarser, rounded particles. The maximum PC1 score is attained by glass beads corresponding to observation 150.

**PC2** The geometrical variables describing particle size distribution,  $d_{50}$  and  $C_u$ , are negatively correlated. In turn, fine-grained, well-graded materials show higher bulk density and lower angle of repose values, as we note for O1 and O2, and with minimum PC2 score for a feed powder (observation 51). Oppositely, monodisperse, coarser granular materials present lower bulk density and higher angle of repose, as the pet food pellets (observation 122) having the maximum PC2 score.

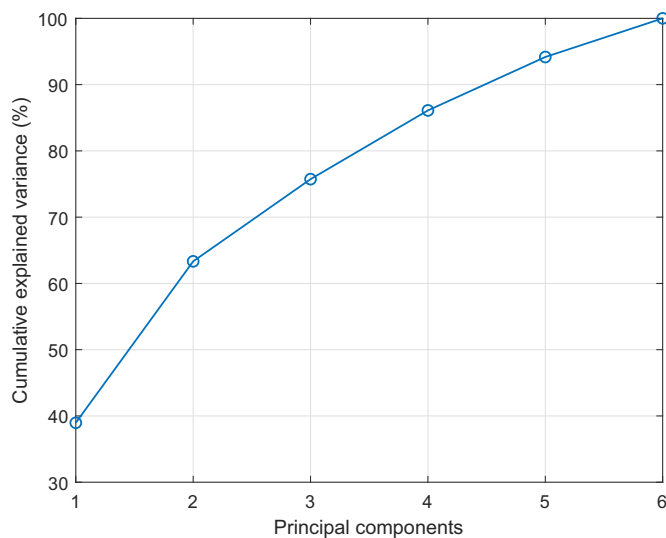


Fig. 6. Cumulative explained variance of the principal components in DS1.

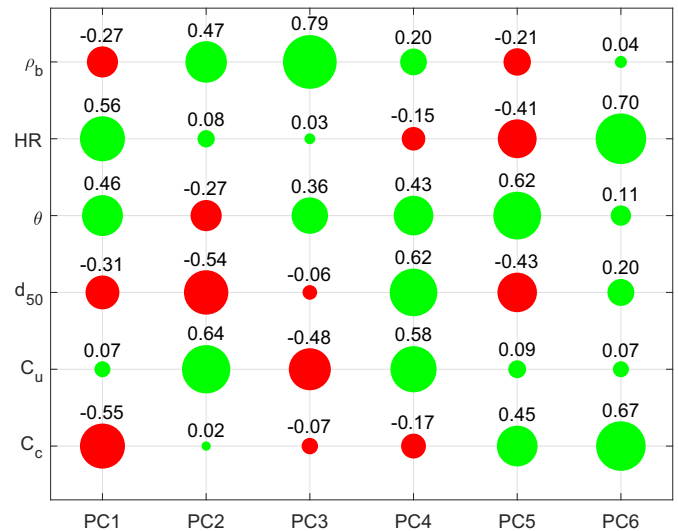


Fig. 7. PC loadings showing the correlation between the original variables and the principal components in DS1.

**PC3** Governed by the state variable  $\rho_b$ , it indicates a positive correlation between  $\rho_b$  and  $\theta$ , both negatively correlated with the  $C_u$  values. We detect the extreme PC3 scores for observations 90, a high-density micronised zirconium silicate powder, and 139, a low-density sawdust sample.

## 2.3. Cluster analysis

Granular materials in DS1 are identified by the feeder systems utilised in actual designs. We remove from the analysis those observations with an undefined feeder type or pertaining to classes amounting to less than 5% of the 154 selected observations. The remaining 131 observations are classified into the predominant bulk feeding techniques: fluidisation chamber (F), gravity (G), screw (S) and screw with deaeration (SD), and belt (T). Fig. 8a illustrates the clustering tendency in the labelled observations, as projected into the 3D space maximising their granular flow description. We perform cluster analysis [26] on the reduced variable set to contrast the given feeder-type classification with the resulting flowability-based clustering of the observations. We fix the number of clusters a priori, equal to the five bulk feeding techniques the analysed materials are classified into from industrial know-how. We use the spatial distribution of the feeder-type centroids to initialise the K-means partitioning algorithm implemented in the MATLAB® Statistics and Machine Learning Toolbox™, with the default square Euclidean distance metric. We validate the cluster analysis a posteriori using various statistical criteria, see Appendix A. Fig. 8b shows the grouping of the analysed granular materials into five clusters:

**C1** The largest cluster consists of 49 granular materials with centroid near the origin of the PC1-PC2-PC3 space. It is mainly populated by powders, ranging from dairy feed (with up to 13 observations) to polymers, among others, including the feed additive sample O3. Few coarser-grained materials are classified into this cluster, albeit with specific properties contributing to a reduced flowability. Observations 21 and 134 are sepiolite and perlite samples, with low and very low  $\rho_b$  respectively, and high  $C_u$  in the case of perlite, whereas observation 153 is a rice sample with low  $C_c$ .

**C2** Its 20 members have the centroid on positive PC2 and PC3, and PC1 values closer to the origin. This cluster shows the minimum pairwise centroid distance with respect to C1, and hence similar

materials are expected in C2. Comparing the reference observations O1 and O2 in C2 with O3 in C1, we find that the samples in C2 show higher  $\rho_b$  and lower  $\theta$ —the negative variable correlation captured by PC2. We note the same data trend between the food additive samples in C2 (observations 101, 103, and 106) and the remaining samples in C1. Moreover, the food additive samples in C2 show higher  $C_c$ , a trend explained by PC3 that is also identified in the flour samples distributed between C1 and C2.

C3 With centroid located on values of positive PC1 and PC2, and negative PC3, this cluster comprises 19 granular materials. It includes samples with high  $\rho_b$  and  $C_c$  values, as in the case of glass beads and crushed glass samples (observations 44, 45, and 71 to 74) or granulated fertilisers (observations 60, 61, 63, 64, and 109 to 113). C4 The most isolated and least populated cluster, with 15 observations, has its centroid on positive PC1, negative PC2, and values near the origin of PC3. It is composed of samples with large  $d_{50}$ , and low  $C_u$  and  $\rho_b$ , such as plastic pellets, cereal flakes or pet food. C5 It contains 28 observations with centroid on negative PC1 and PC2, and PC3 values closer to the origin. It is populated by powders and bulk solids mainly characterised by high  $HR$  and  $\theta$  values, as expected from the positive correlation of the mechanical variables revealed by PC1. This cluster includes the maximum observed values

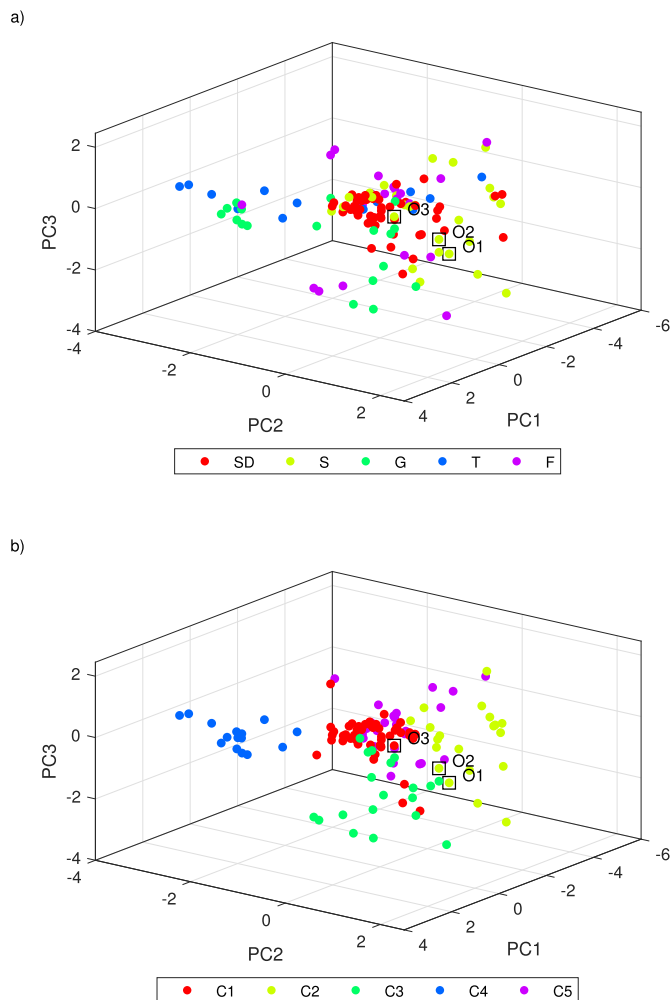


**Fig. 8.** Projections of DS1 into the first three principal directions. Labels: a) feeder-type classification from industrial know-how; b) flowability-based clustering. Please find the interactive MATLAB® figure files in [23].

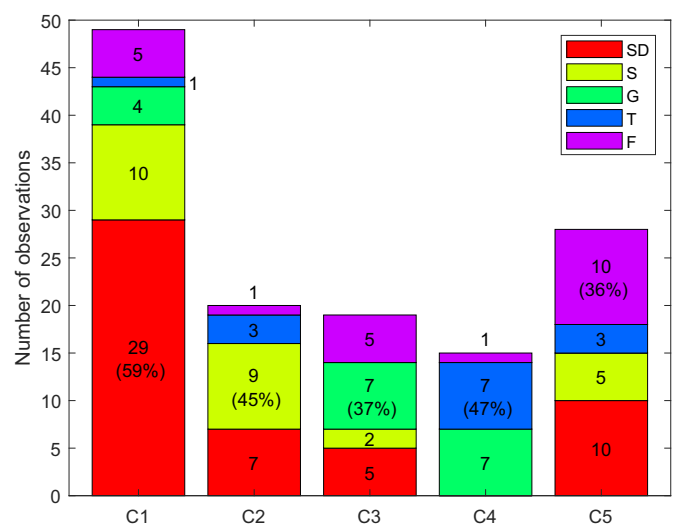
of  $HR$  and  $\theta$ , respectively for a filter aid sample (observation 148) and a kaolin powder (observation 30).

Fig. 9 shows the goodness of match between the feeder-type classification and the flowability-based clustering of the analysed granular materials, as typically obtained from the contingency table. We find 59% of pairs matching with the feeder type SD in cluster C1. This strong interrelation is indicative that SD-fed systems are the most suitable bulk feeding technique for handling granular materials within the C1 borders. However, we observe matching pairs below 50% for the other clusters and the best-fitted feeder types. We attribute this significant degree of independence between classes and clusters to several factors:

- A single bagging machine is often employed by the end user to pack a product range with distinct mechanical behaviours. This can lead the designer to a suboptimal solution for bulk feeding of the different granular materials. For instance, we consider the reference observations O1, O2, and O3 highlighted in Fig. 8. The implemented screw feeder (S) solution is indeed appropriate for handling O1 and O2, whereas bag deaeration (SD) is also necessary for adequate O3 feeding performance.
- Project requirements are decisive in the design phase of a bagging line. Common industrial practices of the producers may nonetheless interfere with performance-oriented solutions. For example, the usage of valve bags is requested by the producer of resin granules (observation 56), imposing the F-type classification on the only material of this class in cluster C4, see Fig. 8.
- The short number of conventional material properties provide insufficient characterisation of granular flow. In fact, relevant state variables such as the particle density and the water content are missing from DS1. Additionally, the available mechanical variables are mostly related to the quasi-static flow regime, typical of stored granular materials at rest.

### 3. Analysis of an extended property data set

As a strategy to refine the presented data analysis, we recognise the need for gaining insight into the dense and dilute flow regimes occurring in actual handling conditions. Hence, we developed the GFT as an ad hoc experimental set-up [11], composed of a rectangular channel with glass walls, and fully-instrumented as depicted in Fig. 10, allowing us to obtain new material properties from the direct observation of granular column collapse tests [27,28]. The testing protocol starts by



**Fig. 9.** Frequency distribution of the feeder type classes, and most frequent fractions for each flowability cluster in the reduced DS1.

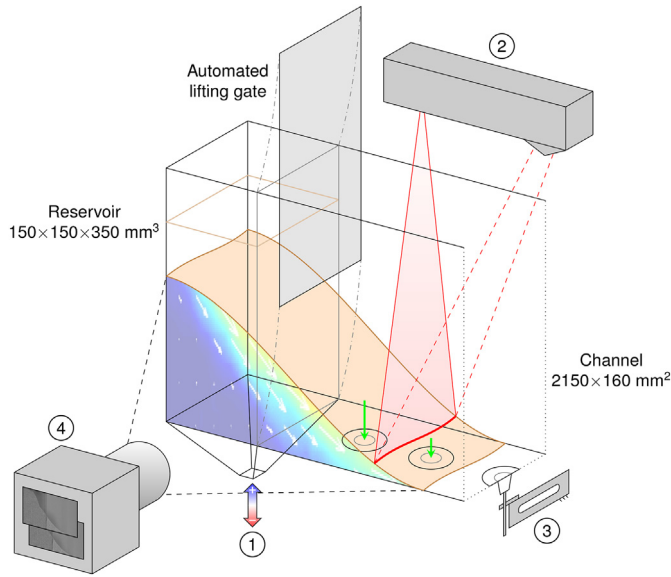


**Fig. 10.** Annotated diagram of the TMI granular flow tester (GFT) with numbered measuring instruments: 1. reversible pneumatic circuit; 2. 3D laser line profile sensor; 3. membranes and beam load cells; 4. high-speed video camera for particle image velocimetry (PIV) analysis.

**Table 2**  
GFT test case numbering: initial column aspect ratio  $a$  against packing state preconditioning.

	Poured	Aeration	Vacuum
$a \leq 1$	1	2	3
$a > 1$	4	5	6

pouring a sample of known mass into the reservoir, enclosed by the gate. Then, the packing state of the granular column is preconditioned with imposed aeration or vacuum conditions. Time zero is set at the beginning of gate lifting, which marks the onset of flow: initially

**Table 3**  
Specialised material properties in DS2, obtained with the numbered measuring instruments in Fig. 10.

Feature	Phenomenon	Symbol	Description
1	Bed expansion	$K$	Intrinsic air permeability ( $m^2$ )
2	Surface morphology	$\rho_p$	Poured granular column bulk density ( $kgm^{-3}$ )
		$h_p$	Poured granular column height (mm)
		$h_0$	Initial column height after pre-conditioning (mm)
		$h_\infty$	Maximum height of the final deposit (mm)
		$l_\infty$	Run-out length (mm)
3	Basal load propagation	$\alpha$	Angle of the final deposit ( $^\circ$ )
		$f_r$	Equilibrium load (mN)
		$t_r$	Ramp time (ms)
		$t_r'$	Ramp shape (ms)
		$f_p$	Peak load (mN)
		$t_p$	Peak time (ms)
		$t_p'$	Peak shape (ms)
4	Near-wall kinematics	$t_\infty$	Run-out time (s)
		$E_{tot}$	Total energy of the granular system (J)
		$E_{pot}^{min}$	Minimum potential energy (J)
		$E_{kin,x}^{min}$	Maximum horizontal kinetic energy (J)
		$t_x$	Time of $E_{kin,x}^{max}$ (s)
		$E_{kin,z}^{min}$	Maximum vertical kinetic energy (J)
		$t_z$	Time of $E_{kin,z}^{max}$ (s)

dominated by vertical collapse, and followed by horizontal propagation of the flow front until the final deposit is formed at run-out.

Table 2 enumerates six test cases covering various initial configurations of the granular column geometry and packing state, for an exhaustive characterisation of any given material. For every test case, we consider at least two representative repetitions to extract the average measurements of the up to 20 specialised material properties listed in Table 3:

- During the pre-conditioning step, the poured random packing state of granular column can be aerated or deaerated with the reversible pneumatic circuit (1). We impose a positive or negative air flow through a porous plate at the reservoir base, reproducing actual bulk handling conditions in fluidisation chamber feeding or bag

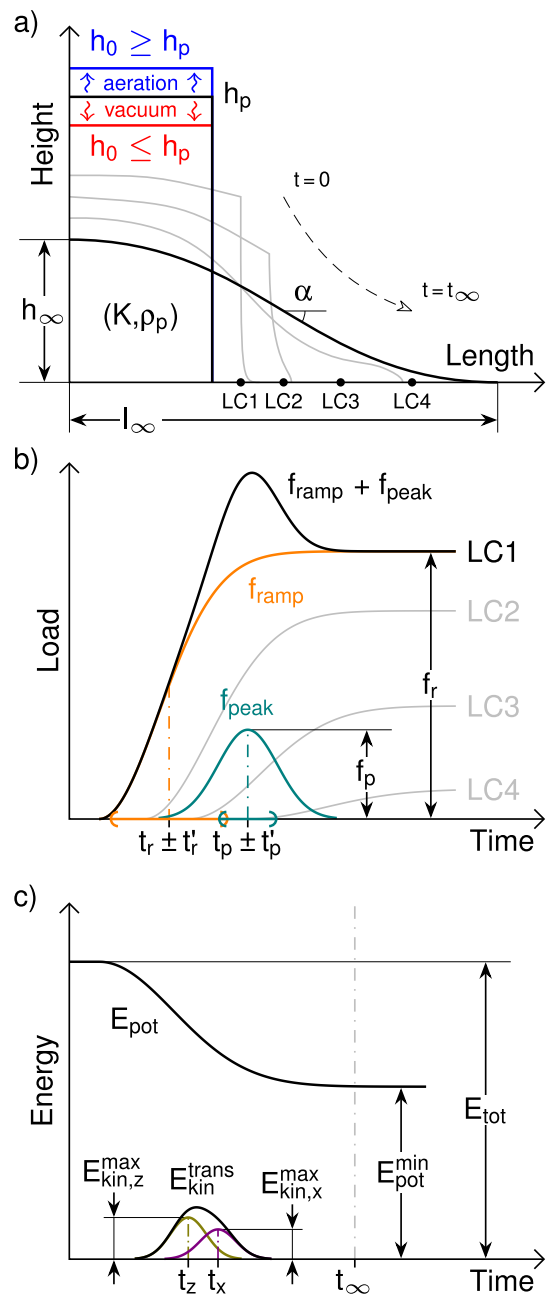


**Fig. 11.** Graphs of the specialised material properties in Table 3: a) geometry of the granular sample at the poured, initial and final states; b) fitting parameters of the basal load profiles; c) evolution of the system energy components.

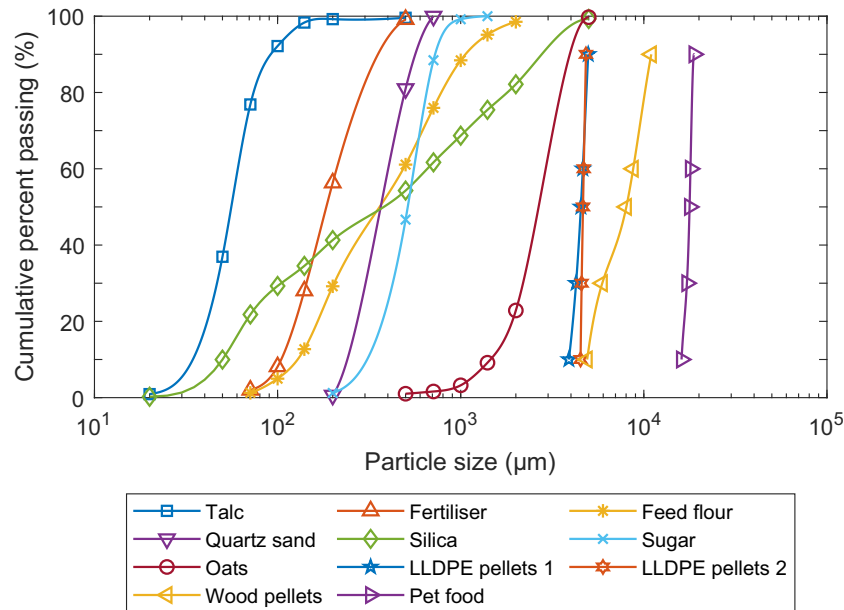


Fig. 12. Particle size distribution curves of the granular materials in DS2.

densification respectively. We estimate the intrinsic air permeability  $K$  from the linearised relationship between the air flow and pressure at the column base.

- Fig. 11a represents the variables acquired from the profile sensor (2) surface scans of the initial granular column and the final deposit at rest. We determine the poured bulk density  $\rho_p$  using the prismatic volume of the granular column of average poured height  $h_p$ . The ratio of the average initial height  $h_0$  to the fixed reservoir length  $l_0 = 150$  mm defines the initial column aspect ratio  $a \leq 2$ . We estimate the angle  $\alpha$  by fitting the surface of the final deposit with a sigmoid function, as the arc tangent of the slope at its central point.
- A depositional process takes place during flow front advance, described by a gradual increase of the loads accumulated on the channel surface, until stabilisation. The force distribution is transmitted to a set of beam load cells (LC) triggered at the onset of flow, through silicone membranes embedded along the channel base (3). Granular flow propagation is monitored by a set of transmitters and the basal load profiles are recorded. For  $a > 1$ , the initial collapse involves a rapid change of momentum of the mobilised mass, resulting in observed load peaks close to the reservoir exit. Fig. 11b shows the fitting parameters for the basal load ramp and peak profiles detected by the first load cell (LC1).
- Using a high-speed video camera (4), we visualise the evolution of the height profiles closer to the glass walls. We derive the incremental kinematic fields from particle image velocimetry (PIV) analysis of the video

recordings using the open-source software PIVlab [29]. More details about our PIV approach to the analysis of granular flows can be found in Appendix B. We define the run-out time  $t_\infty$  as the first instant at which mobilisation is completed. The evolution of the dominant energy components of the granular system can be seen in Fig. 11c. The total energy  $E_{\text{tot}}$  is preserved, and equal to the potential energy  $E_{\text{pot}}$  at the onset of flow. The kinetic energy of the system is governed by its translational component  $E_{\text{kin}}^{\text{trans}}$ , found from the combined contributions of the vertical and horizontal components of velocity. A further description of the estimation of kinetic energy from PIV analysis is available in [11].

We build a second data set (DS2) [23] with 11 selected granular materials covering particle sizes of the order of  $10^1 \mu\text{m}$  to  $10^4 \mu\text{m}$  in the range of the granular materials in DS1, as shown in the sieving analysis results in Fig. 12. DS2 includes polydisperse materials, such as the well-graded silica, the study of which is still an open topic in granular mechanics [30]. We take into account 118 specialised variables characterising each observation in DS2, in addition to the 8 conventional material properties presented in Table 4. Compared to the variable set in DS1, the conventional variables in DS2 incorporate the gravimetric water content  $w$ , measured according to the standardised procedures in [31], as well as values found in the literature of the particle density  $\rho_s$ —otherwise measured by fluid displacement—and the friction coefficient  $\mu_s$ .

Table 4

Conventional material properties in DS2.

Material	$\rho_b(\text{kgm}^{-3})$	$HR(-)$	$d_{50}(\mu\text{m})$	$C_u(-)$	$C_c(-)$	$w(\%)$	$\rho_s(\text{kgm}^{-3})$	$\mu_s(-)$
Talc	354	1.76	56	1.76	0.35	0.38	2750 [57]	0.4–0.8 [58]
Fertiliser	957	1.08	185	2.01	0.76	1.18	2284 [57]	0.08–0.15 [59]
Feed flour	633	1.21	361	3.78	0.58	9.73	582–739 [60]	0.49–0.69 [60]
Quartz sand	1388	1.10	366	1.67	0.71	0.09	2650	0.58 [61]
Silica	1603	1.25	380	13.1	0.30	0.08	2160–2200	0.49–0.50 [62]
Sugar	833	1.16	514	1.80	0.70	0.28	1576 [63]	0.60–0.71 [64]
Oats	414	1.12	$2.66 \times 10^3$	2.00	0.63	12.3	950–1397 [65]	0.53–0.62 [65]
LLDPE pellets 1	456	1.05	$4.53 \times 10^3$	1.19	0.66	0.20	922 [66]	0.28–0.47 [67]
LLDPE pellets 2	585	1.04	$4.65 \times 10^3$	1.04	0.84	0.09		
Wood pellets	660	1.16	$8.02 \times 10^3$	1.78	0.60	8.76	1236	0.70–0.84 [9]
Pet food	466	1.10	$1.78 \times 10^4$	1.12	0.76	9.46	924	0.21–0.47 [68]

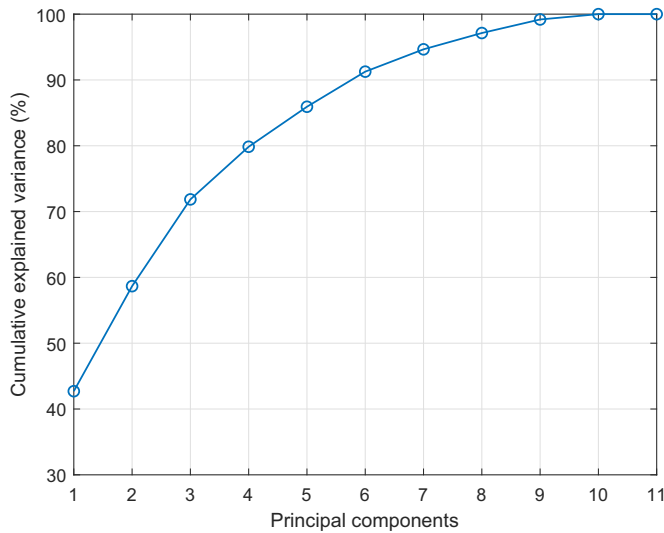


Fig. 13. Cumulative explained variance of the principal components in DS2.

We investigate the variable reduction of DS2, dealing with the data gaps by means of the procedure detailed in [32], which allows us to recover the PCA decomposition of the full data set from the already known material properties. Fig. 13 shows the cumulative explained variance of the projected data set, which carries in the first six principal components over 90% of the information in DS2. In contrast with the decomposition of DS1, a smaller fraction of the total number of PC is required to capture the same amounts of data variability in DS2. We interpret the relative increase of the explained variance as an effect of the comprehensive material characterisation with the GFT. Furthermore, we examine the independence between the conventional and

specialised variables in DS2. Fig. 14 shows the poor correlation between the respective PC1-PC2-PC3 of the two variable subsets, thereby confirming that the conventional variables alone cannot explain the new data trends captured by the specialised variables.

We project the observations in DS2 into their first two principal directions, from analysis of the 8 conventional variables in Fig. 15a, and in comparison with the total of 126 conventional and specialised variables in Fig. 15b. For the sake of visualisation, we perform isometric scalings of the observations in Fig. 15 to a unitary average distance. We observe close flowability in both 2D spaces for the two linear low-density polyethylene (LLDPE) pellet samples (labelled P1 and P2), supporting the idea that these materials can be handled by the same bulk feeding technique. Moreover, the detection of similar flow behaviour is enhanced in Fig. 15b for the oats (Q1) and pet food (Q2), which we attribute to an avalanching mechanism noticed during flow propagation in the GFT [11]. This phenomenon is identified by the material properties describing the near-wall kinematics, see Table 3, and related to particle interlocking of irregular-shaped materials—oat flakes and flat ellipsoidal pellets, in this case. Additionally, we consider the silica (R1) and quartz sand (R2), showing similar conventional material properties apart from a much wider particle size distribution in the case of R1, with larger  $C_u$  though around similar  $d_{50}$ , and less rounded particles, with lower  $C_c$ . The estimated flowability of R1 in Fig. 15a is approximately as close to that of R2 as to that of talc (R3). Despite the disparity in conventional properties, we estimate analogous specialised properties of R1 and R2 by GFT testing, especially the large  $l_\infty$ ,  $f_p$ , and  $E_{kin,x}^{max}$  and  $E_{kin,z}^{max}$ , which we relate with free-flowing materials. As a result, R1 and R2 are relatively closer in Fig. 15a, and their expected flow behaviour is very distant from that of the poorly flowing R3.

These findings indicate that the extended property data set helps in refining the feeder selection by reducing the uncertainty in grouping similar granular materials based on a thorough flowability characterisation. Flowability is a multiphysical, multiscale, coupled phenomenon that has traditionally been approached by selecting a reduced

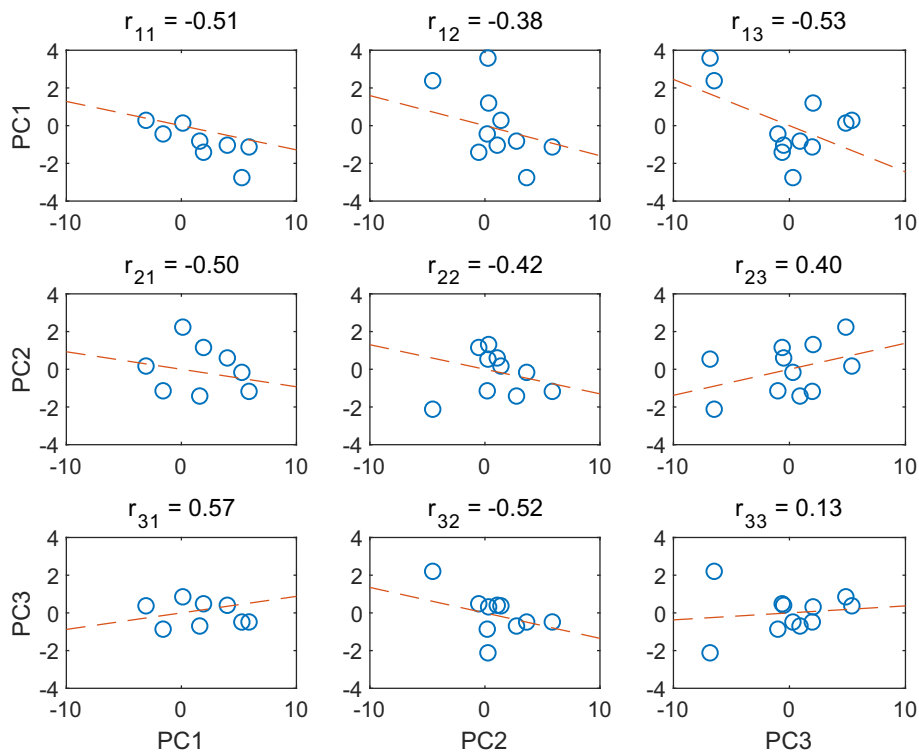


Fig. 14. Correlation between the first three principal components of the conventional (rows  $i$ ) and specialised (columns  $j$ ) variable subsets in DS2, annotated with the pairwise Pearson's linear correlation coefficients  $r_{ij}$ .



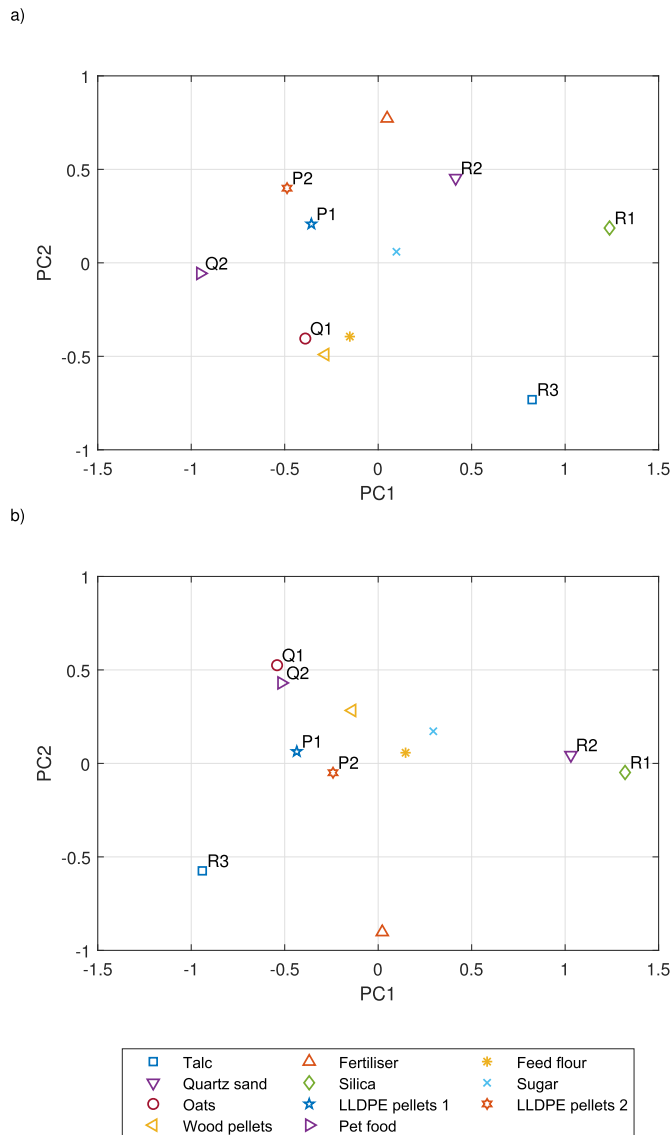


Fig. 15. Scaled projections of DS2 into the first two principal directions, considering: a) the conventional variables; b) the conventional and specialised variables.

set of material properties partially capturing granular flow behaviour. We discuss variable selection for DS2 in Appendix C, as a trade-off between the interpretability of the data—providing us with a fundamental understanding of the underlying flow mechanisms—and the accuracy of the estimation of flowability—improving the performance of our data analysis methodology for industrial application.

#### 4. Conclusions

We have investigated feeder selection among five bulk feeding techniques used in the packaging industry to handle a wide range of powders and bulk solids from  $10^1\mu\text{m}$  to  $10^4\mu\text{m}$ . We have devised a data analysis methodology, applied to the study of DS1, a large data set of 174 granular materials characterised by 6 conventional material properties. We have found that:

- The reduced number of conventional tests, apt for day-to-day industrial practice, allows seeing relevant clustering tendencies in the data. Cluster analysis by K-means partitioning groups similarly flowing materials into an optimum number of clusters equal to the five main bulk feeding techniques.

- As expected, qualitative feeder-type classification based on industrial know-how shows a noticeable disagreement with quantitative flowability based predictions. The best match, between the SD feeder class and cluster C1, has a 59% of matching pairs.

New decision-making strategies can be put forward to select the most suitable feeding systems, from the evidence offered by the mismatched materials, as discussed for the reference observation O3. In this way, the end user can be advised about alternative bulk feeding solutions, concerning the recommended type of bag or the number of feeding systems needed to deal with a product range.

We have refined our analysis on the extended property data set DS2, of 11 representative materials characterised by 8 conventional, plus 118 specialised material properties obtained from different test cases with the GFT. Our PCA results show that more data variability in DS2 is explained by fewer principal components with respect to DS1, as well as that there is a lack of correlation between the decomposition of the conventional versus specialised variables in DS2. In sum, the new specialised variables provide a complementary description of granular flow that enhances the detection of similarly flowing materials, such as in the case of observation R1. The GFT is also validated as a powerful tool for the investigation of the flowability of powders and grains.

In this paper, we have approached flowability as a complex phenomenon through proper statistical treatment of experimental data, in contrast with existing qualitative empirical methods and quantitative testing techniques with limited application. Our findings have implications for improving feeder selection towards an actual flowability-based process, by building robust data sets with a representative variety of granular materials, and fully-characterised with conventional and specialised material properties. Visualisation of the clustering tendencies in the data, by principal component and cluster analysis techniques, groups powders and grains with similar estimated granular flow behaviour. And then, the observed groupings can be verified against uncertain classifications of the adequate bulk feeding techniques, obtained from industrial know-how, for both the analysed granular materials and any new materials being incorporated for classification.

We suggest that further research should address the following topics:

- Verifying the data analysis methodology for larger data sets with extended material properties.
- Validating the clustering through feeder performance assessment by full-scale pilot plant testing.
- Adapting the proposed methodology to selection processes for other bagging machine appliances, such as weighing systems and bag sealing techniques.
- Analysing the influence of the conventional material properties on the specialised flow descriptors, such as the maximum kinetic energy of the granular systems tested with the GFT.
- Extending the specialised characterisation with reverse-calibrated material properties, for instance by discrete element modelling of the GFT set-up to find the mechanical contact parameters.

#### Declaration of Competing Interest

None.

#### Acknowledgements

This work was supported by the Industrial Doctorates Plan of the Government of Catalonia (2014 DI 075) and the Centre for the Development of Industrial Technology of the Government of Spain (IDI-20160298). The authors would like to thank Joan Caba, Xavier Arderiu, Josep-Manel Padullés, and Juanjo González at TMI for their valuable contribution to the design and start-up of the TMI granular flow tester.

### Appendix A. Cluster analysis validation

We estimate the randomness in DS1 throughout the three analysis steps in Section 2 with the Hopkins statistic [33], averaged over 1000 trials and a sampling window of 10% of the remaining observations in the data set. Typical values of the Hopkins statistic  $H$  range between 0.5 for random data and 1 for well clustered data. The original DS1 has  $H = 0.59$ , justifying for the data treatment steps before cluster analysis. We calculate  $H = 0.90$  after the observation selection step, reaching up to  $H = 0.98$  after variable reduction, as evidence for the clustering tendency in the projected space. We perform cluster analysis on the first three principal components of the reduced DS1, which retain most of the clusteriness of the full decomposition, with an average value of the Hopkins statistic of 0.94.

We evaluate the dispersion of the clustering structure, focusing on the probable number of clusters  $k$  in the reduced data set. To this end, we assess the six internal validation indices summarised in [34], each using different criteria to find the optimum number of clusters  $k^*$ , see Table A.1. The variety of indices show a discrepancy in  $k^*$  found in PC1-PC2-PC3. The number of clusters fixed a priori is only validated by the Hartigan index, defined as the smallest number scoring below the threshold value  $\eta = 10$ , and which is especially intended to be applied in the K-means algorithm. However, as can be seen in Fig. A.1, all the indices determine the same  $k^* = 5$ , having discarded as outliers those granular materials with a median particle size  $d_{50} > 3$  mm. Therefore, we confirm that the most probable number of clusters in the flowability data coincides with the five bulk feeding techniques of interest. Having a different optimum number of clusters  $k^* \neq 5$  would not allow us to establish a direct correspondence between classes and clusters. If  $k^* < 5$ , several feeding techniques might be interchangeable to handle granular materials in the same flowability cluster. Otherwise, if  $k^* > 5$ , the flowability of different clusters of granular materials within the same feeder-type class might be best fitted by feeding techniques other than the five main ones.

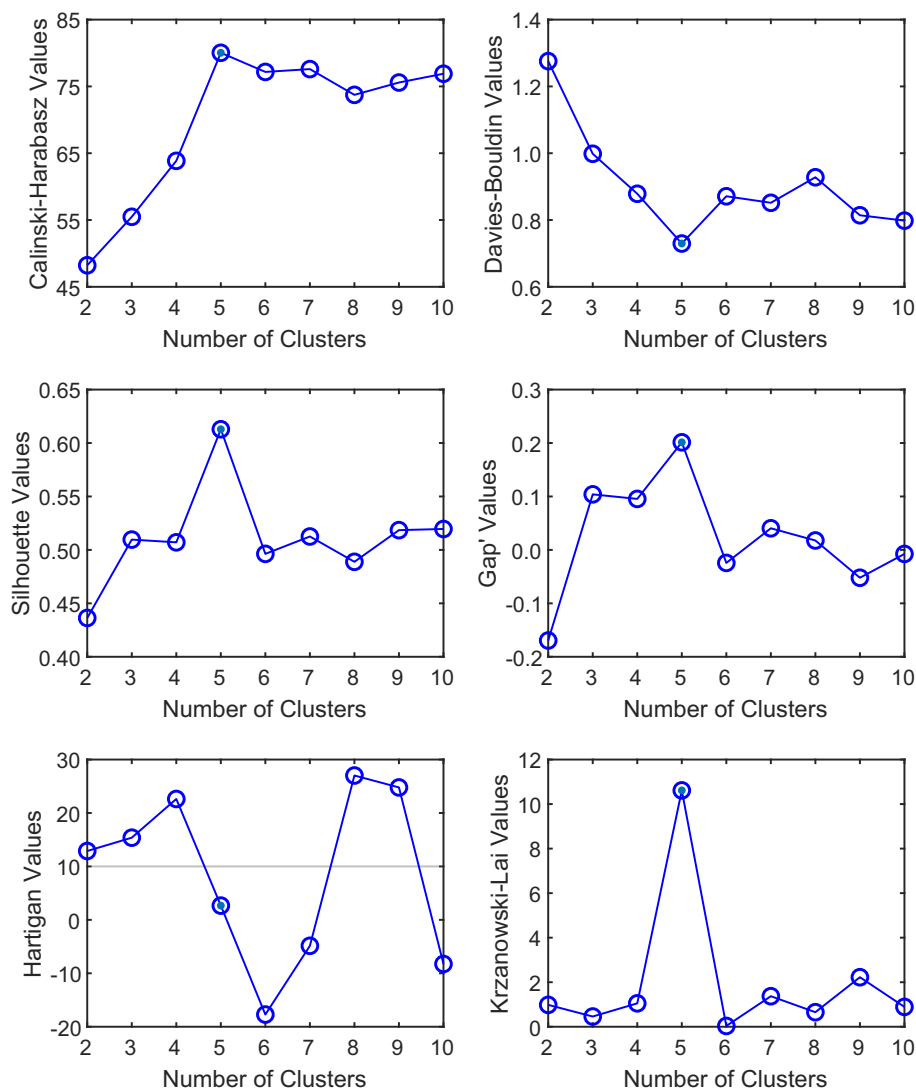


Fig. A.1. Internal validation indices for the reduced DS1, having removed 17 observations with  $d_{50} > 3$  mm. The Calinski-Harabasz, Davies-Bouldin, and silhouette indices are evaluated with the MATLAB® Statistics and Machine Learning Toolbox™.

Finally, we assess the similarity between the feeder-type classification and the flowability-based clustering of the reduced DS1 from the observed frequencies of the two groupings, i.e. the contingency table, as depicted in Fig. 9. The Pearson's  $\chi^2$  test measures the deviation of the observed frequencies from expectation, with a probability  $P(\chi^2 \geq 84) = 1.4 \times 10^{-11}$  on 16 degrees of freedom, a highly significant  $p$ -value indicative of the association between the two partitions. We study the goodness of match with different external validation indices [35], also obtained from calculations on the values of the contingency table. From the pairwise comparison of the observations, the Rand index  $RI$  is defined between 0 for completely mismatching and 1 for identical clusterings. We find  $RI = 0.69$  for the reduced data set, showing a fair agreement between the external classification and the internal

clustering. Alternatively, we measure cluster similarity using the amounts of intra- and inter-cluster information, defining the normalised mutual information index  $NMI \in [0, 1]$ , with lower values for independent clustering scenarios. We compute  $NMI = 0.22$ , which tells us that the feeder-type classification has limited knowledge about the flowability-based clustering. A reasoning for the clustering disagreement is given at the end of Subsection 2.3.

**Table A.1**

Internal validation indices, as summarised in [34], with criteria to determine the optimum number of clusters  $k^*$  in each case.

Index	Criterion for $k^*$
Calinski-Harabasz	Maximum
Davies-Bouldin	Minimum
Silhouette	Maximum
Gap'	Maximum
Hartigan	Smallest $k$ at or below $\eta$
Krzanowski-Lai	Maximum

## Appendix B. Granular PIV approach

Granular PIV (g-PIV) refers to the application of the PIV technique to the visualisation of granular flows. In the g-PIV, the velocity of particles is measured at a flow boundary illuminated by a lighting system [36], and is mainly used for quasi-two-dimensional set-ups [37], such as unsteady granular column collapse [38,39], and steady rotating drum and chute flows [40,41]. The PIV analysis of an image pair, e.g. two consecutive frames from a video recording, recovers the most probable particle displacements by cross-correlation of smaller interrogation areas [29]. We utilise PIVlab version 2.31 [42], with the following default settings: image pre-processing by contrast-limited adaptive histogram equalization (CLAHE), to reduce the uncertainty in locating the correlation peaks, using a window size of 20 pixels (px, [L<sup>2</sup>]); cross-correlation by fast Fourier transform (FFT) with window deformation, accounting for non-uniform particle motion within the interrogation areas; and a Gaussian 2 × 3-point fit of the integer displacements of the interrogation areas, to refine the correlation peak location.

We employ a three-pass cross-correlation algorithm with interrogation areas 64 × 64, 32 × 32, and 16 × 16 (px), and 50% overlap. Multi-pass approaches yield reliable g-PIV estimations depending on the number of particles in the successive interrogation areas, ideally around four and one for the first and last passes, respectively [43]. These optimal conditions are feasible for coarse-grained materials with sufficient inherent texture to detect motion [36], compatible with the experimental lighting conditions and physical resolution of the technique. As a workaround for fine powders and other materials producing low-texture images, we use seeding with tracer particles, also known as markers, which are coarse particles mixed with small mass fractions, of contrasting colour, and similar or lower particle density. As a result, we obtain a mixture of light and dark particles helping to reduce the g-PIV uncertainty [37]. We apply seeding to granular flows of the light-coloured talc, sugar, and the two LLDPE pellet samples in DS2, mixed at 10%, 5%, and 10% mass fractions, respectively. For the talc and sugar, we use blue polystyrene masterbatch granules of median particle size  $d_{50} = 2.7$  mm, and particle density  $\rho_s = 1.1 \times 10^3$  kg m<sup>-3</sup>. Compared GFT experiments of mixed LLDPE pellets and markers are presented in [44]. In addition, we enhance the multi-pass algorithm using different combinations of cross-correlation types and window deformation interpolators, implemented from PIVlab version 2.2 [45]. Correlation quality options include the recommended 'Normal' (circular cross-correlation, linear interpolation), and also 'High' (linear cross-correlation, spline interpolation), which is expected to reduce the measurement errors and improve the robustness of the algorithm for low-quality image pairs. Hence, we apply the 'High' correlation quality to analyse granular flows showing poor g-PIV estimations with the default 'Normal' option, as in the case of the talc, fertiliser, and silica in DS2.

We evaluate the accuracy of the proposed g-PIV approach on semi-synthetic image pairs from GFT recordings of the materials in DS2 with minimum and maximum  $d_{50}$ , as shown in Fig. B.1. We select 128 × 128 px regions of interest in original images of granular columns at rest of the talc and pet food samples. We impose an incremental displacement with equal horizontal and vertical components  $\Delta u_x = \Delta u_z = 16$  px on Fig. B.1a and Fig. B.1c to obtain the shifted Fig. B.1b and Fig. B.1d, respectively. Table B.1 shows the sample means,  $\overline{\Delta u_x}$  and  $\overline{\Delta u_z}$ , and standard deviations,  $s_{\Delta u_x}$  and  $s_{\Delta u_z}$ , of the estimated  $\Delta u_x$  and  $\Delta u_z$  by one-pass (64 × 64), two-pass (64 × 64, 32 × 32), and three-pass (64 × 64, 32 × 32, 16 × 16) cross-correlation algorithms—interrogation areas in px—with both 'Normal' and 'High' quality enhancements. We discard missing vectors and outliers in the PIVlab analyses with the MATLAB® functions `rmmissing` and `rmoutliers`. We observe accurate  $\overline{\Delta u_x}$  and  $\overline{\Delta u_z}$  in the case of talc, with  $s_{\Delta u_x}$  and  $s_{\Delta u_z}$ , below 1 px in all the tested configurations except for the two-pass estimation of  $\Delta u_x$ . In the case of pet food, we note increasing accuracy of  $\overline{\Delta u_x}$  and  $\overline{\Delta u_z}$  with the number of passes, and a greater robustness of the estimations, evidenced by the reduced  $s_{\Delta u_x}$  and  $s_{\Delta u_z}$ . In conclusion, the increasing number of passes improve accuracy, and more clearly for higher-texture images, whereas correlation quality shows a minor impact on the overall acceptable accuracy of the g-PIV estimations. Consequently, we verify our PIV approach to describing the flowability of industrial granular materials, complemented by the measurement redundancy of the fully-instrumented GFT.

**Table B.1**

Granular PIV accuracy of the estimated horizontal and vertical displacements, for different multi-pass, enhanced cross-correlation algorithms.

Material	Number of passes	Correlation quality	$\overline{\Delta u_x}$ (px)	$s_{\Delta u_x}$ (px)	$\overline{\Delta u_z}$ (px)	$s_{\Delta u_z}$ (px)
Talc	1	Normal	15.9	0.13	16.0	0.02
		High	15.9	0.08	16.0	0.02
	2	Normal	16.0	1.51	16.0	0.45
		High	15.8	1.79	15.9	0.57
	3	Normal	16.0	0.31	16.0	0.13
		High	16.0	0.36	15.9	0.18
Pet food	1	Normal	15.8	0.15	15.8	0.20
		High	15.8	0.08	15.8	0.09
	2	Normal	15.9	0.09	15.9	0.05
		High	15.9	0.09	15.9	0.03
	3	Normal	16.0	0.06	15.9	0.13
		High	16.0	0.06	15.9	0.13

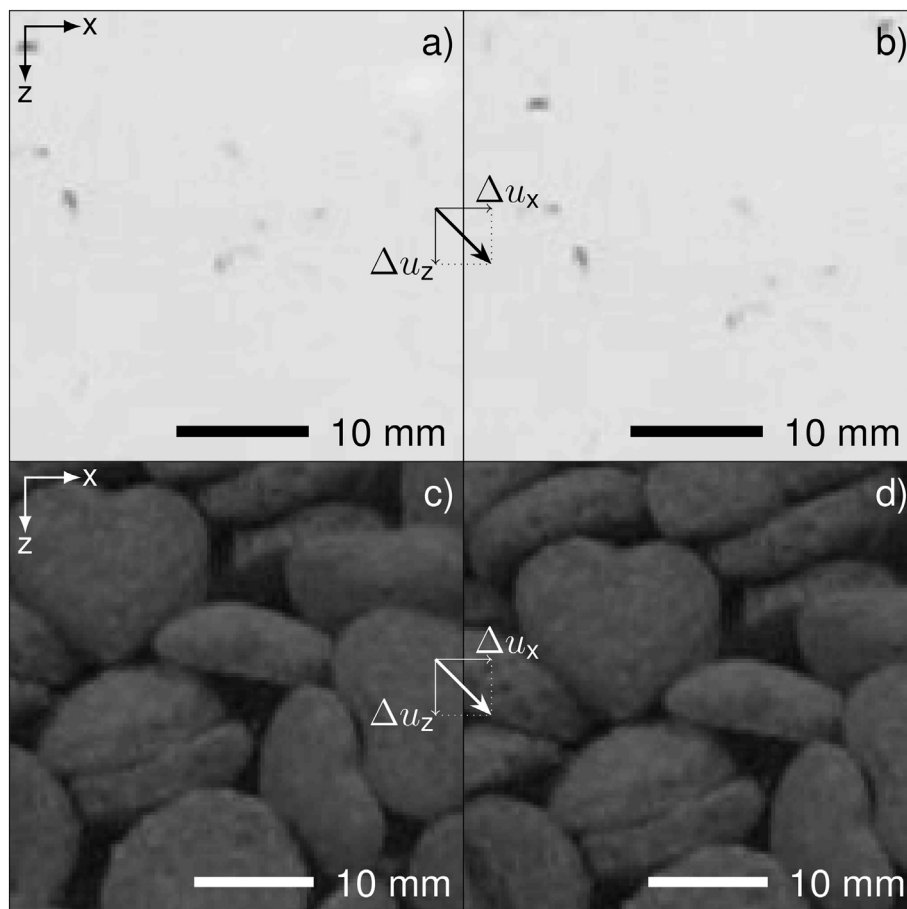


Fig. B.1. Semi-synthetic, 8-bit grayscale image pairs of: a, b) talc with added marker particles; c, d) pet food.

### Appendix C. Interpretation of PCA in high dimensions

We use PCA to explain flowability by capturing the most data variability in the data sets. Each PC is a linear combination of all the original variables, and thus interpreting the PCA results on the basis of material properties is difficult for data sets with an elevated number of variables, e.g. 126 in the case of DS2. In response to this limitation, simplified PCA approaches have been introduced, see [25], allowing us to try to approximate the complex granular flow behaviour by a subset of the original variables. Sparse PCA (SPCA) is increasingly used in the study of multiscale phenomena [46], as a technique for selecting the governing coefficients at different scales from traditional PCA decompositions. We examine the variable selection of DS2 using the SPCA algorithm with soft-thresholding regularisation presented in [47], adapted for data sets with a significantly larger number of variables than observations [48], and implemented for MATLAB® in [49].

We observe the decrease of explained variance with increasing sparsity of the PC1 loadings in Fig. C.1. The first principal component obtained by PCA explains 43% of the variance in DS2, whereas a minimum of 67 non-zero loadings are required to have a reasonable information loss below 5% of the total variance for the first sparse principal component (SPC1). With a 47% sparsity, the non-zero PC1 loadings correspond to the conventional variables  $\rho_b$  and  $C_u$ —with weights 0.17 and 0.05, respectively—and to the specialised variables shown in Fig. C.2. The specialised material properties are described in Table 3, and the test cases are numbered according to Table 2. SPC1 identifies a dominant positive correlation between all the energy components, the poured bulk density, and the ramp and peak loads, across all test cases. Other variables describing surface morphology are also selected, which are negatively correlated with measures of three characteristic times, and air permeability in vacuum conditions. It seems that the granular materials in DS2 are distinctively characterised with the GFT, and that all the different measurements resulting from the sample pre-conditioning and the instrumentation redundancy of the apparatus are necessary as a whole to explain flowability.

In spite of the above findings, SPCA may still be used as a rough estimate of the governing material properties in the data trends revealed by PCA. We approximate the first two principal components of DS2 by selecting a manageable subset of ten original variables in each case. Fig. C.3 shows that SPC1 and SPC2 are dominated by the evolution of the potential energy, and by the initial and final heights, respectively, of the granular systems tested with the GFT. However, compared to the traditional PCA results in Fig. 15b, we note poorer grouping of the materials included in DS2 when projected into SPC1-SPC2, as illustrated in Fig. C.4. The relative positions of the observations in the SPC1-SPC2 space are distorted, affecting the identification of distinctive traits for similarly flowing materials, and even more so for data sets with larger number of observations. Ultimately, we expect the clustering tendency of the data to be affected by variable selection, thereby justifying for the full characterisation of granular materials for practical applications.

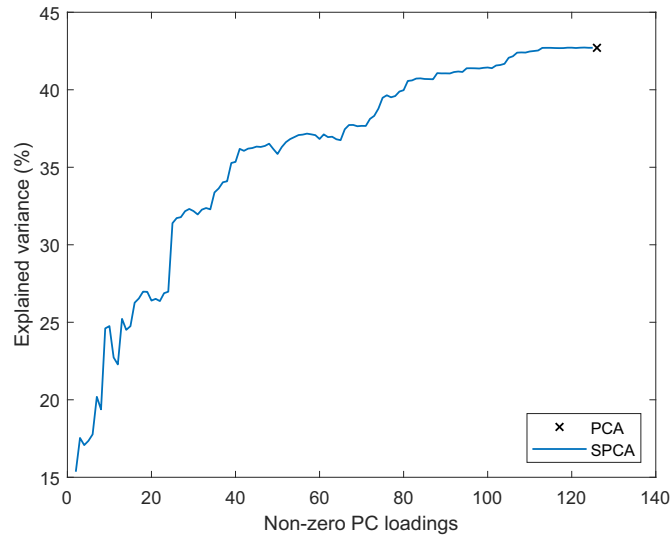


Fig. C.1. Explained variance of the first principal component of DS2 obtained by PCA, and as a function of the number of selected variables by sparse PCA (SPCA).

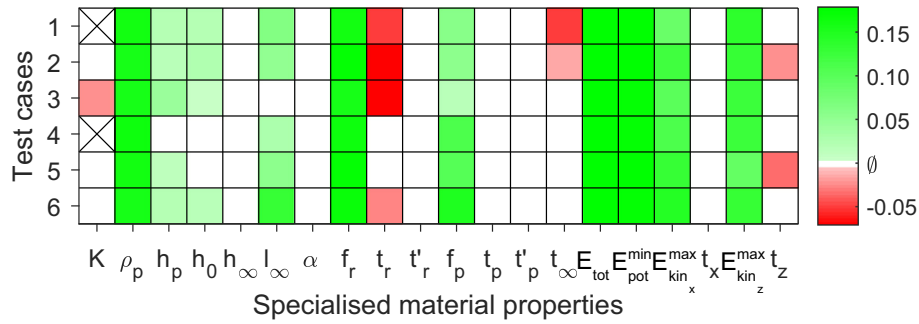


Fig. C.2. PC loadings of the specialised variables in the sparse PC1 (SPC1), explaining 38% of the total variance in DS2 with 67 non-zero loadings.

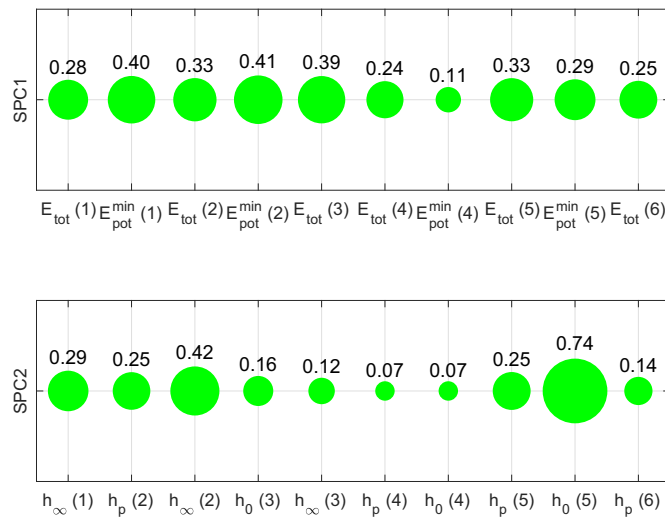


Fig. C.3. Non-zero PC loadings of the SPC1 and SPC2 of DS2, explaining 25% and 13% of the total variance in DS2, respectively.

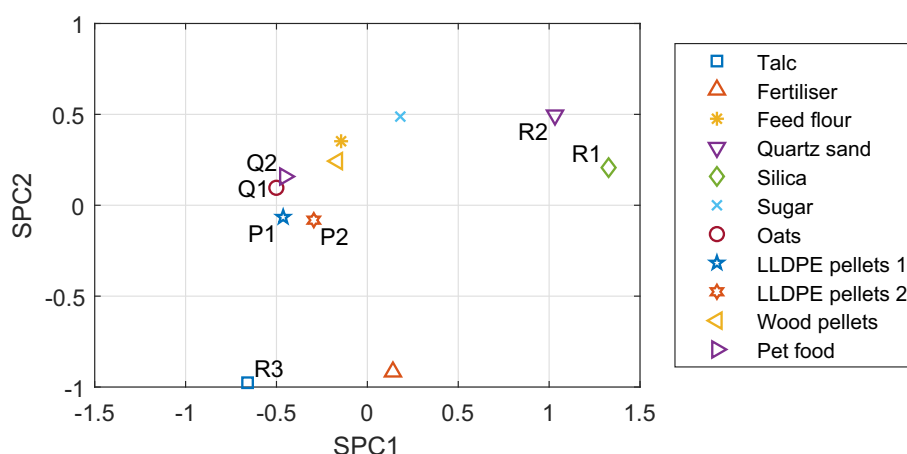


Fig. C.4. Scaled projection of DS2 into SPC1-SPC2 with ten non-zero PC loadings.

## References

- Técnicas Mecánicas Ilerdenses, S.L., TMI, Ensacado, Paletizado, Protección de cargas y Pesaje, <https://www.tnipal.com/> 2020.
- J. Marinelli, Choosing a feeder that works in unison with your bin, *Powder Bulk Eng.* (1996) 43–57.
- Center for Chemical Process Safety, Appendix B: equipment overview, Guidelines for Safe Handling of Powders and Bulk Solids, John Wiley & Sons Ltd 2004, pp. 577–766, <https://doi.org/10.1002/9780470925072.app2>.
- L. Bates, Characterisation of Bulk Solids – Industrial Practice, in: D. McGlinchey (Ed.), Characterisation of Bulk Solids, John Wiley & Sons Ltd 2005, pp. 206–229, <https://doi.org/10.1002/9781444305456.ch7>.
- D. Schulze, Powders and Bulk Solids, Springer-Verlag, Berlin Heidelberg, 2008 <https://doi.org/10.1007/978-3-540-73768-1>.
- Y. Endo, M. Alonso, An estimate of hopper outlet size and slope for mass flow from the flowability index, *Chem. Eng. Res. Des.* 80 (6) (2002) 625–630, <https://doi.org/10.1205/026387602760312827>.
- D. Geldart, Types of gas fluidization, *Powder Technol.* 7 (5) (1973) 285–292, [https://doi.org/10.1016/0032-5910\(73\)80037-3](https://doi.org/10.1016/0032-5910(73)80037-3).
- R. Freeman, Measuring the flow properties of consolidated, conditioned and aerated powders – a comparative study using a powder rheometer and a rotational shear cell, *Powder Technol.* 174 (1) (2007) 25–33, <https://doi.org/10.1016/j.powtec.2006.10.016>.
- J.M. Craven, J. Swithenbank, V.N. Sharifi, Investigation into the Flow Properties of Coarse Solid Fuels for Use in Industrial Feed Systems, *J. Powder Technol.* (2015) 786063, <https://doi.org/10.1155/2015/786063>.
- J.K. Prescott, R.A. Barnum, On powder flowability, *Pharm. Technol.* 24 (10) (2000) 60+.
- J. Torres-Serra, E. Romero, A. Rodríguez-Ferran, A new column collapse apparatus for the characterisation of the flowability of granular materials, *Powder Technol.* 362 (2020) 559–577, <https://doi.org/10.1016/j.powtec.2019.11.080>.
- Técnicas Mecánicas Ilerdenses, S.L., Dispositivo para ensayo de colapso de una columna de material pulverulento o granular, inventors: J. Torres Serra, X. Arderiu Cabau, J.M. Padullés Ribalta, J. Caba Muntada, J.J. González Toledano, E.E. Romero Morales, A. Rodríguez Ferran, Spanish Patent ES2695451B2 (2019). URL <https://patentscope.wipo.int/search/en/detail.jsf?docId=ES235596513>.
- A.J. Rogers, A. Hashemi, M.G. Ierapetritou, Modeling of particulate processes for the continuous manufacture of solid-based pharmaceutical dosage forms, *Processes* 1 (2) (2013) 67–127, <https://doi.org/10.3390/pr1020067>.
- W. Yu, K. Muteki, L. Zhang, G. Kim, Prediction of bulk powder flow performance using comprehensive particle size and particle shape distributions, *J. Pharm. Sci.* 100 (1) (2011) 284–293, <https://doi.org/10.1002/jps.22254>.
- Z.A. Worku, D. Kumar, J.V. Gomes, Y. He, B. Glennon, K.A. Ramisetty, Á.C. Rasmuson, P. O'Connell, K.H. Gallagher, T. Woods, N.R. Shastri, A.M. Healy, Modelling and understanding powder flow properties and compactability of selected active pharmaceutical ingredients, excipients and physical mixtures from critical material properties, *Int. J. Pharm.* 531 (1) (2017) 191–204, <https://doi.org/10.1016/j.ijpharm.2017.08.063>.
- B. Van Snick, J. Dhondt, K. Pandelaere, J. Bertels, R. Mertens, D. Klingeleers, G. Di Pretoro, J.P. Remon, C. Vervaeet, T. De Beer, V. Vanhoorne, A multivariate raw material property database to facilitate drug product development and enable in-silico design of pharmaceutical dry powder processes, *Int. J. Pharm.* 549 (1) (2018) 415–435, <https://doi.org/10.1016/j.ijpharm.2018.08.014>.
- M. Fonteyne, A. Correia, S. De Plecker, J. Verduyck, I. Ilić, Q. Zhou, C. Vervaeet, J.P. Remon, F. Onofre, V. Bulone, T. De Beer, Impact of microcrystalline cellulose material attributes: a case study on continuous twin screw granulation, *Int. J. Pharm.* 478 (2) (2015) 705–717, <https://doi.org/10.1016/j.ijpharm.2014.11.070>.
- J. Falk, R.J. Berry, M. Broström, S.H. Larsson, Mass flow and variability in screw feeding of biomass powders – relations to particle and bulk properties, *Powder Technol.* 276 (2015) 80–88, <https://doi.org/10.1016/j.powtec.2015.02.023>.
- Y. Wang, T. Li, F.J. Muzzio, B.J. Glasser, Predicting feeder performance based on material flow properties, *Powder Technol.* 308 (2017) 135–148, <https://doi.org/10.1016/j.powtec.2016.12.010>.
- N. Bostijn, J. Dhondt, A. Ryckaert, E. Szabó, W. Dhondt, B. Van Snick, V. Vanhoorne, C. Vervaeet, T. De Beer, A multivariate approach to predict the volumetric and gravimetric feeding behavior of a low feed rate feeder based on raw material properties, *Int. J. Pharm.* 557 (2019) 342–353, <https://doi.org/10.1016/j.ijpharm.2018.12.066>.
- F. Tahir, J. Palmer, J. Khoo, J. Holman, I.K. Yadav, G. Reynolds, E. Meehan, A. Mitchell, G. Bajwa, Development of feed factor prediction models for loss-in-weight powder feeders, *Powder Technol.* (2019) <https://doi.org/10.1016/j.powtec.2019.09.071>.
- J. Clayton, Chapter 17 - An Introduction to Powder Characterization, in: A.S. Narang, S.I. Badawy (Eds.), Handbook of Pharmaceutical Wet Granulation, Academic Press 2019, pp. 569–613, <https://doi.org/10.1016/B978-0-12-810460-6.00021-X>.
- J. Torres-Serra, Data for: Classification of granular materials via flowability-based clustering with application to bulk feeding, Mendeley data version V1 (2020) <https://doi.org/10.17632/sxg3hg3txw.1>.
- K.R. Koch, Robust estimation by expectation maximization algorithm, *J. Geod.* 87 (2) (2013) 107–116, <https://doi.org/10.1007/s00190-012-0582-3>.
- I.T. Jolliffe, J. Cadima, Principal component analysis: a review and recent developments, *Philos. Trans. R. Soc. A Math. Phys. Eng. Sci.* 374 (2016) 20150202, <https://doi.org/10.1098/rsta.2015.0202>.
- A.K. Jain, Data clustering: 50 years beyond K-means, *Pattern Recogn. Lett.* 31 (8) (2010) 651–666, <https://doi.org/10.1016/j.patrec.2009.09.011>.
- G. Lube, H.E. Huppert, R.S.J. Sparks, M.A. Hallworth, Axisymmetric collapses of granular columns, *J. Fluid Mech.* 508 (2004) 175–199, <https://doi.org/10.1017/S0022212004009036>.
- E. Lajeunesse, A. Mangeney-Castelnau, J.P. Vilotte, Spreading of a granular mass on a horizontal plane, *Phys. Fluids* 16 (7) (2004) 2371–2381, <https://doi.org/10.1063/1.1736611>.
- W. Thielicke, E.J. Stamhuis, PIVlab – towards user-friendly, affordable and accurate digital particle image velocimetry in MATLAB, *J. Open Res. Softw.* 2 (1) (2014) e30, <https://doi.org/10.5334/jors.bl>.
- M. Cabrera, N. Estrada, Granular column collapse: analysis of grain-size effects, *Phys. Rev. E* 99 (1) (2019) 012905, <https://doi.org/10.1103/PhysRevE.99.012905>.
- ASTM D4959-16, Standard Test Method for Determination of Water Content of Soil By Direct Heating, ASTM International, 2016 <https://doi.org/10.1520/D4959-16>.
- R. Everson, L. Sirovich, Karhunen–Loève procedure for gappy data, *J. Opt. Soc. Am. A* 12 (8) (1995) 1657–1664, <https://doi.org/10.1364/JOSAA.12.001657>.
- A. Banerjee, R. Davé, Validating clusters using the Hopkins statistic, 2004 IEEE International Conference on Fuzzy Systems (IEEE Cat. No.04CH37542), 1, 2004, pp. 149–153, <https://doi.org/10.1109/FUZZY.2004.1375706>.
- A. Albalade, D. Suendermann, A combination approach to cluster validation based on statistical quantiles, in: 2009 International Joint Conference on bioinformatics, Systems Biology and Intelligent Computing, 2009, pp. 549–555, <https://doi.org/10.1109/IJBCS.2009.116>.
- A.J. Gates, I.B. Wood, W.P. Hetrick, Y.Y. Ahn, Element-centric clustering comparison unifies overlaps and hierarchy, *Sci. Rep.* 9 (2019) 8574, <https://doi.org/10.1038/s41598-019-44892-y>.
- W. Eckart, J.M.N.T. Gray, K. Hutter, Particle image velocimetry (PIV) for granular avalanches on inclined planes, in: K. Hutter, N. Kirchner (Eds.), Lecture Notes in Applied and Computational Mechanics, 11, Springer, Berlin, Heidelberg 2003, pp. 195–218, doi:10.1007/978-3-540-36565-5\_6.

- [37] R.M. Lueptow, A. Akonur, T. Shinbrot, PIV for granular flows, *Exp. Fluids* 28 (2) (2000) 183–186, <https://doi.org/10.1007/s003480050023>.
- [38] G. Lube, H.E. Huppert, R.S.J. Sparks, A. Freundt, Collapses of twodimensional granular columns, *Phys. Rev. E* 72 (4) (2005) 041301, <https://doi.org/10.1103/PhysRevE.72.041301>.
- [39] E. Lajeunesse, J.B. Monnier, G.M. Homsy, Granular slumping on a horizontal surface, *Phys. Fluids* 17 (10) (2005) 103302, <https://doi.org/10.1063/1.2087687>.
- [40] D. Gollin, W. Brevis, E.T. Bowman, P. Shepley, Performance of PIV and PTV for granular flow measurements, *Granul. Matter* 19 (3) (2017) 42, <https://doi.org/10.1007/s10035-017-0730-9>.
- [41] L. Sarno, A. Carravetta, Y.C. Tai, R. Martino, M.N. Papa, C.Y. Kuo, Measuring the velocity fields of granular flows – employment of a multipass two-dimensional particle image velocimetry (2D-PIV) approach, *Adv. Powder Technol.* 29 (12) (2018) 3107–3123, <https://doi.org/10.1016/j.apt.2018.08.014>.
- [42] W. Thielicke, PIVlab - particle image velocimetry (PIV) tool, MATLAB central file exchange version 2.31 (2019). URL <https://www.mathworks.com/matlabcentral/fileexchange/27659-pivlab-particle-image-velocimetry-piv-tool>.
- [43] L. Sarno, Y.C. Tai, A. Carravetta, R. Martino, M.N. Papa, C.Y. Kuo, Challenges and improvements in applying a particle image velocimetry, (PIV) approach to granular flows, *J. Phys. Conf. Ser.* 1249 (2019) 012011, <https://doi.org/10.1088/1742-6596/1249/1/012011>.
- [44] J. Torres-Serra, E. Romero, A. Rodríguez-Ferran, A new granular column collapse device to characterise Flowability of bulk materials, *Proceedings 2* (8) (2018) 488, <https://doi.org/10.3390/ICEM18-05389>.
- [45] W. Thielicke, Evaluation of the new PIVlab (v2.2) settings (2019). URL <https://pivlab.blogspot.com/2019/09/evaluation-of-new-pivlab-v21-settings.html>.
- [46] N.B. Erichson, P. Zheng, K. Manohar, S.L. Brunton, J.N. Kutz, A.Y. Aravkin, Sparse principal component analysis via variable projection, *SIAM J. Appl. Math.* 80 (2) (2020) 977–1002, <https://doi.org/10.1137/18M1211350>.
- [47] H. Zou, T. Hastie, R. Tibshirani, Sparse principal component analysis, *J. Comput. Graph. Stat.* 15 (2) (2006) 265–286, <https://doi.org/10.1198/106186006X113430>.
- [48] H. Zou, T. Hastie, Elasticnet: elastic-net for sparse estimation and sparse PCA, R package version 1.3, <https://CRAN.R-project.org/package=elasticnet> 2020.
- [49] M. Ali, Sparse kernel principal component analysis, MATLAB central file exchange version 1.0 (2016). URL <https://www.mathworks.com/matlabcentral/fileexchange/58939-sparse-kernel-principal-component-analysis>.
- [50] ASTM D7481-18, Standard Test Methods for Determining Loose and Tapped Bulk Densities of Powders using a Graduated Cylinder, ASTM International, 2018 <https://doi.org/10.1520/D7481-18>.
- [51] ASTM D4253-16, Standard Test Methods for Maximum Index Density and Unit Weight of Soils Using a Vibratory Table, ASTM International, 2016 <https://doi.org/10.1520/D4253-16>.
- [52] US Pharmacopeial Convention, (1174) Powder Flow, USP 35–NF 30, 2012.
- [53] H.M.B. Al-Hashemi, O.S.B. Al-Amoudi, A review on the angle of repose of granular materials, *Powder Technol.* 330 (2018) 397–417, <https://doi.org/10.1016/j.powtec.2018.02.003>.
- [54] ASTM, C136 / C136M-14, Standard Test Method for Sieve Analysis of Fine and Coarse Aggregates, ASTM International, 2014 [https://doi.org/10.1520/C0136\\_C0136M-14](https://doi.org/10.1520/C0136_C0136M-14).
- [55] ISO 3310-1, Test sieves – Technical requirements and testing – Part 1: Test sieves of metal wire cloth, 2016.
- [56] ISO 9276-6, Representation of results of particle size analysis – Part 6: Descriptive and quantitative representation of particle shape and morphology, 2008.
- [57] S. Kim, J. Chen, T. Cheng, A. Gindulyte, J. He, S. He, Q. Li, B.A. Shoemaker, P.A. Thiessen, B. Yu, L. Zaslavsky, J. Zhang, E.E. Bolton, Pub-Chem 2019 update: improved access to chemical data, *Nucleic Acids Res.* 47 (D1) (2018) D1102–D1109, <https://doi.org/10.1093/nar/gky1033>.
- [58] X. Chen, A.S. Elwood Madden, Z. Reches, The frictional strength of talc gouge in high-velocity shear experiments, *J. Geophys. Res. Solid Earth* 122 (5) (2017) 3661–3676, <https://doi.org/10.1002/2016JB013676>.
- [59] T. Oishi, M. Goto, A. Kasahara, M. Tosa, Low frictional copper oxide film prepared with sodium hydroxide solution, *Surf. Interface Anal.* 36 (8) (2004) 1259–1261, <https://doi.org/10.1002/sia.1889>.
- [60] M. Molenda, M.D. Montross, J. Horabik, I.J. Ross, Mechanical Properties of Corn and Soybean Meal, *Trans. ASAE* 45 (6) (2002) 1929–1936, <https://doi.org/10.13031/2013.11408>.
- [61] G.C. Cho, J. Dodds, J.C. Santamarina, Particle shape effects on packing density, stiffness, and strength: natural and crushed sands, *J. Geotech. Geoenviron. Eng.* 132 (5) (2006) 591–602, [https://doi.org/10.1061/\(ASCE\)1090-0241\(2006\)132:5\(591\)](https://doi.org/10.1061/(ASCE)1090-0241(2006)132:5(591)).
- [62] K. Kawai, H. Sakuma, I. Katayama, K. Tamura, Frictional characteristics of single and polycrystalline muscovite and influence of fluid chemistry, *J. Geophys. Res. Solid Earth* 120 (9) (2015) 6209–6218 [doi:10.1002/2015JB012286](https://doi.org/10.1002/2015JB012286).
- [63] L.C. dos Santos, R. Condotta, M.C. Ferreira, Flow properties of coarse and fine sugar powders, *J. Food Process Eng.* 41 (2) (2018), e12648. <https://doi.org/10.1111/jfpe.12648>.
- [64] A. Ramírez, M. Moya, F. Ayuga, Determination of the mechanical properties of powdered agricultural products and sugar, *Part. Part. Syst. Charact.* 26 (4) (2009) 220–230, <https://doi.org/10.1002/ppsc.200800016>.
- [65] J.M. Boac, M.E. Casada, R.G. Maghirang, J.P. Harner III, Material and interaction properties of selected grains and oilseeds for modeling discrete particles, *Trans. ASABE* 53 (4) (2010) 1201–1216, <https://doi.org/10.13031/2013.32577>.
- [66] M.A. Spalding, D.E. Kirkpatrick, K.S. Hyun, Coefficients of dynamic friction for low density polyethylene, *Polym. Eng. Sci.* 33 (7) (1993) 423–430, <https://doi.org/10.1002/pen.760330708>.
- [67] A. Akinci, S. Yilmaz, U. Sen, Wear behavior of basalt filled low density polyethylene composites, *Appl. Compos. Mater.* 19 (3) (2012) 499–511, <https://doi.org/10.1007/s10443-011-9208-9>.
- [68] N. White, D. Jayas, Physical properties of canola and sunflower meal pellets, *Can. Biosyst. Eng.* 43 (2001) 3.49–3.52. <http://www.csbe-scga.ca/docs/journal/43/c0124.pdf>.





## Chapter 4

# STUDY OF GRAIN-SCALE EFFECTS IN BULK HANDLING USING DISCRETE ELEMENT SIMULATIONS

---

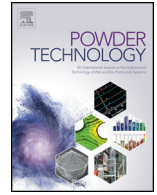
Reproduced from: J. Torres-Serra, A. Rodríguez-Ferran, and E. Romero, Study of grain-scale effects in bulk handling using discrete element simulations, *Powder Technology*, vol. 382, pp. 284–299, 2021. DOI: [10.1016/j.powtec.2020.12.029](https://doi.org/10.1016/j.powtec.2020.12.029)





Contents lists available at ScienceDirect

Powder Technology

journal homepage: [www.elsevier.com/locate/powtec](http://www.elsevier.com/locate/powtec)

# Study of grain-scale effects in bulk handling using discrete element simulations

J. Torres-Serra<sup>a,b,\*</sup>, A. Rodríguez-Ferran<sup>b</sup>, E. Romero<sup>b</sup>

<sup>a</sup> *Técnicas Mecánicas Ilerdenses, S.L., Polígono industrial Camí dels Frares, c. Alcarràs, parc. 66, 25190 Lleida, Spain*

<sup>b</sup> *Department of Civil and Environmental Engineering, Universitat Politècnica de Catalunya, Campus Nord, c. Jordi Girona, 1-3, 08034 Barcelona, Spain*

## ARTICLE INFO

### Article history:

Received 8 August 2020

Received in revised form 30 November 2020

Accepted 8 December 2020

Available online 16 December 2020

### Keywords:

Particle size

Particle shape

Hygroscopicity

Discrete element method

Granular column collapse

Hopper design

## ABSTRACT

Industrial granular flow issues are affected by the particle properties and environmental conditions of the materials. To understand the impact of grain-scale effects on flowability, experimental testing should be complemented with particle-based modelling. In this study, we simulate the effects of particle size, shape, and hygroscopicity by the discrete element method (DEM) for different bulk handling problems. We examine a granular column collapse set-up, comparing flow propagation of dry, mono-sized sphere packings to granular systems with particle size dispersity, prolate spheroidal particles, and liquid contents in pendular capillary states. Our results corroborate the experimental observations of evolving height profiles, velocity fields, energy balance, and particle orientation. We also analyse different hopper design alternatives dealing with particle size segregation in an industrial case study of the filling operation. This study illustrates the usability of the DEM as an effective support tool to characterise complex granular flows and improve bulk handling technology.

© 2020 Elsevier B.V. All rights reserved.

## 1. Introduction

Bulk handling of granular materials, typically in the range of  $\mu\text{m}$  to mm, is a major issue within the packaging industry. Flowability of industrial granular materials is key to the performance of bulk solids handling equipment [1]. Excluding cohesive effects, the different granular flow regimes are mainly governed by collision and friction of the particles [2]. In addition to the equipment and handling conditions, flowability is affected by the physical particle properties—namely the size, shape, density, and surface properties—as well as by environmental conditions such as the relative humidity and ambient temperature [3]. However, the influence at the bulk scale of complex grain-scale effects is yet to be completely understood.

Various experimental approaches to granular flow description have been proposed, from small-scale standard laboratory tests [4], to full-scale bulk handling systems [5]. Despite the availability of these quantitative methods, long-established empirical tests are still used in industrial practice for qualitative assessments of flowability. In collaboration with the bagging line manufacturer Técnicas Mecánicas

Ilerdenses, S.L. (TMI) [6], we recently conceptualised and developed the TMI granular flow tester (GFT) [7]. The GFT implements a quasi-two-dimensional granular column collapse experiment [8,9], fully-instrumented to monitor, among others: the initial column packing state, flow propagation by analysis of the basal loads and near-wall kinematics, and the surface morphology of the deposit at run-out [10]. Regarding its industrial application, the GFT provides the designer with a specialised characterisation of flowability, complementary to conventional testing, thereby improving the decision-making strategies for selecting the adequate bulk feeding techniques [11].

Numerical modelling of granular flow is of interest to bridge the gap between experimental observations and a more fundamental understanding of the underlying phenomena affecting flowability. Many continuum approaches to granular flow simulations have been studied, using the mesh-based finite element method [12], and particle-based methods including the material point method [13], smoothed particle hydrodynamics [14], or particle finite element method [15]. Continuum constitutive relations are generally unable to capture the discrete nature of industrial granular materials [16]. On this account, the discrete element method (DEM) [17] for modelling natural and industrial granular flow problems is becoming widespread [18]. The DEM enables the influence of material properties and particle contacts at the microscopic scale to be included in the flow behaviour at the macroscopic scale, which is often difficult to achieve experimentally [19]. The characterisation of particle size, shape, and hygroscopicity, the associated flowability issues, and the DEM simulation of their effects on granular

\* Corresponding author at: Department of Civil and Environmental Engineering, Universitat Politècnica de Catalunya, Campus Nord, c. Jordi Girona, 1-3, 08034 Barcelona, Spain.

E-mail addresses: [joel.torres@upc.edu](mailto:joel.torres@upc.edu) (J. Torres-Serra), [antonio.rodriguez-ferran@upc.edu](mailto:antonio.rodriguez-ferran@upc.edu) (A. Rodríguez-Ferran), [enrique.romero-morales@upc.edu](mailto:enrique.romero-morales@upc.edu) (E. Romero).

column collapse and other industrial flow problems are briefly reviewed in the following subsections.

### 1.1. Particle size

Depending on the size range, the particle size distribution of granular materials is characterised experimentally using laser, microscopy, sedimentation, and sieving techniques [20]. Materials with narrow size distribution in general show better flowability with increasing median particle size and decreasing dispersity [21]. Flowability is further affected by the fraction of fine particles in a material, controlling its cohesive behaviour [22].

Particle size segregation is a current bulk handling issue found in industrial practice [23]. Inefficient bulk feeding performance, affected by particle size segregation during filling of the material reception hopper, results in an uneven particle size distribution of the output material batches, thus affecting their marketability. As regards segregation, two main effects are associated to the hopper filling operation:

- Horizontal segregation, explained by percolation or sifting [24], or combined kinetic sieving and squeeze expulsion mechanisms [25], is expected if a single inlet is used for filling the hopper, under which fine fractions are deposited. Coarse fractions slide over the surface of the formed heap, which are deposited near the slope foot. This segregation behaviour favours a horizontal distribution of the material with higher concentration of fines closer to the filling point and a mobilisation of the coarse particles towards the hopper walls.
- Vertical segregation by fluidization [26]. For areatable materials, i.e. with high contents of fine particles, the coarse fraction accumulates firstly on the lower layers of the deposit, whereas the smaller fluidised particles are deposited afterwards onto the upper layers closer to the heap surface.

2D DEM analysis of the effect of particle size on granular column collapse experiments has been presented in [27]. Run-out length and duration are mostly influenced by the grain-size effect, which vanishes for high system-size to grain-size ratios, and depending on the initial column aspect ratios. DEM simulations have been also applied to study segregation of bi- and polydisperse particle systems for conical hopper filling [28] and for pharmaceutical tableting set-ups [29,30]. The number of particles in the simulations critically affects the required computational time [31], justifying for particle scaling in simplified models for practical applications.

### 1.2. Particle shape

Both natural and industrial flows are strongly impacted by the shape of their constituting particles [32,33]. Image analysis techniques for particle shape characterisation range from digital imaging [34], to optical and electron microscopy, and X-ray tomography [35]. Irregular-shaped particles have a large influence on the particle interactions, whereas round particles usually show better flowability [22]. Flow of non-spherical particles has been reviewed in [36]. Depending on the aspect ratio of the particles, random packings of ellipsoids show higher packing densities, related to jamming issues. Moreover, orientation of elongated particles in the flow direction is observed in pile avalanche and shear flow experiments.

Columns of non-spherical particles have been simulated to examine collapse by several DEM approaches, including 2D analysis of glued disks [37], 3D analysis of glued spheres in axi-symmetrical column geometries [38], and even spherical particles with an added rolling law to account for the effect of shape in quasi-two-dimensional set-ups [39]. The latter approach has also been investigated to approximate the degree of true sphericity of sands [40], applied to particles with moderate-to-high sphericity. In spite of the higher computational

costs, simulations with non-spherical particle packings are able to reproduce the effect of shape on the rotational motion of the particles [41].

### 1.3. Particle hygroscopicity

Among environmental conditions, relative humidity has important consequences for flowability by affecting the amount of stored water in granular materials. Hygroscopicity describes the ability of particles to absorb ambient moisture, which is related to slip-stick and caking phenomena [42,43]. Flowability of hygroscopic powders decreases with increasing water content within a low-to-moderate degree of saturation, experimentally controlled using environmental chambers [44,45]. At the particle level, isolated interparticle liquid bridges are formed in the so-called pendular state, yielding a significant increase of capillary cohesion at low water contents [46].

Collapse tests with wet granular columns have been reproduced by 3D DEM simulations in [47]. For increasing water contents in the pendular state, steeped final height profiles are observed. However, the capillary effect is reduced for lower liquid surface tensions and larger particle sizes, which is related to the ratio between body and capillary forces. More recent works have resorted to diverse 2D continuum and 3D coupled DEM-based continuum-discrete approaches to study granular column collapse in pendular and fully-saturated regimes [48,49].

### 1.4. Motivation

The aim of this study is to employ the DEM as a support tool to gain insight into relevant grain-scale effects for bulk handling. Unfortunately, DEM models of particle size dispersity and segregation, shape non-sphericity, and hygroscopicity are difficult to validate separately by experiments. Furthermore, the wide range of industrial granular materials found in practice entail a specific calibration of the DEM simulation parameters for each case. See, for instance, the cases of fine maltodextrin and titanium dioxide particles in [50] and of coarse limestone gravel in [51]. Therefore, we resort to synthetic DEM simulations allowing us to observe the changing granular flow behaviour in general working conditions, beyond the quantitative calibration of the model parameters with case-by-case experimental testing. We implement the DEM contact model described in Section 2 utilising the open-source software MercuryDPM [52]. In Section 3, we investigate two different problem set-ups with industrial application, namely the intermediate-scale GFT experiment and a full-scale hopper filling operation.

## 2. DEM contact model

We describe the translational and rotational motion of rigid spherical particles in a granular system by Newton's equations of motion [53]. In DEM simulations, we solve the following governing equations for every  $i$ -th particle:

$$m_i \ddot{\mathbf{x}}_i = \mathbf{f}_i + m_i \mathbf{g} \quad I_i \dot{\boldsymbol{\omega}}_i = \mathbf{q}_i \quad (1)$$

where  $m_i$  and  $I_i$  are the mass and moment of inertia of particle  $i$ ,  $\ddot{\mathbf{x}}_i$  and  $\dot{\boldsymbol{\omega}}_i$  its linear and angular acceleration,  $\mathbf{f}_i$  and  $\mathbf{q}_i$  the total force and torque acting on it, respectively, and  $\mathbf{g}$  is the acceleration of gravity. We use a linear normal contact model to describe the translational degrees of freedom of particle motion, defining a material of type LinearViscoelasticFrictionSpecies in Mercury-DPM. The parameters of sphere interparticle contact comprise normal stiffness  $k_n$  and viscous dissipation  $\gamma_n$  as well as the tangential or sliding counterparts  $k_s$  and  $\gamma_s$ . Additionally, we use the sliding friction coefficient  $\mu_s$  to define a Coulomb-type coupling between the normal,  $f_n$ , and tangential,  $f_t$ , components of  $\mathbf{f}_i$ , due to contact with the neighbouring particles  $j$ :

$$\mathbf{f}_i = \sum_j (f_n \mathbf{n} + f_t \mathbf{t}) \quad (2a)$$

$$f_n = \begin{cases} 0 & \delta_n \leq 0 \\ k_n \delta_n + \gamma_n v_n & \delta_n > 0 \end{cases} \quad (2b)$$

$$f_t = \min \{ \mu_s f_n, k_s \delta_t + \gamma_s v_t \} \quad (2c)$$

where  $\mathbf{n}$  and  $\mathbf{t}$  are the normal and tangential unit vectors,  $\delta_n$  is the inter-particle overlap,  $\delta_t$  is the tangential spring of active contacts, and  $v_n$  and  $v_t$  are the normal and tangential components of relative velocity, respectively. Overdamping of the particle system is affected by the contact eigenfrequencies in the linear spring-dashpot model [53]. We ensure system stability by the following relation between normal contact parameters:

$$\gamma_n = \sqrt{2k_n m_{\min}} \quad (3)$$

where  $m_{\min}$  is the minimum particle mass. Regarding the rotational degrees of freedom, we account for the contribution to torque of the inter-particle rolling and torsional resistance adapting the tangential contact model in Eq. (2c), see [53] for more details. We compute the rolling,  $\mathbf{f}_r$ , and torsional,  $\mathbf{f}_o$ , quasi-forces using the respective stiffness ( $k_r$  and  $k_o$ ), dissipation ( $\gamma_r$  and  $\gamma_o$ ), and friction ( $\mu_r$  and  $\mu_o$ ) coefficients. Hence, we define the total torque on the spherical particle  $i$  as:

$$\mathbf{q}_i = \sum_j [\mathbf{l}_i \times \mathbf{f}_i + r_{ij}(\mathbf{n} \times \mathbf{f}_r + \mathbf{f}_o)] \quad (4)$$

where  $\mathbf{l}_i = (r_i - \delta_n/2)\mathbf{n}$  is the branch vector and  $r_{ij} = r_i r_j / (r_i + r_j)$  is the reduced radius.

Due to our synthetic modelling approach, we set the simulation parameters as fractions of the given normal stiffness  $k_n$  and viscous dissipation  $\gamma_n$ , and the sliding friction coefficient  $\mu_s$ , as in [53]. For example, we use  $\mu_s = 0.50$  to  $0.58$  and set  $\mu_r = 0.1\mu_s$  throughout this study. According to the DEM calibration process described in [54], based on angle of repose experiments with quartz sand, the reasonably chosen  $\mu_s$  and  $\mu_r$  yield angles of repose between  $30.5^\circ$  and  $32.0^\circ$ , typical of quartz sands [55].

Non-spherical, superquadric particle modelling in MercuryDPM follows the procedure described in [56] for the SuperQuadricParticle class. Contact detection is guaranteed for ellipsoidal particles using a Newton-Raphson method. First, neighbourhood search [57] is performed on the minimum bounding spheres of the non-spherical particles. Then, for every pair of candidate contacting particles, an iterative procedure is carried out to update the contact point location whilst approximating the actual particle surface.

Liquid bridges are modelled using the approximation in [58], according to which the contribution of capillary force  $f_c$  is combined with the linear normal force  $f_n$ , see [59]:

$$f_n = \begin{cases} 0 & \delta_n \leq -d \\ -f_c & -d < \delta_n \leq 0 \\ k_n \delta_n + \gamma_n v_n - f_c & \delta_n > 0 \end{cases} \quad (5)$$

where  $d > 0$  is the rupture distance, acting only during particle separation. We consider the liquid phase to be distributed on the particle surface in the form of adsorbed liquid films and capillary liquid bridges between particles [60], as implemented in the LiquidMigrationWilletSpecies class in MercuryDPM. We assume the liquid bridge formation mechanism to neglect adsorption effects during particle approach, i.e. liquid bridges are created when particles come into contact  $\delta_n > 0$ .

### 3. Results and discussion

#### 3.1. Problem set-up

In Subsections 3.2, 3.3, and 3.4, we study the quasi-two-dimensional granular column collapse problem. The domain along which flow takes place, based on the GFT experimental set-up, consists of a prismatic

horizontal channel of total length 2150 mm, width 150 mm, and height 350 mm, respectively aligned with the  $x$ -,  $y$ -, and  $z$ -axis directions of the global coordinate system, as shown in Fig. 1. An auxiliary vertical wall is initially placed at length 150 mm, which forms a cuboid-shaped reservoir where the granular columns are generated. Granular piles are allowed settling in the reservoir under gravity, until stationary initial packing conditions are reached. After that, particles are instantaneously released onto the channel by removing the boundary condition of null horizontal displacement along the channel length.

Furthermore, in Subsection 3.5, we investigate an industrial case of hopper filling of a sugar powder in a screw-fed bagging machine. The mean particle size of the sugar powder is determined experimentally by sieving around  $200\mu\text{m}$ , with a minimum of 70% by mass of particles larger than  $53\mu\text{m}$  and a maximum of 40% larger than  $250\mu\text{m}$ . From in situ observations, quality of the first filled bags is compliant with the particle size distribution requirements, but the fine fraction in the bags is progressively reduced during the production run. As a result, fines are retained in the hopper, thus preventing its complete emptying. A preferential zone of material withdrawal is also formed at the back of the hopper outlet, typically attributed to screw feeder design issues [61].

We evaluate the redesign of the problem geometry illustrated in Fig. 2. The hopper inlet is located on its top face and above the outlet at the bottom, see Fig. 2a. At the oblong hopper outlet, a screw feeder is attached, as shown in Fig. 2b. The simulation domain depicted in Fig. 2c consists of a hopper of total height 2100 mm, a top square face of  $1200 \times 1200 \text{ mm}^2$  and a rectangular face of  $600 \times 300 \text{ mm}^2$  at the bottom. Joining the upper and lower faces are four walls, two of them inclined.

#### 3.2. Particle size dispersity

We simulate spherical particles with particle density  $2000 \text{ kg m}^{-3}$ . We consider two different granular systems by particle size distribution (PSD):

- Mono-sized particles of radius 10 mm;
- Narrow PSD with median particle radius 10 mm. We obtain randomly generated radii by linear interpolation between input values from 5 mm to 15 mm, as shown in Fig. 3. The coefficient of uniformity of the disperse particles is  $C_u = 1.8$ , defined as the ratio between particle sizes at cumulative 60% and 10%.

For each case we simulate two different systems by number of particles:  $N_1 = 500$  and  $N_2 = 1000$  for assemblies of mono-sized spheres, and  $N'_1 = 405$  and  $N'_2 = 809$  in the disperse case, respectively. The total mass of the system is  $m = 4.2 \text{ kg}$  for both  $N_1$  and  $N'_1$ , and  $m =$

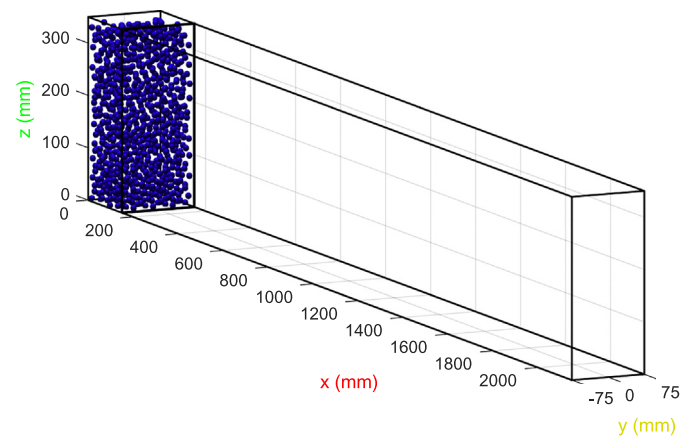


Fig. 1. Simulation domain of the granular column collapse problem.

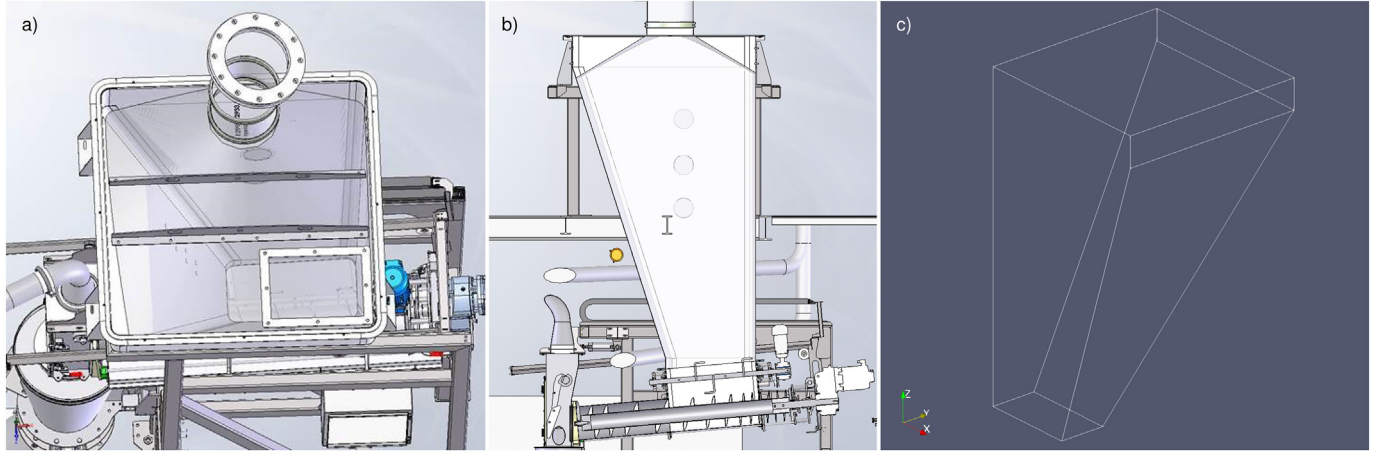


Fig. 2. Hopper geometry: CAD design a) top view, b) side view; c) general view of the simulation domain.

8.4 kg and 8.5 kg for  $N_2$  and  $N'_2$ , respectively. Therefore, the simulated configurations are equivalent with respect to their total mass.

Table 1 shows the mechanical properties of the contacts. Mechanical parameters governing particle-wall interactions are not modified with respect to interparticle contact properties. Concerning system stability, we apply Eq. (3) to obtain a critical contact time  $t_c = 1.4 \times 10^{-3}$  s and a coefficient of restitution  $e = 0.92$  in the case of mono-sized particles, whereas  $t_c = 3.3 \times 10^{-4}$  s and  $e = 0.69$  in the disperse case. Introducing size dispersity, while preserving the median particle size by mass, leads to smaller stable time increments in the numerical scheme, as well as a moderate decrease of the critical restitution coefficient.

### 3.2.1. Height profiles

We track the evolution of the free surface in the  $xz$ -plane, from the onset of flow at time  $t = 0$ . For  $N_1$  and  $N'_1$ , the initial column heights  $h_0 = 162$  mm and 158 mm result in the initial column aspect ratio  $a = 1.1$ , defined as the quotient between the average height of the granular column and the column base length of 150 mm. At the same time,  $h_0 = 332$  mm and 323 mm, respectively, for  $N_2$  and  $N'_2$ , with  $a = 2.2$ .

Since we note a homogeneous flow propagation over the channel width, we average the particle positions along the  $y$ -axis to obtain the height profiles shown in Fig. 4. We find that flow propagation after

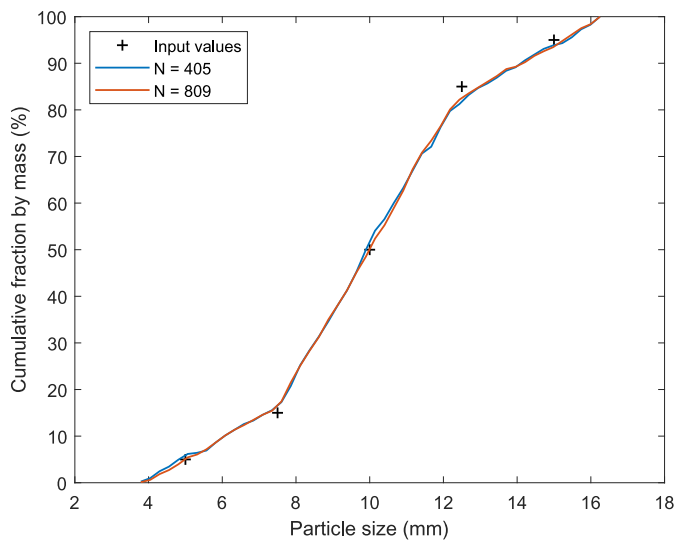


Fig. 3. Particle size distribution (PSD) curves of the disperse spherical particles.

Table 1

Interparticle contact parameters of the granular column collapse simulations of the effect of particle size dispersity.

Degree of freedom	Stiffness ( $\text{Nm}^{-1}$ )	Dissipation ( $\text{Ns m}^{-1}$ )	Friction coefficient (-)
Normal	$k_n = 2.0 \times 10^4$	$\gamma_n = 0.5$	-
Sliding	$k_s = 0.1k_n$	$\gamma_s = 0.2\gamma_n$	$\mu_s = 0.5$
Rolling	$k_r = 0.01k_n$	$\gamma_r = 0.2\gamma_n$	$\mu_r = 0.1\mu_s$
Torsional	$k_o = 0.01k_n$	$\gamma_o = 0.2\gamma_n$	$\mu_o = 0.1\mu_s$

collapse is completed by  $t = 1$  s in every configuration. Thereafter, the system is found to remain stationary with a stable free surface morphology and a few scattered particles located near the flow front. We define the final run-out length as the channel length from  $x = 0$  comprising 95% of the total deposited mass, assuming 5% of the total mass corresponding to particles ahead of the flow front. At  $t = 1$  s, the final run-out lengths for  $N_1$  and  $N'_1$  are  $l_\infty = 477$  mm and 457 mm, respectively, and  $l_\infty = 678$  mm for both  $N_2$  and  $N'_2$ . Consequently, the effect of particle size dispersity results in a reduction of the mobilised mass after collapse for granular columns with  $a = 1.1$ . However, larger mono-sized and disperse particle systems up to  $a = 2.2$  show similar flowability in terms of their mobility reach, considering the narrow PSD and relative particle size of the simulated configurations.

### 3.2.2. Micro-macro mapping

We map the particle data onto a continuum field using an accurate averaging technique known as *coarse-graining* [62]. We obtain the averaged velocity field, fully averaged over the channel width  $y$ -axis, by:

$$\langle \mathbf{v}(\mathbf{x}, t) \rangle_y = \frac{\left\langle \sum_{i=1}^N m_i \mathbf{v}_i(t) \phi(\mathbf{x} - \mathbf{x}_i(t)) \right\rangle_y}{\left\langle \sum_{i=1}^N m_i \phi(\mathbf{x} - \mathbf{x}_i(t)) \right\rangle_y} \quad (6)$$

where  $\mathbf{v}_i$  is the time-dependent velocity of particle  $i$ , and  $\phi$  is an averaging function. We use a Gaussian  $\phi$  of width equal to the maximum particle radius [63]. Fig. 5 shows maps of the vertical  $v_z$  (negative downwards) and horizontal  $v_x$  components of velocity, at the respective peak times during flow propagation. In all the simulated systems, the maximum vertical velocity  $v_z^{\max}$  is attained before the maximum horizontal velocity  $v_x^{\max}$ . We observe  $v_z^{\max}$  close to the free surface during an early flow stage of downward vertical acceleration after collapse, whereas  $v_x^{\max}$  characterises the formation of a flow front close to the channel base, in a late flow stage of horizontal propagation. Although

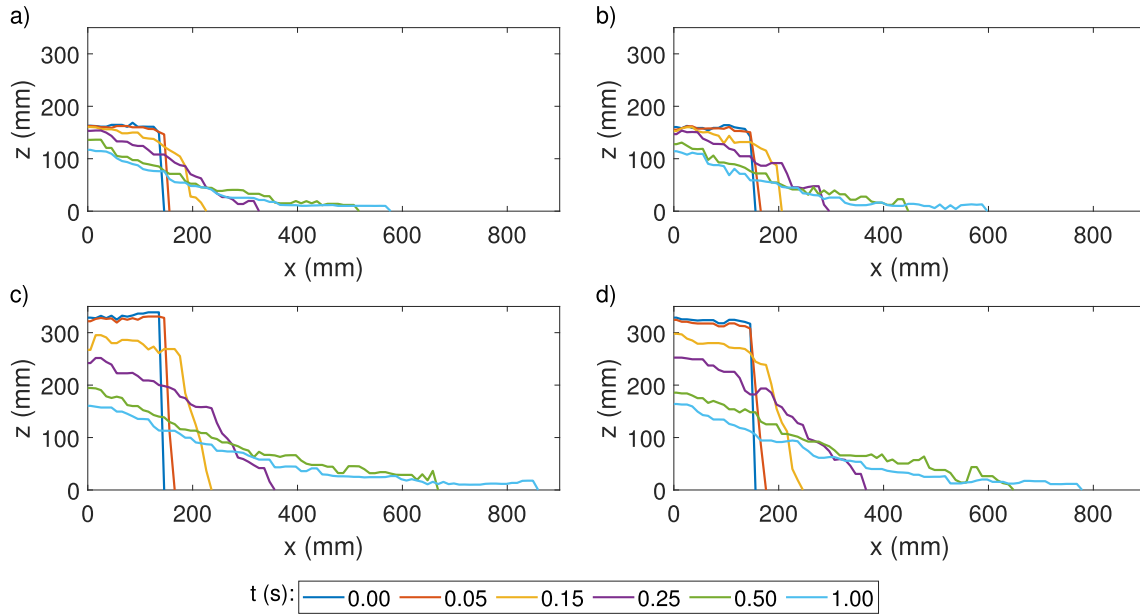


**Fig. 4.** Height profile tracking from  $t = 0$  s to 1 s: a)  $N_1 = 500$  mono-sized particles; b)  $N'_1 = 405$  disperse particles; c)  $N_2 = 1000$  mono-sized particles; d)  $N'_2 = 809$  disperse particles.

we note similar  $v_x^{\max}$  for  $N_2$  and  $N'_2$ , the configurations with particle size dispersity,  $N'_1$  and  $N'_2$ , generally show larger maximum velocities compared to the respective mono-sized counterparts.

### 3.3. Particle shape non-sphericity

We investigate the effect of particle shape on collapse of a system of 15500 prolate spheroidal particles of equivalent radius 4 mm. The mechanical properties of the linear spring-dashpot contact model are shown in Table 2. Contact forces are computed at the estimated inter-particle contact points, albeit with the corresponding curvature radii at the contact points. The surface of a prolate spheroidal particle, see Fig. 6, is given in its local coordinate system by:

$$\frac{x^2}{b^2} + \frac{y^2 + z^2}{c^2} = 1 \quad (7)$$

where  $b$  and  $c$  are the semi-axis lengths. We obtain an equivalent particle volume,  $V_{\text{spheroid}} = 4/3\pi bc^2$ , to that of a sphere of radius  $r = 4$  mm,  $V_{\text{sphere}} = 4/3\pi r^3$ , by scaling the semi-axis lengths by the factor  $\kappa \in [1, 2]$ :

$$b = \kappa r \quad c = \frac{r}{\sqrt{\kappa}} \quad (8)$$

Particle sphericity is defined as:

$$\Psi = \frac{\pi^{1/3}(6V_p)^{2/3}}{S_p} \quad (9)$$

where  $V_p$  is the particle volume, and  $S_p$  is the particle surface area. Sphericity of the simulated particles decreases with increasing non-sphericity, from  $\Psi = 1$  in the case of spheres, to  $\Psi = 0.86$  for  $\kappa = 2$ .

#### 3.3.1. Granular column porosity

Fig. 7 shows the average porosity  $\varepsilon$  of the granular columns at the stationary random packing state before collapse. We observe larger average porosity at lower values of the scaling factor, around  $\kappa = 1$ . Porosity drops by around 9% for  $\kappa > 1.3$ , reaching closer packing states for particle systems of the same mass. We note minimum porosity around

$\kappa = 1.5$ , in agreement with results on the packing of prolate spheroids of equivalent radius  $r = 1$  mm in [64]. Scaling factors  $\kappa > 1.7$  result in looser random packing states, which we attribute to particle interlocking of the prolate spheroids.

#### 3.3.2. Particle orientation

We express particle orientation by Euler's rotation theorem, in terms of three angles  $\alpha$  around the local coordinate system attached to the particle axes, see Fig. 6, and with respect to the global coordinate system attached to the channel base, see Fig. 1. On the one hand, the angle  $\alpha_x$  around the  $x$ -axis corresponds to the vertical orientation of particles along the channel width, i.e. in perpendicular planes to the direction of flow. Considering the quasi-two-dimensional hypothesis on the setup geometry, no particular rearrangement of  $\alpha_x$  is expected for the initially randomised orientation of particles during flow propagation. On the other hand, the angles  $\alpha_y$  and  $\alpha_z$ , around the  $y$ - and  $z$ -axis, respectively measure the orientation of particles on vertical and horizontal planes in the direction of flow. As reported for sheared spherocylindrical particles [65], we expect the alignment of the mobilised particles in the direction of flow to increase with the scaling factor  $\kappa$ .

At the three simulation times illustrated in Fig. 8, we depict the orientation distributions of particle systems with scaling factors  $\kappa = 1$  and 2 in Figs. 9 and 10, respectively. In Fig. 9, for  $\kappa = 1$ , no significant rotation is noted for the spheres forming the initial granular column ( $t = 0$ ), compared to the instant of particle creation ( $t < 0$ ). At run-out ( $t > 0$ ), the orientations are randomly distributed around all three axes, as expected in the case of spheres. However, in Fig. 10 we observe a more random orientation of the spheroids with  $\kappa = 2$  at  $t = 0$ , which we relate to the particle interlocking effect explaining the noted increase in average porosity for granular columns with larger  $\kappa$  values. At  $t > 0$ , we find a random distribution of particles along the channel width in Fig. 10g, confirming the plane strain hypothesis for non-spherical particles. The orientation distribution around the  $y$ -axis in Fig. 10h shows frequency peaks around  $\alpha_y = 0^\circ$  and  $\pm 90^\circ$ , consistently with the dominant directions in the kinematic fields during flow stages of vertical collapse and horizontal flow propagation, as observed experimentally in [10]. Similarly, the orientation of particles around the  $z$ -axis represented

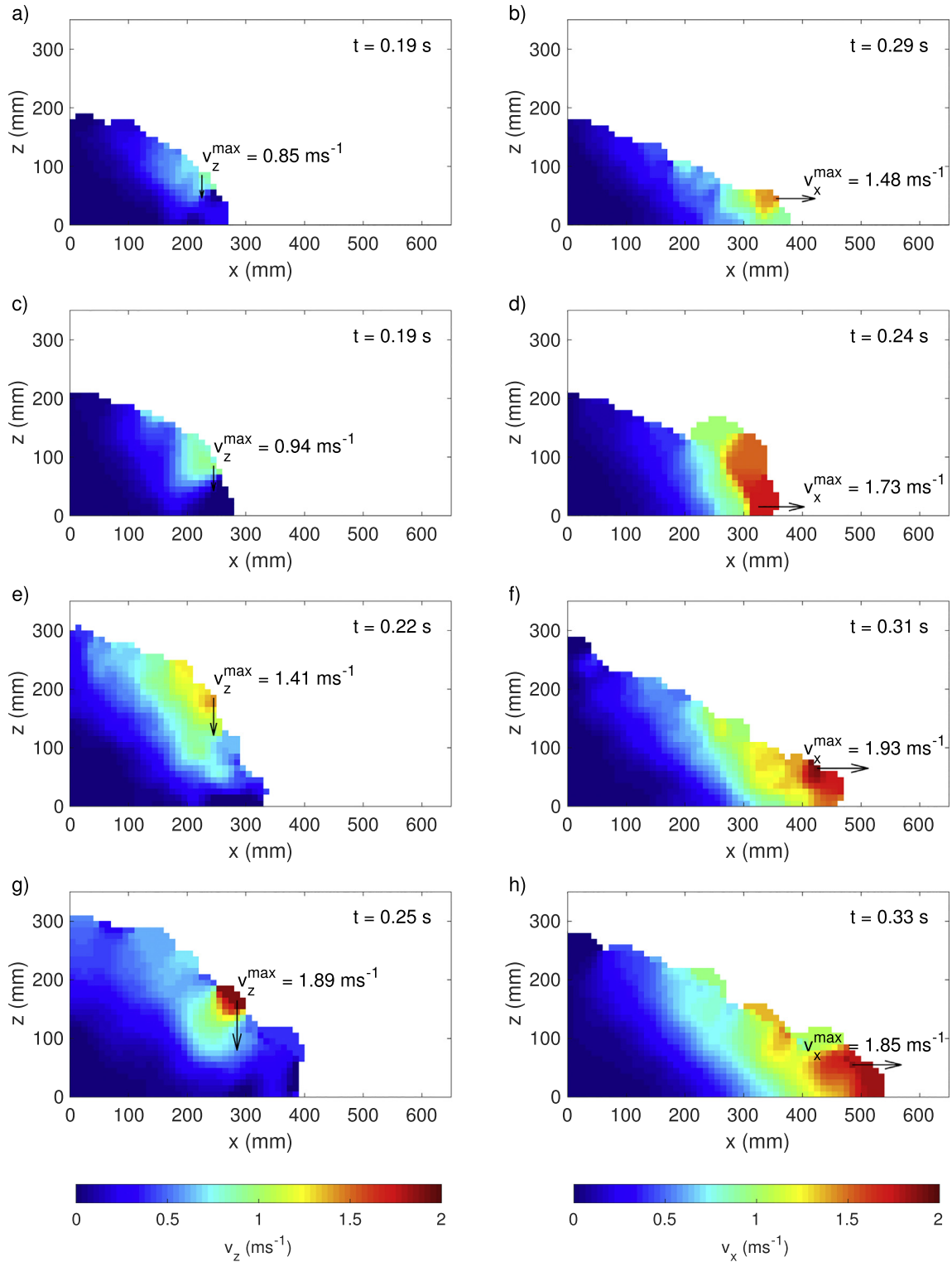


**Fig. 5.** Peak  $v_z$  (left) and  $v_x$  (right) velocity maps: a, b)  $N_1 = 500$  mono-sized particles; c, d)  $N_1' = 405$  disperse particles; e, f)  $N_2 = 1000$  mono-sized particles; g, h)  $N_2' = 809$  disperse particles.

in Fig. 10i shows two frequency peaks around  $\alpha_z = 0^\circ$  and  $\pm 90^\circ$ . The first peak around  $\alpha_z = 0^\circ$  is indicative of an alignment of the prolate spheroids on their major axis in the direction of flow, whereas the second peak around  $\alpha_z = \pm 90^\circ$  reveals a significant fraction of particles oriented transversally to the channel length. We interpret this as a result of a dominant rolling mechanism in the mobilisation of spheroidal

particles, especially for those closer to the surface of the granular deposit, as can be seen in Fig. 11.

### 3.3.3. Height profiles

Frontal views of the height profiles are represented in Fig. 12, averaged along the  $y$ -axis by assuming the quasi-two-dimensionality of



**Table 2**

Interparticle contact parameters of the granular column collapse simulations of the effect of particle shape non-sphericity.

Degree of freedom	Stiffness (Nm <sup>-1</sup> )	Dissipation (Ns m <sup>-1</sup> )	Friction coefficient (-)
Normal	$k_n = 1.0 \times 10^4$	$\gamma_n = 0.3$	-
Sliding	$k_s = 0.2k_n$	$\gamma_s = 0.2\gamma_n$	$\mu_s = 0.5$
Rolling	$k_r = 0.1k_n$	$\gamma_r = 0.05\gamma_n$	$\mu_r = 0.1\mu_s$
Torsional	$k_o = 0.1k_n$	$\gamma_o = 0.05\gamma_n$	$\mu_o = 0.1\mu_s$

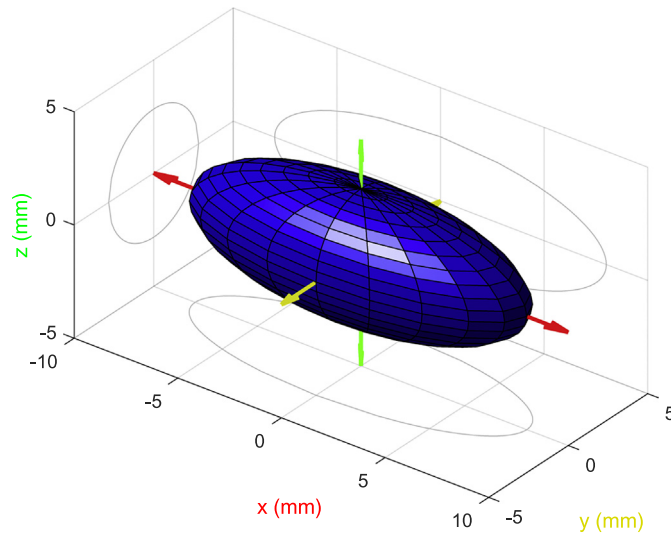


**Fig. 6.** View of an ellipsoidal particle of scaling factor  $\kappa = 2$ , with equivalent volume to a sphere of radius 4 mm.

the problem. Initial column aspect ratios  $a = 2.3, 1.9,$  and  $2.1$  are obtained for  $\kappa = 1, 1.5,$  and  $2$ , respectively. The final deposit is formed between  $t = 0.5$  s and  $1$  s. In addition, the run-out lengths reach  $l_\infty = 497$  mm,  $377$  mm, and  $407$  mm for  $\kappa = 1, 1.5,$  and  $2$ , respectively. Flow front propagation is slowest for the more densely packed spheroids of  $\kappa = 1.5$ . In contrast, we observe larger mobility for  $\kappa = 2$  until  $t = 0.25$  s, in comparison with  $\kappa = 1$ . Therefore, in the case of  $\kappa = 2$ , the

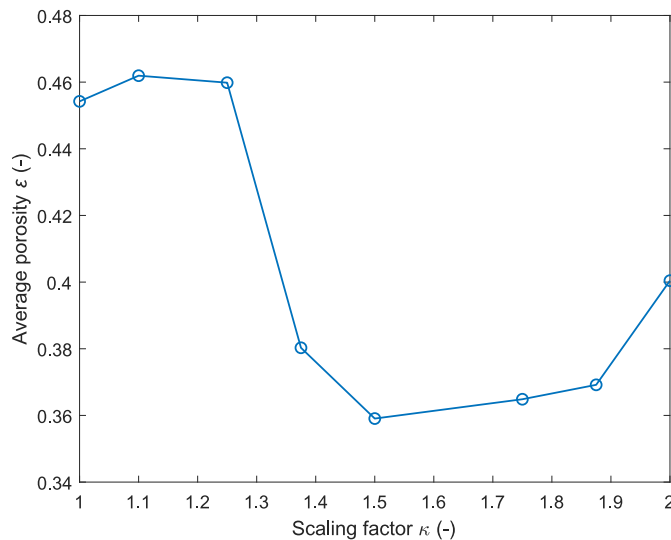


**Fig. 7.** Variation of the granular column porosity  $\epsilon$  at  $t = 0$  against the scaling factor  $\kappa$ .

dominant flow stage corresponds to the initial vertical collapse, which is followed by a longer flow stage of horizontal propagation in the case of  $\kappa = 1$ . These results corroborate the dominant flow stages identified by GFT testing in [10], for the avalanching of irregularly-shaped oat flakes against the sliding of fertiliser particles.

### 3.3.4. Energy balance

We discuss the granular flow behaviour after collapse in terms of the energy balance of the granular system:

$$E_{\text{tot}} = E_{\text{pot}} + E_{\text{kin}}^{\text{trans}} + E_{\text{kin}}^{\text{rot}} + U \quad (10)$$

where  $E_{\text{tot}}$  is the constant total energy,  $E_{\text{pot}}$  is the gravitational potential energy,  $E_{\text{kin}}^{\text{trans}}$  and  $E_{\text{kin}}^{\text{rot}}$  are the translational and rotational components of the kinetic energy, respectively, and  $U$  is the internal energy accounting for the conservative and dissipative particle interactions [10]. Fig. 13 shows the evolution of the energy balance during flow of spheroids of  $\kappa = 1$  and  $2$ . At  $t = 0$ , the different initial aspect ratio of the granular columns results in higher  $E_{\text{pot}}$  for  $\kappa = 1$ , which is reduced by 64% around  $t = 0.8$  s. We observe a similar initial decay of  $E_{\text{pot}}$  for  $\kappa = 2$ , though followed by a gradual energy decrease reaching 66% at  $t = 2$  s. The evolution of kinetic energy is controlled by  $E_{\text{kin}}^{\text{trans}}$ , as detailed in Fig. 14, attaining peak values around 12% of  $E_{\text{tot}}$  for both  $\kappa = 1$  and  $2$ , between  $t = 0.15$  s and  $0.2$  s. We note a differentiated behaviour for the evolution of  $E_{\text{kin}}^{\text{rot}}$ , depending on the scaling factor of the particles. In the spherical case,  $E_{\text{kin}}^{\text{rot}}/E_{\text{tot}}$  is negligible in the overall energy balance, as already known for granular flows of spheres, see [39], since we observe a peak value of 0.15% of  $E_{\text{tot}}$  at  $t = 0.3$  s. Nevertheless, in the case of prolate spheroids, we find a relative  $E_{\text{kin}}^{\text{rot}}$  peak of 1.5% at  $t = 0.05$  s in Fig. 14b, which we relate directly to the rearrangement of non-spherical particle orientation after the onset of flow, as can be seen at run-out in Fig. 10.

### 3.4. Particle hygroscopicity

We investigate the effect of particle hygroscopicity on column collapse, starting from the dry sphere set-up simulated in Subsection 3.3, and with gravimetric liquid contents between  $w = 0\%$  and  $5\%$ , i.e. lying within the pendular state [66]. We impose  $w$  so that the total liquid volume  $V_l$  is homogeneously distributed among the particles at start, which is calculated as:

$$V_l = w \frac{\rho_p}{\rho_l} \sum_i V_{p_i} \quad (11)$$

where  $\rho_p = 950$  kg m<sup>-3</sup> is the particle density,  $\rho_l = 1000$  kg m<sup>-3</sup> the liquid density of water at a room temperature of 20°C, and the sum of  $V_p$  is the total volume of the spherical particle system. Table 3 shows the employed parameters in the capillary model. According to the capillary force  $f_c$  model of [58], the impact of  $f_c$  on the granular flow behaviour increases with the liquid surface tension  $\sigma$ . Contrarily, with increasing particle size and density, the inertial forces control the flowability of wet granular materials. We thus increase  $\sigma$  with respect to the reference water surface tension of  $0.073$  N m<sup>-1</sup> at room temperature to clearly observe the effect of the liquid bridges using coarse particles.

#### 3.4.1. Height profiles

Fig. 15 shows  $y$ -averaged lateral views of the granular pile after the onset of flow. The initial column aspect ratio is in the range of  $a = 2.2$  and  $2.5$ , increasing slightly with the liquid content. At time  $1$  s after the onset of flow, propagation has taken place and the final deposit is formed. We observe the effect of liquid bridges on the run-out length to increase with the total liquid content, by slowing down collapse for  $w \leq 3\%$ , and even stopping flow out of the reservoir for  $w \geq 4\%$ . Liquid contents in the pendular regime induce a reduced mobilisation of the

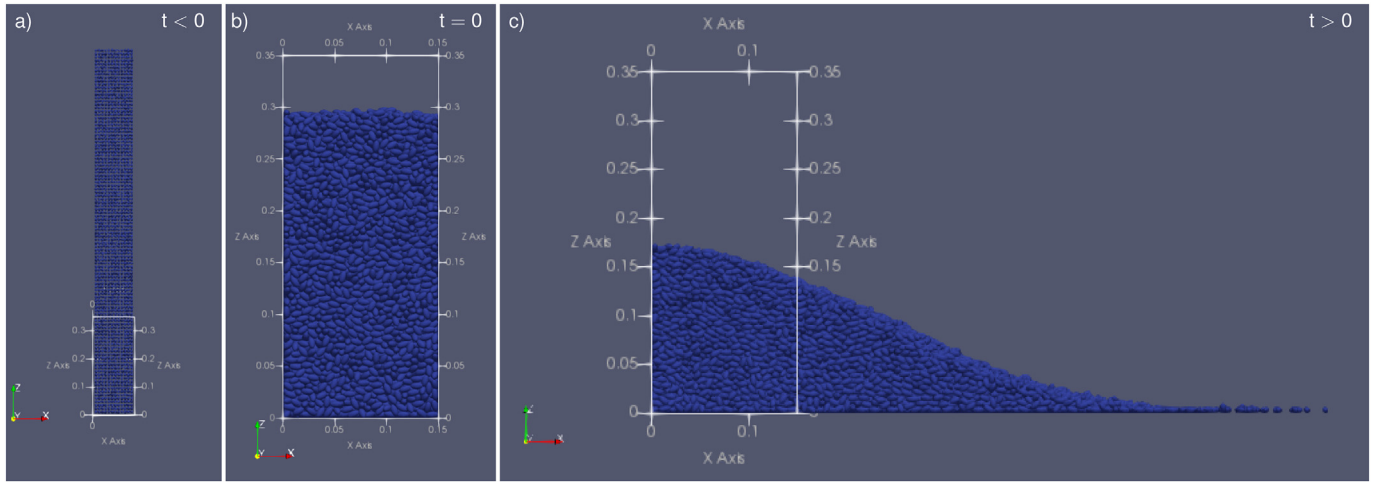


Fig. 8. Three representative times during simulation with spheroidal particles ( $\kappa = 1.5$ ): a) particle creation; b) onset of flow; c) run-out.

granular deposit. We interpret this behaviour as the contribution of the liquid bridges to caking.

### 3.4.2. Energy balance

As can be seen in Fig. 16, the potential energy at the onset of flow  $E_{\text{pot}}(t = 0) = E_{\text{tot}}$  is slightly larger in the wet case with  $w = 2\%$ , whereas we observe a larger final reduction of  $E_{\text{pot}}$  by 64% in the dry case,  $w = 0\%$ . We attribute the lower decrease of  $E_{\text{pot}}$  in the wet case by 42% to the inhibiting effect of capillary forces on mass mobilisation. With respect

to the total energy  $E_{\text{tot}}$ , we note in Fig. 17 peak values of the translational component of the kinetic energy  $E_{\text{kin}}^{\text{trans}}$  of 12% and 6.1% at  $t = 0.2\text{ s}$  and  $0.4\text{ s}$ , respectively, for  $w = 0\%$  and  $2\%$ . The rotational component of the kinetic energy  $E_{\text{kin}}^{\text{rot}}$  attains maximum relative values of 0.16% and 0.056% around 50 ms after the respective  $E_{\text{kin}}^{\text{trans}}$  peaks, in the dry and wet cases. Therefore, in line with the numerical results for dry spheres in Subsubsection 3.3.4, the contribution of  $E_{\text{kin}}^{\text{rot}}$  to the kinetic energy evolution during flow propagation can also be neglected for wet spherical particle systems.

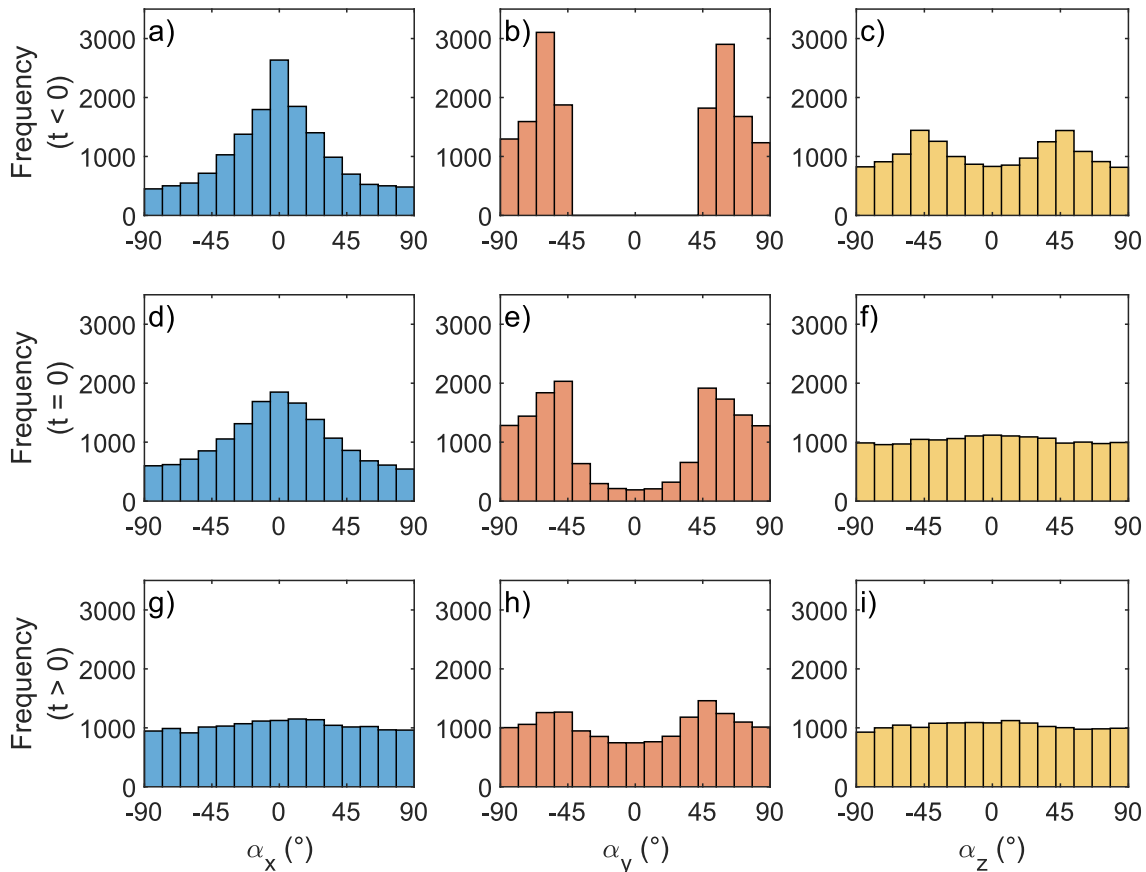


Fig. 9. Orientation distributions around the  $x$ -,  $y$ -, and  $z$ -axis for spheres ( $\kappa = 1$ ) at three representative times during simulation.

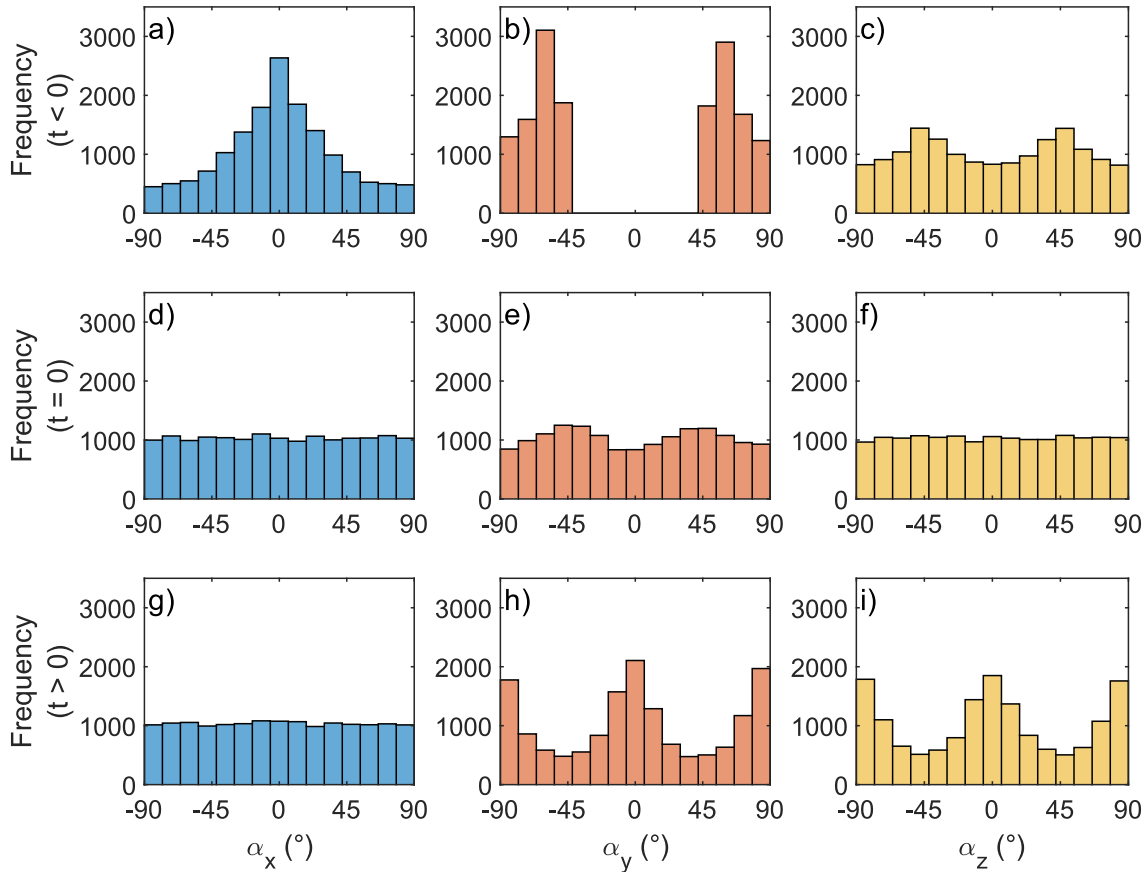


Fig. 10. Orientation distributions around the  $x$ -,  $y$ -, and  $z$ -axis for spheroids of scaling factor  $\kappa = 2$  at three representative times during simulation.

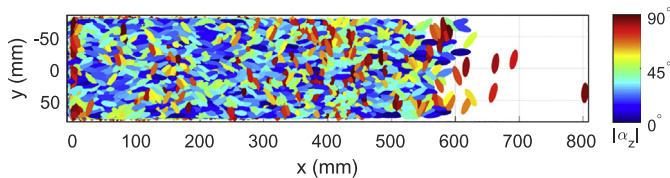


Fig. 11. Top view of the final deposit at run-out for spheroids of scaling factor  $\kappa = 2$ .

### 3.5. Particle size segregation

We utilise the PolydisperseInsertionBoundary class in MercuryDPM to reproduce the hopper filling operation. With this insertion boundary [52], we generate particles initially at rest, free falling from a rectangular region of the simulation domain, functioning as the hopper inlet. Given the large number of particles involved in the actual industrial problem, we perform particle upscaling by increasing the particle sizes and maintaining the domain geometry [31]. We impose particle size dispersity to generate a quasi-bidisperse mixture of 5518 spheres of particle density  $1540 \text{ kg m}^{-3}$ . We obtain the PSD curves in Fig. 18, depicting the higher concentration of small particles of sizes around  $20 \text{ mm}$  and the lower proportion of large particles of around  $60 \text{ mm}$ . Table 4 details the mechanical parameters of the implemented linear spring-dashpot model describing interparticle contacts. The DEM parameters are derived from imposing the values of the coefficient of restitution,  $e = 0.2$ , and of the normal stiffness. For the latter, a Hertzian contact stiffness between two spheres is considered, assuming a contact modulus of  $7 \times 10^7 \text{ MPa}$  and an estimated contact radius of  $4 \text{ mm}$ .

#### 3.5.1. Zero alternative

We model the unaltered configuration for hopper filling as the zero alternative (A0). Fig. 19a shows the particle insertion from the  $265 \times 265 \text{ mm}^2$  square inlet on the top face of the reception hopper, adjacent to the vertical wall along the outlet length, see Fig. 2c. We observe the accumulation of fine particles around the vertical of the filling point in Fig. 19b, where we also note the displacement of coarse particles to the hopper walls. Granular mobility takes place mainly in the direction of the outlet elongation: a slope is formed, with small particles at the head and large particles near the foot, sliding over the surface of the deposited material.

Fig. 20 illustrates the extent to which the A0 set-up is able to reproduce the actual bulk handling conditions. As highlighted in Fig. 20a, we observe hopper emptying by the screw feeder to generate a preferential zone of material withdrawal at the back of the screw. In addition, the granular deposit in Fig. 20b shows a tendency of the large particles to accumulate on the preferential zone for the screw feeder. Therefore, we expect the coarse fraction of the sugar powder to be discharged first, allowing for the uneven PSD in the filled bags.

#### 3.5.2. Analysis of alternatives

We simulate three hopper design alternatives helping to improve screw feeder operation downstream. We analyse two alternative strategies to mitigate horizontal segregation: a deflector to deviate flow from the filling point (A1) and a distributor to fill the hopper from two separate filling points (A2). The addition of a distributor at the hopper inlet minimises horizontal segregation problems by creating multiple deposits [67]. We propose a third alternative aimed at reducing vertical segregation by lowering the filling point height with respect to the hopper base (A3). The addition of a distributor at the hopper

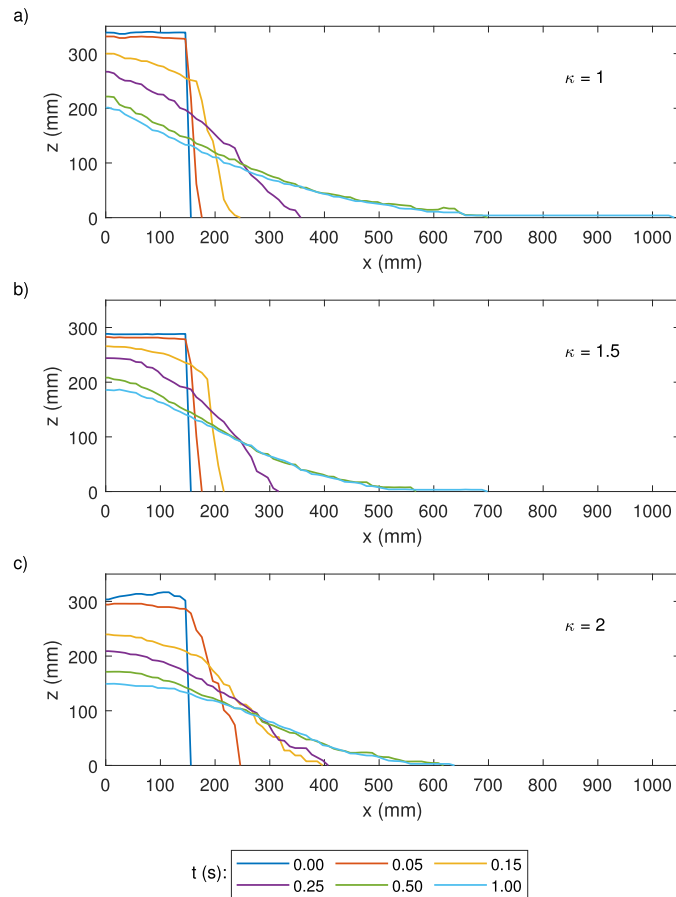


Fig. 12. Evolution of the height profiles of three particle systems with scaling factors  $\kappa = 1, 1.5,$  and  $2$ .

inlet minimises horizontal segregation problems by creating multiple deposits [67]. We discuss the three modified hopper geometry set-ups tackling particle size segregation:

A1 We add a deflector to the initial geometry, shifting the particle trajectory with respect to the vertical of the filling point and closer to the preferential zone of material withdrawal. As shown in Fig. 21a, the deflector consists of a prism of right-

angled triangular section, of base 265 mm and inclination angle  $45^\circ$ , placed horizontally below the inlet with a minimum separation of 200 mm. In comparison with A0, the accumulation of coarse particles is shifted away from the preferential zone of material withdrawal, as shown in Fig. 21b. However, a slope-shaped deposit is formed inside the reception hopper and the horizontal segregation effect pushing the large particles to the hopper walls is still appreciable.

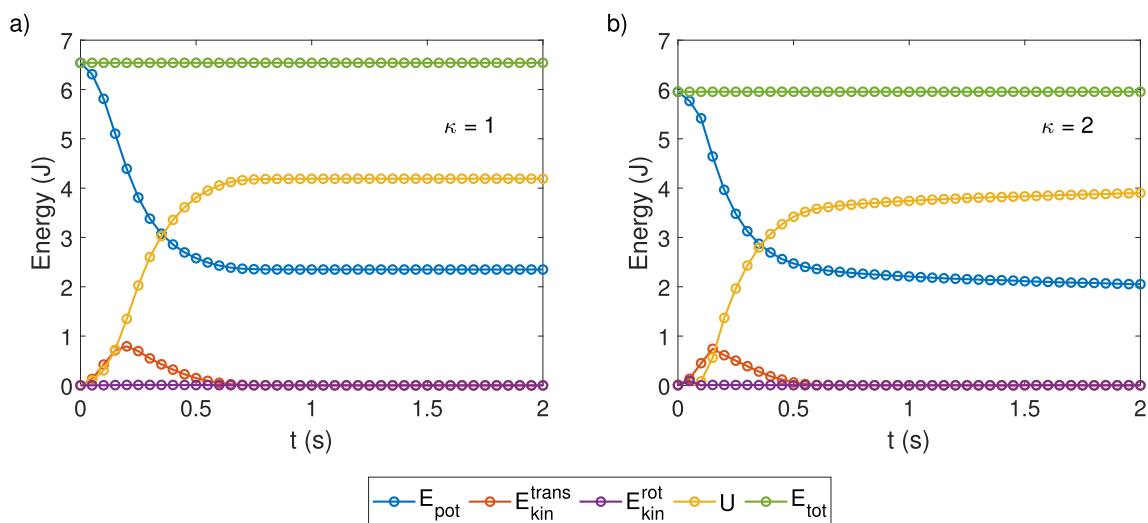


Fig. 13. Energy balance of two particle systems with scaling factors  $\kappa = 1$  and  $2$ .

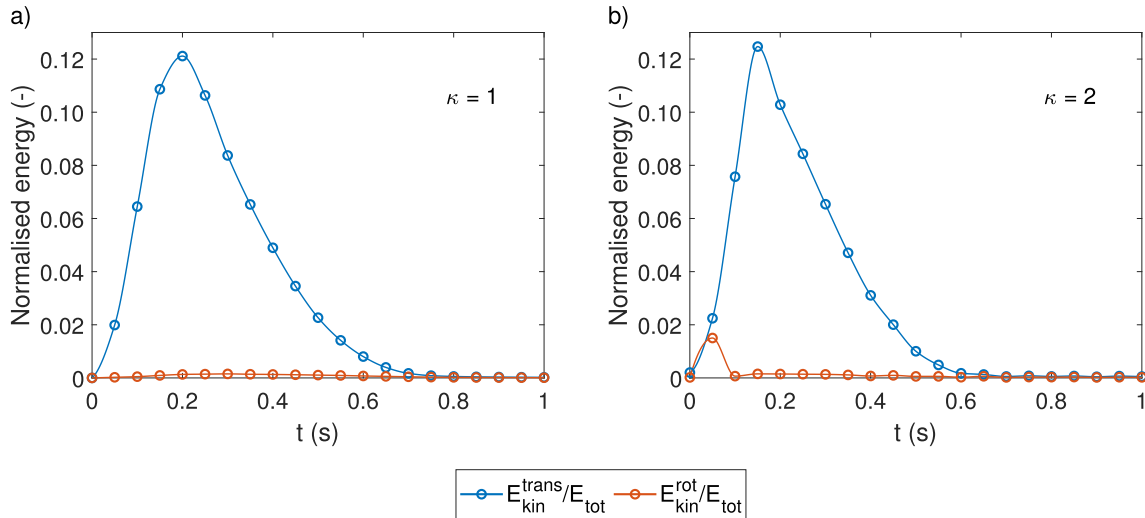


Fig. 14. Evolution of the normalised components of kinetic energy of two particle systems with scaling factors  $\kappa = 1$  and 2.

Table 3

Liquid bridge model parameters.

Parameter	Value
Surface tension, $\sigma$ ( $\text{Nm}^{-1}$ )	1
Contact angle ( $^\circ$ )	30
Maximum liquid bridge volume ( $\text{m}^3$ )	$2.0 \times 10^{-8}$
Distribution coefficient (-)	0.8

A2 In Fig. 21c, a distributor generates two filling points along the outlet length. The distributor is formed by a horizontal prism of triangular section, of base 397.5 mm and two symmetrical slopes at  $45^\circ$ , centered below the inlet at a minimum distance of 200 mm. Fig. 21d shows a more levelled free surface for A2, compared to the slope observed for A0 and A1. Moreover, the displacement of large particles to the sides is avoided with this configuration, resulting in a better mixing of the fine and coarse fractions.

A3 We lower the filling point height by 725 mm from the top face of the hopper, see Fig. 21e, to assess the design alternative of extending the inlet tube length inside the hopper. We observe in Fig. 21f that a granular slope mainly with large particles near the preferential zone for the screw feeder is formed for A3, which we attribute to A3 maintaining a single filling point in the vertical of the inlet, as in the case of A0.

#### 4. Concluding remarks

We have presented the discrete element modelling of the effects at the particle level of two granular flow problems. From simulations of the GFT granular column collapse set-up, we investigated:

- The effect of particle size dispersity on the height profiles, final run-out lengths, and averaged maximum velocities for granular columns with initial column aspect ratios  $a = 1.1$  and 2.2, using mono-sized

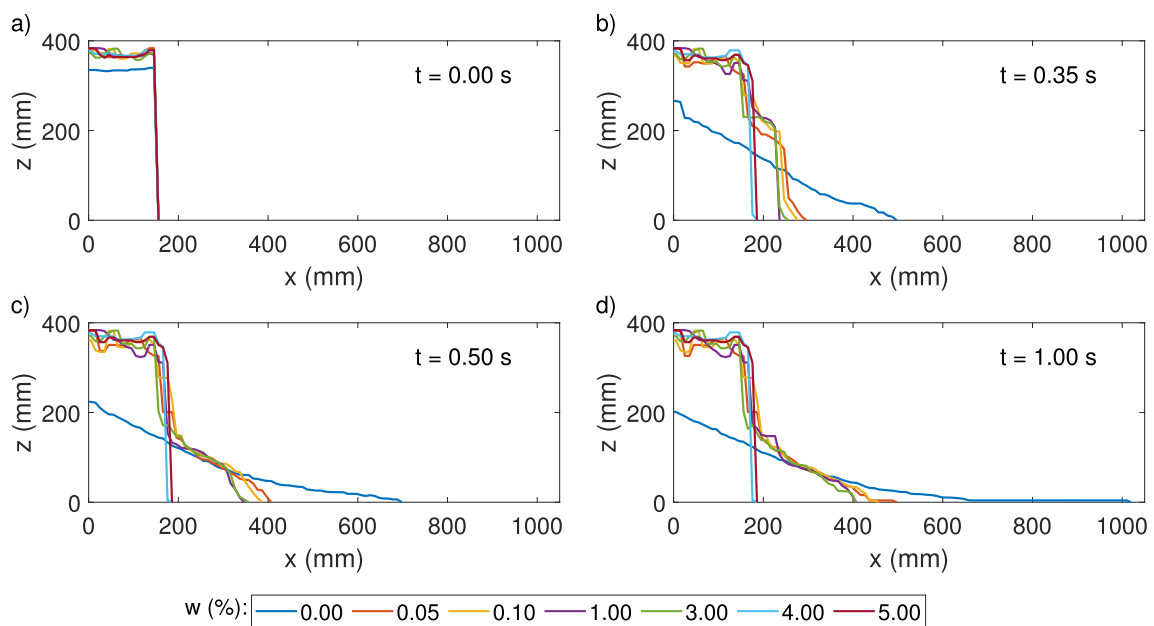


Fig. 15. Evolution of the height profiles with varying gravimetric liquid contents  $w$ .

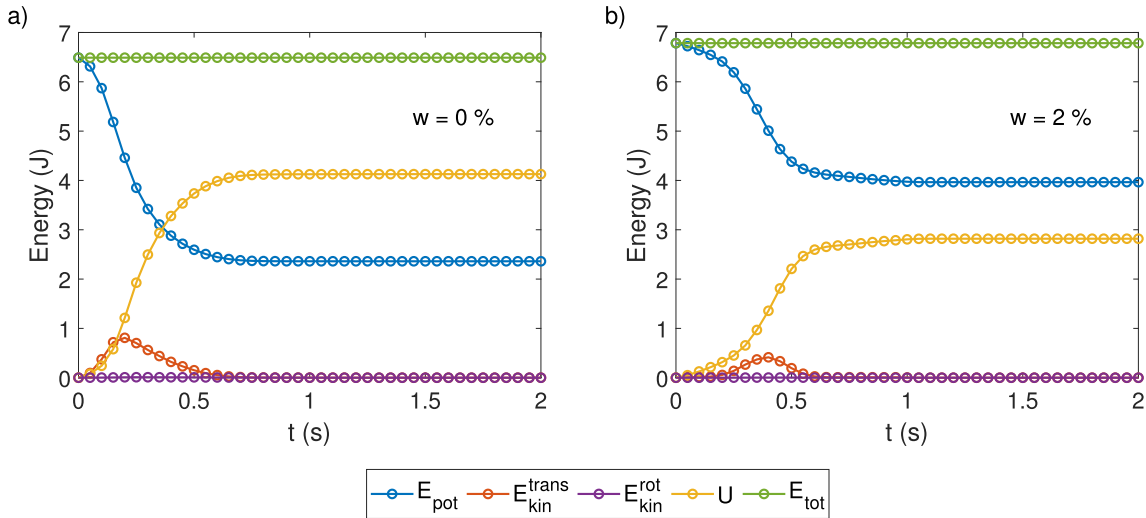


Fig. 16. Energy balance of two particle systems with gravimetric liquid contents  $w = 0\%$  and  $2\%$ .

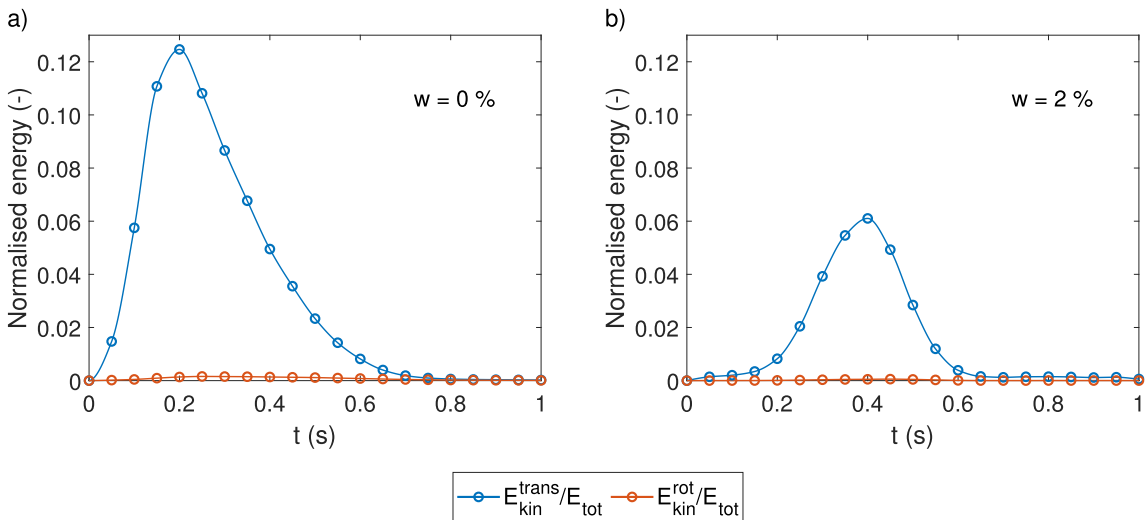


Fig. 17. Evolution of the normalised components of kinetic energy of two particle systems with gravimetric liquid contents  $w = 0\%$  and  $2\%$ .

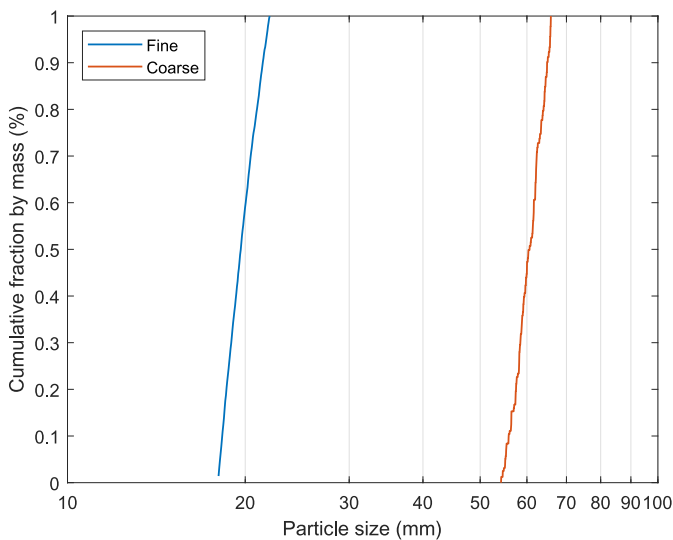


Fig. 18. PSD curves of the quasi-bidisperse mixture of fine and coarse spheres.

and disperse spherical particle packings of median radius  $r = 10$  mm. The evolution of compared height profiles is analogous, whereas the mobilised mass at run-out is indicative of the reduced flowability of disperse granular columns with lower  $a$ . Additionally, the averaged velocity fields of the discrete simulation results show similar or larger maximum velocities for systems of disperse particles.

- The particle shape effect for spheroids with scaling factors between  $\kappa = 1$  and 2. Porosity of the granular systems before collapse shows the closest particle packings for intermediate scaling factors around  $\kappa = 1.5$ . Particle orientation increases with non-sphericity

Table 4  
Mechanical parameters of the linear spring–dashpot contact model.

Degree of freedom	Stiffness ( $\text{Nm}^{-1}$ )	Dissipation ( $\text{Ns m}^{-1}$ )	Friction coefficient (-)
Normal	$k_n = 4.2 \times 10^5$	$\gamma_n = 34$	–
Sliding	$k_s = 0.2k_n$	$\gamma_s = 0.2\gamma_n$	$\mu_s = 0.58$
Rolling	$k_r = 0.1k_n$	$\gamma_r = 0.05\gamma_n$	$\mu_r = 0.1\mu_s$
Torsional	$k_o = 0.1k_n$	$\gamma_o = 0.05\gamma_n$	$\mu_o = 0.1\mu_s$

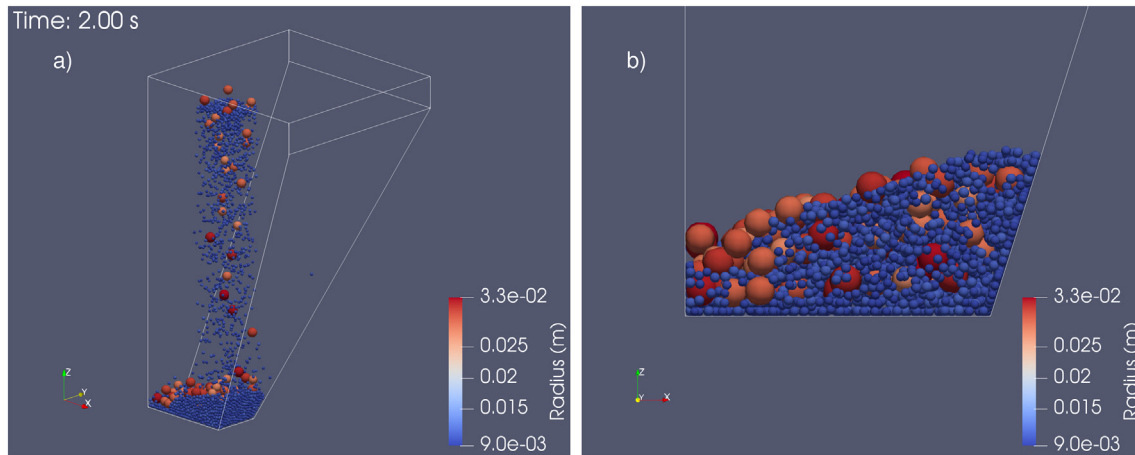


Fig. 19. A0: a) general view of the hopper filling simulation; b) side view of the deposited particles at rest.

throughout the simulations, the particles aligning primarily in the dominant directions of flow. Height profile evolution reveals the flow front propagation behaviour to be in agreement with the flow stages analysed experimentally for irregularly-shaped particles in [10]. Moreover, the findings for energy balance of non-spherical particles provide evidence that the rotational component of the kinetic energy is not negligible as conventionally assumed for spheres.

- The impact of liquid content on the run-out of spherical particle packings. We have upscaled the surface tension to  $\sigma = 1 \text{ Nm}^{-1}$ , illustrating the effect of particle hygroscopicity for packings of coarse spheres. Simulations with increasing liquid content between  $w = 0\%$  and  $5\%$  show reduced flow propagation as expected within the pendular state. We confirm this behaviour in the energy balance, evidencing the decrease and time delay of the peak kinetic energy, governed by its translational component.

From analysis of alternatives for the hopper filling problem modelled with size-bidisperse spheres, alternative A3 would seem not to present advantages with respect to the zero alternative. Nevertheless, vertical segregation is critically dependent on the particle-air interactions, which is a limitation of the utilised interparticle contact model. Therefore, the design alternative of lowering the inlet height should not be disregarded based on the available observations. In spite of this, alternatives A1 and A2 address horizontal segregation. Considering

both proposals, together with the observed preferential zone of material withdrawal due to screw-fed discharge, the installation of a deflector or distributor could be applied to improve withdrawal of the fraction of fine particles in both cases—more evenly throughout hopper emptying in the case of A2—also avoiding excessive retention of small particles at the end of every production run.

In this paper we have exploited the capabilities of the MercuryDPM software for modelling various grain-scale effects by the DEM. The results of this study have implications for the identification of key granular flow measures from GFT testing. In comparison with reference simulations with dry, mono-sized, spherical particles, we have mainly obtained differentiated velocity maps and peak values for disperse particles, prevailing particle orientations and energy components for non-spherical particles, and distinctive height profile evolutions with increasing liquid contents. In sum, these findings highlight relevant flow phenomena hardly detected from direct observation of experimental results. Incorporating these effects in the experimental data can thus improve the flowability characterisation of industrial granular materials. Finally, the hopper filling simulations have proven that a simple model for particle size segregation can effectively avoid costly trial-and-error redesign strategies based on full-scale pilot plant testing.

This study has raised questions in need of further investigation in the following areas:

- Micro-macro mapping or *coarse-graining* [63] aimed at contrasting simulated kinematic fields of the granular column collapse set-up

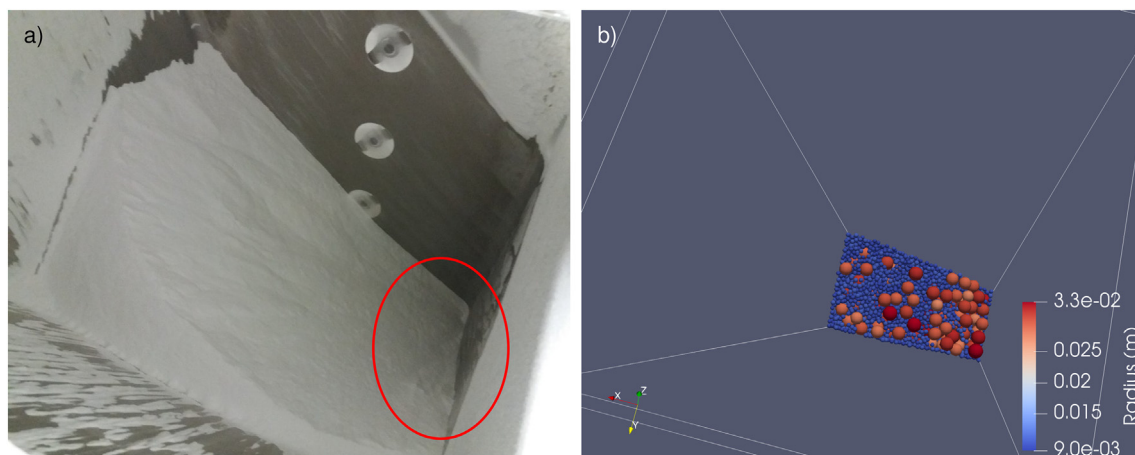
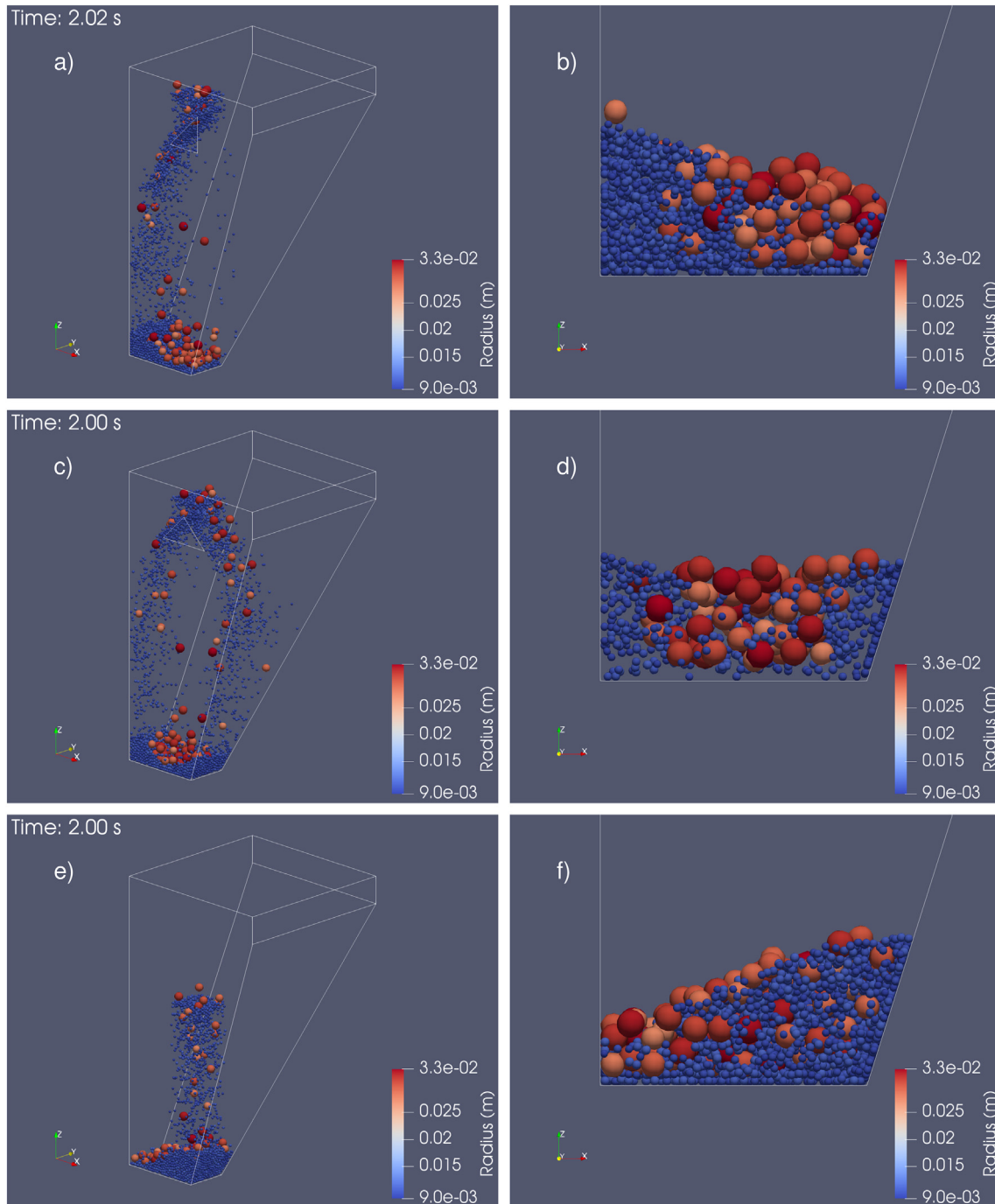


Fig. 20. Views of the filled material reception hopper for A0: a) preferential zone of material withdrawal; b) distribution of particle size fractions in the simulated granular deposit.



**Fig. 21.** General views of the hopper filling simulations (left) and side views of the granular deposits at rest (right): a, b) A1; c, d) A2; e, f) A3.

against experimental observations with the GFT by particle image velocimetry analysis.

- Reverse DEM calibration [68] for finding the mechanical parameters at the particle level from replicating several macroscopic measures obtained in granular column collapse experiments, such as high-resolution scans of the granular deposits and time evolution of the energy balance of the system or the basal load distributions during flow front propagation.

- Coupled particle-scale effects, such as particle shape and size segregation [69], in complex granular flows for both experimental and industrial set-ups.
- Particle-air interaction by coupling DEM with computational fluid dynamics methods [70] and particle-wall interaction from experimental characterisation of the mechanical parameters.
- Number of particles for DEM simulation of powder flows and full-scale industrial set-ups, by different strategies ranging from scaling



laws by calibration with experiments [71] to parallel and GPU computing [72].

### List of symbols

#### Latin symbols

$a$	Initial column aspect ratio (–)
$C_u$	Uniformity coefficient (–)
$e$	Coefficient of restitution (–)
$E_{kin}^{rot}$	Rotational kinetic energy of the granular system (J)
$E_{kin}^{trans}$	Translational kinetic energy of the granular system (J)
$E_{pot}$	Potential energy of the granular system (J)
$E_{tot}$	Total energy of the granular system (J)
$f_c$	Capillary force (N)
$\mathbf{f}_i$	Total force acting on the $i$ -th particle (N)
$f_n$	Normal component of force (N)
$\mathbf{f}_o$	Torsional quasi-force (N)
$\mathbf{f}_r$	Rolling quasi-force (N)
$f_t$	Tangential component of force (N)
$h_0$	Initial column height (mm)
$I_i$	Moment of inertia of the $i$ -th particle ( $\text{kgm}^2$ )
$k_n$	Normal stiffness ( $\text{Nm}^{-1}$ )
$k_o$	Torsional stiffness ( $\text{Nm}^{-1}$ )
$k_r$	Rolling stiffness ( $\text{Nm}^{-1}$ )
$k_s$	Sliding stiffness ( $\text{Nm}^{-1}$ )
$l_\infty$	Final run-out length (mm)
$\mathbf{l}_i$	Branch vector (m)
$m$	Total mass of the particle system (kg)
$m_i$	Mass of the $i$ -th particle (kg)
$m_{min}$	Minimum particle mass of the system (kg)
$\mathbf{q}_i$	Total torque acting on the $i$ -th particle ( $\text{Nm}$ )
$r$	Radius of a spherical particle (mm)
$r_{ij}$	Reduced radius (m)
$S_p$	Particle surface area ( $\text{m}^2$ )
$t$	Time (s)
$t_c$	Critical contact time (s)
$U$	Internal energy of the granular system (J)
$\mathbf{v}$	Instantaneous velocity field ( $\text{ms}^{-1}$ )
$\mathbf{v}_i$	Velocity of the $i$ -th particle ( $\text{ms}^{-1}$ )
$V_l$	Total liquid volume ( $\text{m}^3$ )
$v_n$	Normal component of relative velocity ( $\text{ms}^{-1}$ )
$V_p$	Particle volume ( $\text{m}^3$ )
$V_{sphere}$	Volume of a spherical particle ( $\text{m}^3$ )
$V_{spheroid}$	Volume of a spheroidal particle ( $\text{m}^3$ )
$v_t$	Tangential component of relative velocity ( $\text{ms}^{-1}$ )
$w$	Gravimetric liquid content (%)
$\ddot{\mathbf{x}}_i$	Linear acceleration of the $i$ -th particle ( $\text{ms}^{-2}$ )

#### Greek symbols

$\alpha$	Angle of particle orientation around the axis specified in the subscript ( $^\circ$ )
$\gamma_n$	Normal viscous dissipation ( $\text{Ns m}^{-1}$ )
$\gamma_o$	Torsional viscous dissipation ( $\text{Nm}^{-1}$ )
$\gamma_r$	Rolling viscous dissipation ( $\text{Nm}^{-1}$ )
$\gamma_s$	Sliding viscous dissipation ( $\text{Nm}^{-1}$ )
$\delta_n$	Normal contact overlap (m)
$\delta_t$	Tangential contact spring (m)
$\varepsilon$	Average porosity (–)
$\kappa$	Scaling factor of the semi-axis lengths of a spheroidal particle (–)

$\mu_o$	Torsional friction coefficient ( $\text{Nm}^{-1}$ )
$\mu_r$	Rolling friction coefficient ( $\text{Nm}^{-1}$ )
$\mu_s$	Sliding friction coefficient ( $\text{Nm}^{-1}$ )
$\rho_l$	Liquid density ( $\text{kg m}^{-3}$ )
$\rho_p$	Particle density ( $\text{kg m}^{-3}$ )
$\sigma$	Liquid surface tension ( $\text{Nm}^{-1}$ )
$\phi$	Averaging function (–)
$\Psi$	Particle sphericity (–)
$\omega_i$	Angular acceleration of the $i$ -th particle (–)

### Declaration of Competing Interest

None.

### Acknowledgements

This work was supported by the Industrial Doctorates Plan of the Government of Catalonia (2014 DI 075).

### References

- [1] D. Barletta, R.J. Berry, S.H. Larsson, T.A. Lestander, M. Poletto, A. Ramírez-Gómez, Assessment on bulk solids best practice techniques for flow characterization and storage/handling equipment design for biomass materials of different classes, *Fuel Process. Technol.* 138 (2015) 540–554, <https://doi.org/10.1016/j.fuproc.2015.06.034>.
- [2] Groupement De Recherche Milieux Divisés (GDR MiDi), On dense granular flows, *Eur. Phys. J. E* 14 (4) (2004) 341–365, <https://doi.org/10.1140/epje/i2003-10153-0>.
- [3] G. Lumay, F. Boschini, K. Traina, S. Bontempi, J.C. Remy, R. Cloots, N. Vandewalle, Measuring the flowing properties of powders and grains, *Powder Technol.* 224 (2012) 19–27, <https://doi.org/10.1016/j.powtec.2012.02.015>.
- [4] ASTM International, Subcommittee D18.24 on Characterization and Handling of Powders and Bulk Solids, URL <https://www.astm.org/COMMIT/SUBCOMMIT/D1824.htm> 2020.
- [5] D. Ilic, C. Wheeler, Measurement and simulation of the bulk solid load on a conveyor belt during transportation, *Powder Technol.* 307 (2017) 190–202, <https://doi.org/10.1016/j.powtec.2016.11.020>.
- [6] Técnicas Mecánicas Ilerdenses, S.L., TMI, Ensacado, Paletizado, Protección de cargas y Pesaje, URL <https://www.tmpal.com/> 2020.
- [7] Técnicas Mecánicas Ilerdenses, S.L., Dispositivo para ensayo de colapso de una columna de material pulverulento o granular, in: J. Torres Serra, X. Arderiu Cabau, J.M. Padullés Ribalta, J. Caba Muntada, J.J. González Toledano, E.E. Romero Morales, A. Rodríguez Ferran (Eds.), Spanish Patent ES2695451B2, Spanish Patent and Trademark Office, 2019, URL <https://patentscope.wipo.int/search/en/detail.jsf?docId=ES235596513>.
- [8] G. Lube, H.E. Huppert, R.S.J. Sparks, A. Freundt, Collapses of two-dimensional granular columns, *Phys. Rev. E* 72 (4) (2005), 041301, <https://doi.org/10.1103/PhysRevE.72.041301>.
- [9] E. Lajeunesse, J.B. Monnier, G.M. Homsy, Granular slumping on a horizontal surface, *Phys. Fluids* 17 (10) (2005) 103302, <https://doi.org/10.1063/1.2087687>.
- [10] J. Torres-Serra, E. Romero, A. Rodríguez-Ferran, A new column collapse apparatus for the characterisation of the flowability of granular materials, *Powder Technol.* 362 (2020) 559–577, <https://doi.org/10.1016/j.powtec.2019.11.080>.
- [11] J. Torres-Serra, A. Rodríguez-Ferran, E. Romero, Classification of granular materials via flowability-based clustering with application to bulk feeding, *Powder Technol.* 378 (2021) 288–302, <https://doi.org/10.1016/j.powtec.2020.09.022>.
- [12] G.B. Crosta, S. Imposimato, D. Roddeman, Granular flows on erodible and non erodible inclines, *Granul. Matter* 17 (5) (2015) 667–685, <https://doi.org/10.1007/s10035-015-0587-8>.
- [13] E.J. Fern, K. Soga, The role of constitutive models in MPM simulations of granular column collapses, *Acta Geotech.* 11 (3) (2016) 659–678, <https://doi.org/10.1007/s11440-016-0436-x>.
- [14] C.T. Nguyen, C.T. Nguyen, H.H. Bui, G.D. Nguyen, R. Fukagawa, A new SPH-based approach to simulation of granular flows using viscous damping and stress regularisation, *Landslides* 14 (1) (2017) 69–81, <https://doi.org/10.1007/s10346-016-0681-y>.
- [15] X. Zhang, K. Krabbenhoft, D.M. Pedroso, A.V. Lyamin, D. Sheng, M. Vicente da Silva, D. Wang, Particle finite element analysis of large deformation and granular flow problems, *Comput. Geotech.* 54 (2013) 133–142, <https://doi.org/10.1016/j.compgeo.2013.07.001>.
- [16] F. Radjai, J.N. Roux, A. Daouadji, Modeling Granular Materials: Century-Long Research across Scales, *J. Eng. Mech.* 143 (4) (2017), 04017002, [https://doi.org/10.1061/\(ASCE\)JEM.1943-7889.0001196](https://doi.org/10.1061/(ASCE)JEM.1943-7889.0001196).
- [17] P.A. Cundall, O.D.L. Strack, A discrete numerical model for granular assemblies, *Géotechnique* 29 (1) (1979) 47–65, <https://doi.org/10.1680/geot.1979.29.1.47>.

- [18] J.Y. Ooi, V. Magnanimo, J. Sun, S. Luding, Particle Modelling with the Discrete Element Method: A success story of PARDEM (www.pardem.eu), *Powder Technol* 293 (2016) 1–2, <https://doi.org/10.1016/j.powtec.2016.03.020>.
- [19] Y. Guo, J.S. Curtis, Discrete Element Method Simulations for Complex Granular Flows, *Annu. Rev. Fluid Mech.* 47 (1) (2015) 21–46, <https://doi.org/10.1146/annurev-fluid-010814-014644>.
- [20] A. Jilavenkatesa, S.J. Dapkunas, L.S.H. Lum, Particle Size Characterization, NIST Special Publication 960-1, U.S. Government Printing Office (2001) <https://doi.org/10.6028/NBS.SP.960-1>.
- [21] L.X. Liu, I. Marziano, A.C. Bentham, J.D. Litster, E.T. White, T. Howes, Effect of particle properties on the flowability of ibuprofen powders, *Int. J. Pharm.* 362 (1) (2008) 109–117, <https://doi.org/10.1016/j.ijpharm.2008.06.023>.
- [22] H.P. Goh, P.W.S. Heng, C.V. Liew, Comparative evaluation of powder flow parameters with reference to particle size and shape, *Int. J. Pharm.* 547 (1) (2018) 133–141, <https://doi.org/10.1016/j.ijpharm.2018.05.059>.
- [23] J.M.N.T. Gray, P. Gajjar, P. Kokelaar, Particle-size segregation in dense granular avalanches, *C. R. Phys.* 16 (1) (2015) 73–85, <https://doi.org/10.1016/j.crhy.2015.01.004>.
- [24] M. Combarros, H.J. Feise, H. Zetzener, A. Kwade, Segregation of particulate solids: Experiments and DEM simulations, *Particuology* 12 (2014) 25–32, <https://doi.org/10.1016/j.partic.2013.04.005>.
- [25] A.N. Edwards, N.M. Vriend, Size segregation in a granular bore, *Phys. Rev. Fluids* 1 (6) (2016), 064201, <https://doi.org/10.1103/PhysRevFluids.1.064201>.
- [26] J. Mosby, S.R. de Silva, G.G. Enstad, Segregation of Particulate Materials – Mechanisms and Testers, *KONA Powder Part. J.* 14 (1996) 31–43, <https://doi.org/10.14356/kona.1996008>.
- [27] M. Cabrera, N. Estrada, Granular column collapse: Analysis of grain-size effects, *Phys. Rev. E* 99 (1) (2019), 012905, <https://doi.org/10.1103/PhysRevE.99.012905>.
- [28] T.F. Zhang, J.Q. Gan, D. Pinson, Z.Y. Zhou, Size-induced segregation of granular materials during filling a conical hopper, *Powder Technol.* 340 (2018) 331–343, <https://doi.org/10.1016/j.powtec.2018.09.031>.
- [29] C. Ramírez-Aragón, F. Alba-Eliás, A. González-Marcos, J. Ordieres-Meré, Segregation in the tank of a rotary tablet press machine using experimental and discrete element methods, *Powder Technol.* 328 (2018) 452–469, <https://doi.org/10.1016/j.powtec.2018.01.054>.
- [30] C. Hildebrandt, S.R. Gopireddy, R. Scherließ, N.A. Urbanetz, Investigation of powder flow within a pharmaceutical tablet press force feeder – A DEM approach, *Powder Technol.* 345 (2019) 616–632, <https://doi.org/10.1016/j.powtec.2019.01.040>.
- [31] C.J. Coetzee, Particle upscaling: Calibration and validation of the discrete element method, *Powder Technol.* 344 (2019) 487–503, <https://doi.org/10.1016/j.powtec.2018.12.022>.
- [32] N. Stark, A.E. Hay, R. Cheel, C.B. Lake, The impact of particle shape on the angle of internal friction and the implications for sediment dynamics at a steep, mixed sand-gravel beach, *Earth Surf. Dyn.* 2 (2) (2014) 469–480, <https://doi.org/10.5194/esurf-2-469-2014>.
- [33] Z. Guo, X. Chen, Y. Xu, H. Liu, Effect of granular shape on angle of internal friction of binary granular system, *Fuel* 150 (2015) 298–304, <https://doi.org/10.1016/j.fuel.2015.02.047>.
- [34] R.M. Carter, Y. Yan, Measurement of particle shape using digital imaging techniques, *J. Phys. Conf. Ser.* 15 (2005) 177–182, <https://doi.org/10.1088/1742-6596/15/1/030>.
- [35] X. Fu, D. Huck, L. Makein, B. Armstrong, U. Willen, T. Freeman, Effect of particle shape and size on flow properties of lactose powders, *Particuology* 10 (2) (2012) 203–208, <https://doi.org/10.1016/j.partic.2011.11.003>.
- [36] T. Börzsönyi, R. Stannarius, Granular materials composed of shape-anisotropic grains, *Soft Matter* 9 (31) (2013) 7401–7418, <https://doi.org/10.1039/C3SM50298H>.
- [37] H. Tapia-McClung, R. Zenit, Computer simulations of the collapse of columns formed by elongated grains, *Phys. Rev. E* 85 (6) (2012), 061304, <https://doi.org/10.1103/PhysRevE.85.061304>.
- [38] Y. Yu, Y.P. Cheng, X. Xu, K. Soga, Discrete element modelling of methane hydrate soil sediments using elongated soil particles, *Comput. Geotech.* 80 (2016) 397–409, <https://doi.org/10.1016/j.compgeo.2016.03.004>.
- [39] S. Uttili, T. Zhao, G.T. Houlisby, 3D DEM investigation of granular column collapse: Evaluation of debris motion and its destructive power, *Eng. Geol.* 186 (2015) 3–16, <https://doi.org/10.1016/j.enggeo.2014.08.018>.
- [40] R. Rorato, M. Arroyo, A. Gens, E. Andò, G. Viggiani, Particle Shape Distribution Effects on the Triaxial Response of Sands: A DEM Study, in: P. Giovine, P.M. Mariano, G. Mortara (Eds.), *Micro to MACRO Mathematical Modelling in Soil Mechanics*, Trends in Mathematics, Birkhäuser, Cham 2018, pp. 277–286, [https://doi.org/10.1007/978-3-319-99474-1\\_28](https://doi.org/10.1007/978-3-319-99474-1_28).
- [41] Z.Y. Zhou, R.P. Zou, D. Pinson, A.B. Yu, Dynamic Simulation of the Packing of Ellipsoidal Particles, *Ind. Eng. Chem. Res.* 50 (16) (2011) 9787–9798, <https://doi.org/10.1021/ie200862n>.
- [42] O. Pozo, B. Soulestin, N. Olivi-Tran, Stick Slip Motion in Grain Grain Friction in a Humid Atmosphere, *Multidiscip. Model. Mater. Struct.* 4 (4) (2008) 393–405, <https://doi.org/10.1163/157361108785963037>.
- [43] U. Zafar, V. Vivacqua, G. Calvert, M. Ghadiri, J.A.S. Cleaver, A review of bulk powder caking, *Powder Technol.* 313 (2017) 389–401, <https://doi.org/10.1016/j.powtec.2017.02.024>.
- [44] E. Juárez-Enriquez, G.I. Olivas, P.B. Zamudio-Flores, E. Ortega-Rivas, S. Perez-Vega, D.R. Sepulveda, Effect of water content on the flowability of hygroscopic powders, *J. Food Eng.* 205 (2017) 12–17, <https://doi.org/10.1016/j.jfoodeng.2017.02.024>.
- [45] J. Torres-Serra, E. Romero, A. Rodríguez-Ferran, Hygroscopicity issues in powder and grain technology, in: C.W.W. Ng, A.K. Leung, A.C.F. Chiu, C. Zhou (Eds.), 7th International Conference on Unsaturated Soils, UNSAT 2018, Hong Kong University of Science and Technology 2018, pp. 805–810, URL <http://hdl.handle.net/2117/129402>.
- [46] J.P. Wang, X. Li, H.S. Yu, A micro-macro investigation of the capillary strengthening effect in wet granular materials, *Acta Geotech.* 13 (3) (2018) 513–533, <https://doi.org/10.1007/s11440-017-0619-0>.
- [47] F. Gabrieli, R. Artoni, A. Santomaso, S. Cola, Discrete particle simulations and experiments on the collapse of wet granular columns, *Phys. Fluids* 25 (10) (2013) 103303, <https://doi.org/10.1063/1.4826622>.
- [48] G. Wang, A. Riaz, B. Balachandran, Smooth particle hydrodynamics studies of wet granular column collapses, *Acta Geotech.* 15 (5) (2020) 1205–1217, <https://doi.org/10.1007/s11440-019-00828-4>.
- [49] F. Ceccato, A. Leonardi, V. Girardi, P. Simonini, M. Pirulli, Numerical and experimental investigation of saturated granular column collapse in air, *Soils Found.* 60 (3) (2020) 683–696, <https://doi.org/10.1016/j.sandf.2020.04.004>.
- [50] L. Gilson, S. Kozhar, S. Antonyuk, U. Bröckel, S. Heinrich, Contact models based on experimental characterization of irregular shaped, micrometer-sized particles, *Granul. Matter* 16 (3) (2014) 313–326, <https://doi.org/10.1007/s10035-013-0464-2>.
- [51] M. Tapias, E.E. Alonso, J. Gili, A particle model for rockfill behaviour, *Géotechnique* 65 (12) (2015) 975–994, <https://doi.org/10.1680/jgeot.14.P.170>.
- [52] T. Weinhart, L. Orefice, M. Post, M.P. van Schrojenstein Lantman, I.F.C. Denissen, D.R. Tunuguntla, J.M.F. Tsang, H. Cheng, M.Y. Shaheen, H. Shi, P. Rapino, E. Grannonio, N. Losacco, J. Barbosa, L. Jing, J.E. Alvarez Naranjo, S. Roy, W.K. den Otter, A.R. Thornton, Fast, flexible particle simulations – An introduction to MercuryDPM, *Comput. Phys. Commun.* 249 (2020) 107129, <https://doi.org/10.1016/j.cpc.2019.107129>.
- [53] S. Luding, Introduction to discrete element methods, *Eur. J. Environ. Civ. Eng.* 12 (7–8) (2008) 785–826, <https://doi.org/10.1080/19648189.2008.9693050>.
- [54] S.M. Derakhshani, D.L. Schott, G. Lodewijks, Micro-macro properties of quartz sand: Experimental investigation and DEM simulation, *Powder Technol.* 269 (2015) 127–138, <https://doi.org/10.1016/j.powtec.2014.08.072>.
- [55] P. Rousé, Comparison of Methods for the Measurement of the Angle of Repose of Granular Materials, *Geotech. Test. J.* 37 (1) (2014) 164–168, <https://doi.org/10.1520/GTJ20120144>.
- [56] A. Podlozhnyuk, S. Pirker, C. Kloss, Efficient implementation of superquadric particles in Discrete Element Method within an open-source framework, *Comput. Part. Mech.* 4 (1) (2017) 101–118, <https://doi.org/10.1007/s40571-016-0131-6>.
- [57] D. Krijgsman, V. Ogarko, S. Luding, Optimal parameters for a hierarchical grid data structure for contact detection in arbitrarily polydisperse particle systems, *Comput. Part. Mech.* 1 (3) (2014) 357–372, <https://doi.org/10.1007/s40571-014-0020-9>.
- [58] C.D. Willett, M.J. Adams, S.A. Johnson, J.P.K. Seville, Capillary Bridges between Two Spherical Bodies, *Langmuir* 16 (24) (2000) 9396–9405, <https://doi.org/10.1021/la000657y>.
- [59] S. Roy, A. Singh, S. Luding, T. Weinhart, Micro-macro transition and simplified contact models for wet granular materials, *Comput. Part. Mech.* 3 (4) (2016) 449–462, <https://doi.org/10.1007/s40571-015-0061-8>.
- [60] A. Zhou, R. Huang, D. Sheng, Capillary water retention curve and shear strength of unsaturated soils, *Can. Geotech. J.* 53 (6) (2016) 974–987, <https://doi.org/10.1139/cgj-2015-0322>.
- [61] J. Marinelli, Choosing a feeder that works in unison with your bin, *Powder Bulk Eng.* 10 (12) (1996) 43–57 <https://www.powderbulk.com/article/choosing-a-feeder-that-works-in-unison-with-your-bin/>.
- [62] T. Weinhart, A.R. Thornton, S. Luding, O. Bokhove, From discrete particles to continuum fields near a boundary, *Granul. Matter* 14 (2) (2012) 289–294, <https://doi.org/10.1007/s10035-012-0317-4>.
- [63] D.R. Tunuguntla, A.R. Thornton, T. Weinhart, From discrete elements to continuum fields: Extension to bidisperse systems, *Comput. Part. Mech.* 3 (3) (2016) 349–365, <https://doi.org/10.1007/s40571-015-0087-y>.
- [64] J.Q. Gan, A.B. Yu, Z.Y. Zhou, DEM simulation on the packing of fine ellipsoids, *Chem. Eng. Sci.* 156 (2016) 64–76, <https://doi.org/10.1016/j.ces.2016.09.017>.
- [65] D.B. Nagy, P. Claudin, T. Börzsönyi, E. Somfai, Rheology of dense granular flows for elongated particles, *Phys. Rev. E* 96 (6) (2017), 062903, <https://doi.org/10.1103/PhysRevE.96.062903>.
- [66] N. Mitarai, F. Nori, Wet granular materials, *Adv. Phys.* 55 (1–2) (2006) 1–45, <https://doi.org/10.1080/00018730600626065>.
- [67] H. Purutyan, J.W. Carson, Predicting, diagnosing, and solving mixture segregation problems, *Powder Bulk Eng.* 21 (1) (2007) 35–43, URL <https://www.powderbulk.com/article/predicting-diagnosing-and-solving-mixture-segregation-problems/>.
- [68] C.J. Coetzee, Calibration of the discrete element method and the effect of particle shape, *Powder Technol.* 297 (2016) 50–70, <https://doi.org/10.1016/j.powtec.2016.04.003>.
- [69] M. Alizadeh, A. Hassanpour, M. Pasha, M. Ghadiri, A. Bayly, The effect of particle shape on predicted segregation in binary powder mixtures, *Powder Technol.* 319 (2017) 313–322, <https://doi.org/10.1016/j.powtec.2017.06.059>.
- [70] K. Vollmar, R. Jasevičius, H. Kruggel-Emden, Experimental and numerical study of fluidization and pressure drop of spherical and non-spherical particles in a model scale fluidized bed, *Powder Technol.* 291 (2016) 506–521, <https://doi.org/10.1016/j.powtec.2015.11.045>.
- [71] S. Lommen, M. Mohajeri, G. Lodewijks, D. Schott, DEM particle upscaling for large-scale bulk handling equipment and material interaction, *Powder Technol.* 352 (2019) 273–282, <https://doi.org/10.1016/j.powtec.2019.04.034>.
- [72] Y. He, T. Evans, A. Yu, R. Yang, A GPU-based DEM for modelling large scale powder compaction with wide size distributions, *Powder Technol.* 333 (2018) 219–228, <https://doi.org/10.1016/j.powtec.2018.04.034>.

### 5.1 Contributions

This thesis deals with the experimental assessment of the flowability of industrial granular materials by a new patented prototype, their classification using a data analysis methodology contrasted with industrial practice, and the simulation of experimental and industrial granular flow problems to shed light on the particle-level effects explaining bulk flow phenomena. The following conclusions are drawn in response to the research objectives outlined in [Section 1.2](#).

The TMI granular flow tester (GFT) is presented in detail in [Chapter 2](#) and displays innovative design features for quasi-two-dimensional granular column collapse testing, concerning the lifting gate to mitigate particle dragging, the silicone membrane arrangements to transmit loads on the channel base to the beam load cells, as well as the scanning laser system composed of a 3D line profile sensor controlled by a linear guide to map the free surface morphology of the samples at rest. The proposed testing protocol effectively integrates the instrumentation of the set-up with some redundant systems, the capabilities of which are demonstrated for oat flakes, fertiliser, and talc powder samples. The GFT incorporates the following innovations:

- Aeration and deaeration reversible pneumatic circuit to study the behaviour of the granular columns at different densification states. The formation of preferential air flow paths and surface cracking can be observed in the case of talc. The intrinsic air permeability of fertiliser is measured to be roughly an order of magnitude smaller in vacuum conditions with respect to the fluidised state.
- Free surface of the initial granular columns is scanned with the 3D laser profile sensor, measuring average expansion and compression by 5 % and 15 % due to packing state-preconditioning of talc. For the final deposits at rest, the measured surface morphology allows comparing the run-out configurations—with fertiliser showing larger spreading—and the mobilised friction angle, with larger variations noted for deaerated talc.
- Basal load profiles, describing flow propagation after collapse, are fitted by load deposition ramps to the measurements obtained at the load cell locations. At higher initial column aspect ratios, the load peaks observed close to the reservoir exit—up to 23 % of the equilibrium load for fertiliser—are included in the modelling approach as overshoots. The basal load cell readings for tributary volumes of accumulated material are verified for deaerated fertiliser at equilibrium against the surface scans of the granular deposit.
- Flow visualisations from image analysis of high-speed video recordings are used to track the flow front location during propagation, showing similar trends for columns of different initial column aspect

ratios in the case of oats. The transient basal loads are compared to frontal views of the deposition process, corroborating the modelled overshoot effect for deaerated fertiliser. Moreover, particle image velocimetry (PIV) analysis of the video recordings is carried out to recover the velocities and shear strain fields near the channel walls, which are used to evaluate the energy balance for the oats and fertiliser. The accuracy of the granular PIV approach is verified in [Section 3.8](#) using semi-synthetic image pairs from GFT test recordings.

The flow measurements discussed in [Chapter 2](#) allow defining up to 20 relevant flow descriptors in every GFT test case. In [Chapter 3](#), the followed experimental approach to fully characterise any given granular material with the GFT is proposed, considering the average measures of the flow descriptors at two different initial column aspect ratios (smaller and larger than 1) and for three different initial packing states (poured, aerated, and deaerated).

A methodology based on cluster analysis is presented in [Chapter 3](#) to classify powders and bulk solids into groups of similarly flowing materials from their measured flow parameters. For every new granular material, the proposed scheme is updated, which consists of three main steps: outlier detection, variable reduction by PCA, and cluster analysis. The clustering results for data set DS1, containing 174 materials defined by 6 standard properties, are compared to their feeder-type classification from industrial know-how. Five flowability-based clusters are found for DS1, as many as feeder-type classes, albeit with matching pairs between 36 % and 59 %. On the one hand, the common industrial practice is shown to produce a mismatched classification for some granular materials. On the other hand, the material characterisation is refined for the extended property data set DS2, containing 11 materials each defined by 8 standard properties and by 118 measurements of the relevant flow descriptors. The PCA projections of standard versus fully-characterised descriptions of the materials in DS2 are compared, showing significant improvement of the detection of similarly flowing materials due to the relevant flow descriptors.

Granular flow problems are modelled by the DEM in [Chapter 4](#). In light of these results, the usefulness of the DEM is confirmed as a support tool providing an in-depth understanding of the underlying phenomena in granular flow experiments and practical industrial applications:

- Particle size dispersity is modelled to observe the granular column collapse of mono-sized and disperse spheres, preserving the average particle size by mass. Analogous flow behaviour is identified when comparing granular collapse of mono-sized spheres with narrow-graded sphere assemblies. Disperse particle systems show an evolution of the height profiles resulting in a reduced mobility reach of final deposits in the form of shallow slopes, and larger velocity peaks during flow propagation.
- Particle shape is investigated by simulations of granular column collapse experiments with spheroidal particles. Closer particle packings of the granular columns before collapse and a rearrangement of particle orientations in the dominant directions of flow are observed, hence the reduced flowability of granular systems with increasing non-sphericity. Flow phenomena observed experimentally for irregular-shaped particles are also noted in the numerical results for elongated spheroids, such as an avalanching mechanism in flow propagation and a non-negligible contribution to the overall energy balance of the rotational component of kinetic energy.
- Hygroscopicity is simulated using a liquid bridge model. A liquid content range from 0 % to 5 % is studied, within the pendular regime. Results of the numerical simulations show that the formation of particle aggregates motivated by the hygroscopic behaviour of the materials can be reproduced by

coarse particle packings and scaling the liquid surface tension accordingly. These findings are used to discuss the energy balance of dry and wet systems in [Section 2.8](#).

- Particle size segregation is simulated during filling of a material reception hopper with quasi-bidisperse spheres. From the analysis of redesign alternatives, modifying the hopper geometry with the inclusion of a flow deflector or distributor below the inlet yields improved mixing of the deposited particles.

## 5.2 Outlook

Future studies should target topics for further research in the following areas:

- The impact of environmental conditions on flowability should be experimentally studied utilising the GFT. Supplementary flow parameters may be derived, characterising the relative humidity and temperature of the granular materials with supplementary instrumentation of the GFT, including various non-contact infrared visualisation techniques [1, 2]. Additionally, modelling of the gravity-driven GFT collapse tests at high gravitational accelerations in a drum centrifuge may closely approximate full-scale bulk handling conditions [3, 4].
- Larger data sets comprising relevant flow descriptors should be used to verify the proposed data analysis methodology, preferably against available feeder type information. Otherwise, the clustering methodology should be validated experimentally with feeder performance assessments coming from full-scale pilot plant testing.
- The data analysis methodology may be adapted to other decision-making processes involving, for instance, other bagging machine appliances (weighing systems, bag sealing techniques, ...)
- Coarse-grained measurements of kinematic fields from DEM granular column collapse simulation results should be reverse-calibrated against experimental GFT observations of the near-wall kinematics by PIV analysis, feasibly improved with advanced PIV post-processing techniques [5]. Similarly, other flow phenomena observed at the macroscale (high-resolution granular deposits scans, time evolution of the energy balance of the system, basal load distributions during flow front propagation, ...) may be used to determine the unknown mechanical contact parameters. The findings of this work would have implications for refining the data analysis methodology with the calibrated material properties.
- Horizontal segregation mechanisms observed in actual handling conditions are modelled with up-scaled particle systems, whereas future studies should address the simulation of vertical segregation in full-scale industrial problems, for instance by discrete-continuum modelling.
- Coupling of multiple microscale effects, e.g. particle shape and size-segregation, should be studied by DEM simulations to gain insight into complex granular flow problems describing the actual experimental and industrial set-up conditions.
- Approximation to powder flow problems with the DEM for full-scale set-ups should be further investigated by different strategies (scaling laws by experimental calibration, parallel computing, GPU computing, ...)

### 5.3 References

- [1] F. Parera, N. Pinyol, and E. Alonso, Image-based measurements of degree of saturation, *E3S Web of Conferences*, vol. 195, p. 03 010, 2020. DOI: [10.1051/e3sconf/202019503010](https://doi.org/10.1051/e3sconf/202019503010).
- [2] M. Adepu, B. Boepple, B. Fox, and H. Emady, Experimental investigation of conduction heat transfer in a rotary drum using infrared thermography, *Chemical Engineering Science*, vol. 230, p. 116 145, 2021. DOI: [10.1016/j.ces.2020.116145](https://doi.org/10.1016/j.ces.2020.116145).
- [3] A. Brucks, T. Arndt, J. M. Ottino, and R. M. Lueptow, Behavior of flowing granular materials under variable  $g$ , *Physical Review E*, vol. 75, p. 032 301, 3 2007. DOI: [10.1103/PhysRevE.75.032301](https://doi.org/10.1103/PhysRevE.75.032301).
- [4] Á. Ruiz, M. Alvarado, N. M. Pinyol, and B. Caicedo, Wetting collapse and failure of and slope tested in centrifuge machine, in *First JTCl Workshop on Advances in Landslide Understanding*, (Barcelona, Spain, 24-26 May 2017), E. Alonso and N. Pinyol, Eds., International Centre for Numerical Methods in Engineering (CIMNE), 2017, pp. 122–125. [Online]. Available: <http://hdl.handle.net/2117/112476>.
- [5] N. M. Pinyol and M. Alvarado, Novel analysis for large strains based on particle image velocimetry, *Canadian Geotechnical Journal*, vol. 54, no. 7, pp. 933–944, 2017. DOI: [10.1139/cgj-2016-0327](https://doi.org/10.1139/cgj-2016-0327).

## Appendix A

### **SPANISH PATENT ES2695451B2: *DISPOSITIVO PARA ENSAYO DE COLAPSO DE UNA COLUMNA DE MATERIAL PULVERULENTO O GRANULAR***

---

Reproduced from: Técnicas Mecánicas Ilerdenses, S.L., *Dispositivo para ensayo de colapso de una columna de material pulverulento o granular*, inventors: J. Torres Serra, X. Arderiu Cabau, J.M. Padullés Ribalta, J. Caba Muntada, J.J. González Toledano, E.E. Romero Morales, A. Rodríguez Ferran, Spanish Patent ES2695451B2, 2019. [Online]. Available: <https://patentscope.wipo.int/search/en/detail.jsf?docId=ES235596513>

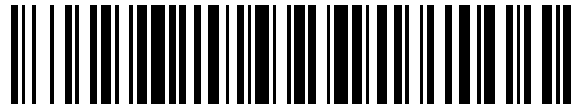




19

OFICINA ESPAÑOLA DE  
PATENTES Y MARCAS

ESPAÑA

11 Número de publicación: **2 695 451**

21 Número de solicitud: 201730862

51 Int. Cl.:

**G01N 11/02** (2006.01)

12

PATENTE DE INVENCION CON EXAMEN

B2

22 Fecha de presentación:

**29.06.2017**

43 Fecha de publicación de la solicitud:

**04.01.2019**

Fecha de modificación de las reivindicaciones:

**29.07.2019**

Fecha de concesión:

**10.10.2019**

45 Fecha de publicación de la concesión:

**17.10.2019**

73 Titular/es:

**TECNICAS MECANICAS ILERDENSES, S.L.**  
**(100.0%)****Pol. Ind. Camí dels Frares, C/ Alcarràs, Parcela 66**  
**25190 LLEIDA (Lleida) ES**

72 Inventor/es:

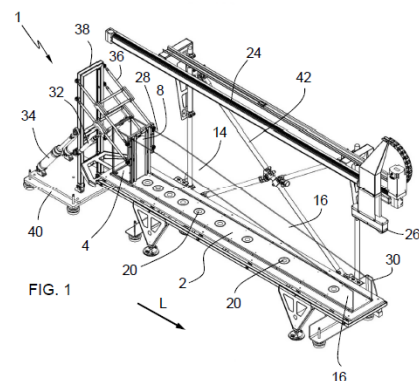
**TORRES SERRA, Joel;**  
**ARDERIU CABAU, Xavier;**  
**PADULLÉS RIBALTA, José Manuel;**  
**CABA MUNTADA, Joan;**  
**GONZÁLEZ TOLEDANO, Juan José;**  
**ROMERO MORALES, Enrique Edgar y**  
**RODRÍGUEZ FERRAN, Antonio**

74 Agente/Representante:

**CURELL AGUILÁ, Mireia**54 Título: **DISPOSITIVO PARA ENSAYO DE COLAPSO DE UNA COLUMNA DE MATERIAL PULVERULENTO O GRANULAR**

57 Resumen:

Dispositivo (1) para ensayo de colapso de una columna de material pulverulento o granular que comprende: una superficie de esparcido (2) plana sobre la que, al colapsar la columna, se esparce el material granular y comprendiendo la superficie de esparcido (2) una zona de formación (4) de columna, y un contenedor (6) para formar la columna sobre la zona de formación (4) de la superficie de esparcido (2). El dispositivo se caracteriza porque el contenedor (6) comprende por lo menos una pared lateral móvil (8) entre una posición de contención y una posición abierta y además porque tiene unos medios de compactación (10) para compactar el material granular de la columna previamente a que la pared lateral móvil (8) adopte la posición abierta.



ES 2 695 451 B2

Aviso: Se puede realizar consulta prevista por el art. 41 LP 24/2015.  
Dentro de los seis meses siguientes a la publicación de la concesión en el Boletín Oficial de la Propiedad Industrial cualquier persona podrá oponerse a la concesión. La oposición deberá dirigirse a la OEPM en escrito motivado y previo pago de la tasa correspondiente (art. 43 LP 24/2015).

## ES 2 695 451 B2

### DESCRIPCIÓN

#### Campo de la invención

5 La invención se refiere a un dispositivo para ensayo de colapso de una columna de material pulverulento o granular según el preámbulo de la reivindicación 1.

En la invención, el concepto de material granular se utiliza indistintamente para referirse tanto a materiales en forma de gránulos, como a materiales pulverulentos con un tamaño de partícula no identificable a ojo desnudo. Más en particular, un material granular según la  
10 invención se refiere a un material de dimensiones inferiores a 25 mm. Ejemplos de materiales granulares según la invención y descritos en la técnica son por ejemplo:

- a) Pellets de biomasa o madera de 22,6 mm, 16,1 mm o 12,6 mm.
- b) Semillas y Granos de 10 y 16 mm o de 12 y 18 mm.

Mientras que los materiales pulverulentos según la invención son del orden de magnitud de  
15 micrómetros.

#### Estado de la técnica

En la industria de la manipulación de materiales a granel, son conocidas las máquinas para ensacar y transportar materiales pulverulentos o granulares. Estos equipos pueden dosificar  
20 materiales granulares, por ejemplo, mediante sistemas alimentadores gravimétricos alimentados a partir de una tolva aguas arriba en la máquina.

La correcta selección del alimentador es crucial para lograr una buena dosificación del material. Entre las distintas soluciones de alimentación, son conocidas las siguientes:

- a) Alimentación por descarga libre, a través de alimentadores por gravedad o por  
25 válvula rotativa,
- b) Alimentación por desplazamiento positivo, por correa, por tornillo sinfín o por bandeja vibratoria, o
- c) Alimentación neumática, utilizando cámaras de fluidificación.

El rendimiento de las instalaciones de manipulación depende en gran medida de esta etapa  
30 de alimentación. A su vez, esta etapa está fuertemente condicionada por las características

## ES 2 695 451 B2

del material granular que se debe alimentar. En particular el flujo de material granular en seco, es decisivo. Una mala elección del alimentador necesario para el material que se debe dosificar, puede conducir a paros en la instalación debidos a acumulaciones no deseadas de material que taponan la salida del alimentador.

- 5 Por ello, las propiedades físicas de los materiales son de especial relevancia a la hora de decidir el equipo idóneo de manipulación del material granular a granel. En este contexto, se constata una falta de estandarización a la hora de caracterizar el material, por ejemplo, en cuanto a su fluidificación.

10 El documento *Continuum viscoplastic simulation of a granular column collapse on large slopes*, Physics of Fluids, American Institute of Physics, 2017, 29, 19/11/2016, Vol. 29 de NATHAN MARTIN et al., divulga la simulación de los flujos granulares secos resultantes del colapso de las columnas granulares en un canal inclinado (hasta 22°) y compara los resultados con los experimentos de laboratorio.

#### Sumario de la invención

- 15 La invención tiene como finalidad proporcionar un dispositivo para ensayo de colapso de una columna de material granular del tipo indicado al principio, que permita caracterizar la capacidad de fluencia del material de forma sencilla y precisa. Gracias a ello, por ejemplo, en el ámbito de las máquinas de manipulación de materiales granulares a granel, se puede elegir con mayores garantías la maquinaria óptima de manipulación del material.
- 20 Esta finalidad se consigue mediante un dispositivo para ensayo de colapso de una columna de material granular del tipo indicado al principio, caracterizado por la parte caracterizadora de la reivindicación 1.

25 Dentro del contexto de la invención los medios de compactación son unos medios que permiten modificar el grado de compactación del material granular para simular distintas situaciones de partida. Medios de compactación preferentes según la invención son, por ejemplo, un émbolo superior adaptado a la sección transversal del contenedor, accionado neumáticamente o por gravedad, un dispositivo de aspiración dispuesto en la parte inferior del contenedor o un dispositivo de soplado dispuesto por la parte superior del contenedor, así como una pluralidad de pesos que ejerzan la fuerza por gravedad.

- 30 Los medios de compactación permiten obtener dos estados de compactación iniciales de la columna de material granular antes de que la pared lateral del contenedor pase de la posición de contención a la posición abierta y empiece el ensayo de colapso, a saber:

## ES 2 695 451 B2

a) Compactación aleatoria, obtenida cuando la pared lateral del contenedor se encuentra en posición de contención y simplemente se vierte el material granular en el interior del contenedor por gravedad, y

5 b) Compactación densa, obtenida cuando la pared lateral del contenedor se encuentra en posición de contención y después de verter el material granular en el contenedor, se compacta la columna de material granular con los medios de compactación.

Con los medios de compactación, se pueden crear situaciones de partida de la columna muy distintas. Al mover la pared lateral del contenedor de la posición de contención a la posición  
10 abierta de la pared lateral, el comportamiento de la columna de material granular es distinto. Así, se puede determinar el comportamiento del colapso de la columna de material granular de forma mucho más precisa. En consecuencia, se simplifica notablemente la correcta elección de la forma óptima de alimentar el material granular en un procedimiento de manipulación del mismo.

15 Además, la invención abarca una serie de características preferentes que son objeto de las reivindicaciones dependientes y cuya utilidad se pondrá de relieve más adelante en la descripción detallada de una forma de realización de la invención.

En una forma de realización preferente que persigue minimizar el efecto de la fricción durante el colapso de la columna de material granular, la superficie de esparcido es una  
20 superficie metálica pulida. Metales adecuados para este tipo de superficies son, por ejemplo, aluminio anodizado.

En una forma de realización del dispositivo dichos medios de compactación son unos medios de accionamiento por gas, estando dichos medios de accionamiento por gas dispuestos en la parte inferior de dicho contenedor para aspirar el aire contenido de dicha  
25 columna de material granular. La aspiración es especialmente efectiva para la compactación de materiales pulverulentos. Medios de accionamiento por gas pueden ser, por ejemplo, un compresor o bien un cilindro neumático. La boca de aspiración de los medios de accionamiento por gas está oportunamente cubierta para evitar la entrada de producto granular en el sistema de aspiración.

30 En otra forma de realización que tiene por objetivo compactar mejor la columna de material granular e incrementar la variedad de estados de compactación de una forma sencilla, dichos medios de accionamiento por gas están dispuestos en dicha zona de formación de columna de dicha superficie de esparcido, distribuidos de manera uniforme y dichos medios

## ES 2 695 451 B2

de accionamiento por gas funcionan de manera reversible aspirando o insuflando gas en dicha columna de material granular para modificar el estado de compactación del material granular en dicha columna. En este caso, los medios de accionamiento por gas combinan un compresor con una bomba de vacío, o el cilindro neumático de doble efecto.

- 5 En primer lugar, la disposición inferior de los medios de accionamiento por gas evita la disposición de elementos en la parte superior del contenedor, con lo que se libera espacio útil, para facilitar el manejo del dispositivo, ya que se facilita el llenado del contenedor. Por otra parte, con una distribución uniforme de los medios de accionamiento por gas en esta parte inferior del contenedor, se puede aspirar o insuflar aire de manera que se obtienen
- 10 condiciones más homogéneas en toda la columna. Finalmente, la posibilidad de insuflar aire, proporciona un nuevo estado de compactación siguiente:

- a) Compactación suelta, es la que se obtiene cuando la pared lateral del contenedor se encuentra en posición de contención y después de verter el material granular en el contenedor, se insufla aire en la columna de material granular.

- 15 Adicionalmente, la posibilidad de insuflar proporciona la ventaja adicional de que si se desea se pueden modificar las condiciones de humedad de la columna, en caso de insuflar aire húmedo.

En otra forma de realización preferente entre dichos medios de accionamiento por gas y dicho contenedor están previstos unos medios de filtro dimensionados al tamaño inferior de

20 gránulo del material granular. Gracias a ello, se evita el paso de material granular hacia el circuito neumático que acciona los medios de accionamiento por gas. Preferentemente, dichos medios de filtro es una lámina de fieltro tupida fabricada a partir de poliéster agujado. Alternativamente, los medios de filtro son una lámina geo-textil o una malla metálica de luz conocida e inferior al gránulo cuyo comportamiento se desea ensayar. De forma

25 especialmente preferente, dichos medios de filtro son amovibles. Así, el dispositivo comprende un juego de medios de filtro que se pueden remplazar en función del material a ensayar. En otra forma de realización preferente, que tiene por objeto obtener condiciones de colapso más homogéneas y repetibles, el dispositivo comprende un canal de esparcido con unas paredes laterales, extendiéndose la longitud de dicho canal de esparcido en una

30 dirección longitudinal de esparcido y extendiéndose la anchura de dicho canal de esparcido en una dirección perpendicular a dicha dirección longitudinal de esparcido, siendo dicha longitud mayor que dicha anchura y dicho contenedor está integrado en dicho canal de esparcido, siendo dicha pared lateral móvil una compuerta practicable para permitir que dicha columna de material granular se esparza en dicha dirección longitudinal de esparcido.

## ES 2 695 451 B2

Una disposición de este tipo en forma de canal de esparcido proporciona condiciones prácticamente bidimensionales permitiendo una mejor inspección de los campos de velocidad del material a granel en las paredes laterales y mejora apreciación de la morfología y distribución de cargas finales.

- 5 De forma especialmente preferente, la relación entre la longitud y el ancho del canal de esparcido está comprendida en el rango de 5:1 a 20:1 y más preferentemente de 10:1 a 15:1, con lo cual se obtienen unas proporciones de canal óptimas en cuanto a la poca perturbación del colapso y un buen comportamiento bidimensional.

Otro objetivo de la invención es el de facilitar la caracterización morfológica y cinemática instantánea del colapso. Para ello, preferentemente, dichas paredes laterales de dicho canal son transparentes y dicho dispositivo comprende unos medios de adquisición de imagen dispuestos lateralmente a dicho canal, en dirección transversal a dicha dirección longitudinal de esparcido. Los medios de adquisición de imagen pueden ser tales como una cámara fotográfica, una cámara de video convencional o de alta velocidad, una cámara de infrarrojos, un sistema de radar o similares.

Otro de los problemas que se plantea la invención es lograr que el contenedor afecte lo mínimo posible al proceso de colapso de la columna de material granular. Para ello, en una forma de realización preferente, dicho contenedor está integrado en dicho canal de esparcido, siendo dicha pared lateral móvil una compuerta basculante en la dirección de alejamiento de dicha columna de material granular para permitir que dicha columna de material granular se esparza en dicha dirección longitudinal de esparcido. Gracias al movimiento basculante de la compuerta cuando la pared lateral pasa de la posición de contención a la posición abierta, lo hace sin fricción alguna sobre la columna de material granular. Con ello, la columna colapsa de forma libre. En cuanto al movimiento de basculación, éste se puede lograr, por ejemplo por rotación de la compuerta alrededor de un eje superior situado por encima del nivel de la columna de material granular. No obstante, alternativamente se puede lograr un solapamiento de movimientos en dos fases. En una primera fase se lleva a cabo una separación prácticamente horizontal de la superficie vertical libre de la columna de material granular, que permite el arranque del colapso. Luego, en una segunda fase, la compuerta se retira lentamente del contenedor fuera del canal para liberar espacio vertical y que el colapso pueda tener lugar sin que la compuerta influya en el comportamiento del material granular al colapsar.

Alternativamente, el contenedor puede ser un cilindro abierto por la base, provisto de unos medios de accionamiento vertical para separar el contenedor de la superficie de esparcido

## ES 2 695 451 B2

durante el ensayo. Otras alternativas para el contenedor serían un semicilindro cerrado verticalmente por una cara vertical plana, lo cual facilita la inspección de la columna.

En otra forma de realización del dispositivo según la invención el dispositivo comprende una pluralidad de sensores de carga dispuesta en dicha superficie de esparcido, y los sensores  
5 de dicha pluralidad de sensores de carga están alineados sobre una recta con una separación entre sensores creciente con la distancia de dicha columna de material granular. Gracias a ello, es posible determinar la evolución de las tensiones en el material a granel durante el colapso de la columna de material granular, ya que los sensores son capaces de registrar distribuciones dinámicas de carga.

10 En otra forma de realización que tiene por objetivo minimizar el número de sensores necesarios para obtener una distribución fiable de las cargas dinámicas durante el colapso, el dispositivo dicha separación entre sensores crece de manera logarítmica en la dirección de alejamiento de la columna, a lo largo de la superficie de esparcido. De forma especialmente preferente, la separación se incrementa a lo largo del canal en la dirección  
15 longitudinal del canal en el sentido de avance del material granular durante el colapso.

En otra forma de realización destinada a la obtención de mapas de la configuración morfológica final del esparcimiento de dicha columna de material granular, dicho dispositivo comprende una guía lineal dispuesta por encima de dicho canal en dicha dirección longitudinal de esparcido que se extiende por lo menos en toda la longitud de dicho canal, y  
20 en dicha guía lineal está montado un escáner láser móvil a lo largo de toda dicha guía lineal, orientado hacia dicho canal.

Asimismo, la invención también abarca otras características de detalle ilustradas en la descripción detallada de una forma de realización de la invención y en las figuras que la acompañan.

25

#### Descripción de los dibujos

Otras ventajas y características de la invención se aprecian a partir de la siguiente descripción, en la que, sin ningún carácter limitativo, se relata una forma preferente de realización de la invención, haciendo mención de los dibujos que se acompañan. Las figuras  
30 muestran:

Fig. 1, una vista esquemática en perspectiva de un primer dispositivo para ensayo de colapso de una columna de material granular según la invención.

## ES 2 695 451 B2

Fig. 2, una vista frontal del dispositivo para ensayo de colapso de una columna de material granular de la figura 1.

Fig. 3, una vista lateral del dispositivo para ensayo de colapso de una columna de material granular de la figura 1.

5 Fig. 4, una vista cortada a lo largo del plano IV-IV de la figura 2, del dispositivo de ensayo para ensayo de colapso de una columna de material granular.

Fig. 5, una vista lateral esquemática, cortada y ampliada de la zona del contenedor y los medios de compactación.

10 Fig. 6, una vista lateral esquemática del ensayo de colapso de una columna de material granular con la pared lateral móvil en posición de contención.

Fig. 7, una vista lateral esquemática del ensayo de colapso de una columna de material granular con la pared lateral móvil en posición abierta y con el material granular esparcido sobre la superficie de esparcido.

### 15 Descripción detallada de una forma de realización de la invención

En las figuras 1 a 5 se muestra una forma de realización del dispositivo 1 para ensayo de colapso de una columna de material granular según la invención, el cual se explica de forma esquemática en las figuras 6 y 7.

20 El dispositivo 1 según la invención presenta en primer lugar una superficie de esparcido 2 plana sobre la que al realizar el ensayo de colapso de la columna de material granular, se esparce material. Esta superficie de esparcido 2 es una superficie lisa para que el material granular pueda esparcirse con una influencia mínima de la rugosidad de la superficie y que por consiguiente, pueda esparcirse de forma homogénea y regular. También, de forma especialmente preferente, la superficie de esparcido puede ser una superficie lisa pulida. En  
25 la forma de realización mostrada, la superficie de esparcido es una placa longitudinal de aluminio anodizado.

La superficie de esparcido 2 presenta también una zona de formación 4 de columna de material granular. La columna se forma mediante un contenedor 6 colocado sobre esta zona de formación 4. Existen múltiples variantes posibles de contenedor 6 y de la superficie de  
30 esparcido 2. Por ejemplo, si se desea ensayar un colapso radial, el contenedor puede ser un cilindro, un paralelepípedo o un prisma, abierto por la base inferior y colocado sobre la zona de formación 4 de una superficie de esparcido configurada para permitir un esparcido



## ES 2 695 451 B2

circular en sentido radial. Para ello, el contenedor tiene asociado un accionador que lo eleva de rápidamente. Este movimiento provoca el colapso de la columna de material granular en sentido radial a la columna.

Por otra parte, en la forma de realización preferente de las figuras, la superficie de esparcido 2 está formada en la base de un canal 14 de esparcido delimitado por unas paredes laterales 16 transparentes. La longitud del canal 14 de esparcido se extiende en una dirección longitudinal L de esparcido, mientras que la anchura del canal 14 de esparcido se extiende en una dirección perpendicular N a la dirección longitudinal L de esparcido.

En las figuras se aprecia que la longitud del canal 14 es mayor que la anchura. Con ello, se obtiene una distribución cuasi-bidimensional de material granular. Esto facilita la determinación de los campos de velocidad del material granular a lo largo de las paredes laterales 16, así como de la morfología longitudinal del material y la distribución de cargas durante el colapso de la columna de material granular. En esta forma de realización, el canal 14 presenta una longitud de 2000 mm y una anchura de 160 mm. A su vez, las paredes laterales 16 del canal 14 de esparcido presentan una altura de 350 mm en su punto más alto 28 al inicio del canal, hasta 150 mm en su punto más bajo 30, al final de canal 14. De forma especialmente preferente, las proporciones entre la longitud y el ancho del canal 14 se seleccionan de manera que por lo menos den cabida a 10 gránulos de material granular en la anchura del canal 14.

En dirección perpendicular N a la dirección longitudinal L de esparcido están montados unos medios de adquisición de imagen 18, dispuestos lateralmente al canal 14 de esparcido. En este caso, se utiliza una cámara de vídeo de alta velocidad, como el modelo PXW-FS5 de SONY Corporation Japan. Mediante sistemas de grabación en vídeo de alta velocidad y técnicas de post-procesado de imagen, tal como la velocimetría de imagen de partículas, se pueden obtener los citados campos de velocidad en las paredes laterales 16 o la distribución de cargas durante el colapso de la columna de material granular.

En esta forma de realización, el contenedor 6 que permite formar la columna de material granular está integrado en el canal 14 de esparcido. Este presenta una de las paredes laterales a modo de pared lateral móvil 8. Esta pared lateral móvil 8 se puede mover entre una posición de contención, mostrada en las figuras 1 a 6, y una posición abierta, mostrada en la figura 7 que permite la caída y el colapso de la columna de material granular. La pared lateral móvil 8 del contenedor 6 es una compuerta frontal basculante en la dirección de alejamiento de la columna de material granular. Este movimiento permite que el material se esparza en la dirección longitudinal L de esparcido.

## ES 2 695 451 B2

- Por otra parte, para resolver el problema de caracterización de la capacidad de fluencia del material de forma sencilla y precisa, el dispositivo 1 además comprende unos medios de compactación 10 que permiten compactar el material granular de la columna previamente a que la pared lateral móvil 8 adopte la posición abierta. Los medios de compactación 10 en este caso, son preferentemente unos medios de accionamiento por gas 12, tales como un cilindro neumático de doble efecto con el correspondiente circuito neumático. Alternativamente se puede utilizar un conjunto compresor / bomba de vacío y el flujo de aire generado se trata con: reductor / manómetro, secador de aire, caudalímetro y un presostato colocado en el colector de los medios de accionamiento por gas.
- 5
- 10 Los medios de accionamiento están dispuestos en la parte inferior del contenedor 6, y más en particular en la zona de formación 4, para aspirar el aire contenido de la columna de material granular. Para conseguir unas condiciones de partida óptimas de compactación de la columna, los medios de accionamiento por gas 12 están distribuidos de manera homogénea. Además, en esta forma de realización preferente, los medios de accionamiento
- 15 por gas 12 funcionan de manera reversible aspirando o insuflando aire de la columna de material granular formada en el contenedor 6. De esta forma se puede modificar el estado de compactación del material granular en la columna. Además, entre los medios de accionamiento por gas 12 y el contenedor 6 están previstos unos medios de filtro 44 dimensionados al tamaño inferior de gránulo del material granular que se desea ensayar.
- 20 El movimiento de basculación de la pared lateral móvil 8 de esta forma de realización se logra mediante dos parejas de cilindros neumáticos. Una primera pareja de cilindros neumáticos 32 está conectada a dos parejas de barras 36 articuladas en un primer soporte 38 articulado en una base 40. El accionamiento con los cilindros produce una separación rápida en el sentido de alejamiento de la columna de material granular, lo cual arranca el
- 25 proceso de colapso de la misma. Luego, una segunda pareja de cilindros neumáticos 34, montada entre la base 40 y el primer soporte 38, retira lentamente la compuerta fuera del canal 14 de esparcido para liberar espacio vertical y no afectar al desarrollo del ensayo de colapso.
- En las figuras, se aprecia también que el dispositivo 1 comprende una pluralidad de
- 30 sensores de carga 20 dispuesta en la superficie de esparcido 2 para registrar distribuciones de carga dinámicas y con ello monitorizar la evolución de las tensiones del material a granel en el canal 14. Para ello, los sensores de carga 20 están alineados sobre una recta 22 con una separación entre sensores creciente con la distancia de dicha columna de material granular, y más en particular la separación entre sensores crece de manera logarítmica. Por

## ES 2 695 451 B2

ejemplo, sensores adecuados para esta función son el modelo 104 de la empresa Utilcell. Unas membranas de silicona moldeadas y colocadas en el canal 14 sufren unas deformaciones elásticas que transmiten las fuerzas de reacción dinámicas a los sensores de carga 20.

- 5 Finalmente, el dispositivo 1 comprende una guía lineal 24 dispuesta en un segundo soporte 42 por encima del canal 14 dispuesta en la dirección longitudinal L de esparcido. La guía lineal 24 se extiende en toda la longitud del canal 14 de esparcido. De esta forma sobre la guía lineal 24 está montado un escáner láser 26 móvil a lo largo de toda la guía lineal 24 gracias a un motor de accionamiento y orientado hacia el canal 14 de esparcido.
- 10 ejemplo un escáner adecuado es el escáner 2D/3D Gocator 2150 de la empresa LMI Technologies Inc. Gracias al movimiento del escáner se puede estudiar la morfología del colapso de la columna, y extraer parámetros tales como el ángulo de reposo del material a granel al final del colapso de la columna.

- De esta manera, el dispositivo 1 según la invención permite caracterizar de forma más precisa y fiable la capacidad de fluencia de materiales de tipo granular o pulverulento.
- 15 otras aplicaciones, esto permite optimizar la elección de los dispositivos dosificadores del material en instalaciones de manipulación de material granular, tales como las instalaciones de ensacado.

## ES 2 695 451 B2

### REIVINDICACIONES

1.- Dispositivo (1) para ensayo de colapso de una columna de material pulverulento o  
5 granular que comprende:

[a] una superficie de esparcido (2) plana sobre la que, al colapsar dicha columna, se  
esparce dicho material granular y comprendiendo dicha superficie de esparcido (2)  
una zona de formación (4) de columna, y

[b] un contenedor (6) para formar dicha columna sobre dicha zona de formación (4)  
10 de dicha superficie de esparcido (2),

[c] comprendiendo dicho contenedor (6) por lo menos una pared lateral móvil (8)  
entre

[i] una posición de contención y

[ii] una posición abierta,

15 **caracterizado por que** dicho dispositivo (1) además comprende

[d] unos medios de compactación (10) para compactar el material granular de dicha  
columna previamente a que dicha pared lateral móvil (8) adopte dicha posición  
abierta,

[e] un canal (14) de esparcido con unas paredes laterales (16), extendiéndose la  
20 longitud de dicho canal (14) de esparcido en una dirección longitudinal (L) de  
esparcido y extendiéndose la anchura de dicho canal (14) de esparcido en una  
dirección perpendicular (N) a dicha dirección longitudinal (L) de esparcido, siendo  
dicha longitud mayor que dicha anchura, y por que

[f] dicho contenedor (6) está integrado en dicho canal (14) de esparcido, siendo dicha  
25 pared lateral móvil (8) una compuerta basculante en la dirección de alejamiento de  
dicha columna de material granular para permitir que dicha columna de material  
granular se esparza en dicha dirección longitudinal (L) de esparcido.

2.- Dispositivo (1) según la reivindicación 1, **caracterizado por que** dichos medios de  
compactación (10) son unos medios de accionamiento por gas (12), estando dichos medios  
30 de accionamiento por gas (12) dispuestos en la parte inferior de dicho contenedor (6) para  
aspirar el aire contenido de dicha columna de material granular.

## ES 2 695 451 B2

- 3.- Dispositivo (1) según la reivindicación 2, **caracterizado por que** dichos medios de accionamiento por gas (12) están dispuestos en dicha zona de formación (4) de columna de dicha superficie de esparcido (2), distribuidos de manera homogénea y por que dichos medios de accionamiento por gas (12) funcionan de manera reversible aspirando o  
5 insuflando gas en dicha columna de material granular para modificar el estado de compactación del material granular en dicha columna.
4. Dispositivo (1) según las reivindicación 2 o 3, **caracterizado por que** entre dichos medios de accionamiento por gas (12) y dicho contenedor (6) están previstos unos medios de filtro (44) dimensionados al tamaño inferior de gránulo del material granular que se desea  
10 ensayar.
- 5.- Dispositivo (1) según cualquiera de las reivindicaciones 1 a 4, **caracterizado por que** dichas paredes laterales (16) de dicho canal (14) de esparcido son transparentes y dicho dispositivo (1) comprende unos medios de adquisición de imagen (18) dispuestos  
15 lateralmente a dicho canal (14) de esparcido, en dirección perpendicular (N) a dicha dirección longitudinal (L) de esparcido.
- 6.- Dispositivo (1) según cualquiera de las reivindicaciones 1 a 5, **caracterizado por que** comprende una pluralidad de sensores de carga (20) dispuesta en dicha superficie de  
20 esparcido (2), y por que los sensores de dicha pluralidad de sensores de carga (20) están alineados sobre una recta (22) con una separación entre sensores creciente con la distancia de dicha columna de material granular.
- 7.- Dispositivo (1) según la reivindicación 6, **caracterizado por que** dicha separación entre sensores crece de manera logarítmica en la dirección de alejamiento de dicha columna.
- 25 8.- Dispositivo (1) según cualquiera de las reivindicaciones 1 a 7, **caracterizado por que** comprende una guía lineal (24) dispuesta por encima de dicho canal (14) de esparcido en dicha dirección longitudinal (L) de esparcido que se extiende por lo menos en toda la longitud de dicho canal (14) de esparcido, y por que en dicha guía lineal (24) está montado un escáner láser (26) móvil a lo largo de toda dicha guía lineal (24), orientado hacia dicho  
30 canal (14) de esparcido.

ES 2 695 451 B2

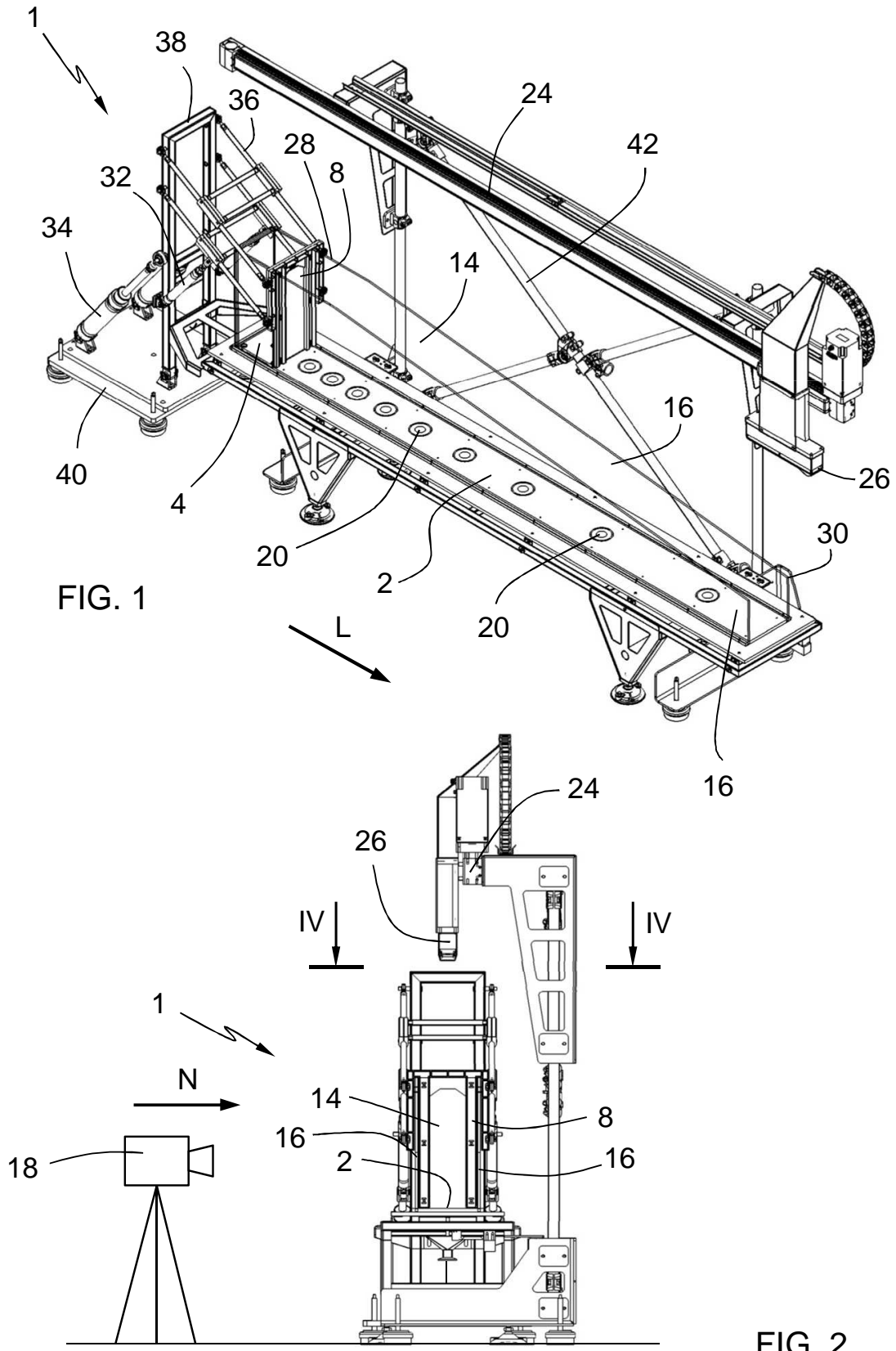


FIG. 1

FIG. 2

ES 2 695 451 B2

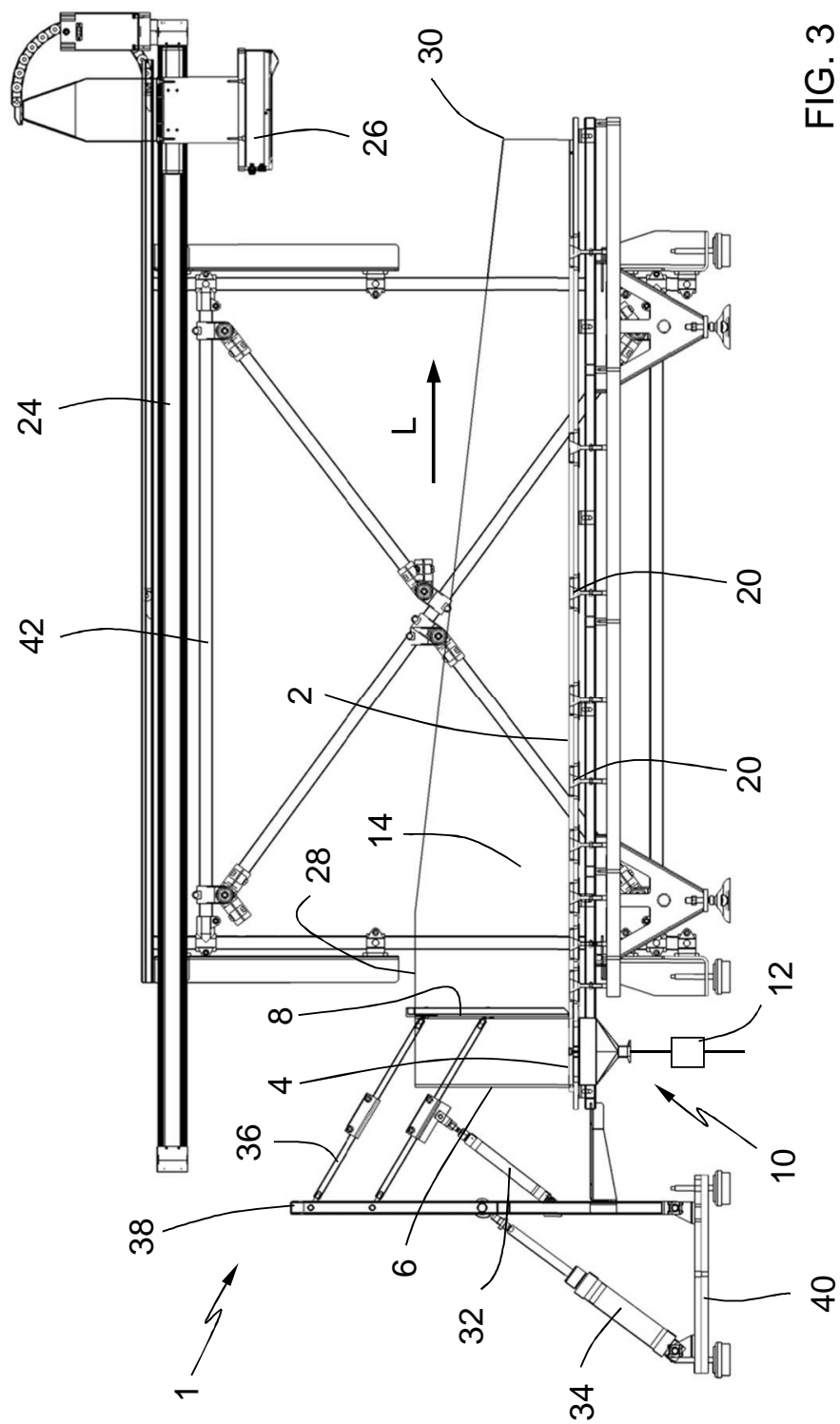


FIG. 3

ES 2 695 451 B2

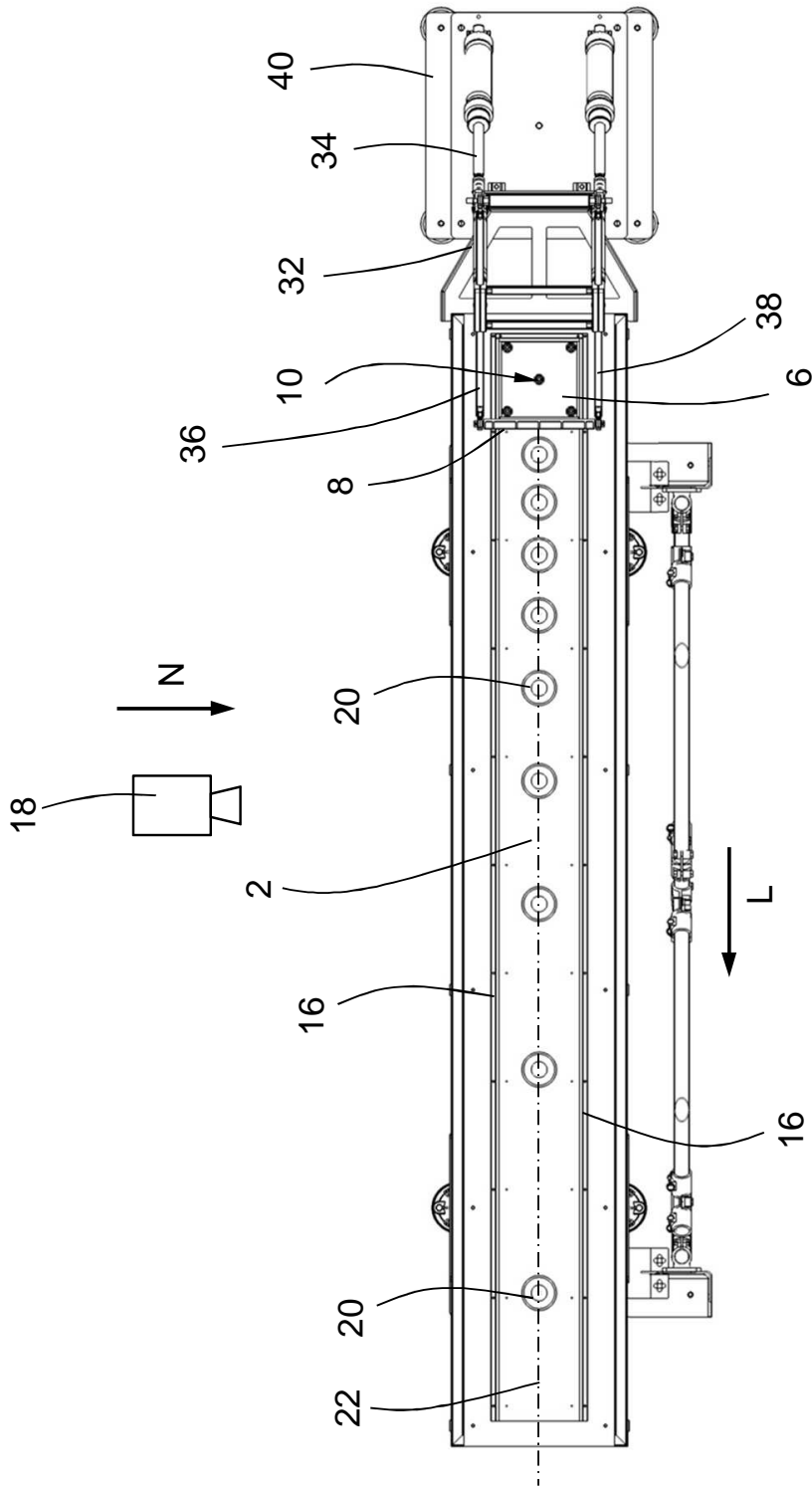


FIG. 4



ES 2 695 451 B2

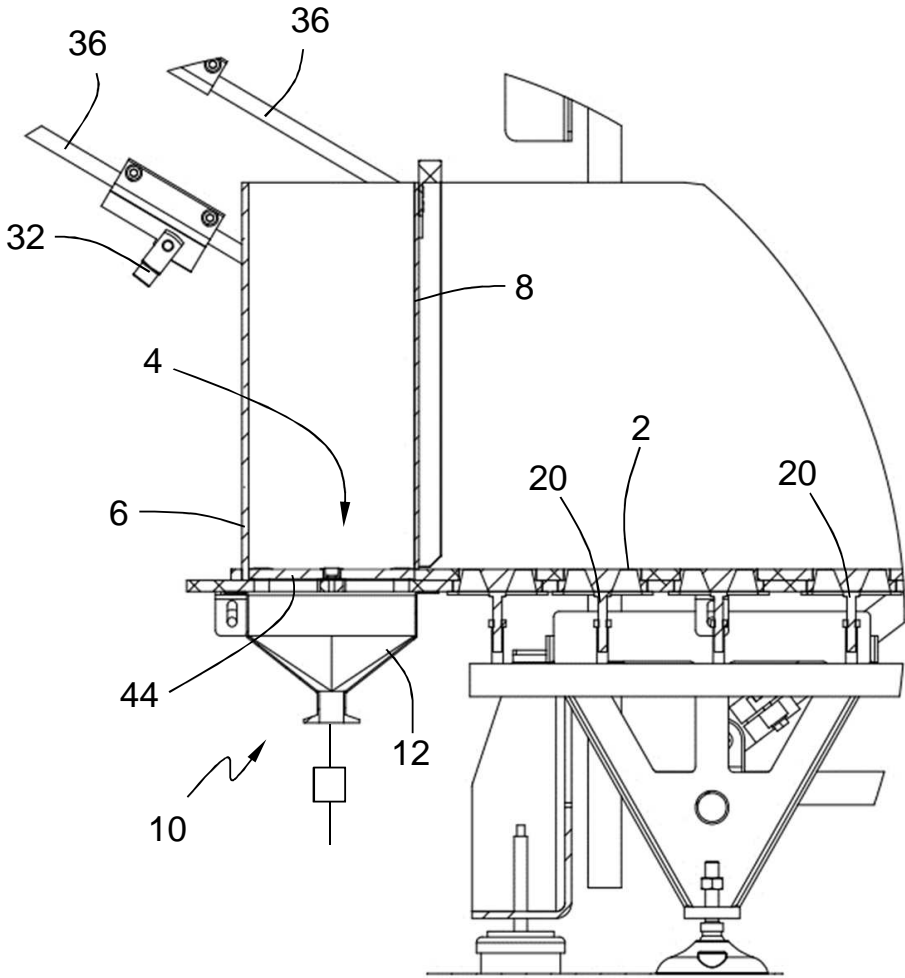
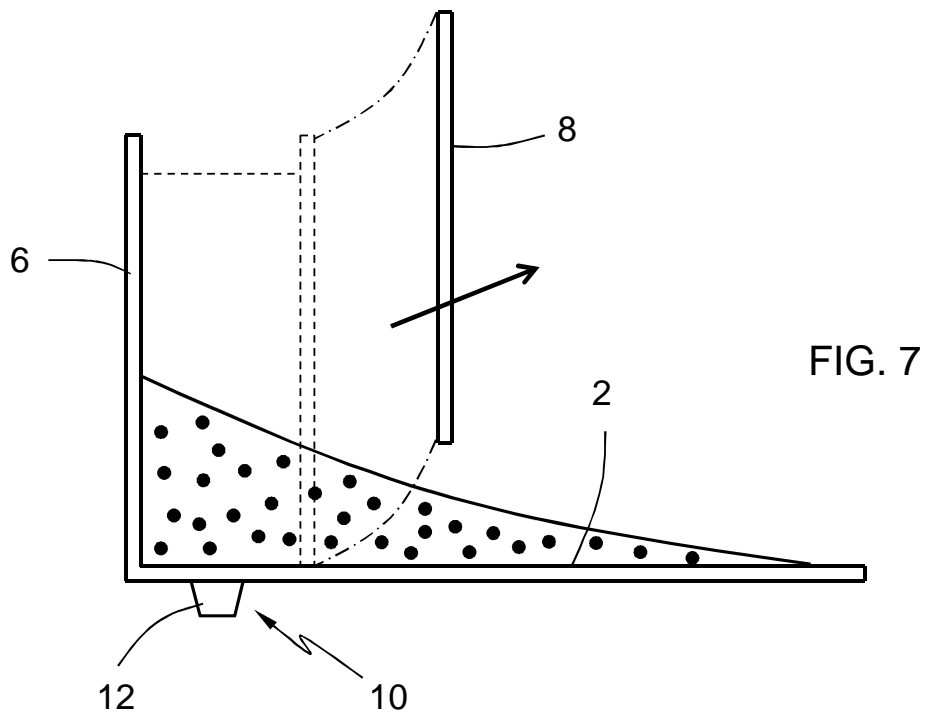
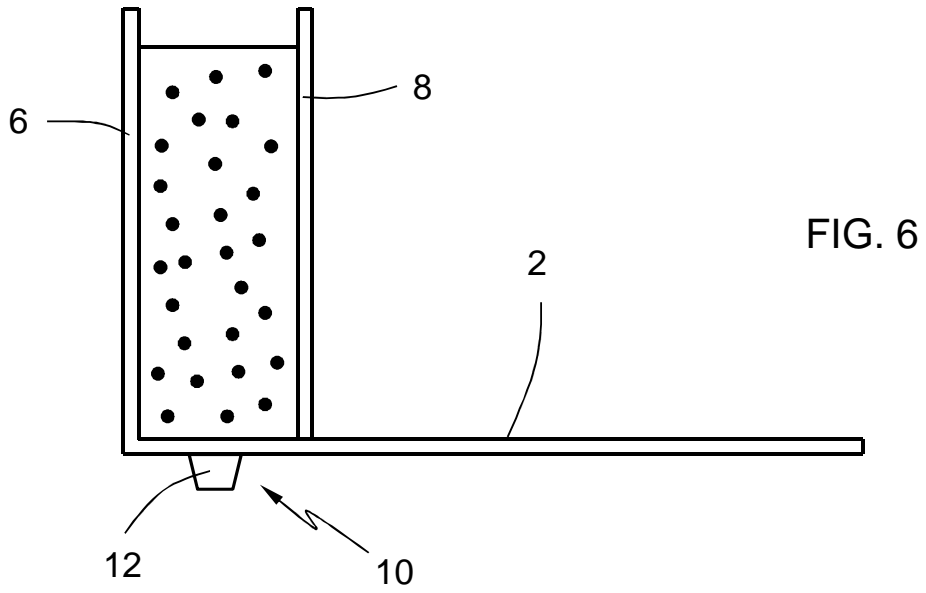


FIG. 5

ES 2 695 451 B2



# IMAGE ANALYSIS MANUAL: PIV ANALYSIS OF SUPERSLOW MOTION VIDEOS

---

In this Appendix, digital image processing for PIV analysis of granular flows is described. The accuracy of the proposed granular PIV approach is evaluated in [Section 3.8](#). Granular column collapse experiments are recorded with a high-speed video camera [1]. The produced MXF videos are pre-processed in the MATLAB environment [2] to obtain the video frames and image masks required for PIV analysis. In [Section B.1](#), the pre-processing steps are detailed as implemented in the `main` script calling a set of functions as well as external video [3] and image [4] editing software. The produced images are post-processed using the PIVlab tool [5], as detailed in [Section B.2](#), to derive the kinematic quantities of interest from each frame pair. Sections [B.3](#) and [B.4](#) respectively incorporate the utilised MATLAB and ImageJ scripts. The local function `external_mask_Callback`, included in the main function `PIVlab_GUI.m` of the PIVlab software, is modified to adapt background removal during granular flow propagation.

## B.1 Pre-process

1. Create a new subfolder structure using function `subfolder_structure`.
2. Extract all frames using FFmpeg and save the produced JPEG images to subfolder `1_input`:

```
| ffmpeg -i <video>.mxf -q:v 1 -ss <t0> -to <t1> ./1_input/input_%04d.jpg
```

3. Crop all frames using ImageJ and save the produced JPEG images to subfolder `2_crop`:
  - a) Determine the region of interest (ROI) on a reference frame, see [Figure B.1](#): Edit > Selection > Specify ...
  - b) Manually save the values for crop selection to file `imagej_settings.txt` (rows 0 to 3, units in pixels):

```
| <Width>  
| <Height>  
| <X coordinate>  
| <Y coordinate>
```

- c) Crop all frames in `1_input` using batch macro `BatchMacro_Crop`, see [Figure B.2](#): Process > Batch > Macro ...
4. Select frames for PIV analysis:

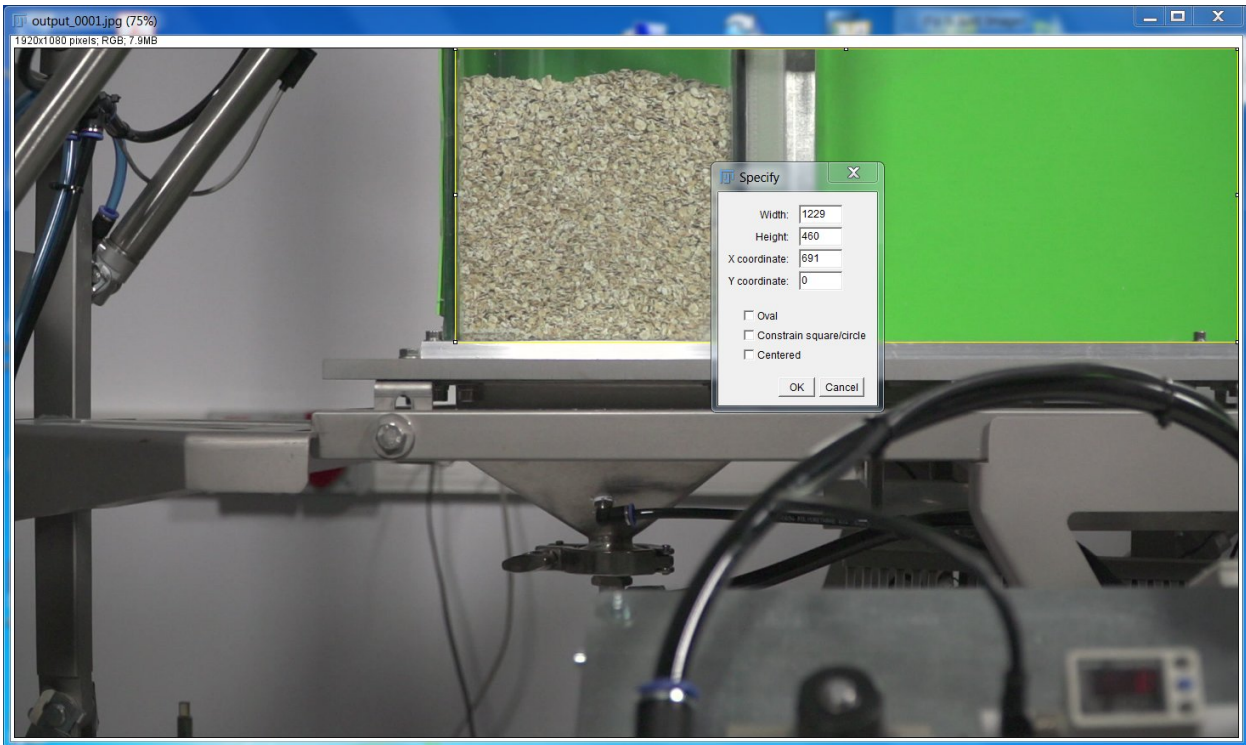


**Figure B.1** ROI selection extending over the reservoir and channel regions where granular flow is observed, from the initial column to the final deposit configurations.

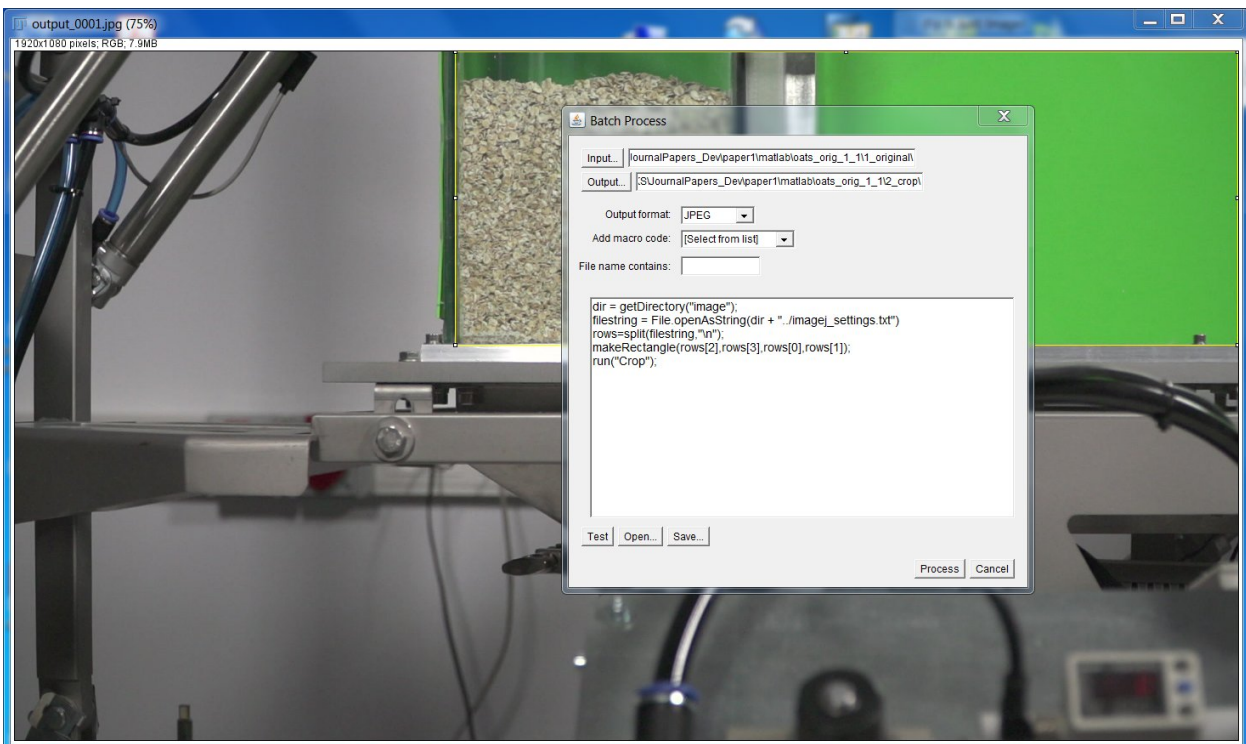


**Figure B.2** Batch process settings for ROI cropping of all extracted frames.

- a) Obtain MAT file with frame difference data, i.e. error measure between consecutive frame pairs, using function `find_first_last_data`.
  - b) Determine start and end frames using function `find_first_last_main` and save the selected frames and grayscale conversions respectively to subfolders `3_output` and `6_piv`.
5. Apply colour thresholding to the selected frames using ImageJ and save the produced PNG images to `4_threshold`:
- a) Determine threshold values in the HSB color space, see [Figure B.3](#): Image > Adjust > Color Threshold ...



**Figure B.3** Colour thresholding for uniform background (chroma key) exclusion.

- b) Manually save HSB range values to `imagej_settings.txt` (rows 4 to 9, ranging from 0 to 255):
 

```

      <min H>
      <max H>
      <min S>
      <max S>
      <min B>
      <max B>
      
```
  - c) Mask all frames in `3_output` using using batch macro `BatchMacro_ColorThreshold`, see [Figure B.4](#): Process > Batch > Macro ...
6. Manually detect objects to remove from the selected frames:
- a) Determine the ROI of all objects of interest on reference frame (with ImageJ) and save them as JPG images in parent folder, see [Figure B.5](#).
  - b) Obtain object pathlines from selected frames and MAT file with object masks along the pathlines using function `pattern_search`, performing 2D cross-correlation (`xcorr2`) enhanced with contrast-limited adaptive histogram equalization, as implemented in function `myclahe` [6].
7. Obtain the masked frames as separate TIF images using function `overlay_mask` and save the set of masks for PIV analysis in file `mask.tif` containing as many images as frame pairs to be analysed.

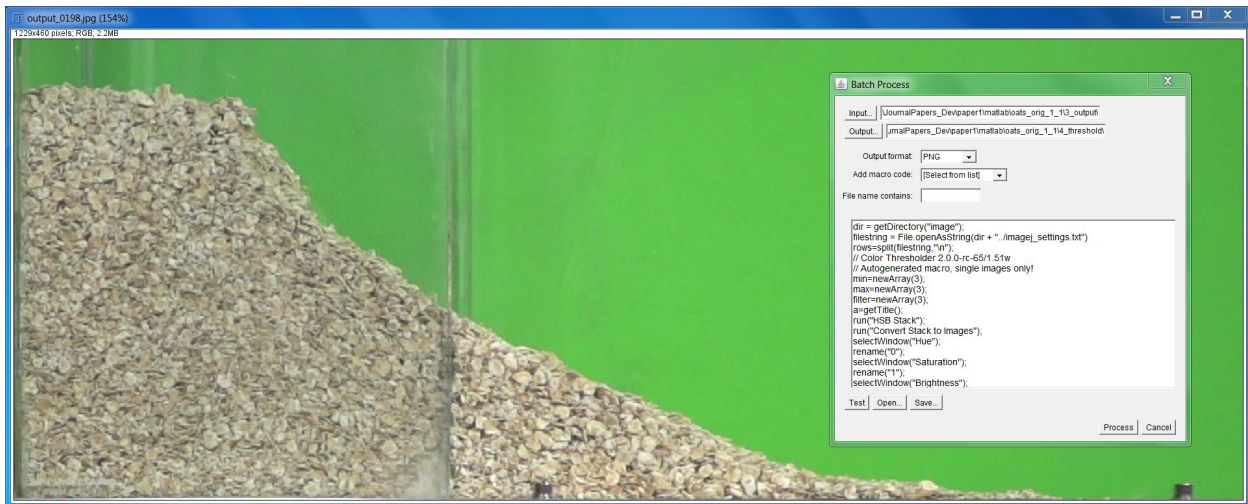


**Figure B.4** Batch process settings for masking selected frames.

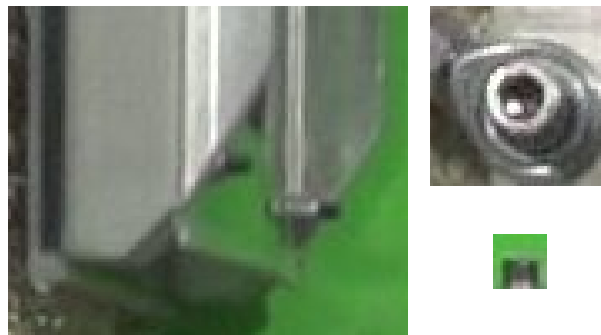


**Figure B.5** Object boundaries for the detection of the moving gate (left) and rod of the parallelogram mechanism (upper right), and the fixed-position bolt (lower right).

## B.2 Post-process

1. File > New session > Load images:
  - a)  Show all files in current directory
  - b)  Sequencing style: 1-2; 2-3; 3 ...
  - c) Select the pre-process output frames in subfolder 6\_piv > Add > Import
2. Load filemask.tif: Image settings > Exclusions (ROI, Mask) > Load external masks
3. Analysis > PIV settings:
  - a)  Pass 3
  - b) Interrogation area [px]:16
  - c) If low resolution or bad image texture, apply linear correlation using Correlation quality: High
4. Analysis > ANALYZE! > Analyze all frames
5. Calibration > Calibrate using current or external image:

- a) Manually set known Real distance [mm] or use reservoir length as reference distance:
    - i. Load calibration image (opt.)
    - ii. Select reservoir base length using Select reference distance
    - iii. Real distance [mm]: 150
  - b) time step [ms]: 5 (1/200 fps)
  - c) Apply calibration
6. Post processing > Vector validation:
- a)  display all frames in scatterplot
  - b) Select and refine ( $u, v$ ) points to discard outliers using Select velocity limits
  - c)  Standard deviation filter Threshold ( $n \cdot \text{stdev}$ )
  - d)  Interpolate missing data
  - e) Apply to all frames
7. File > Save > MAT file

## Optional actions:

- Plot > Derive parameters/ modify data:
  - Display parameter > Velocity magnitude [px/frame]
  - Input maximum value:  autoscale map:
    - \* min [px/frame]: 0
    - \* max [px/frame]:  $\langle \text{max} \rangle$
  - Apply to all frames
- Plot > Modify plot appearance:
  - Vector scale >  autoscale vectors
  - Vector colors > Valid vectors on derivatives: 010 (green)
  - Derived parameter appearance > Color map: Jet
  - Choose colorbar position:
    - \*  Display color bar, position: East
    - \* Colorbar label color: w
  - Apply
- File > Save > Image or movie (jpg, avi, bmp, eps, pdf):
  - AVI file
  - use compression
  - fps: 25
  - Save  $\langle \text{PIVlab\_out} \rangle$ .avi
- File > Save > PIVlab settings:  $\langle \text{PIVlab\_settings} \rangle$ .mat
- File > Save > PIVlab session:  $\langle \text{PIVlab\_session} \rangle$ .mat

### B.3 MATLAB scripts

```

main.m
1 %% 1
2 foldername = './';
3 subfoldernames = {'input','crop','output','threshold','mask','piv'};
4 subfolder_structure(foldername,subfoldernames);
5 %% 2
6 system(['ffmpeg -i "Clip0001.mxf" -q:v 1 -ss 10 -to 25 "',fullfile(
    foldername,subfolder(1,subfoldernames),[subfoldernames{1},'_%04d.jpg"
    ])]);
7 %% 3
8 system(['ImageJ-win64 "',fullfile(foldername,subfolder(1,subfoldernames),[
    subfoldernames{1},'_0001.jpg"'])]);
9 files = dir(fullfile(foldername,subfolder(2,subfoldernames),[
    subfoldernames{1},'*.*jpg']));
10 for i = 1:length(files)
11     newname = strrep(files(i).name,subfoldernames{1},subfoldernames{2});
12     movefile(fullfile(files(i).folder,files(i).name),fullfile(files(i).
        folder,newname));
13 end
14 %% 4a
15 find_first_last_data(foldername,subfoldernames,1);
16 %% 4b
17 n = 3; % odd-order median filter (noise peak distance)
18 th = 2e-2; % difference variation detection threshold
19 [i1,i2] = find_first_last_main(foldername,subfoldernames,n,th,1,1,1);
20 %% 5
21 system(['ImageJ-win64 "',fullfile(foldername,subfolder(3,subfoldernames),[
    subfoldernames{3},'_',sprintf('%04d',i1+ceil(0.3*(i2 - i1))),'.jpg"'])
    ]);
22 files = dir(fullfile(foldername,subfolder(4,subfoldernames),[
    subfoldernames{3},'*.*png']));
23 for i = 1:length(files)
24     newname = strrep(files(i).name,subfoldernames{3},subfoldernames{4});
25     movefile(fullfile(files(i).folder,files(i).name),fullfile(files(i).
        folder,newname));
26 end
27 %% 6
28 objectnames = {'gate','rod','bolt'};
29 clip = 0.5; % default clip limit : 0.2
30 for i = 1:length(objectnames)
31     if isfile(fullfile(foldername,[objectnames{i},'.jpg']))
32         pattern_search(foldername,subfoldernames,objectnames{i},clip
            ,1,1,1);
33     end
34 end
35 %% 7
36 overlay_mask(foldername,subfoldernames,objectnames,1,0);

```



## subfolder\_structure.m

```

1 function subfolder_structure(foldername , subfoldernames)
2 for i = 1:length(subfoldernames)
3     if ~exist(fullfile(foldername , subfolder(i, subfoldernames)), 'dir')
4         mkdir(fullfile(foldername , subfolder(i, subfoldernames)));
5     end
6 end
7 fileID = fopen(fullfile(foldername , '/imagej_settings.txt'), 'a');
8 fclose(fileID);
9 end

```

## subfolder.m (auxiliary function)

```

1 function y = subfolder(x, str)
2 y = [num2str(x), '_', str{x}];
3 end

```

## find\_first\_last\_data.m

```

1 function find_first_last_data(foldername , subfoldernames , doplots)
2 n = numel(dir(fullfile(foldername , subfolder(2, subfoldernames), [
3     subfoldernames{2}, '*.jpg'])));
4 x = zeros(n-1, 1);
5 img_old = imread(fullfile(foldername , subfolder(2, subfoldernames), [
6     subfoldernames{2}, '_0001.jpg']));
7 if doplots, figure; end
8 for i = 1:n-1
9     img_new = imread(fullfile(foldername , subfolder(2, subfoldernames), [
10        subfoldernames{2}, '_', sprintf('%4d', i+1), '.jpg']));
11     y = rgb2gray(im2double(img_new)) - rgb2gray(im2double(img_old));
12     x(i) = norm(y);
13     if doplots
14         [~, j] = max(y(:)); [~, k] = min(y(:));
15         [jy, jx] = ind2sub(size(y), j); [ky, kx] = ind2sub(size(y), k);
16         imshow((y - min(y(:))) ./ (max(y(:)) - min(y(:))), '
17             InitialMagnification', 'fit'), hold on
18         plot(jx, jy, 'rx', kx, ky, 'bx', 'LineWidth', 1.5, 'MarkerSize', 10), hold
19             off
20         title(['Frame pair ', num2str(i-1), '-', num2str(i), ' (err ', num2str(
21             x(i), 3), ')'], 'position', [0 1], 'HorizontalAlignment', 'left')
22         pause(1e-3)
23     end
24     img_old = img_new;
25 end
26 save(fullfile(foldername , 'find_first_last.mat'), 'x');
27 end

```

## find\_first\_last\_main.m

```

1 function [t0, t1] = find_first_last_main(foldername , subfoldernames , n, th,
2     docopy, doplots, saveplots)

```

```

2 load(fullfile(foldername,'find_first_last.mat'),'x')
3 N = length(x);
4 z = movmedian(x,n);
5 zz = abs(diff(z));
6 zz = [0;zz;0]; % padd with 0s to original number of frames
7 t0 = find(zz > th*max(zz),1,'first');
8 t1 = find(zz > th*max(zz),1,'last');
9 if doplot
10     figure
11     plot(1.5:N+0.5,x,'*-')
12     hold all
13     plot(1.5:N+0.5,z,'o-')
14     xlabel('Video frames')
15     ylabel('Norm of frame difference')
16     legend('Original signal',[''movmedian'' (k = ',num2str(n),')'])
17     figure
18     plot(1:N+1,100*zz/max(zz),'.-')
19     hold on
20     plot([1 N+1],100*th*ones(1,2),'r','LineWidth',1.5)
21     hold on
22     plot(t0,100*zz(t0)/max(zz),'or',t1,100*zz(t1)/max(zz),'or','LineWidth',
23           ,1.5)
24     text(t0,100*zz(t0)/max(zz),num2str(t0),'HorizontalAlignment','right','
25           VerticalAlignment','bottom')
26     text(t1,100*zz(t1)/max(zz),num2str(t1),'HorizontalAlignment','left','
27           VerticalAlignment','bottom')
28     xlabel('Video frames')
29     ylabel('Variation of frame difference')
30     legend('1st derivative',[ 'Threshold w.r.t. Max value: ',num2str(100*th
31           ),'%'])
32     if saveplot, hgexport(gcf,fullfile(foldername,'filtering')); end
33 end
34 if docopy
35     files = dir(fullfile(foldername,subfolder(2,subfoldernames),[
36         subfoldernames{2}, '*.jpg']));
37     newfoldername = fullfile(foldername,subfolder(6,subfoldernames),'
38         PIVlab_in');
39     if ~isfolder(newfoldername), mkdir(newfoldername); end
40     for i = t0:t1
41         currentfile = fullfile(files(i).folder,files(i).name);
42         newname_out = strrep(files(i).name,subfoldernames{2},
43             subfoldernames{3});
44         copyfile(currentfile,fullfile(foldername,subfolder(3,
45             subfoldernames),newname_out));
46         newname_piv = strrep(files(i).name,subfoldernames{2},
47             subfoldernames{6});
48         imwrite(rgb2gray(imread(currentfile)),fullfile(newfoldername,
49             newname_piv));
50     end

```

```
41 end
42 end
```

pattern\_search.m

```
1 function [mask,I] = pattern_search(foldername, subfoldernames, object, clip,
   savedata, doplot, saveplot)
2 if nargin < 7, clip = 0.2; end
3 files_gray = dir(fullfile(foldername, subfolder(6, subfoldernames), '
   PIVlab_in', [subfoldernames{6}, '*.jpg']));
4 X_raw = double(imread(fullfile(files_gray(1).folder, files_gray(1).name)));
5 sizX1 = size(X_raw,1);
6 sizX2 = size(X_raw,2);
7 Y_raw = double(rgb2gray(imread(fullfile(foldername, [object, '.jpg']))));
8 sizY1 = size(Y_raw,1);
9 sizY2 = size(Y_raw,2);
10 % improve local contrast (CLAHE)
11 m = ceil(sizX1/sizY1);
12 n = ceil(sizX2/sizY2);
13 X0 = myclahe(X_raw,m,n,clip);
14 Y0 = myclahe(Y_raw,1,1,clip);
15 % center data
16 Xmean = mean(X0(:));
17 X = X0 - Xmean;
18 Y = Y0 - Xmean;
19 % 2D cross-correlation
20 C = xcorr2(X,Y);
21 [~,idx] = max(C(:));
22 [i1,i2] = ind2sub(size(C),idx);
23 % iterate
24 k = 1;
25 dist = -Inf;
26 tol = 50;
27 mask = false(sizX1,sizX2,length(files_gray));
28 I = nan(length(files_gray),2);
29 fprintf('Searching for object ''%s'' ... \n',object)
30 while dist < tol && k < length(files_gray)
31     switch object
32         case 'gate'
33             mask(1:min(sizX1,i1),i2-sizY2+1:end,k) = true;
34         case 'rod'
35             img_gray = X_raw(1:i1,1:i2);
36             threshold = 0.125; % [0, 1)
37             a_min = 20; % angle wrt horizontal (deg)
38             a_max = 40; % angle wrt horizontal (deg)
39             % Edge detection (Sobel filter) -- alternative: 'edge'
               function: edge(img_gray,'canny');
40             g1 = [1 2 1]; g2 = [1 0 -1];
41             Gx = conv2(g1',g2,img_gray,'same'); Gx = (Gx - mean(Gx(:))) ./
               std(Gx(:));
```

```

42     Gy = conv2(g2',g1,img_gray,'same'); Gy = (Gy - mean(Gy(:))) ./
        std(Gy(:));
43     G = sqrt(Gx.^2 + Gy.^2); G = (G - min(G(:))) ./ (max(G(:)) -
        min(G(:)));
44     img_edge = zeros(size(img_gray));
45     img_edge(G > threshold) = 1;
46     % Line detection (Hough transform)
47     [H,T,R] = hough(img_edge,'Theta',(a_min:a_max) - 90);
48     peaks = houghpeaks(H,2);
49     r = R(peaks(:,1));
50     t = T(peaks(:,2));
51     % Masking 'rod'
52     [X,Y] = meshgrid(1:size(img_gray,2),1:size(img_gray,1));
53     Z = X*cos(deg2rad(mean(t))) + Y*sin(deg2rad(mean(t)));
54     img_mask = false(size(img_gray));
55     img_mask(Z > min(r) & Z < max(r)) = true;
56     mask(1:i1,1:i2,k) = img_mask;
57     case 'bolt'
58         bolt_mask = fullfile(foldername,[object,'_mask.png']);
59         if isfile(bolt_mask)
60             silhouette = logical(imread(bolt_mask));
61             mask(i1-sizY1+1:min(sizX1,i1),i2-sizY2+1:i2,k) =
                silhouette(1:(min(sizX1,i1) + sizY1 - i1),:);
62         else
63             mask(i1-sizY1+1:min(sizX1,i1),i2-sizY2+1:i2,k) = true;
64         end
65     otherwise
66         error('unecognised pattern')
67     end
68     I(k,:) = [i1,i2];
69     fprintf('iter %d\t(%s) : \ti1 = %d;\ti2 = %d;\tdist = %.1f\n',k,
        files_gray(k).name,i1,i2,dist);
70     k = k + 1;
71     X_raw = double(imread(fullfile(files_gray(k).folder,files_gray(k).name
        )));
72     X0 = myclahe(X_raw,m,n,clip);
73     Xmean = mean(X0(:));
74     X = X0 - Xmean;
75     Y = Y0 - Xmean;
76     C = xcorr2(X,Y);
77     [~,idx] = max(C(:));
78     [i1,i2] = ind2sub(size(C),idx);
79     dist = sqrt((i1 - I(k-1,1))^2 + (i2 - I(k-1,2))^2);
80 end
81 if strcmp(object,'gate') % keep final 'gate' mask for all remaining frames
82     mask(1:min(sizX1,I(k - 1,1)), ...
83         I(k - 1,2)-sizY2+1:end,k:end) = true;
84 end
85 if savedata

```

```

86     save(fullfile(foldername,[object, '.mat']), 'mask', 'I');
87 end
88 if doplot
89     files_rgb = dir(fullfile(foldername, subfolder(3, subfoldernames), [
90         subfoldernames{3}, '*.jpg']));
91     hf = figure;
92     imagesc(imread(fullfile(files_rgb(k).folder, files_rgb(k).name)))
93     hold on
94     p = imagesc(imread(fullfile(files_rgb(1).folder, files_rgb(1).name)));
95     p.AlphaData = 0.5;
96     hold on
97     plot(I(:,2)-0.5*sizY2, I(:,1)-0.5*sizY1, 'rx-')
98     axis equal tight off
99     if saveplot
100         figstr = fullfile(foldername,[object, '_centroid_pathline']);
101         hf.Units = hf.PaperUnits;
102         hf.PaperSize = [hf.Position(3) hf.Position(4)];
103         print(hf, figstr, '-dpdf');
104     end
105 end
end

```

myclahe.m

```

1 function X = myclahe(x, div_i, div_j, clip)
2 L = 256; % all possible intensity values i = {0, ... 255}
3 [M,N] = size(x); % define grid size : minimum grid size 16 px^2
4 mmax = max(round(M / div_i), 16);
5 nmax = max(round(N / div_j), 16);
6 m = mmax*ones(1, floor(M / mmax));
7 m(1) = m(1) + ceil(0.5*mod(M, mmax));
8 m(end) = m(end) + floor(0.5*mod(M, mmax));
9 msum = cumsum(m);
10 if msum(end) ~= M, error('X-grid does not match actual size.');

```

```

27     % clip the histogram :
28     pmax = max(pdf);
29     clip_sup = clip;
30     clip_inf = 0;
31     clip_mid = 0;
32     bins = 1;
33     excess = 0;
34     iter = 0;
35     while abs(clip_sup - clip_inf) > tol && iter < 100
36         clip_mid = .5*(clip_sup + clip_inf);
37         bins = find(pdf > clip_mid*pmax);
38         excess = (sum(pdf(bins) - clip_mid*pmax)) / L / pmax;
39         if excess + clip_mid > clip
40             clip_sup = clip_mid;
41         elseif excess + clip_mid < clip
42             clip_inf = clip_mid;
43         elseif excess + clip_mid == clip
44             break
45         end
46         iter = iter + 1;
47     end
48     pdf(bins) = clip_mid*pmax;
49     pdf = pdf + excess*pmax;
50     % calculate the cdf :
51     cdf(:,i,j) = round((L - 1)*cumsum(pdf));
52 end
53 end
54 % map intensities using cdf of neighboring grid points :
55 P = msum - floor(0.5*m); dP = P(2:end) - P(1:end-1);
56 Q = nsum - floor(0.5*n); dQ = Q(2:end) - Q(1:end-1);
57 I = [1,P(1);P(end) + 1,M];
58 J = [1,Q(1);Q(end) + 1,N];
59 K = [1,length(m);1,length(n)];
60 X = nan(M,N);
61 % corners are transformed :
62 for i = 1:2
63     for j = 1:2
64         X(I(i,1):I(i,2),J(j,1):J(j,2)) = reshape(cdf(1 + x(I(i,1):I(i,2),J
65             (j,1):J(j,2)),K(1,i),K(2,j)), ...
66             I(i,2) - I(i,1) + 1,J(j,2) - J(j,1) + 1);
67     end
68 end
69 % boundaries are lineary interpolated :
70 for i = 1:(length(m) - 1)
71     u = linspace(0,1,dP(i));
72     U = [diag(1 - u),diag(u)];
73     for j = 1:2
74         f1 = reshape(cdf(1 + x(P(i) + 1:P(i + 1),J(j,1):J(j,2)),i,K(2,j)),
75             ...

```

```

74         P(i + 1) - P(i), J(j, 2) - J(j, 1) + 1);
75     f2 = reshape(cdf(1 + x(P(i) + 1:P(i + 1), J(j, 1):J(j, 2)), i + 1, K(2,
76         j)), ...
77         P(i + 1) - P(i), J(j, 2) - J(j, 1) + 1);
78     X(P(i) + 1:P(i + 1), J(j, 1):J(j, 2)) = U*[f1;f2];
79     end
80 end
81 for j = 1:(length(n) - 1)
82     v = linspace(0, 1, dQ(j));
83     V = [diag(1 - v);diag(v)];
84     for i = 1:2
85         g1 = reshape(cdf(1 + x(I(i, 1):I(i, 2), Q(j) + 1:Q(j + 1)), K(1, i), j),
86             ...
87             I(i, 2) - I(i, 1) + 1, Q(j + 1) - Q(j));
88         g2 = reshape(cdf(1 + x(I(i, 1):I(i, 2), Q(j) + 1:Q(j + 1)), K(1, i), j +
89             1), ...
90             I(i, 2) - I(i, 1) + 1, Q(j + 1) - Q(j));
91         X(I(i, 1):I(i, 2), Q(j) + 1:Q(j + 1)) = [g1, g2]*V;
92     end
93 end
94 % bulk is bilinearly interpolated :
95 for i = 1:(length(m) - 1)
96     u = linspace(0, 1, dP(i));
97     U = [diag(1 - u),diag(u)];
98     for j = 1:(length(n) - 1)
99         v = linspace(0, 1, dQ(j));
100        V = [diag(1 - v);diag(v)];
101        h11 = reshape(cdf(1 + x(P(i) + 1:P(i + 1), Q(j) + 1:Q(j + 1)), i, j),
102            ...
103            dP(i), dQ(j));
104        h12 = reshape(cdf(1 + x(P(i) + 1:P(i + 1), Q(j) + 1:Q(j + 1)), i, j +
105            1), ...
106            dP(i), dQ(j));
107        h21 = reshape(cdf(1 + x(P(i) + 1:P(i + 1), Q(j) + 1:Q(j + 1)), i +
108            1, j), ...
109            dP(i), dQ(j));
110        h22 = reshape(cdf(1 + x(P(i) + 1:P(i + 1), Q(j) + 1:Q(j + 1)), i +
111            1, j + 1), ...
112            dP(i), dQ(j));
113        X(P(i) + 1:P(i + 1), Q(j) + 1:Q(j + 1)) = U*[h11 h12;h21 h22]*V;
114    end
115 end
116 % map intensities to range [0,L) :
117 X = floor((L - 1)*(X - min(X(:))) ./ (max(X(:)) - min(X(:))));
118 end

```

overlay\_mask.m

```

1 function overlay_mask(foldername, subfoldernames, objectnames, saveallmasks,
    remask)

```

```

2  foldernum = 4;
3  if remask, foldernum = 5; end
4  files = dir(fullfile(foldername, subfolder(foldernum, subfoldernames), [
        subfoldernames{foldernum}, '*.png']));
5  n = length(files);
6  dummy = imread(fullfile(files(1).folder, files(1).name));
7  % load objects
8  mask0 = false(size(dummy,1), size(dummy,2), n);
9  for i = 1:length(objectnames)
10     matfile = fullfile(foldername, [objectnames{i}, '.mat']);
11     if isfile(matfile)
12         load(matfile, 'mask');
13         if strcmp(objectnames{i}, 'rod')
14             mask_rod = mask;
15         else
16             mask0 = or(mask0, mask);
17         end
18     end
19 end
20 % remove object(s) from threshold images
21 mask1 = false(size(mask0));
22 for i = 1:n
23     threshold = imread(fullfile(files(i).folder, files(i).name));
24     overlay = or(threshold, mask0(:,:,i));
25     mask1(:,:,i) = overlay;
26     if saveallmasks
27         [~, filename] = fileparts(fullfile(files(i).folder, files(i).name));
28         newname1 = strrep(filename, subfoldernames{4}, subfoldernames
            {5});
29         imwrite(mask1(:,:,i), fullfile(foldername, subfolder(5,
            subfoldernames), [newname1, '.png']));
30     end
31     if exist('mask_rod', 'var')
32         mask1(:,:,i) = or(mask1(:,:,i), mask_rod(:,:,i));
33     end
34 end
35 % overlay masks with "Sequencing style 1-2, 2-3, 3-4, ..."
36 area = round(1e-3*numel(dummy));
37 filename = [subfoldernames{5}, '.tif'];
38 if isfile(filename), delete(filename); end
39 for i = 1:n-1
40     % area opening (remove small objects from binary image)
41     mask2 = ~imfill(bwareaopen(or(~mask1(:,:,i), ~mask1(:,:,i+1)), area),
        'holes');
42     imwrite(mask2, filename, 'WriteMode', 'append');
43 end
44 movefile(filename, fullfile(foldername, subfolder(6, subfoldernames)));
45 end

```



external\_mask\_Callback

```

1 function external_mask_Callback(~, ~, ~)
2 uiwait(helpdlg(['You can load a grayscale *.tif image here:' newline '
   White = masked, black = no mask.']));
3 filepath=retr('filepath');
4 handles=gethand;
5 if size(filepath,1) > 1
6     [FileName,PathName] = uigetfile('*.tif','Select the binary image mask
   file');
7     if isequal(FileName,0) || isequal(PathName,0)
8     else
9         filename = fullfile(PathName,FileName);
10        num_img = length(imfinfo(filename));
11        for i = 1:num_img
12            A = bwboundaries(imread(filename,i));
13            for j = 1:length(A)
14                maskiererx{j,2*i-1} = A{j}(:,2);
15                maskiererx{j,2*i} = A{j}(:,2);
16                maskierery{j,2*i-1} = A{j}(:,1);
17                maskierery{j,2*i} = A{j}(:,1);
18            end
19        end
20        put('maskiererx' ,maskiererx);
21        put('maskierery' ,maskierery);
22        set(handles.mask_hint, 'String', 'Mask active', 'backgroundcolor',
   [0.5 1 0.5]);
23        dispMASK(0.5)
24    end
25 end

```

## B.4 ImageJ scripts

BatchMacro\_Crop.ijm

```

1 dir = getDirectory("image");
2 filestring = File.openAsString(dir + "../imagej_settings.txt")
3 rows=split(filestring,"\n");
4 makeRectangle(rows[2],rows[3],rows[0],rows[1]);
5 run("Crop");

```

BatchMacro\_ColorThreshold.ijm

```

1 dir = getDirectory("image");
2 filestring = File.openAsString(dir + "../imagej_settings.txt")
3 rows=split(filestring,"\n");
4 // Color Thresholder 2.0.0-rc-65/1.51w
5 min=newArray(3);
6 max=newArray(3);

```

```
7 filter=newArray(3);
8 a=getTitle();
9 run("HSB Stack");
10 run("Convert Stack to Images");
11 selectWindow("Hue");
12 rename("0");
13 selectWindow("Saturation");
14 rename("1");
15 selectWindow("Brightness");
16 rename("2");
17 min[0]=rows[4];
18 max[0]=rows[5];
19 filter[0]="pass";
20 min[1]=rows[6];
21 max[1]=rows[7];
22 filter[1]="pass";
23 min[2]=rows[8];
24 max[2]=rows[9];
25 filter[2]="pass";
26 for (i=0;i<3;i++){
27     selectWindow(""+i);
28     setThreshold(min[i], max[i]);
29     run("Convert to Mask");
30     if (filter[i]=="stop")        run("Invert");
31 }
32 imageCalculator("AND create", "0","1");
33 imageCalculator("AND create", "Result of 0","2");
34 for (i=0;i<3;i++){
35     selectWindow(""+i);
36     close();
37 }
38 selectWindow("Result of 0");
39 close();
40 selectWindow("Result of Result of 0");
41 rename(a);
```

## B.5 References

- [1] Sony Corporation, *PXW-FS5/FS5K Solid-State Memory Camcorder. Operating Guide*, version 4-581-849-11 (1), 2015. [Online]. Available: [https://pro.sony/en\\_GB/support-resources/pxw-fs5/manual](https://pro.sony/en_GB/support-resources/pxw-fs5/manual).
- [2] The MathWorks, Inc. (2019). MATLAB®. version R2019a, [Online]. Available: <https://www.mathworks.com/products/matlab.html>.

- [3] FFmpeg Team. (2019). ffmpeg. version 4.1.3, [Online]. Available: <https://www.ffmpeg.org/>.
- [4] W. Rasband. (2019). ImageJ. version 1.52p, [Online]. Available: <https://imagej.net/>.
- [5] W. Thielicke. (2019). PIVlab - particle image velocimetry (PIV) tool. version 2.31, [Online]. Available: <https://www.mathworks.com/matlabcentral/fileexchange/27659-pivlab-particle-image-velocimetry-piv-tool>.
- [6] S. M. Pizer, E. P. Amburn, J. D. Austin, R. Cromartie, A. Geselowitz, T. Greer, B. ter Haar Romeny, J. B. Zimmerman, and K. Zuiderveld, Adaptive histogram equalization and its variations, *Computer Vision, Graphics, and Image Processing*, vol. 39, no. 3, pp. 355–368, 1987. DOI: [10.1016/S0734-189X\(87\)80186-X](https://doi.org/10.1016/S0734-189X(87)80186-X).